

國 立 清 華 大 學  
動力機械工程學系  
博 士 論 文

平面凸輪機構之機械誤差分析及其應用  
Analysis of Mechanical Errors in Planar Cam  
Mechanisms and Its Applications

研 究 生：張 文 桐 (Wen-Tung Chang)  
指 導 教 授：吳 隆 庸 博 士 (Dr. Long-Iong Wu)

中 華 民 國 九 十 六 年 五 月

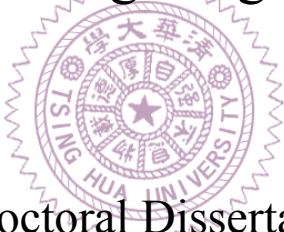
# Analysis of Mechanical Errors in Planar Cam Mechanisms and Its Applications

by

Wen-Tung Chang

Advisor

Dr. Long-Long Wu



A Doctoral Dissertation  
Submitted to

Department of Power Mechanical Engineering  
at  
National Tsing Hua University

In Partial Fulfillment  
of the Requirements for the Degree of  
Doctor of Philosophy

May 2007

國立清華大學博士學位論文  
指導教授推薦書

學系  
動力機械工程研究所 張文桐 君所提之論文

平面凸輪機構之機械誤差分析及其應用，

經由本人指導撰述，同意提付審查。

指導教授 吳隆廟 (簽章)

中華民國 九十六 年 五 月 二十六 日

國立清華大學博士學位論文

考試委員審定書

學 系

動力機械工程研究所 張文桐 君所提之論文

平面凸輪機構之機械誤差分析及其應用，

經本委員會審查，符合博士資格標準。

學位考試委員會

主持人 傅光華 (簽章)

委員 杜頤洲

宋雲國

陳建仁

劉壁達

翁國生

吳隆南

中華民國 九十六 年 五 月 二十六 日

## 摘要

凸輪機構已被廣泛地應用於各種機器與機械裝置中。至今，凸輪仍在機械工業中扮演不可取代的重要角色。由於凸輪為不規則形狀的機械元件，其輪廓較不容易被精確地加工。因此，凸輪輪廓的公差設定及誤差檢測成為設計與製造精密凸輪機構時的重要工作。

凸輪機構的機械誤差分析旨在建立各設計參數之公差量（或偏差量）與從動件運動誤差之間的理論關係。換言之，機械誤差分析為精密凸輪機構之公差設計的基礎。本論文的主要目的為提出一套簡易且有系統的解析方法以進行平面凸輪機構的機械誤差分析。此解析方法並可延伸應用於平面凸輪機構的公差最佳化配置，以及應用於盤形凸輪與共軛凸輪的輪廓誤差檢測。

首先，藉由等效連桿的概念，以及透過凸輪輪廓的徑向尺寸誤差與法線方向誤差間之理論關係的建立，本研究發展出一套稱為等效連桿法的解析方法以預測由盤形凸輪機構之各設計參數偏差量所導致的從動件運動誤差。此方法可以簡易且有系統地進行平面凸輪機構的機械誤差分析，以推導出從動件的位置、速度及加速度誤差方程式。此方法透過分析一個具有確切解的偏心圓凸輪機構以及評估一個因誤用從動件運動曲線所導致之凸輪輪廓誤差的誇張案例以進行理論上的驗證。然後，此方法透過四種常用盤形凸輪機構及一平面凸輪從動件式取放裝置的機械誤差分析以進行演示。

其次，結合等效連桿法以及易製性與易組裝性設計的概念，本研究發展出一套平面凸輪機構的公差最佳化配置程序。此最佳化程序的目標在於使凸輪機構達到最大的易製性與易組裝性，同時確保從動件維持所需的運動精度。此最佳化程序透過一平面凸輪從動件式取放裝置的公差配置以進行演示。

再者，為了檢測盤形凸輪的輪廓誤差，本研究提出一直接且簡潔的解析方式以

處理由三次元量床所量得的座標量測資料。此方法是基於盤形凸輪輪廓的徑向尺寸誤差與法線方向誤差間之理論關係。為了驗證此方法，一對盤形共軛凸輪的檢測實驗被加以進行。由此方法所得到的實驗結果與 Hermite 內插法進行比較。結果顯示此方法可以精確且更有效率地處理座標量測資料以進行盤形凸輪的輪廓誤差檢測。

本研究亦說明如何使用特殊的檢測治具以量測組裝式共軛凸輪機構之共軛條件，以間接地評估共軛凸輪輪廓的誤差量；對於這種間接量測方法，所需要的量具只有針盤指示錶。對於被檢測的共軛凸輪機構，利用等效連桿法，可推導出共軛條件變化量與凸輪輪廓誤差量之間的理論關係。基於此理論關係，用於組裝式共軛凸輪之品質管制的保守準則被加以提出。此間接量測方法特別適用於大量生產之共軛凸輪的品質管制。此外，如果能額外再備有一對已知輪廓誤差之樣板共軛凸輪的話，則透過檢測由一個樣板凸輪併合另一個是待檢測凸輪所搭配組成之共軛凸輪時所量得的共軛條件變化量，將可以估算出待檢測凸輪的輪廓誤差。此間接量測方法透過兩實例以進行演示。同時，一對盤形共軛凸輪透過此方法以進行檢測，並使用三次元量床進行量測，以測試此方法的精確度。結果顯示預測值與實驗值之間具有相當良好的吻合度。

綜合以上所述，本論文提供簡單且有效率的方法以進行各種盤形凸輪與共軛凸輪的機械誤差分析、公差配置與輪廓誤差檢測。

**關鍵詞：**平面凸輪機構，盤形凸輪，等效連桿，機械誤差分析，公差最佳化配置，易製性與易組裝性設計，輪廓誤差檢測，三次元量床，盤形共軛凸輪，共軛凸輪檢測治具，共軛條件分析。

# ABSTRACT

Cam mechanisms have been applied in a wide variety of machines and mechanical devices. Up to now, cams still play an important role in the mechanical industry and cannot be superseded. Because cams are irregular-shaped mechanical components, their profiles cannot be accurately machined with relative ease. Therefore, the cam profile tolerancing and error inspection become important tasks in the design and manufacture of precision cam mechanisms.

The purpose of the mechanical error analysis of the cam mechanism is to establish the theoretical correlation between the tolerance (or deviation) of each design parameter and the follower motion deviation. That is, the analysis of mechanical errors is a fundamental of tolerance design of precision cam mechanisms. The main purpose of this dissertation is to present a relatively simple and systematic analytical method to perform the mechanical error analysis of planar cam mechanisms. This analytical method can also be extended to apply to the optimal tolerance allocation for planar cam mechanisms and to the profile error inspection of disk cams and conjugate cams.

Firstly, by employing the concept of equivalent linkage and the derived correlation between the radial-dimension errors and the normal-direction errors of the cam profile, an analytical method, called the equivalent linkage method, is developed to analytically predict the kinematic errors of the follower caused by the deviation in each design parameter of planar cam mechanisms. This method can effectively and systematically perform the mechanical error analysis of planar cam mechanisms to obtain the displacement, velocity, and acceleration error equations of the follower motion. Here, this method is validated through analyzing an eccentric circular cam mechanism whose exact solution is available, and also examined through evaluating the profile error of an exaggerated case whose relatively large profile error is caused by adopting an incorrect follower motion program. Then the method is illustrated through analyzing the mechanical

errors of all four types of commonly used disk cam mechanisms and a planar cam-follower type pick-and-place device.

Secondly, by incorporating the equivalent linkage method and the concept of design for manufacture and assembly (DFMA), this study develops a procedure of optimal tolerance allocation for planar cam mechanisms. The objective of this optimal procedure is to maximize the manufacturability and assembly of the cam mechanism while maintaining acceptable kinematic accuracy of the follower motion. This optimal procedure is illustrated by allocating the tolerances in a planar cam-follower type pick-and-place device.

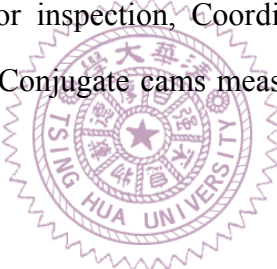
Furthermore, in order to inspect the profile deviations of disk cams, a direct and concise analytical method for dealing with the coordinate measurement data obtained from a coordinate measuring machine (CMM) is proposed. The method is based on the derived correlation between the radial-dimension errors and the normal-direction errors of disk cam profiles. To verify this method, an experiment of inspecting a pair of conjugate disk cams was conducted. The experimental results obtained from the proposed method were compared with those obtained by using the Hermite interpolation method. It shows that this method is accurate and more efficient for dealing with the coordinate measurement data to inspect the profile errors of disk cams.

This study also demonstrates how to use a special measuring fixture to measure the conjugate condition of an assembled conjugate cam mechanism so as to indirectly evaluate the deviations of conjugate cam profiles; for such an indirect measurement method, the only required measuring instrument is a dial indicator. For a conjugate cam mechanism being examined, by employing the equivalent linkage method, the correlation between the conjugate condition variations and the cam profile errors can be derived analytically. Based on the correlation, conservative criteria for quality control of assembled conjugate cams are proposed. This indirect measurement method is particularly suitable for the quality control in mass production of conjugate cams. Furthermore, if a pair of master conjugate cams with known profile errors is additionally available, through the measured conjugate

condition variations of a pair of assembled conjugate cams consisting of one master cam and the other being an inspected cam, then the profile errors of each individual inspected cam can be estimated. This indirect measurement method is illustrated by two examples. Also, a pair of conjugate cams were examined by the method and also measured using a CMM to test the accuracy of the method. It shows quite a good agreement between prediction and experimental results.

In summary, this dissertation provides simple and efficient means for analyzing the mechanical errors, for allocating the tolerances, and for examining the profile errors of various types of disk cams and conjugate cams.

**Keywords:** Planar cam mechanism, Disk cam, Equivalent linkage, Mechanical error analysis, Optimal tolerance allocation, Design for manufacture and assembly (DFMA), Profile error inspection, Coordinate measuring machine (CMM), Conjugate disk cam, Conjugate cams measuring fixture, Conjugate condition analysis.



## 誌 謝

承蒙指導教授吳隆庸博士對於本人在專業領域上的細心指導，使本論文得以順利完成，在此謹向吾師致上衷心的感謝與敬意。同時，亦感謝傅光華教授及林鎮洲教授於本論文之實驗工作進行期間不吝提供實驗場地、設備及實驗研究的寶貴經驗與建議。此外，特別感謝林鎮洲教授及劉進賢教授在我攻讀碩士學位期間給予我學術研究理念的啟蒙以及研究能力的基礎訓練，並感謝已故曾錦煥教授於生前給予我專利相關知識的啟蒙與科技寫作的幫助，使我得以有今日的發展。謹以本論文之研究成果敬獻給五位恩師，以感念他們多年來亦師亦友的支持、鼓勵與提攜。

感謝博士學位考試委員傅光華教授、林鎮洲教授、宋震國教授、陳達仁教授、劉霆教授及鍾添東教授所給予的指教及諸多寶貴意見，使本論文得以更趨完整。

感念機構設計實驗室劉俊賢等學弟們的砥礪與幫助，在此一併誌謝。最後，謹以本論文獻給關心我的父母親與家人們及所有支持我的朋友們。

## **ACKNOWLEDGEMENTS**

I would like to express my most grateful appreciation to my respectable advisor, Professor Long-Iong Wu, for his expert guidance and valuable suggestions throughout this dissertation. I am also grateful to Professor Kuang-Hua Fuh and Professor Chen-Chou Lin for their technical support and advice for the experimental work of this dissertation. In addition, I would like to specially thank Professor Chen-Chou Lin and Professor Chein-Shan Liu for giving me basic training and assistance in academic research during my pursuit of a Master's degree, and Professor Ching-Huan Tseng (deceased) for giving me patent related training and his assistance in technical writing. I would like to dedicate this dissertation to the said five professors, who are also my mentors of life, for their support, encouragement and guidance for many years.

I am grateful to my committee members, Professor Kuang-Hua Fuh, Professor Chen-Chou Lin, Professor Cheng-Kuo Sung, Professor Dar-Zen Chen, Professor Tyng Liu, and Professor Tien-Tung Chung, for their time and efforts in reviewing this dissertation and also their valuable comments and suggestions.

I appreciate Chun-Hsien Liu and other members in the Mechanism Design Laboratory for their encouragement and assistance. Finally, I would like to dedicate this dissertation to my parents, family and friends.

# TABLE OF CONTENTS

<b>ABSTRACT (in CHINESE) .....</b>	<b>I</b>
<b>ABSTRACT (in ENGLISH) .....</b>	<b>III</b>
<b>ACKNOWLEDGEMENTS (in CHINESE) .....</b>	<b>VI</b>
<b>ACKNOWLEDGEMENTS (in ENGLISH) .....</b>	<b>VII</b>
<b>TABLE OF CONTENTS .....</b>	<b>VIII</b>
<b>LIST OF FIGURES .....</b>	<b>XII</b>
<b>LIST OF TABLES .....</b>	<b>XVII</b>
<b>LIST OF SYMBOLS .....</b>	<b>XVIII</b>
<b>ACRONYMS .....</b>	<b>XXX</b>
<b>CHAPTER 1 INTRODUCTION .....</b>	<b>1</b>
1.1 OVERVIEW .....	1
1.2 LITERATURE REVIEW .....	8
1.2.1 Theoretical Design Phase .....	8
1.2.2 Practical Implementation Phase .....	13
1.3 MOTIVATION AND PURPOSE .....	16
1.4 DISSERTATION OUTLINE .....	16
<b>CHAPTER 2 ANALYTICAL PARAMETRIC EXPRESSIONS FOR DISK CAM PROFILES .....</b>	<b>19</b>
2.1 INTRODUCTION .....	19
2.2 FUNDAMENTALS OF DISK CAM PROFILE DETERMINATION .....	19
2.3 DISK CAM WITH AN OFFSET TRANSLATING ROLLER FOLLOWER .....	23
2.4 DISK CAM WITH AN OFFSET TRANSLATING OBLIQUE FLAT-FACED FOLLOWER .....	26
2.5 DISK CAM WITH AN OSCILLATING ROLLER FOLLOWER .....	28
2.6 DISK CAM WITH AN OSCILLATING FLAT-FACED FOLLOWER .....	31
2.7 CONJUGATE DISK CAMS WITH AN OSCILLATING ROLLER FOLLOWER .....	33

## **CHAPTER 3 EQUIVALENT LINKAGE AND MECHANICAL ERROR**

<b>ANALYSIS OF DISK CAM MECHANISMS .....</b>	<b>37</b>
3.1 INTRODUCTION .....	37
3.2 FUNDAMENTALS OF THE EQUIVALENT LINKAGE METHOD .....	38
3.2.1 Sensitivity Analysis Method for Equivalent Linkages .....	39
3.2.2 Radial Profile Error and Normal-Direction Error of Disk Cams .....	42
3.2.3 Analysis Procedure .....	44
3.3 MECHANICAL ERRORS IN DISK CAM MECHANISMS .....	46
3.3.1 Disk Cam with an Offset Translating Roller Follower .....	46
3.3.2 Disk Cam with an Offset Translating Oblique Flat-faced Follower .....	50
3.3.3 Disk Cam with an Oscillating Roller Follower .....	54
3.3.4 Disk Cam with an Oscillating Flat-faced Follower .....	58
3.4 VELOCITY AND ACCELERATION ERROR FUNCTIONS .....	62
3.5 THEORETICAL VALIDATIONS OF THE METHOD .....	63
3.5.1 Validity of the Equivalent Linkage Method .....	64
3.5.2 Validity of the Shift Angle .....	72
3.6 EXAMPLES .....	77
3.6.1 Disk Cam with an Offset Translating Roller Follower .....	77
3.6.2 Disk Cam with an Offset Translating Oblique Flat-faced Follower .....	80
3.6.3 Disk Cam with an Oscillating Roller Follower .....	83
3.6.4 Disk Cam with an Oscillating Flat-faced Follower .....	86
3.7 A PRACTICAL CASE STUDY .....	89
3.7.1 Cam Profiles Determination .....	92
3.7.2 Output Error Equations .....	98
3.7.3 Mechanical Error Analysis Results .....	103
3.8 CONCLUDING REMARKS .....	107

## **CHAPTER 4 OPTIMAL TOLERANCE ALLOCATION FOR DISK CAM**

<b>MECHANISMS .....</b>	<b>110</b>
4.1 INTRODUCTION .....	110
4.2 FUNDAMENTALS OF THE OPTIMAL TOLERANCE ALLOCATION .....	110
4.2.1 The Manufacturability and Assemblability Indices .....	111
4.2.2 The Optimization Model .....	113
4.3 A PRACTICAL CASE STUDY .....	115

4.3.1	Optimization Problem Description .....	115
4.3.2	Optimization Process and Results .....	118
4.4	CONCLUDING REMARKS .....	123

## **CHAPTER 5 INSPECTING PROFILE ERRORS OF DISK CAMS WITH COORDINATE MEASUREMENT .....** **125**

5.1	INTRODUCTION .....	125
5.2	COORDINATE MEASUREMENT AND PROFILE ERRORS INSPECTION OF DISK CAMS .....	125
5.3	EXPERIMENTAL DETAILS .....	130
5.4	RESULTS AND DISCUSSION .....	132
5.5	CONCLUDING REMARKS .....	138

## **CHAPTER 6 SIMPLIFIED METHODS FOR EXAMINING PROFILE ERRORS OF CONJUGATE DISK CAMS — PART I: MEASURING FIXTURES AND CONJUGATE CONDITION ANALYSIS .....** **140**

6.1	INTRODUCTION .....	140
6.2	FUNDAMENTALS OF THE CONJUGATE CAMS MEASURING FIXTURES .....	141
6.3	EQUIVALENT LINKAGE AND CONJUGATE CONDITION ANALYSIS ....	144
6.3.1	Analysis of Subtending Angle Variation .....	145
6.3.2	Analysis of Center Distance Variation .....	151
6.4	EXAMPLES AND DISCUSSION .....	156
6.4.1	Application of Subtending Angle Variation .....	157
6.4.2	Application of Center Distance Variation .....	163
6.5	CONCLUDING REMARKS .....	169

## **CHAPTER 7 SIMPLIFIED METHODS FOR EXAMINING PROFILE ERRORS OF CONJUGATE DISK CAMS — PART II: PROFILE ERRORS ESTIMATION AND EXPERIMENTAL VERIFICATION .....** **170**

7.1	INTRODUCTION .....	170
7.2	CONJUGATE CONDITIONS AND THE PROFILE ERRORS ESTIMATION .....	171
7.2.1	Application of Subtending Angle Variation .....	171

7.2.2 Application of Center Distance Variation .....	173
7.3 EXPERIMENTAL APPARATUS .....	175
7.4 EXPERIMENTAL PROCEDURE .....	184
7.5 RESULTS AND DISCUSSION .....	187
7.6 CONCLUDING REMARKS .....	200
<b>CHAPTER 8 CONCLUSIONS AND RECOMMENDATIONS .....</b>	<b>202</b>
8.1 CONCLUSIONS .....	202
8.2 RECOMMENDATIONS .....	206
<b>APPENDIX A VELOCITY AND ACCELERATION ERROR FUNCTIONS FOR DISK CAM MECHANISMS .....</b>	<b>208</b>
A.1 DISK CAM WITH AN OFFSET TRANSLATING ROLLER FOLLOWER ...	208
A.2 DISK CAM WITH AN OFFSET TRANSLATING OBLIQUE FLAT-FACED FOLLOWER .....	211
A.3 DISK CAM WITH AN OSCILLATING ROLLER FOLLOWER .....	214
A.4 DISK CAM WITH AN OSCILLATING FLAT-FACED FOLLOWER .....	219
<b>APPENDIX B GENERATION OF FIFTH-DEGREE HERMITE INTERPOLATION CURVES .....</b>	<b>223</b>
<b>APPENDIX C MEASURING FIXTURES FOR OTHER TYPES OF CONJUGATE CAM MECHANISMS .....</b>	<b>227</b>
C.1 CONJUGATE DISK CAMS WITH AN OFFSET TRANSLATING ROLLER FOLLOWER .....	227
C.2 CONJUGATE DISK CAMS WITH AN OFFSET TRANSLATING OBLIQUE FLAT-FACED FOLLOWER .....	229
C.3 CONJUGATE DISK CAMS WITH AN OSCILLATING FLAT-FACED FOLLOWER .....	231
<b>REFERENCES.....</b>	<b>234</b>
<b>VITA .....</b>	<b>245</b>
<b>PUBLICATION LIST .....</b>	<b>246</b>

# LIST OF FIGURES

Figure 1.1	Commonly used disk cam mechanisms: (a) disk cam with an offset translating roller follower; (b) disk cam with an offset translating oblique flat-faced follower; (c) disk cam with an oscillating roller follower; (d) disk cam with an oscillating flat-faced follower. ....	2
Figure 1.2	Positive-drive cam mechanisms: (a) grooved cam with an oscillating roller follower; (b) constant-diameter cam with a translating roller follower; (c) constant-breadth cam with a translating flat-faced follower; (d) conjugate disk cams with an oscillating roller follower. ....	3
Figure 1.3	Manufacturing drawing of a disk cam [5]. ....	5
Figure 1.4	Manufacturing drawing of a pair of conjugate disk cams machined in one piece [3]. ....	5
Figure 1.5	Flowchart for producing precision cam mechanisms. ....	7
Figure 1.6	Assembled conjugate cams with a measuring fixture consisting of two oscillating roller followers [3]. ....	15
Figure 2.1	Three-link direct-contact mechanism (oscillating follower case). ....	20
Figure 2.2	Three-link direct-contact mechanism (translating follower case). ....	21
Figure 2.3	Overconstrained direct-contact mechanism. ....	22
Figure 2.4	Disk cam with an offset translating roller follower. ....	24
Figure 2.5	Disk cam with an offset translating oblique flat-faced follower. ....	26
Figure 2.6	Disk cam with an oscillating roller follower. ....	29
Figure 2.7	Disk cam with an oscillating flat-faced follower. ....	31
Figure 2.8	Conjugate disk cams with an oscillating roller follower. ....	34
Figure 3.1	Three-link direct-contact mechanism and its equivalent four-bar linkage. ....	38
Figure 3.2	Actual and theoretical profiles of disk cams. ....	43
Figure 3.3	Flowchart of the analysis procedure for the equivalent linkage method. ....	45
Figure 3.4	Disk cam with an offset translating roller follower and its equivalent slider-crank linkage. ....	47
Figure 3.5	Disk cam with an offset translating roller follower and its actual	

cam profile. ....	49
Figure 3.6 Disk cam with an offset translating oblique flat-faced follower and its equivalent Scotch yoke mechanism. ....	50
Figure 3.7 Disk cam with an offset translating oblique flat-faced follower and its actual cam profile. ....	54
Figure 3.8 Disk cam with an oscillating roller follower and its equivalent four-bar linkage. ....	55
Figure 3.9 Disk cam with an oscillating roller follower and its actual cam profile. ....	58
Figure 3.10 Disk cam with an oscillating flat-faced follower and its equivalent Whithworth mechanism. ....	59
Figure 3.11 Disk cam with an oscillating flat-faced follower and its actual cam profile. ....	62
Figure 3.12 Eccentric circular cam with an oscillating roller follower and its invariant equivalent four-bar linkage. ....	64
Figure 3.13 Exact and approximate solutions and their comparisons for a circular cam profile with a tolerance grade of IT6. ....	68
Figure 3.14 Comparisons between exact and approximate solutions for a circular cam profile with a tolerance grade raised from IT6 to IT13. ....	69
Figure 3.15 Geometric correlation between the radial profile error and the normal-direction error of a circular cam. ....	70
Figure 3.16 Comparisons between exact and approximate solutions for a circular cam profile with a tolerance grade raised from IT6 to IT13 after considering the compensated shift angle and the second-order terms of the Taylor expansions of the displacement equation. ....	72
Figure 3.17 Theoretical and actual cam profiles of an exaggerated case. ....	73
Figure 3.18 Cam profile errors of an exaggerated case. ....	74
Figure 3.19 Comparisons between exact and approximate solutions of an exaggerated case. ....	75
Figure 3.20 Tangential deviation angle of an exaggerated case. ....	77
Figure 3.21 Mechanical error analysis results of a disk cam with an offset translating roller follower. ....	79
Figure 3.22 Velocity and acceleration error functions of a disk cam with an offset translating roller follower. ....	79

Figure 3.23	Mechanical error analysis results of a disk cam with an offset translating oblique flat-faced follower. ....	82
Figure 3.24	Velocity and acceleration error functions of a disk cam with an offset translating oblique flat-faced follower. ....	82
Figure 3.25	Mechanical error analysis results of a disk cam with an oscillating roller follower. ....	85
Figure 3.26	Velocity and acceleration error functions of a disk cam with an oscillating roller follower. ....	85
Figure 3.27	Mechanical error analysis results of a disk cam with an oscillating flat-faced follower. ....	87
Figure 3.28	Velocity and acceleration error functions of a disk cam with an oscillating flat-faced follower. ....	88
Figure 3.29	The MEG X6061 planar cam-follower type pick-and-place device [106]. ....	90
Figure 3.30	Planar cam-follower type pick-and-place device and its equivalent ten-bar linkage. ....	91
Figure 3.31	Functional requirements of a planar cam-follower type pick-and-place device: (a) motion programs; (b) locus of the functional output (the reference point P); (c) angular displacements of the dual primary oscillating followers. ....	95
Figure 3.32	Profiles of the dual cams A and B in a planar cam-follower type pick-and-place device. ....	96
Figure 3.33	Angles of a planar cam-follower type pick-and-place device. ....	97
Figure 3.34	Mechanical error analysis results of a planar cam-follower type pick-and-place device. ....	104
Figure 4.1	Maximum expected deviations of a planar cam-follower type pick-and-place device caused by the optimized tolerances. ....	120
Figure 4.2	Maximum expected deviations of a planar cam-follower type pick-and-place device caused by the re-optimized tolerances. ....	123
Figure 5.1	Measuring a disk cam profile with a touch-trigger probe. ....	126
Figure 5.2	Conjugate cam mechanism and its actual cam profiles. ....	128
Figure 5.3	Experiment for inspecting conjugate cam profiles by using a CMM: (a) the CMM used in this experiment; (b) the touch-trigger probe used in this experiment; (c) the inspection of cam A; (d) the	

inspection of cam B .....	131
Figure 5.4 Evaluated results of profile errors of cam A .....	133
Figure 5.5 Evaluated results of profile errors of cam B .....	134
Figure 5.6 Pressure angles and shift angles of the conjugate cam mechanism .....	135
Figure 6.1 Assembled conjugate cams with a measuring fixture consisting of two oscillating roller followers .....	142
Figure 6.2 Assembled conjugate cams with a measuring fixture consisting of a floating roller follower pivoted to a slider. ....	143
Figure 6.3 Conjugate cam mechanism with two oscillating roller followers and its equivalent six-bar linkage. ....	146
Figure 6.4 Conjugate cam mechanism with a slider-pivoted floating roller follower and its equivalent six-bar linkage. ....	152
Figure 6.5 Mechanical error analysis results of an assembled conjugate cam mechanism with two oscillating roller followers. ....	160
Figure 6.6 Subtending angle variation of an assembled conjugate cam mechanism with two oscillating roller followers. ....	161
Figure 6.7 Relative variations of the subtending angle with respect to the radial profile errors. ....	163
Figure 6.8 Mechanical error analysis results of an assembled conjugate cam mechanism with a slider-pivoted floating roller follower. ....	166
Figure 6.9 Upper and lower limits of the center distance variation. ....	166
Figure 6.10 Relative variations of the center distance with respect to the radial profile errors. ....	168
Figure 7.1 Solid CAD model of an assembled conjugate cam mechanism with an integrated-type measuring fixture and its exploded assemblies. ....	176
Figure 7.2 Partially sectional drawing of the conjugate cam subassembly. ....	178
Figure 7.3 Partially sectional drawing of the follower subassembly. ....	178
Figure 7.4 Solid CAD model of the follower subassembly. ....	179
Figure 7.5 Setup of the follower subassembly for measuring the subtending angle variation. ....	180
Figure 7.6 Setup of the follower subassembly for measuring the center distance variation. ....	181
Figure 7.7 Built assembled conjugate cams with integrated-type measuring fixture. ....	182

Figure 7.8	Schematic of the experimental apparatus and instrumentation. ....	183
Figure 7.9	Identifying the initial angular position for the cam rotation by using a fiber optic sensor. ....	184
Figure 7.10	Experiment for measuring the subtending angle variation by using a digimatic indicator. ....	185
Figure 7.11	Experiment for measuring the center distance variation by using a digimatic indicator. ....	186
Figure 7.12	Measured and predicted results of the subtending angle variation. ....	188
Figure 7.13	Measured and predicted results of the cam profile errors (based on the experiment for measuring the subtending angle variation). ....	189
Figure 7.14	Differences between the measured and predicted results (based on the experiment for measuring the subtending angle variation). ....	191
Figure 7.15	Measured and predicted results of the center distance variation. ....	193
Figure 7.16	Measured and predicted results of the cam profile errors (based on the experiment for measuring the center distance variation). ....	194
Figure 7.17	Differences between the measured and predicted results (based on the experiment for measuring the center distance variation). ....	197
Figure 7.18	Allowable upper and lower limits of the conjugate condition variations. ....	199
Figure C.1	Conjugate disk cams with an offset translating roller follower. ....	227
Figure C.2	Assembled conjugate cams with a measuring fixture consisting of two offset translating roller followers. ....	228
Figure C.3	Conjugate disk cams with an offset translating oblique flat-faced follower. ....	229
Figure C.4	Assembled conjugate cams with a measuring fixture consisting of two offset translating oblique flat-faced followers. ....	230
Figure C.5	Conjugate disk cams with an oscillating flat-faced follower. ....	231
Figure C.6	Assembled conjugate cams with a measuring fixture consisting of two oscillating flat-faced followers. ....	232
Figure C.7	Assembled conjugate cams with a measuring fixture consisting of a floating flat-faced follower pivoted on a slider. ....	233

## LIST OF TABLES

Table 3.1	Input angles and extreme values of the example for the mechanical error analysis of a disk cam with an offset translating roller follower. ....	80
Table 3.2	Input angles and extreme values of the example for the mechanical error analysis of a disk cam with an offset translating oblique flat-faced follower. ....	83
Table 3.3	Input angles and extreme values of the example for the mechanical error analysis of a disk cam with an oscillating roller follower. ....	86
Table 3.4	Input angles and extreme values of the example for the mechanical error analysis of a disk cam with an osillating flat-faced follower. ....	88
Table 3.5	Input angles and extreme values of angles of a planar cam-follower type pick-and-place device. ....	98
Table 4.1	Weighting factors and lower and upper bounds of tolerances. ....	115
Table 4.2	Initial design and computation results for the optimization. ....	119
Table 4.3	Initial design and computation results for the re-optimization. ....	122
Table 5.1	Input angles and extreme values of the experiment for inspecting conjugate cam profiles by using a CMM and the profile errors evaluation. ....	136
Table 6.1	Input angles and extreme values of an example for the application of subtending angle variation. ....	162
Table 6.2	Tolerance grades and relative variations of the subtending angle. ....	163
Table 6.3	Input angles and extreme values of an example for the application of center distance variation. ....	167
Table 6.4	Tolerance grades and relative variations of the center distance. ....	168
Table 7.1	Nominal and actual values of the constant parameters. ....	187
Table 7.2	Input angles and extreme values of the experiment for measuring the subtending angle variation and the profile errors estimation. ....	190
Table 7.3	Input angles and extreme values of the experiment for measuring the center distance variation and the profile errors estimation. ....	195

## LIST OF SYMBOLS

$a, a(\theta)$	linear or angular acceleration program of the follower
A	theoretical contact point of the cam and the follower
$A, A(t)$	linear or angular acceleration of the follower (in time domain)
$A_e$	projection point of point A <sub>r</sub> on line KA
$A_i$	the $i$ -th measured point at the cam surface
$\mathbf{A}_i$	positional vector of the $i$ -th measured point at the cam surface
$A_n$	intersection of the contact normal of point A and the actual cam profile
$A_r$	intersection of line O <sub>2</sub> A and the actual cam profile
$A_t$	actual contact point under the radial vector touch mode
AI	asembility index
$b$	theoretical or constant breadth of the offset translating oblique flat-faced follower
$b^*$	actual or variable breadth between two offset translating oblique flat-faced followers
B	theoretical contact point of the cam and the follower
$B_n$	intersection of the contact normal of point B and the actual cam profile
$B_r$	intersection of line O <sub>2</sub> B and the actual cam profile
C	roller center
CI	comprehensive index
$d$	theoretical or constant distance between roller centers of the offset translating roller follower
$d^*$	actual or variable distance between roller centers of two offset translating roller followers
D	roller center
$D$	perpendicular distance from the follower pivot center O <sub>3</sub> to the measuring axis of the dial indicator
$e$	follower offset
E	auxiliary point

$f$	theoretical or constant distance from the cam center to the follower pivot point
$f^*$	actual or variable distance from the cam center to the follower pivot point
$f_h$	horizontal component of $f$
$f_v$	vertical component of $f$
$F$	auxiliary point
$F$	constraint function of an equivalent linkage
$\mathbf{F}$	constraint function vector of a mechanism
$F_1, F_2, \dots, F_m$	constraint functions of a mechanism
$F_A, F_B$	constraint functions of an equivalent linkage
$G$	roller center
$G_A, G_B$	constraint equations of four-bar loops
$G_n$	stylus ball center of the touch-trigger probe recorded through the DCC measurement with the normal vector touch mode
$G_r$	stylus ball center of the touch-trigger probe recorded through the DCC measurement with the radial vector touch mode
$H$	roller center
$\mathbf{H}, \mathbf{H}(w)$	Hermite interpolation curve
$H_x, H_y, H_z$	x-, y- and z-components of the Hermite interpolation curve
$I_{ij}$	velocity instant center of links $i$ and $j$
$j$	linear or angular jerk function of the follower
$J$	sensitivity Jacobian matrix of a mechanism
$J_G$	half joint
$J_H$	half joint
$\mathbf{J}_i$	sensitivity Jacobian vector relating of the functional output variables and the $i$ -th link-length parameter
$K$	center of curvature of the cam profile, center of the circular cam
$K_2$	center of curvature of the cam profile
$K_3$	center of curvature of the follower profile
$K_A$	center of curvature of cam A
$K_B$	center of curvature of cam B
$l$	arm length of the oscillating roller follower
$l_5$	link length

$l_6$	link length
$l_A$	arm length of the oscillating roller follower
$l_B$	arm length of the oscillating roller follower
$l_C$	arm length of the oscillating roller follower
$l_D$	arm length of the oscillating roller follower
$l_G$	arm length of the oscillating roller follower
$l_H$	arm length of the oscillating roller follower
$L, L(\theta)$	theoretical displacement function of the translating follower
$L_h, L_h(\theta)$	horizontal displacement function of the follower
$L_v, L_v(\theta)$	vertical displacement function of the follower
<b>M</b>	reference point on the follower
<b>M</b>	coefficient matrix
MI	manufacturability index
$n-n$	normal line
$n'-n'$	normal line
<b>n, n</b> ( $\theta$ )	unit normal vector to the theoretical cam profile
<b>n</b> <sub>A</sub> , <b>n</b> <sub>A</sub> ( $\theta$ )	unit normal vector to the theoretical cam profile
<b>n</b> <sub>B</sub> , <b>n</b> <sub>B</sub> ( $\theta$ )	unit normal vector to the theoretical cam profile
$O_2$	fixed pivot of the cam, the cam center
$O_3$	fixed pivot of the oscillating follower
P	reference point on the follower
$P_i$	the $i$ -th position of reference point P
$q$	distance from the cam center to instant center $I_{23}$
$q_A$	distance from the cam center to instant center $I_{23}$
$q_B$	distance from the cam center to instant center $I_{24}$
Q	location of instant center $I_{23}$
$Q_A$	location of instant center $I_{23}$
$Q_B$	location of instant center $I_{24}$
$r$	radial dimension of the cam profile
<b>r</b>	link-length parameter vector of a mechanism
$r_1, r_2, \dots, r_n$	link-length parameters of a mechanism
$r_{1h}$	horizontal component of $r_1$
$r_{1v}$	vertical component of $r_1$

$r_{2A}$	link-length parameter of an equivalent linkage
$r_{2B}$	link-length parameter of an equivalent linkage
$r_{3A}$	link-length parameter of an equivalent linkage
$r_{3B}$	link-length parameter of an equivalent linkage
$r_{3C}$	link-length parameter of an equivalent linkage
$r_{3G}$	link-length parameter of an equivalent linkage
$r_{4D}$	link-length parameter of an equivalent linkage
$r_{4H}$	link-length parameter of an equivalent linkage
$r_A$	radial dimension of cam A
$r_B$	radial dimension of cam B
$r_b$	radius of the base circle
$r_{bA}$	radius of the base circle of cam A
$r_{bB}$	radius of the base circle of cam B
$r_f$	theoretical radius of the follower roller
$r_{fC}$	actual radius of follower roller C
$r_{fD}$	actual radius of follower roller D
$r_i$	constant parameter of link $i$ , the $i$ -th dimensional parameter of a mechanism
$r_i^*$	dimensional variable of a mechanism
$r_t$	radius of the stylus ball of the touch-trigger probe
$R$	radius of the circular cam
$\mathbf{R}, \mathbf{R}(\theta)$	theoretical cam profile coordinates
$\mathbf{R}_A, \mathbf{R}_A(\theta)$	theoretical cam profile coordinates
$\mathbf{R}_B, \mathbf{R}_B(\theta)$	theoretical cam profile coordinates
$R_F$	higher-order terms
$S, S(\theta)$	linear or angular motion program of the follower
$S_h, S_h(\theta)$	horizontal motion program of the follower
$S_v, S_v(\theta)$	vertical motion program of the follower
$t$	time
$T$	point on the stylus ball of the touch-trigger probe
$u$	distance from point P to point A
$U$	coefficient matrix
$\mathbf{U}_i$	coefficient vector of parameter $w$ to the power of $i$

$U_{ix}, U_{iy}, U_{iz}$	x-, y- and z-components of coefficient vector $\mathbf{U}_i$
$v, v(\theta)$	linear or angular velocity program of the follower
$v_h, v_h(\theta)$	horizontal velocity program of the follower
$v_v, v_v(\theta)$	vertical velocity program of the follower
$V, V(t)$	linear or angular velocity of the follower (in time domain)
$V_Q$	speed of point Q
$w$	independent parameter of the Hermite interpolation curve
$w_{Ai}$	weighting factor assigned to the $i$ -th assembly tolerance
$w_{C,A}$	weighting factor assigned to AI
$w_{C,M}$	weighting factor assigned to MI
$w_{Mi}$	weighting factor assigned to the $i$ -th manufacturing tolerance
$W_{a1}, W_{a2}, W_{a3}$	derived sub-terms
$W_{b1}, W_{b2}, \dots, W_{b5}$	derived sub-terms
$W_{c1}, W_{c2}, \dots, W_{c7}$	derived sub-terms
$W_{d1}, W_{d2}, \dots, W_{d5}$	derived sub-terms
X-Y	Cartesian coordinate system fixed on the cam
Z	axial position
$\alpha$	auxiliary angle
$\alpha_2$	angular acceleration of the cam
$\alpha_A$	auxiliary angle
$\alpha_B$	auxiliary angle
$\alpha_E$	subtending angle of the follower translation and the horizontal line
$\alpha_f$	subtending angle of line $O_2O_3$ and the horizontal line
$\beta$	auxiliary angle
$\gamma$	auxiliary angle
$\gamma_A$	angular displacement of the oscillating roller follower
$\gamma_B$	angular displacement of the oscillating roller follower
$\delta$	motion variation of the indicator reading
$\delta_A$	difference between $\Delta r_{A, \text{mea}}$ and $\Delta r_{A, \text{int}}$
$\delta_B$	difference between $\Delta r_{B, \text{mea}}$ and $\Delta r_{B, \text{int}}$
$\delta_f$	difference between $\Delta f_{\min}^+$ and $\Delta f_{\max}^-$

$\delta_{L_h}$	difference between the maximum and minimum values of $\Delta L_{h, \text{rss}}$
$\delta_{L_h}^{(u)}$	upper bound of $\delta_{L_h}$
$\delta_{L_v}$	difference between the maximum and minimum values of $\Delta L_{v, \text{rss}}$
$\delta_{L_v}^{(u)}$	upper bound of $\delta_{L_v}$
$\delta_n$	difference between $\Delta n_{\text{ap}}$ and $\Delta n_{\text{ex}}$
$\delta_r$	difference between $\Delta r_{\text{ap}}$ and $\Delta r_{\text{ex}}$
$\delta_S$	difference between $\Delta S_{\text{ap}}$ and $\Delta S_{\text{ex}}$
$\delta_\eta$	difference between $\Delta \eta_{\min}^+$ and $\Delta \eta_{\max}^-$
$\delta_{\psi_j}$	difference between the maximum and minimum values of $\Delta \psi_{j, \text{rss}}$
$\delta_{\psi_j}^{(u)}$	upper bound of $\delta_{\psi_j}$
$\Delta$	delta, variation, increment
$\Delta a, \Delta a(\theta)$	linear or angular acceleration error of the follower
$\Delta A, \Delta A(t)$	linear or angular acceleration error of the follower (in time domain)
$\Delta A_e$	$\Delta A$ caused by $\Delta e$
$\Delta A_f$	$\Delta A$ caused by $\Delta f$
$\Delta A_l$	$\Delta A$ caused by $\Delta l$
$\Delta A_r$	$\Delta A$ caused by $\Delta r$
$\Delta A_{rf}$	$\Delta A$ caused by $\Delta r_f$
$\Delta A_\phi$	$\Delta A$ caused by $\Delta \phi$
$\Delta b$	variation of the breadth between two offset translating oblique flat-faced followers
$\Delta d$	variation of the distance between roller centers of two offset translating roller followers
$\Delta e$	deviation of the follower offset
$\Delta f$	deviation of the distance from the cam center to the follower pivot point
$\Delta f_{\text{est}}$	predicted center distance variation between the cam and follower pivots
$\Delta f_h$	horizontal component of the deviation of the distance from the

	cam center to the follower pivot point
$\Delta f_l$	$\Delta f$ caused by $\Delta l_A$ and $\Delta l_B$
$\Delta f_{\text{mea}}$	measured center distance variation between the cam and follower pivots
$\Delta f_n$	$\Delta f$ caused by $\Delta n_A$ and $\Delta n_B$
$\Delta f_r$	$\Delta f$ caused by $\Delta r_A$ and $\Delta r_B$
$\Delta f_{rf}$	$\Delta f$ caused by $\Delta r_{fC}$ and $\Delta r_{fD}$
$\Delta f_v$	vertical component of the deviation of the distance from the cam center to the follower pivot point
$\Delta f_\eta$	$\Delta f$ caused by $\Delta \eta$
$\Delta f^+$	upper limit of allowable $\Delta f_{\text{mea}}$
$\Delta f_{\min}^+$	minimum value of $\Delta f^+$
$\Delta f^-$	lower limit of allowable $\Delta f_{\text{mea}}$
$\Delta f_{\max}^-$	minimum value of $\Delta f^-$
$\Delta l$	deviation of the arm length of the oscillating roller follower
$\Delta l_5$	deviation of the link length
$\Delta l_6$	deviation of the link length
$\Delta l_A$	deviation of the arm length of the oscillating roller follower
$\Delta l_B$	deviation of the arm length of the oscillating roller follower
$\Delta l_C$	deviation of the arm length of the oscillating roller follower
$\Delta l_D$	deviation of the arm length of the oscillating roller follower
$\Delta l_G$	deviation of the arm length of the oscillating roller follower
$\Delta l_H$	deviation of the arm length of the oscillating roller follower
$\Delta L, \Delta L(\theta)$	displacement error of the translating follower
$\Delta L_h, \Delta L_h(\theta)$	horizontal displacement error of the follower
$\Delta L_h^{(u)}$	upper bound of $\Delta L_{h, \text{rss}}$
$\Delta L_{h(i)}$	horizontal displacement error of the follower caused by the error of the $i$ -th dimensional parameter
$\Delta L_{h, \max}$	maximum value of $\Delta L_h$
$\Delta L_{h, \text{rss}}$	root-sum-square form of $\Delta L_h$
$\Delta L_{h, \text{wor}}$	worst-case form of $\Delta L_h$

$\Delta L_v$ , $\Delta L_v(\theta)$	vertical displacement error of the follower
$\Delta L_v^{(u)}$	upper bound of $\Delta L_{v, \text{rss}}$
$\Delta L_{v(i)}$	vertical displacement error of the follower caused by the error of the $i$ -th dimensional parameter
$\Delta L_{v, \text{max}}$	maximum value of $\Delta L_v$
$\Delta L_{v, \text{rss}}$	root-sum-square form of $\Delta L_v$
$\Delta L_{v, \text{wor}}$	worst-case form of $\Delta L_v$
$\Delta n$	normal-direction error of the cam profile
$\Delta n_{\text{ap}}$	approximate expression of $\Delta n$
$\Delta n_A$	normal-direction error of cam A
$\Delta n_{A, \text{mea}}$	measured normal-direction error of cam A
$\Delta n_B$	normal-direction error of cam B
$\Delta n_{B, \text{mea}}$	measured normal-direction error of cam B
$\Delta n_{\text{ex}}$	exact value of $\Delta n$
$\Delta r$	radial-dimension error of the cam profile
$\Delta r$	deviations of the link-length parameters of a mechanism
$\Delta r_{\text{ap}}$	approximate expression of $\Delta r$
$\Delta r_A$	radial-dimension error of cam A
$\Delta r_{A, \text{est}}$	estimated radial-dimension error of cam A
$\Delta r_{A, \text{int}}$	interpolated radial-dimension error of cam A
$\Delta r_{A, \text{mea}}$	measured radial-dimension error of cam A
$\Delta r_{A1}, \Delta r_{A2}, \dots, \Delta r_{Ak}$	assembly tolerances
$\Delta r_B$	radial-dimension error of cam B
$\Delta r_{B, \text{est}}$	estimated radial-dimension error of cam B
$\Delta r_{B, \text{int}}$	interpolated radial-dimension error of cam B
$\Delta r_{B, \text{mea}}$	measured radial-dimension error of cam B
$\Delta r_e$	incorrect radial-dimension error of the cam profile
$\Delta r_{\text{ex}}$	exact expression of $\Delta r$
$\Delta r_f$	deviation of the radius of the follower roller
$\Delta r_{fC}$	deviation of the radius of follower roller C
$\Delta r_{fD}$	deviation of the radius of follower roller D

$\Delta r_i$	deviation of the length of link $i$ , the $i$ -th dimensional variation or tolerance of a mechanism
$\Delta r_i^{(l)}$	lower bound of the $i$ -th dimensional tolerance of a mechanism
$\Delta r_i^{(u)}$	upper bound of the $i$ -th dimensional tolerance of a mechanism
$\Delta r_{M1}, \Delta r_{M2}, \dots, \Delta r_{Mh}$	manufacturing tolerances
$\Delta S, \Delta S(\theta)$	linear or angular motion error of the follower
$\Delta S_{ap}$	approximate expression of $\Delta S$
$\Delta S_A$	angular motion error of the oscillating roller follower
$\Delta S_{Af}$	$\Delta S_A$ caused by $\Delta f$
$\Delta S_{Al}$	$\Delta S_A$ caused by $\Delta l_A$
$\Delta S_{An}$	$\Delta S_A$ caused by $\Delta n_A$
$\Delta S_{Ar}$	$\Delta S_A$ caused by $\Delta r_A$
$\Delta S_{Arf}$	$\Delta S_A$ caused by $\Delta r_{fc}$
$\Delta S_B$	angular motion error of the oscillating roller follower
$\Delta S_{Bf}$	$\Delta S_B$ caused by $\Delta f$
$\Delta S_{Bl}$	$\Delta S_B$ caused by $\Delta l_B$
$\Delta S_{Bn}$	$\Delta S_B$ caused by $\Delta n_B$
$\Delta S_{Br}$	$\Delta S_B$ caused by $\Delta r_B$
$\Delta S_{Brf}$	$\Delta S_B$ caused by $\Delta r_{fd}$
$\Delta S_e$	$\Delta S$ caused by $\Delta e$
$\Delta S_{ex}$	exact expression of $\Delta S$
$\Delta S_f$	$\Delta S$ caused by $\Delta f$
$\Delta S_l$	$\Delta S$ caused by $\Delta l$
$\Delta S_{\max}$	maximum value of $\Delta S$
$\Delta S_n$	$\Delta S$ caused by $\Delta n$
$\Delta S_r$	$\Delta S$ caused by $\Delta r$
$\Delta S_{rf}$	$\Delta S$ caused by $\Delta r_f$
$\Delta S_{rss}$	root-sum-square form of $\Delta S$
$\Delta S_{wor}$	worst-case form of $\Delta S$
$\Delta S_\phi$	$\Delta S$ caused by $\Delta \phi$
$\Delta v, \Delta v(\theta)$	linear or angular velocity error of the follower

$\Delta V, \Delta V(t)$	linear or angular velocity error of the follower (in time domain)
$\Delta V_e$	$\Delta V$ caused by $\Delta e$
$\Delta V_f$	$\Delta V$ caused by $\Delta f$
$\Delta V_l$	$\Delta V$ caused by $\Delta l$
$\Delta V_r$	$\Delta V$ caused by $\Delta r$
$\Delta V_{rf}$	$\Delta V$ caused by $\Delta r_f$
$\Delta V_\phi$	$\Delta V$ caused by $\Delta\phi$
$\Delta w$	increment of the parameter of the Hermite interpolation curve
$\Delta\alpha_E$	deviation of the subtending angle of the follower translation and the horizontal line
$\Delta\eta$	deviation of the subtending angle of the follower arms
$\Delta\eta_A$	deviation of the subtending angle of the follower arms
$\Delta\eta_B$	deviation of the subtending angle of the follower arms
$\Delta\eta_{\text{est}}$	predicted subtending angle variation of the follower arms
$\Delta\eta_f$	$\Delta\eta$ caused by $\Delta f$
$\Delta\eta_l$	$\Delta\eta$ caused by $\Delta l_A$ and $\Delta l_B$
$\Delta\eta_{\text{mea}}$	measured subtending angle variation of the follower arms
$\Delta\eta_n$	$\Delta\eta$ caused by $\Delta n_A$ and $\Delta n_B$
$\Delta\eta_r$	$\Delta\eta$ caused by $\Delta r_A$ and $\Delta r_B$
$\Delta\eta_{rf}$	$\Delta\eta$ caused by $\Delta r_{fC}$ and $\Delta r_{fD}$
$\Delta\eta^+$	upper limit of allowable $\Delta\eta_{\text{mea}}$
$\Delta\eta_{\min}^+$	minimum value of $\Delta\eta^+$
$\Delta\eta^-$	lower limit of allowable $\Delta\eta_{\text{mea}}$
$\Delta\eta_{\max}^-$	maximum value of $\Delta\eta^-$
$\Delta\theta$	increment of the cam rotation angle
$\Delta\boldsymbol{\theta}$	deviations of the input variables of a mechanism
$\Delta\theta_i$	deviation of the angular displacement of link $i$
$\Delta\xi, \Delta\xi(\theta)$	displacement error of the oscillating follower
$\Delta\xi_l$	$\Delta\xi$ caused by $\Delta l_A$ and $\Delta l_B$
$\Delta\xi_n$	$\Delta\xi$ caused by $\Delta n_A$ and $\Delta n_B$
$\Delta\xi_r$	$\Delta\xi$ caused by $\Delta r_A$ and $\Delta r_B$

$\Delta\xi_{rf}$	$\Delta\xi$ caused by $\Delta r_{fc}$ and $\Delta r_{fd}$
$\Delta\xi_\eta$	$\Delta\xi$ caused by $\Delta\eta$
$\Delta\phi$	deviation of the oblique angle (invariant pressure angle) of the translating flat-faced follower
$\Delta\Psi, \Delta\Psi(\theta)$	overall mechanical errors of the functional output variables of a mechanism
$\Delta\Psi_{(i)}$	mechanical error of the functional output variables caused by the deviation of the $i$ -th link-length parameter
$\Delta\Psi_j^{(u)}$	upper bound of $\Delta\Psi_{j, rss}$
$\Delta\Psi_{j(i)}$	mechanical error of the $j$ -th functional output variable caused by the deviation of the $i$ -th link-length parameter
$\Delta\Psi_{j, rss}$	root-sum-square form of the $j$ -th functional output error
$\Delta\Psi_{j, wor}$	worst-case form of the $j$ -th functional output error
$\Delta\Psi_{rss}$	root-sum-square form of the functional outputs of a mechanism
$\Delta\Psi_{wor}$	worst-case form of the functional outputs of a mechanism
$\varepsilon_A$	relative deviation between $\Delta r_{A, mea}$ and $\Delta r_{A, int}$
$\varepsilon_B$	relative deviation between $\Delta r_{B, mea}$ and $\Delta r_{B, int}$
$\varepsilon_n$	relative deviation between $\Delta n_{ap}$ and $\Delta n_{ex}$
$\varepsilon_r$	relative deviation between $\Delta r_{ap}$ and $\Delta r_{ex}$
$\varepsilon_S$	relative deviation between $\Delta S_{ap}$ and $\Delta S_{ex}$
$\eta$	theoretical or constant subtending angle of the follower arms
$\eta^*$	actual or variable subtending angle of the follower arms
$\eta_A$	theoretical subtending angle of the follower arms
$\eta_B$	theoretical subtending angle of the follower arms
$\theta$	cam rotation angle, input variable of a cam mechanism
$\boldsymbol{\theta}$	input variable vector of a mechanism
$\theta_i$	angular displacement of link $i$ or the $i$ -th value of $\theta$
$\hat{\theta}_1, \hat{\theta}_2, \dots, \hat{\theta}_N$	input variables of a mechanism
$\lambda$	shift angle, subtending angle of lines $AA_n$ and $AA_r$
$\lambda_A$	shift angle of cam A, subtending angle of lines $AA_n$ and $AA_r$
$\lambda_B$	shift angle of cam B, subtending angle of lines $BB_n$ and $BB_r$

$\sigma$	compensated shift angle, subtending angle of lines KA <sub>r</sub> and KA
$\tau$	tangential deviation angle, subtending angle of lines A <sub>r</sub> A <sub>e</sub> and A <sub>r</sub> A <sub>n</sub>
$\xi, \xi(\theta)$	angular displacement function of the oscillating follower
$\xi_A, \xi_A(\theta)$	angular displacement function of the oscillating follower
$\xi_B, \xi_B(\theta)$	angular displacement function of the oscillating follower
$\phi$	pressure angle, oblique angle (invariant pressure angle) of the translating flat-faced follower
$\phi_A$	pressure angle of cam A
$\phi_B$	pressure angle of cam B
$\psi, \psi(\theta)$	displacement function of the follower, output variable of a cam mechanism
$\Psi$	functional output variable vector of a mechanism
$\psi_0$	initial position of the follower
$\psi_1, \psi_2, \dots, \psi_m$	functional output variables of a mechanism
$\omega_2$	angular velocity of the cam
( ) <sub>max</sub>	maximum value of the term in parenthesis
( ) <sub>min</sub>	minimum value of the term in parenthesis

## ACRONYMS

AISI	American Iron and Steel Institute
BFGS	Broyden-Fletcher-Goldfarb-Shanno
B-spline	basis spline
CAD	computer aided design
CMM	coordinate measuring machine
CNC	computer numerical control
CPU	central processing unit
DC	direct current
DCC	direct computer control
DFMA	design for manufacture and assembly
EDM	electro-discharge machining
IT	ISO (International Standards Organization) tolerance
JIS	Japanese Industrial Standards
KT	Kuhn-Tucker
MEMS	microelectromechanical systems
MCV	modified constant velocity
MS	modified sine
MT	modified trapezoidal
NURBS	non-uniform rational B-spline (basis spline)
RSS	root sum of squares
QP	quadratic programming
SQP	sequential quadratic programming
USB	universal serial bus

# CHAPTER 1

## INTRODUCTION

### 1.1 OVERVIEW

Cam mechanisms can provide a simple, compact, and reliable means for motion control in machinery. In fact, they are frequently the first choice of many machine designers when high precision, repeatability, and long life are required. Cam mechanisms are found in a wide variety of machines and mechanical devices [1-9], such as machine tools, printing presses, assembly machines, textile machines, sewing machines, packing machines, forming machines, agricultural machines, food processing machines, vending machines, transportation equipment, control systems, internal combustion engines, and more recently in microelectromechanical systems (MEMS) [7]. Evidently, cams are extensively used in most automated production machinery. Also, most automobile engines nowadays use poppet valves, which are spring-loaded closed and pushed open by overhead cams with a flat-faced follower attached to the valve stem [9]. Therefore, up to now, cams still play an important role in the mechanical industry and cannot be superseded.

A cam mechanism, basically consisting of a frame, a cam, and a follower, is a type of three-link direct-contact mechanism. Cams are irregular-shaped mechanical components. They usually rotate with constant angular velocity to drive the followers by direct contact to make the followers generate prescribed motion programs with respect to cam rotation angles (or time). Cams can be further classified in terms of their shapes into planar cams, spatial cams, and spherical cams. Planar cams, especially disk cams (also called plate cams or radial cams), are the simplest ones in design and manufacture and are the most popular industrial production cams. Kinematically, disk cam mechanisms can be regarded as link-lengths-variable four-bar function generators [6] without structural error. (The term “structural error” in a mechanism refers to the kinematic error of the output link of the

mechanism caused by insufficient precision points for the function generation problem [10, 11].) Theoretically, infinite precision points for the follower position can be achieved by the cam geometry design. Thus, almost any reasonably designed (or chosen) follower motion curve can be accomplished.

For disk cam mechanisms, the commonly used followers are roller and flat-faced followers, which may be required to have translating or oscillating motions, as shown in Fig. 1.1. To keep the follower always in contact with the cam, a return spring or a positive drive must be employed [1-8, 12]. The specifications of return springs must be properly chosen to avoid excessive contact stresses and the jump phenomenon of the follower [1, 6-8]. A positive-drive cam mechanism characterized by eliminating the return-spring force can result in lower contact stresses as compared to the spring-loaded type. Positive drive action can be achieved by using grooved cams, yoke cams (constant-diameter cams and

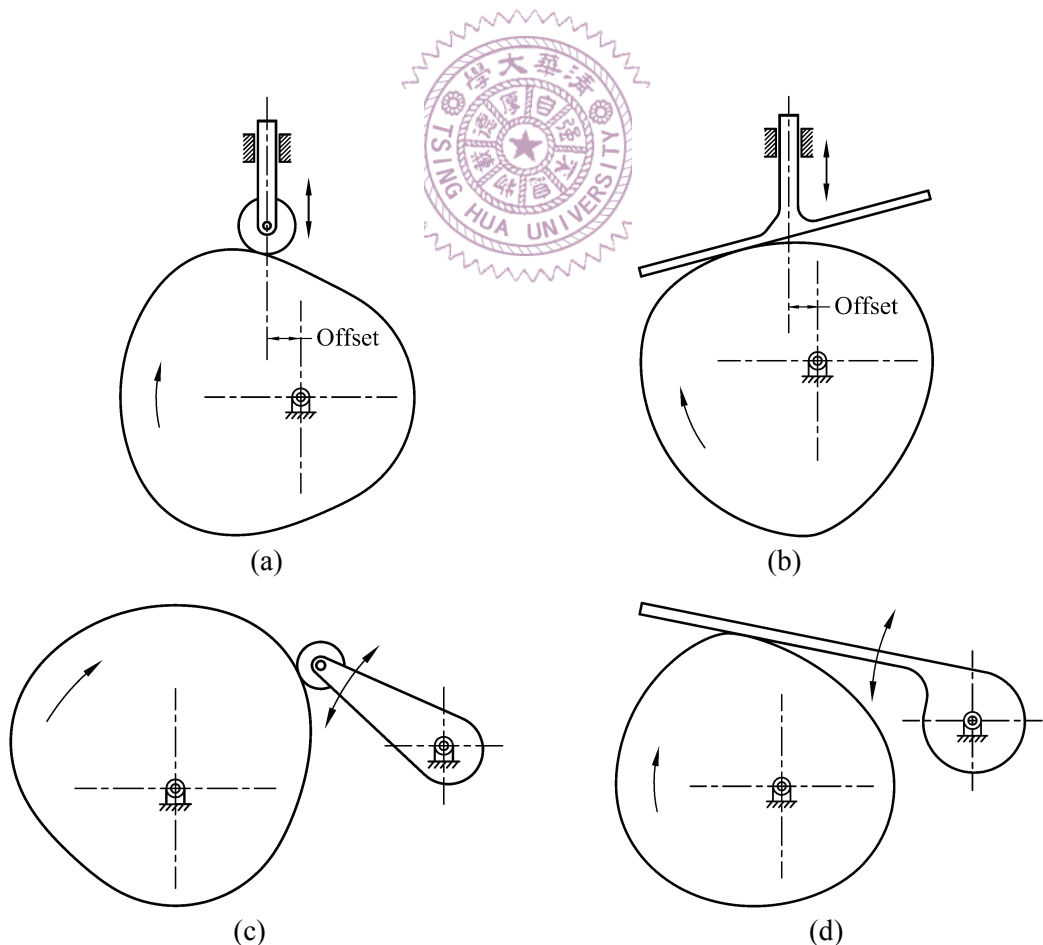


**Figure 1.1** Commonly used disk cam mechanisms: (a) disk cam with an offset translating roller follower; (b) disk cam with an offset translating oblique flat-faced follower; (c) disk cam with an oscillating roller follower; (d) disk cam with an oscillating flat-faced follower.

constant-breadth cams) or conjugate cams, as shown in Fig. 1.2. The disadvantage of using grooved cams is that the necessary clearance (backlash) between the cam and follower roller surfaces (about 20  $\mu\text{m}$  in general [8]) may cause excessive noise, wear, vibration,

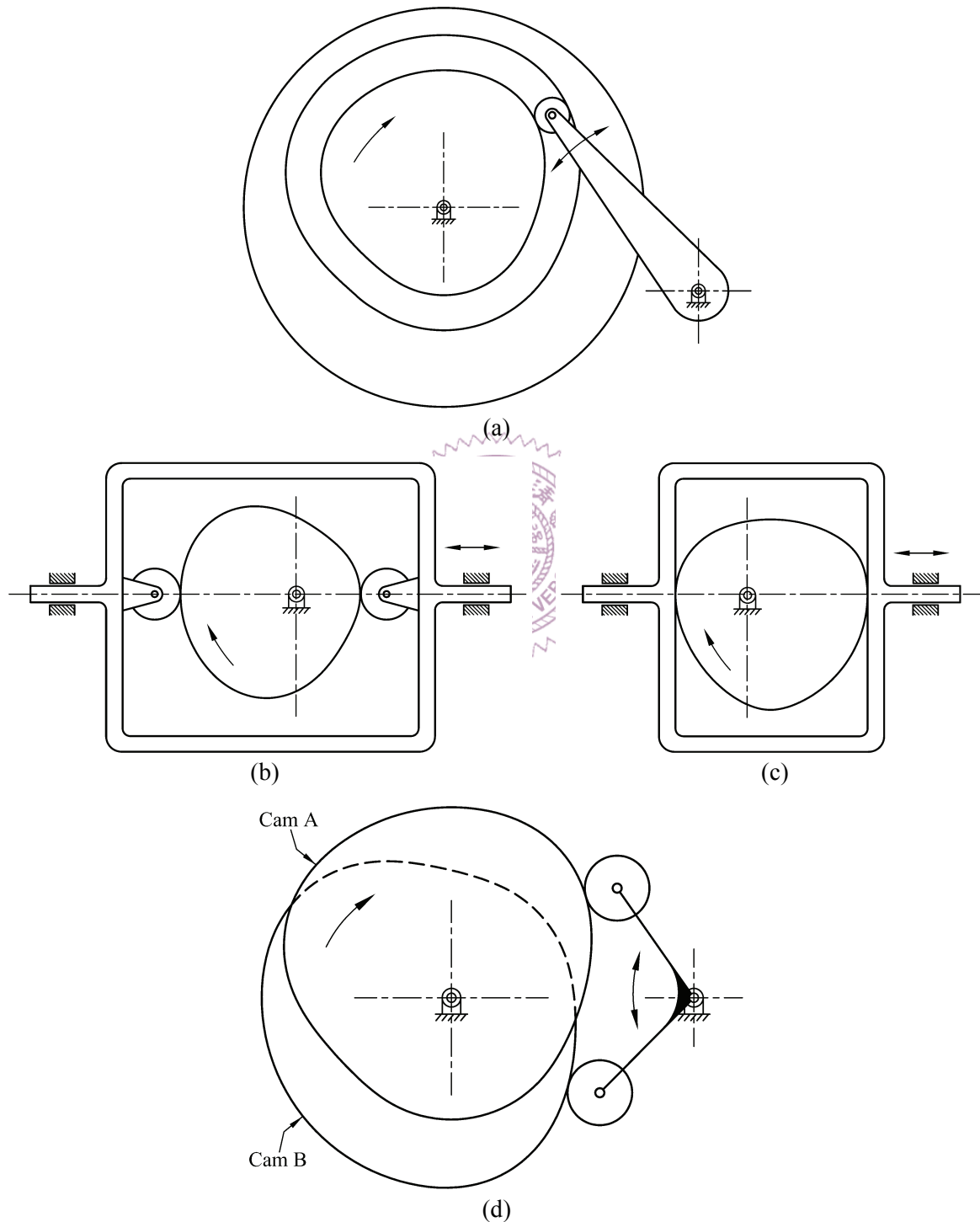


**Figure 1.2** Positive-drive cam mechanisms: (a) grooved cam with an oscillating roller follower; (b) constant-diameter cam with a translating roller follower; (c) constant-breadth cam with a translating flat-faced follower; (d) conjugate disk cams with an oscillating roller follower.

and shock at high speeds [2, 4, 6-8]. Yoke cams employ a single disk cam enclosed by a follower with opposite rollers or flat faces constant distance apart, which may also cause poor quality of work at high speeds by the clearance produced by wear [7]. Another shortcoming of yoke cams is that the follower motion curve can only be designed for a half cycle of cam rotation. Conjugate cam mechanisms, applying a pair of conjugate disk cams fixed on a common shaft to respectively push two followers joining together in opposite directions, can accomplish an exact positive-driven action by eliminating the clearance between the cam and follower surfaces with proper preload [4, 6, 7]. This significant benefit makes them especially suitable for high-speed applications. Although conjugate cam mechanisms are more expansive and more complex than single disk cam mechanisms, good-quality conjugate cams, as well as single disk cams, are industrial products with high added value.

In recent years, cam design and manufacturing processes have been substantially improved because of the development and application of computers in engineering design and numerical control manufacturing. Currently, through the use of computer-aided cam geometry design and computer numerical control (CNC) milling, grinding, or wire electro-discharge machining (EDM) equipment [6, 7], it is possible to produce cams with high precision to more correctly achieve higher derivatives (velocities, accelerations, and jerks) of the chosen follower motion program than in the past. For such precision design and machining, cam profile tolerancing becomes an important task. For example, Figs. 1.3 and 1.4 show typical manufacturing drawings of a disk cam and a pair of conjugate disk cams machined in one piece, respectively; both cams are designed to drive an oscillating roller follower. The radial-dimensional tolerances of the cam contours in the illustrated drawings are specified to be 0.02 mm in the form of either a bilateral or unilateral tolerance. That is, the disk cam contour must have a tolerance grade ranging from IT6 to IT7, and the conjugate cam contours must have a tolerance grade ranging from IT5 to IT6. Each cam should be accurately machined through milling, heat treatment, and grinding processes, and then carefully inspected to check whether its radial dimensions meet such small

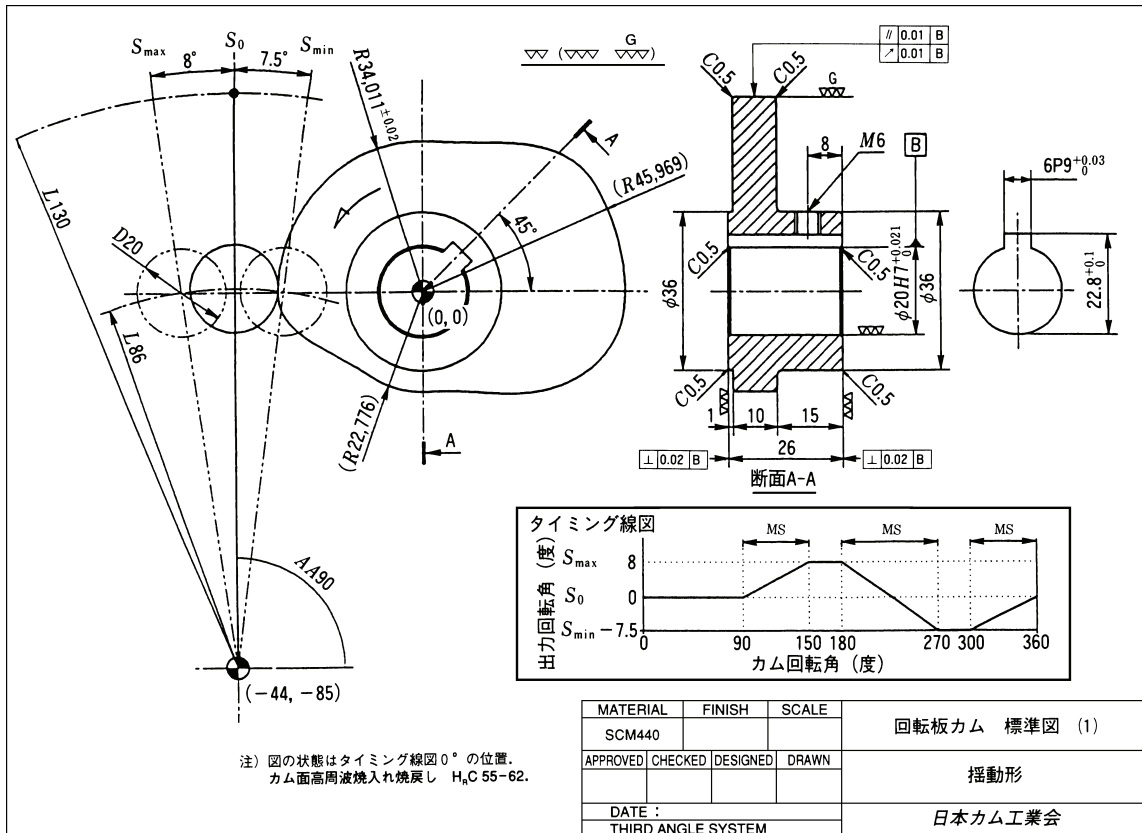


Figure 1.3 Manufacturing drawing of a disk cam [5].

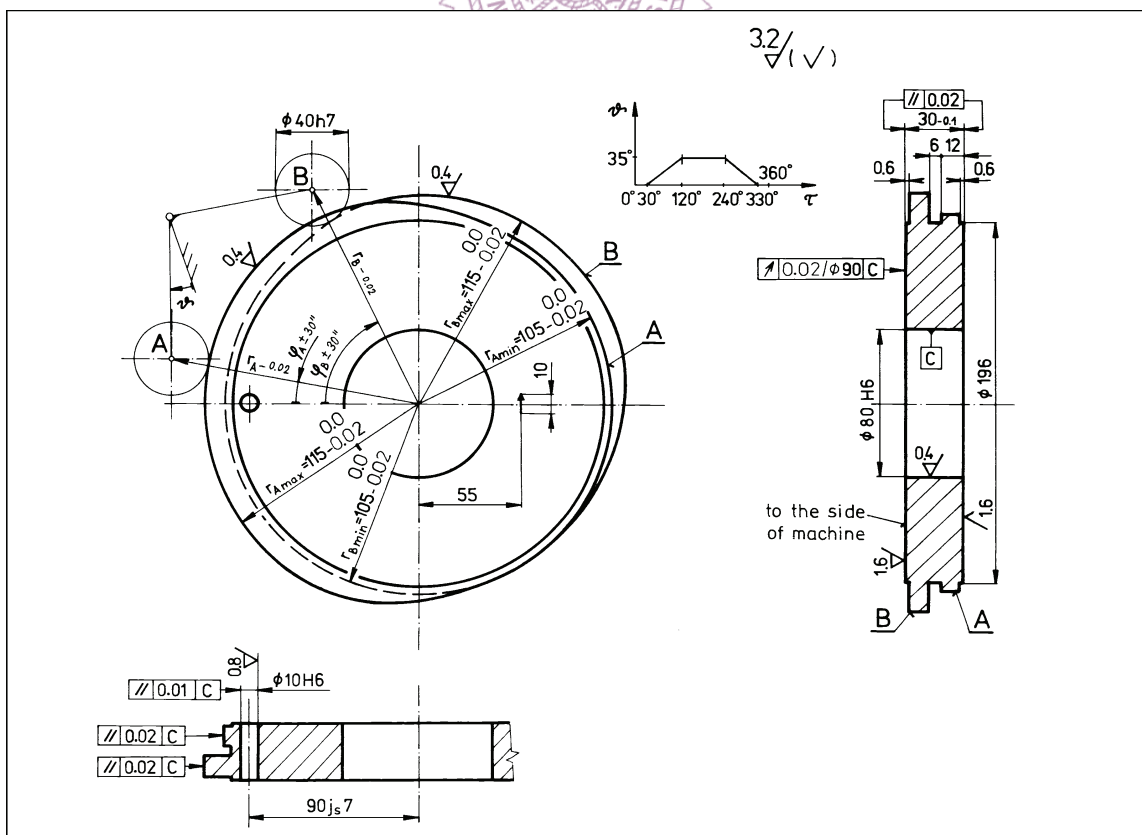


Figure 1.4 Manufacturing drawing of a pair of conjugate disk cams machined in one piece [3].

tolerances for quality control. The qualified cams will have smooth surface roughness and only slight profile deviations.

In high-speed machinery, however, even small errors in cam contour may still produce excessive noise, wear, and vibrations [6, 7, 13-15]. The expected kinematic accuracy of the follower motion, as well as the dynamic performance, of the cam mechanism may thus degrade considerably. To maintain reasonably acceptable kinematic accuracy and dynamic performance of cam mechanisms, the manufacturing and assembly errors in a cam mechanism cannot exceed their specified tolerances. Although small manufacturing and assembly tolerances may give higher quality work, the costs of manufacture and assembly increase rapidly as the tolerances are reduced. In order to achieve a cam mechanism with high quality at a competitive cost, it is important that the tolerances are specified at the largest or optimal values which the operating or functional considerations permit [16]. To this end, the effect of tolerance of each design parameter on the follower motion must be evaluated, and the tolerance allocation of each design parameter should be optimized. That is, designers should not only know the effect of the tolerance of a cam profile and that of each design parameter on the follower output function, but must also decide the levels of tolerances on various members of the mechanism for a specified maximum limit of the follower motion deviation. Therefore, a theoretical correlation between the tolerance level of each design parameter and the follower motion deviation, that is, the mechanical error, must be established; such tolerance analysis procedure is usually called the analysis of mechanical errors [10, 11, 17, 18]. In other words, the analysis of mechanical errors is a fundamental of optimal tolerance allocation for precision cam mechanisms. (The term “mechanical error” in a mechanism refers to the kinematic error of the output link of the mechanism caused by deflections and thermal expansions of links, clearances in joints, manufacturing and assembly tolerances of members, and so on [10, 18]. Only the effects of tolerances on the follower motion deviation of cam mechanisms will be discussed in this dissertation.)

However, for practical consideration in cam mechanism design, before allocating

tolerance for each design parameter, the allowable kinematic accuracy of the follower motion must be specified first. That is, the extremes of mechanical errors must be directly specified by designers to further allocate the tolerances, namely, a reversion of the mechanical error analysis. Because different combinations of allocated tolerance amounts for all design parameters may result in the same level of kinematic accuracy of the follower output motion, an optimal design procedure is required to search the optimal tolerance combination; such tolerance synthesis procedure is also called the synthesis of mechanical errors [17, 18].

In addition, after the members of a cam mechanism are fabricated and before they are assembled together, they should be carefully checked whether their dimensions meet the allocated tolerances, especially the machined cam profile. Up to now, tolerance inspection for machined cams is still a complex task. To inspect the curved contour or surface of a machined cam, a highly sensitive and accurate coordinate measuring machine (CMM) is frequently adopted [3, 6-8, 19-23]. Currently, an ultra-high accuracy CMM, such as the Mitutoyo Legex 574 CMM [24], can reach a resolution of  $0.01 \mu\text{m}$  and an accuracy of about  $\pm 0.5 \mu\text{m}$ . The coordinate measurement data of a machined cam profile are compared with its theoretical coordinates for further evaluation of profile errors. It provides a reliable means for the quality control of cams. However, it is costly and time

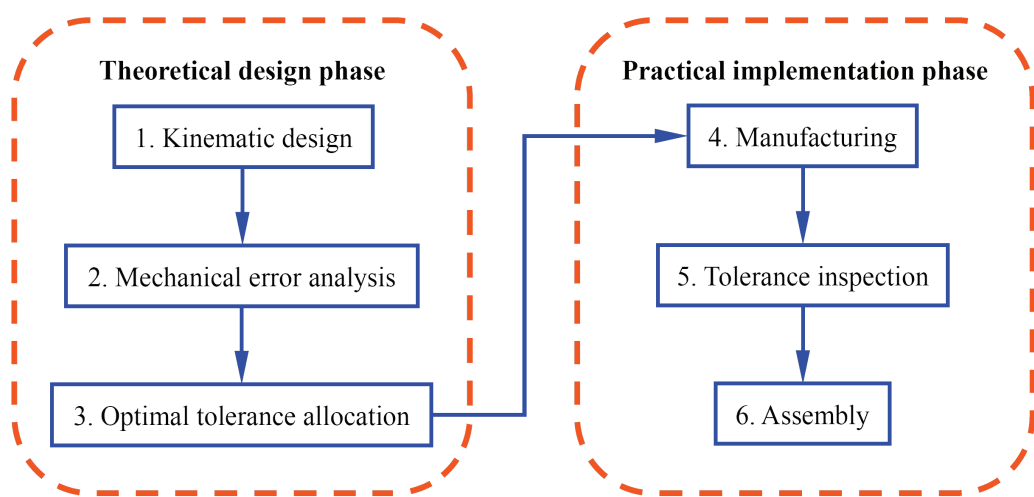


**Figure 1.5** Flowchart for producing precision cam mechanisms.

consuming, especially for conjugate cams. Hence, some simpler and more efficient means for examining cam profile errors should be developed.

Based on the overview, a fundamental and compendious flowchart for producing precision cam mechanisms can be given in Fig. 1.5, in which, kinematic design, mechanical error analysis (tolerance analysis), optimal tolerance allocation (tolerance synthesis), manufacturing, tolerance inspection, and assembly are involved in sequence. The kinematic design, mechanical error analysis, and optimal tolerance allocation belong to the theoretical design phase, and the manufacturing, tolerance inspection, and assembly belong to the practical implementation phase.

## 1.2 LITERATURE REVIEW

Previous work on dealing with the theoretical design and practical implementation phases of producing precision cam mechanisms (as shown in the flowchart in Fig. 1.5) is reviewed in this section to give an essential understanding of current methodologies and technologies.

### 1.2.1 Theoretical Design Phase

At the kinematic design stage, follower motion curve design and cam profile geometry determination are the most important tasks. Traditional motion curves, such as cycloidal curves, modified sine (MS) curves, modified trapezoidal (MT) curves, modified constant velocity (MCV) curves, and polynomial curves [1-8], have been frequently adopted for many years. They are applied directly or blended into piecewise functions for functional or operational requirements. In the last two decades, using spline functions on synthesizing follower motion curves has become a trend [6, 7, 25-33]. Piecewise continuous polynomials called basis splines (B-splines) [34-36] are employed to define the displacement curves of followers. An advantage of using B-splines, instead of traditional polynomial curves, is that piecewise polynomials constructed of cubic B-splines can satisfy

numerous kinematic constraints while traditional polynomials with a higher degree are required. Because high-degree polynomials often produce some undesirable characteristics between constraints [7], follower motion curves synthesized by B-splines can be smoother than those synthesized by traditional polynomials.

Once the follower motion curve design is performed and the constant dimensional parameters of the cam mechanism are specified, the corresponding cam profile geometry can be determined by graphical or analytical approaches. Until about the late 1960s, cam profiles were graphically determined through the principle of kinematic inversion [1, 2, 6, 7, 11, 37-44]. The cam is considered stationary, and the follower is then located in its prescribed positions relative to the cam corresponding to a number of different cam rotation angles. The cam contour is the envelope of the follower contour rotating around the cam. Because there is no graphical way of determining the contact point between the cam and the follower, the graphical layout technique can only give approximate cam contours with poor accuracy, and consequently, this results in low-quality cam products applicable only at low speeds. Thus, in order to calculate cam profile coordinates accurately so as to reduce manufacturing errors, analytical approaches are required. Hanson and Churchill [45], employing the theory of envelopes [46], presented an analytical method for computing disk cam profile coordinates. This analytical method is widely adopted and can be found in some textbooks [1, 44]. The theory of envelopes has been extended by several researchers [47-50] in the design of planar cams with an irregular-shaped follower and also spatial and spherical cams. On the other hand, the conjugate surface theory [18, 51-54] and the instant center method [12, 55-58] have also been applied to calculate cam profile coordinates. Among these analytical approaches, the use of the instant center method, first suggested by Davidson [55], especially provides a convenient means for determining planar cam profiles and cutter (or grinder) center coordinates. By following Davidson's concept [55], Wu and colleagues [12, 57] developed a systematic analytical approach for calculating disk cam and conjugate cam profiles using velocity instant centers. Recently, Wu et al. [58] employed the concept of velocity instant

centers to design a varying-velocity translating cam mechanism, a planar five-link cam-linkage combined mechanism. Through their approaches for determining planar cam profiles [12, 57, 58], the cam profile, the path of the cutter, the pressure angle, and the radius of curvature of the cam can all be analytically expressed in an explicit parametric form. Therefore, up to the present, theoretical tools for cam profile determination of planar cam mechanisms have been well developed.

The mechanical error analysis of cam mechanisms has been studied for many years. For instance, Giordana et al. [59, 60] considered a disk cam with an oscillating roller follower from its equivalent four-bar linkage to deal with the influence of construction, measurement, and assembly errors on the motion deviation of the follower. Their method requires locating the curvature center of the cam profile by dealing with the data of measured cam profile coordinates through approximating small pieces of cam contours as circular arcs. Then the link lengths of the equivalent four-bar linkage corresponding to each cam angle must be estimated to perform the kinematic analysis. Rothbart [7] used a finite difference method suggested by Johnson [61] to approximately evaluate the effect of surface roughness of disk cam profiles on the follower acceleration. Dhande and Chakraborty [17, 18] adopted the probability theory and the sensitivity analysis [62] (by taking partial derivatives of derived nonlinear constraint equations of cam mechanisms) to propose a stochastic approach for estimating the follower displacement error caused by tolerances of the cam profile and of other design parameters. Kim and Newcombe [63] employed the stochastic approach [17, 18] combining finite differences and the maximum likelihood method to further estimate the follower displacement, velocity, and acceleration errors. Then by using the concept of normal-distributed profile tolerance with stochastic simulation [63], Kim and Newcombe [64] investigated the effect of two-dimensional tolerances of disk cam profiles on the follower motion, simultaneously considering the system flexibility. Rao and Gavane [65], as well as Rao [66], also considered tolerances of the cam profile and of other design parameters as random variables, and employed the stochastic approach [17, 18] for evaluating the actual kinematic and dynamic response of

the follower output. Wang et al. [67] adopted the concept of normal-distributed profile tolerance [64] and the Monte-Carlo method to simulate the machining error of the disk cam profile and the corresponding kinematic error of an oscillating roller follower. They also presented an optimization model to minimize the follower output deviation. As can be seen, the stochastic-based approaches have been frequently applied for the mechanical error analysis. Watanabe et al. [68] developed a sensitivity analysis procedure for estimating the kinematic errors of disk cams with a roller follower, in which the displacement output of the follower must be numerically obtained. Wang et al. [69, 70] used surface contact analysis [52, 53] to study the mechanical errors in a roller-gear cam mechanism. The above-mentioned methods provide a valuable source of ideas for the mechanical error analysis of cam mechanisms; however, most of them are not based on analytical means for predicting the mechanical errors of cam mechanisms. Thus, a numerical evaluation for most of them involves complicated computation.

Up to now, only a few of the analytical approaches for mechanical error analysis have been presented. For instance, Chiu et al. [71] applied the principle of the offset curve of a plane curve to perform the influence analysis of manufacturing and assembly errors of disk cam mechanisms. Zhang and Wang [72] employed the sensitivity analysis [17, 18, 62] to derive output error equations of a disk cam with an offset translating roller follower caused by the tolerance of the cam profile and those of other design parameters. The sensitivity analysis itself requires deriving the nonlinear constraint equation of the cam mechanism relating the design parameters and input and output variables. This is a complicated task without generality, especially when cam-linkage combined mechanisms are considered. Lin and Hwang [73] used the homogeneous transformation matrix to establish the kinematic error model of a cylindrical cam mechanism. These analytical approaches appear to have to deal with cumbersome equations and thus may not provide a convenient means for cam designers. It seems that few of existing methods can be applied to derive and express the output error equations of cam mechanisms in concise forms through a simple and systematic procedure. In other words, to achieve a shorter duration of the tolerance

analysis stage of cam mechanisms, greater effort should be exerted on developing an easily applied analytical approach for mechanical error analysis.

A variety of research work on optimal tolerance allocation have been carried out for assembled mechanical parts [62, 74-81] and linkage mechanisms [82-88]. However, very few studies have been reported regarding the tolerance allocation for cam mechanisms. With the aid of developed approaches for mechanical error analysis, several procedures for the optimal tolerance allocation of cam mechanisms have been suggested by Chakraborty and Dhande [17, 18], Rao and Gavane [65], Rao [66], and Zhang and Wang [72]. For such optimization problems, the extremes of mechanical errors in cam mechanisms are usually treated as constraints, the tolerances as variables to be optimized, and the production cost of cam mechanisms as the objective to be minimized. Moreover, in these problems, the production cost is a criterion for evaluating the feasibility of tolerance combinations. In the existing research, production cost is simply defined as the summation of separate manufacturing and assembly costs with respect to each dimensional tolerance in cam mechanisms. That is, the specified manufacturing or assembly tolerance of each design parameter has its own respective cost. These manufacturing and assembly cost models are in relatively simple mathematical forms, such as reciprocals [17, 18, 65, 66] or exponential functions [72] of the tolerance amounts, so as to simplify the optimization problems. In fact, the production cost of cam mechanisms involves not only tolerances but also practical consideration of manufacturing, assembly, and inspecting processes. Thus, production cost evaluation is an important and complex task, and may not be easily and explicitly performed in the tolerance design stage. Therefore, the existing cost-tolerance models for cam mechanisms can give a reasonably qualitative estimation, but not an exact quantitative prediction. If the used cost-tolerance models cannot reasonably reflect the actual situations in the manufacturing and assembly of cam mechanisms, the sequential optimization results may be inapplicable. Therefore, establishing a more appropriate optimization model for allocating the tolerances of cam mechanisms is still a matter of concern until now.

### 1.2.2 Practical Implementation Phase

Nowadays, a detailed introduction of cam manufacturing methods can be found in related cam design handbooks [6-8]. Most importantly, to produce high-quality cams, CNC milling and grinding or wire EDM processes are required. The cam surface is usually milled and possibly ground after heat treatment. Excellent surface finish, correction of distortion after heat treatment, and close tolerances of cams can be achieved by grinding. Wire EDM is only suitable for generating disk cam contours. The path motion of the wire is controlled by CNC to electrically cut pre-hardened cam blanks. Wire EDM itself can make disk cams with excellent surface finish and close tolerances, although the surface finish is not quite as good as when it is ground [6]. However, due to limitations in the resolution and accuracy of CNC machines, the occurrence of cam profile deviations during machining processes cannot be avoided. In fact, it is quite difficult to produce perfect disk cams without profile deviations since most of the radial dimensions of disk cams are usually irrational numbers. Several researchers [6, 7, 13, 14, 89, 90] have investigated the effect of cam profile errors caused by various manufacturing methods on the kinematic and dynamic performance of cam mechanisms through experiments. Their efforts can provide valuable information to cam manufacturers. Nevertheless, cam manufacturers may be more concerned with how cam profile errors can be accurately and efficiently inspected for quality control.

By using a CMM, the inspection of an entire contour or surface of a machined cam has become possible. The coordinate data of discrete points at the cam surface are measured by a CMM in order to further evaluate the actual cam profile with some developed interpolation algorithms [20-23, 34-36, 91-93], and then the cam contour approximated by these algorithms may be compared with the theoretical one to obtain profile errors. Typical interpolation curves including Hermite curves, B-spline curves, Bézier curves, and non-uniform rational B-spline (NURBS) curves are frequently employed to model the measured contours or surfaces. Representing measured contours or surfaces as NURBS is now widely applied in computer-aided design (CAD) modeling. The

B-spline and Bézier curves can be regarded as special cases of NURBS curves, which are the combinations of B-spline basis functions [34-36]. One important advantage of using NURBS curves, instead of Hermite curves, is that one fitted NURBS contour or surface can be considered as a single element, which avoids the evaluation of derivatives and twists at inner points [92]. Also, a relatively small number of points is required for modeling complicated geometry. Therefore, NURBS curves are suitable for approximating free-form sculptured surfaces for the reverse engineering. For the cam contour modeling, since the measured points at the cam surface represent the actual contact points between the cam and follower surfaces, their coordinate data must be accurately recorded for profile error inspection and mechanical error analysis. The use of Hermite or NURBS curves can ensure the interpolated polynomial curves passing through all measured points exactly. Considering that disk cams are in essence two-dimensional contours, it is less significant to evaluate the twist effects on the cam surfaces. In other words, the Hermite interpolation algorithm is sufficiently applicable for modeling disk cam contours with coordinate measurement data. Although the existing algorithms provide valuable contributions for cam contour modeling, it appears that they have to deal with cumbersome equations and iterative processes, and further, the numerical evaluation of them involves complicated computation. A simple and direct method of dealing with coordinate measurement data to evaluate cam profile errors is thus preferred.

On the other hand, some indirect methods of inspecting disk cam profiles have been proposed to possibly replace the expensive direct measurement by using a CMM. For example, Tsay et al. [23] developed a measuring system whose principle is similar to that of a camshaft measuring instrument [94], in order to directly measure the displacement of a translating follower that comes in contact with an inspected cam by using a linear encoder. Then a numerical approach of solving the contact conditions between the two-dimensional cam and follower profiles was applied to evaluate the actual cam contour and the corresponding velocity and acceleration curves of the follower. In addition, a simple method of inspecting conjugate cam profiles was reported by Koloc and Václavík [3], in

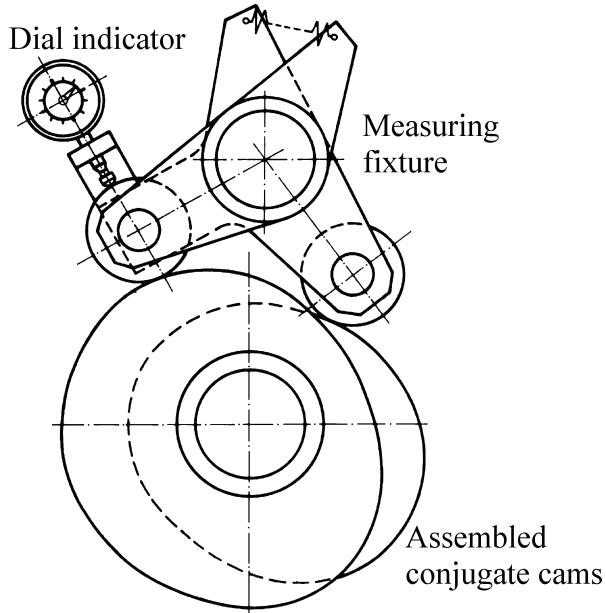


**Figure 1.6** Assembled conjugate cams with a measuring fixture consisting of two oscillating roller followers [3].

which, the profile deviations of conjugate cams can be indirectly examined by using a special measuring fixture as shown in Fig. 1.6. The measuring fixture can measure the conjugate condition for each pair of conjugate disk cams. The measuring fixture is modified from the original oscillating roller follower to make the two oscillating follower arms pivot together with a variable subtending angle. The subtending angle variation may thus indicate the cam profile deviations. As compared to using a CMM to inspect conjugate cams, such a measurement method is convenient and inexpensive, and the only required measuring instrument is a dial indicator. Hence, it is especially suitable for the quality control in mass production of conjugate cams. However, this concise measurement method has no mathematical model yet to relate the conjugate condition variation and the cam profile errors. Therefore, an analytical approach for the conjugate condition analysis should be provided to help in the indirect inspection.

As to the assembly stage, the performance quality of assembled cam mechanisms strongly depends on the sufficient experience and high level of dedication of the machine shop workers. Importantly, the misalignment in assembly should be eliminated as far as possible, and proper fit and preload of all bearing surfaces including the cam and follower

engagement should be ensured [7]. Tests of kinematic and dynamic performance of assembled cam mechanisms [6, 8] are then undertaken if necessary.

### 1.3 MOTIVATION AND PURPOSE

From the literature review, it is understood that more convenient, efficient, and systematic means of dealing with the analysis, synthesis, and inspection of tolerances in cam-follower systems are still required to possibly simplify the complexity of producing precision cam mechanisms. Such simplified means can consequently contribute to reduced cost and time for both the theoretical design and practical implementation phases of the production. Thus, this dissertation focuses on the improvement of methodologies for mechanical error analysis, optimal tolerance allocation, and tolerance inspection of planar cam mechanisms. The main purpose of this dissertation is to develop a simple and systematic analytical method for analyzing the mechanical errors of planar cam mechanisms. This developed method can be advantageously extended to deal with optimal tolerance allocation and tolerance inspection problems. Both theoretical investigation and experimental verification are performed in this work. It is hoped that this work would be helpful in the design and manufacture of precision planar cam mechanisms.

### 1.4 DISSERTATION OUTLINE

In this dissertation, the analytical parametric expressions for disk cam profiles are first derived in Chapter 2 by using the instant center method [12, 55-58]. Then an analytical approach, called the equivalent linkage method, is developed in Chapter 3 to analyze the mechanical errors of disk cam mechanisms. This method is based on the concept of equivalent linkage and the derived correlation between the radial-dimension errors and the normal-direction errors of the cam profile. Displacement, velocity, and acceleration errors

of the follower can be determined analytically. Examples and a practical case study are given to illustrate the presented method.

In Chapter 4, a systematic procedure of optimal tolerance allocation for disk cam mechanisms is established. The concept of design for manufacture and assembly (DFMA) [95-98] is adopted as criteria for searching the optimal tolerance combination leading to allowable mechanical errors. A quantitative comprehensive index for evaluating the manufacturability and assembly of disk cam mechanisms, rather than a traditional cost-tolerance model, is proposed as the objective function. A practical case study is given to illustrate the presented optimal procedure.

Based on the derived correlation between the radial-dimension errors and the normal-direction errors of the cam profile, Chapter 5 proposes an analytical method for inspecting the profile deviations of disk cams directly from the coordinate measurement data obtained by using a CMM. An experiment of inspecting a pair of conjugate disk cam profiles was conducted to verify the proposed data approach method. The experimental results obtained from the proposed method were then compared with those obtained by using the Hermite interpolation method [91].

In Chapter 6, the principle of designing measuring fixtures for indirectly examining assembled conjugate cams using a dial indicator is demonstrated. Then by applying the equivalent linkage method, mathematical models for relating the conjugate condition variations and the profile errors of conjugate disk cams with an oscillating roller follower are established. Based on the mathematical models, conservative criteria for quality control of assembled conjugate cams are proposed with two examples illustrated.

Chapter 7 presents a simple means of estimating profile deviations of conjugate cams from the indicator reading by extending the indirect measurement methods introduced in Chapter 6. To verify the presented method, experiments of examining a pair of conjugate disk cams by using a built integrated-type measuring fixture to measure the conjugate condition variations and to estimate the cam profile errors were conducted. The measured conjugate condition variations were then compared with the predicted ones, and the

estimated cam profile errors were also compared with the measured ones obtained from the experiment of Chapter 5 by using a CMM.

Finally, Chapter 8 presents conclusions of the dissertation and discusses future research directions.

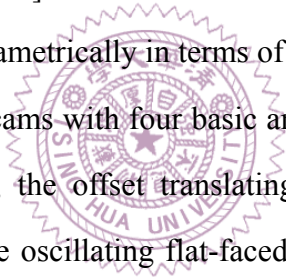


# CHAPTER 2

## ANALYTICAL PARAMETRIC EXPRESSIONS FOR DISK CAM PROFILES

### 2.1 INTRODUCTION

In order to find how the manufacturing error (or tolerance) of a machined cam profile effects the corresponding output deviation of its follower, as well as to inspect the profile deviation of the machined cam, the analytical expressions for the theoretical cam profile should be derived first. The profile of a disk cam can be determined through the use of velocity instant centers [12, 55-58]. For ease reference, the analytical approach for determining disk cam profiles parametrically in terms of the cam rotation angle [12, 57, 58] is provided. In this chapter, disk cams with four basic and common types of followers, the offset translating roller follower, the offset translating oblique flat-faced follower, the oscillating roller follower, and the oscillating flat-faced follower, are demonstrated. Then conjugate disk cams with an oscillating roller follower is also demonstrated.



### 2.2 FUNDAMENTALS OF DISK CAM PROFILE DETERMINATION

By using the concept of velocity instant centers, the parametric vector equations of the disk cam profiles can be derived analytically. For a three-link direct-contact mechanism shown in Fig. 2.1, it consists of a frame link (link 1), a cam (link 2), and a follower (link 3). For simplicity, in the following context, the frame link will be consistently numbered as 1, the cam as 2, and the follower as 3. This mechanism simply has three instant centers  $I_{12}$ ,  $I_{13}$ , and  $I_{23}$ , where 'I' denotes the instant center and subscripts indicate the related links. The instant centers  $I_{12}$  and  $I_{13}$  locate at the fixed pivots  $O_2$  and  $O_3$ , respectively. The instant

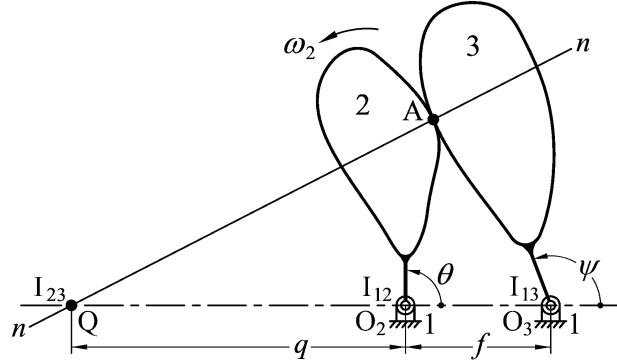


**Figure 2.1** Three-link direct-contact mechanism (oscillating follower case).

center  $I_{23}$  locates at the intersection of the normal line through the point of contact (line  $n-n$ ) and the line of centers. By labeling instant center  $I_{23}$  as  $Q$ , the location of point  $Q$  can be directly determined by the velocity ratio between the cam and the follower [12, 57, 58]. Let  $\theta$  and  $\psi$  be the input and output variables of the mechanism, respectively, the speed of point  $Q$  on the cam can be expressed as

$$V_Q = q \frac{d\theta}{dt} = q\omega_2 \quad (2.1)$$

where  $q = O_2Q$  and  $\omega_2$  is the angular velocity of the cam. On the other hand, the speed of point  $Q$  on the follower can be expressed as

$$V_Q = (f + q) \frac{d\psi}{dt} = (f + q) \frac{d\psi}{d\theta} \frac{d\theta}{dt} = (f + q) \frac{d\psi}{d\theta} \omega_2 \quad (2.2)$$

where  $f = O_2O_3$ . By definition of the instant center, instant center  $I_{23}$  (point  $Q$ ) is a point common to links 2 (cam) and 3 (follower) having the same velocity. Therefore, from Eqs. (2.1) and (2.2) and after some algebraic manipulation,

$$q = \frac{f \frac{d\psi}{d\theta}}{1 - \frac{d\psi}{d\theta}} \quad (2.3)$$

If the follower is in pure translation, as shown in Fig. 2.2, variable  $\psi$  represents the linear displacement of the follower, and the speed of point  $Q$  on the follower can be expressed as

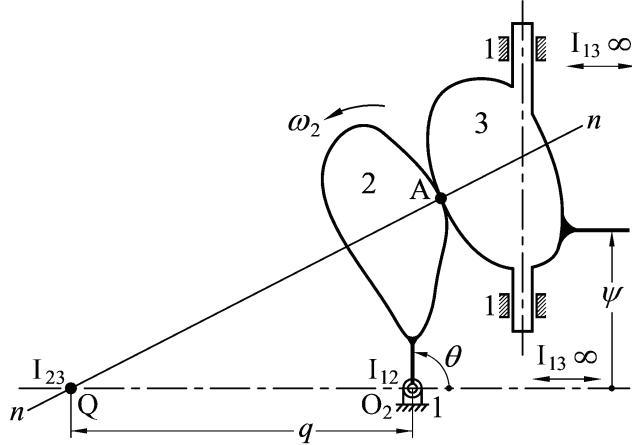


**Figure 2.2** Three-link direct-contact mechanism (translating follower case).

$$V_Q = \frac{d\psi}{dt} = \frac{d\psi}{d\theta} \frac{d\theta}{dt} = \frac{d\psi}{d\theta} \omega_2 \quad (2.4)$$

From Eqs. (2.1) and (2.4),

$$q = \frac{d\psi}{d\theta} \quad (2.5)$$

As shown in Eqs. (2.3) and (2.5), the location of point Q can be determined by using the velocity ratio ( $d\psi/d\theta$ ) since  $\psi = \psi(\theta)$ . Then the location of contact point A with respect to the cam center  $O_2$  can be expressed as

$$\mathbf{O}_2\mathbf{A} = \mathbf{O}_2\mathbf{Q} + \mathbf{QA} \quad (2.6)$$

where  $\mathbf{QA}$  can be determined by the prescribed location and geometric property of the follower.

Similarly, Fig. 2.3 shows an overconstrained direct-contact mechanism with two contact points between links 2 and 3, which may be regarded as a conjugate cam mechanism or a gear mechanism. The two normal lines through the points of contact (lines  $n-n$  and  $n'-n'$ ) and the line of centers must always intersect at a common point, the instant center  $I_{23}$  (point Q), to make this mechanism with constrained motion [12]. The location of contact point B with respect to the cam center  $O_2$  can thus be expressed as

$$\mathbf{O}_2\mathbf{B} = \mathbf{O}_2\mathbf{Q} + \mathbf{QB} \quad (2.7)$$

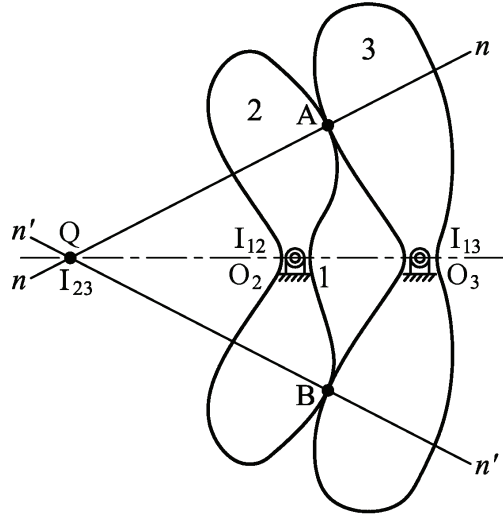


**Figure 2.3** Overconstrained direct-contact mechanism.

where **QB** can also be determined by the prescribed location and geometric property of the follower.

For simplicity, in the following chapters, the linear or angular motion programs (the displacement curves) of the followers are all denoted by  $S(\theta)$ , the linear or angular velocities of the followers by  $V(t)$ , and the linear or angular accelerations of the followers by  $A(t)$ . Note that  $\psi(\theta) = \psi_0 + S(\theta)$ , in which,  $\psi_0$  represents the initial position of the follower. If the cam rotates at a constant angular velocity of  $\omega_2$  rad/s, the velocity and acceleration of the follower can respectively be expressed as [41, 99]

$$V(t) = \frac{dS(\theta)}{dt} = v(\theta)\omega_2 \quad (2.8)$$

$$A(t) = \frac{d^2S(\theta)}{dt^2} = a(\theta)\omega_2^2 \quad (2.9)$$

where  $\theta (= \omega_2 t)$  is the cam rotation angle, and

$$v(\theta) = S'(\theta) = \frac{dS(\theta)}{d\theta} \quad (2.10)$$

$$a(\theta) = S''(\theta) = \frac{d^2S(\theta)}{d\theta^2} \quad (2.11)$$

in which,  $S(\theta)$  may have the unit of length or radian (or degree). Here,  $v(\theta)$  and  $a(\theta)$  are functions of the cam rotation angle  $\theta$  only. For translating followers,  $v(\theta)$  and  $a(\theta)$  have units of length/rad and length/rad<sup>2</sup>, respectively. On the other hand, for oscillating followers,  $v(\theta)$  is non-dimensional and  $a(\theta)$  has the unit of 1/rad. The magnitude of  $\omega_2$  is irrelevant to the geometry of cam contour, and if  $\omega_2 \equiv 1$  rad/s, then  $V(t) = v(\theta)$  and  $A(t) = a(\theta)$ , numerically. Therefore, while dealing with the geometry of cam contour design, it is convenient to assume  $\omega_2 \equiv 1$  rad/s; finally,  $v(\theta)$  times the actual magnitude of  $\omega_2$  may obtain  $V(t)$ , and  $a(\theta)$  times  $\omega_2^2$  may obtain  $A(t)$ . For this reason, for simplicity,  $\omega_2 \equiv 1$  rad/s (i.e.,  $\theta \equiv t$ ) is consistently assumed in the following context, and thus  $v(\theta)$  and  $a(\theta)$  are also called the (linear or angular) velocity and acceleration functions of the follower, respectively.

### 2.3 DISK CAM WITH AN OFFSET TRANSLATING ROLLER FOLLOWER

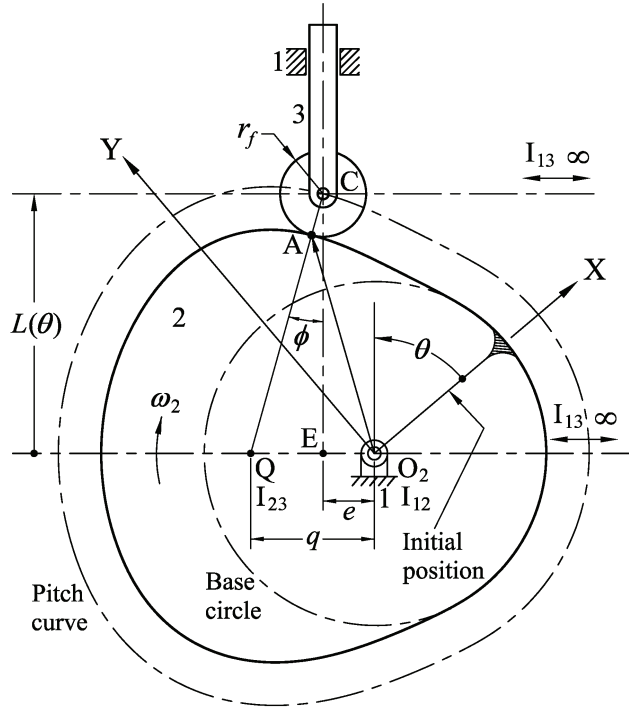


Figure 2.4 shows a disk cam mechanism with an offset translating roller follower. By setting up a Cartesian coordinate system X-Y fixed on the cam and with its origin at the fixed pivot  $O_2$ , the cam profile coordinates may be expressed in terms of the cam rotation angle  $\theta$ , which is measured against the direction of cam rotation from the reference radial on the cam to cam centerline parallel to follower translation. By labeling instant center  $I_{23}$  as Q and  $O_2Q = q$ , the speed of point Q on the cam can be expressed as

$$V_Q = q\omega_2 \quad (2.12)$$

where  $\omega_2$  is the angular velocity of the cam and must be expressed in rad/s. In order to let  $\theta$  have a counterclockwise angle, the cam is to rotate clockwise.

On the other hand, for a translating follower, all points on the follower have the same velocity. Therefore, the speed of point Q on the follower can be expressed as



**Figure 2.4** Disk cam with an offset translating roller follower.

$$V_Q = \frac{dL(\theta)}{dt} = \frac{dL(\theta)}{d\theta} \frac{d\theta}{dt} = \frac{dL(\theta)}{d\theta} \omega_2 \quad (2.13)$$

where  $L(\theta)$  is the linear displacement function of the follower:

$$L(\theta) = \sqrt{(r_b + r_f)^2 - e^2} + S(\theta) \quad (2.14)$$

where  $r_b$  is the radius of the base circle,  $r_f$  is the radius of the follower roller,  $e$  is the offset, and  $S(\theta)$  is the linear motion program (the linear displacement curve) of the follower. (Since the cam is to rotate clockwise, the quantity  $e$  is negative if the offset is to the right; in the position shown it is positive.) It can be seen that  $\psi(\theta) \equiv L(\theta)$  in this case. When  $\theta = 0^\circ$ ,  $S(0) = 0$ , the initial value of the linear displacement function will be

$$L(0) = \sqrt{(r_b + r_f)^2 - e^2} \quad (2.15)$$

which is independent of the cam rotation angle  $\theta$ . From Eqs. (2.12) and (2.13),

$$q = \frac{dL(\theta)}{d\theta} = \frac{dS(\theta)}{d\theta} = v(\theta) \quad (2.16)$$

where  $v(\theta)$  is the linear velocity program of the follower. Then after  $r_b$ ,  $r_f$ ,  $e$ , and  $S(\theta)$  have been selected, for each specified value of  $\theta$ , the roller center C may be located by applying Eq. (2.14) and point Q by applying Eq. (2.16). As shown in Fig. 2.4, the pressure angle  $\phi$  is the angle between lines QC and CE. From  $\triangle CQE$ , it can be expressed as

$$\phi = \tan^{-1} \left[ \frac{q - e}{L(\theta)} \right] = \tan^{-1} \left[ \frac{v(\theta) - e}{L(\theta)} \right] \quad (2.17)$$

Also,

$$QC = L(\theta) \sec \phi \quad (2.18)$$

Therefore, the vectors of the theoretical cam profile coordinates are

$$\mathbf{O}_2\mathbf{A} = \mathbf{O}_2\mathbf{Q} + \mathbf{QA} \quad (2.19)$$

where

$$\mathbf{O}_2\mathbf{Q} = q \begin{Bmatrix} \cos(\theta + 90^\circ) \\ \sin(\theta + 90^\circ) \end{Bmatrix} = q \begin{Bmatrix} -\sin \theta \\ \cos \theta \end{Bmatrix} \quad (2.20)$$

$$\mathbf{QA} = (QC - r_f) \begin{Bmatrix} \cos(\theta - \phi) \\ \sin(\theta - \phi) \end{Bmatrix} \quad (2.21)$$

Hence, the parametric vector equations of the theoretical cam profile coordinates are

$$\mathbf{R}(\theta) = \mathbf{O}_2\mathbf{A} = \begin{Bmatrix} (QC - r_f) \cos(\theta - \phi) - q \sin \theta \\ (QC - r_f) \sin(\theta - \phi) + q \cos \theta \end{Bmatrix} \quad (2.22)$$

The common normal at the contact point must always pass through points Q, A, and C. Therefore, from Eq. (2.21), the unit normal vector to the theoretical cam profile can be expressed as

$$\mathbf{n}(\theta) = -\frac{\mathbf{QA}}{\|\mathbf{QA}\|} = \begin{Bmatrix} -\cos(\theta - \phi) \\ -\sin(\theta - \phi) \end{Bmatrix} \quad (2.23)$$

## 2.4 DISK CAM WITH AN OFFSET TRANSLATING OBLIQUE FLAT-FACED FOLLOWER

Figure 2.5 shows a disk cam mechanism with an offset translating oblique flat-faced follower. By setting up a Cartesian coordinate system X-Y fixed on the cam and with its origin at the fixed pivot  $O_2$ , the cam profile coordinates may be expressed in terms of the cam rotation angle  $\theta$ , which is measured against the direction of cam rotation from the reference radial on the cam to cam centerline parallel to follower translation. By labeling instant center  $I_{23}$  as Q and  $O_2Q = q$ , the speed of point Q on the cam can be expressed as

$$V_Q = q\omega_2 \quad (2.24)$$

On the other hand, the speed of point Q on the follower can be expressed as

$$V_Q = \frac{dL(\theta)}{dt} = \frac{dL(\theta)}{d\theta} \frac{d\theta}{dt} = \frac{dL(\theta)}{d\theta} \omega_2 \quad (2.25)$$

where  $L(\theta)$  is the linear displacement function of any reference point on the follower. If point P, the intersection of the follower surface and the ray passing through point E on the

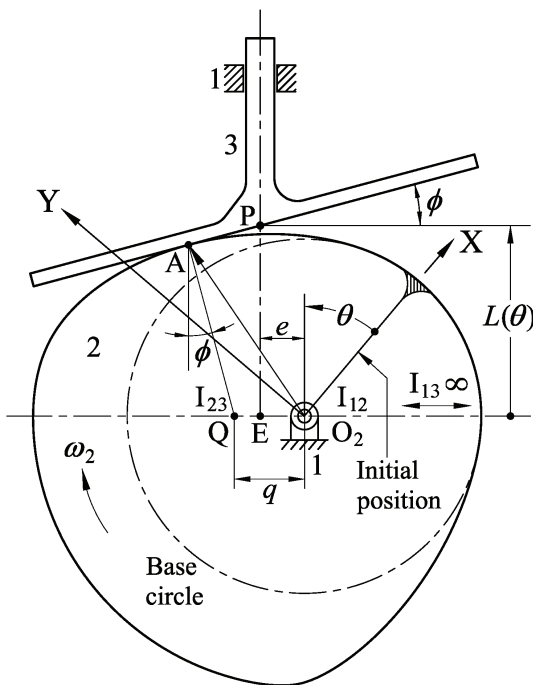


**Figure 2.5** Disk cam with an offset translating oblique flat-faced follower.

cam ( $O_2E = e$ ) parallel to follower translation, is selected,

$$L(\theta) = r_b \sec \phi - e \tan \phi + S(\theta) \quad (2.26)$$

Here,  $r_b$  is the radius of the base circle,  $\phi$  is the oblique angle of the follower (i.e., the invariant pressure angle),  $e$  is the offset, and  $S(\theta)$  is the linear motion program (the linear displacement curve) of the follower. (The quantity  $\phi$  is positive if the follower face is counterclockwise oblique from the horizontal; in the position shown it is positive. Also, since the cam is to rotate clockwise, the quantity  $e$  is negative if the offset is to the right; in the position shown it is positive.) It can be seen that  $v(\theta) \equiv L(\theta)$  in this case. When  $\theta = 0^\circ$ ,  $S(0) = 0$ , the initial value of the linear displacement function will be

$$L(0) = r_b \sec \phi - e \tan \phi \quad (2.27)$$

which is independent of the cam rotation angle  $\theta$ . From Eqs. (2.24) and (2.25),

$$q = \frac{dL(\theta)}{d\theta} = \frac{dS(\theta)}{d\theta} = v(\theta) \quad (2.28)$$

where  $v(\theta)$  is the linear velocity program of the follower. After  $r_b$ ,  $\phi$ ,  $e$ , and  $S(\theta)$  have been selected, for each specified value of  $\theta$ , the reference point P may be located by applying Eq. (2.26) and point Q by applying Eq. (2.28). From quadrangle EQAP,

$$QA = L(\theta) \cos \phi - (q - e) \sin \phi \quad (2.29)$$

Therefore, the vectors of the theoretical cam profile coordinates are

$$\mathbf{O}_2\mathbf{A} = \mathbf{O}_2\mathbf{Q} + \mathbf{QA} \quad (2.30)$$

where

$$\mathbf{O}_2\mathbf{Q} = q \begin{Bmatrix} \cos(\theta + 90^\circ) \\ \sin(\theta + 90^\circ) \end{Bmatrix} = q \begin{Bmatrix} -\sin \theta \\ \cos \theta \end{Bmatrix} \quad (2.31)$$

$$\mathbf{QA} = \mathbf{QA} \begin{Bmatrix} \cos(\theta + \phi) \\ \sin(\theta + \phi) \end{Bmatrix} \quad (2.32)$$

Hence, the parametric vector equations of the theoretical cam profile coordinates are

$$\mathbf{R}(\theta) = \mathbf{O}_2 \mathbf{A} = \begin{cases} QA \cos(\theta + \phi) - q \sin \theta \\ QA \sin(\theta + \phi) + q \cos \theta \end{cases} \quad (2.33)$$

For a translating flat-faced follower with zero oblique angle,  $\phi = 0^\circ$ , then

$$QA = L(\theta) = r_b + S(\theta) \quad (2.34)$$

That is, with zero oblique angle, the quantity  $e$  is not essential for determining the cam profile. The common normal at the contact point must always pass through points Q and A. Therefore, from Eq. (2.32), the unit normal vector to the theoretical cam profile can be expressed as

$$\mathbf{n}(\theta) = -\frac{\mathbf{QA}}{\|\mathbf{QA}\|} = \begin{cases} -\cos(\theta + \phi) \\ -\sin(\theta + \phi) \end{cases} \quad (2.35)$$



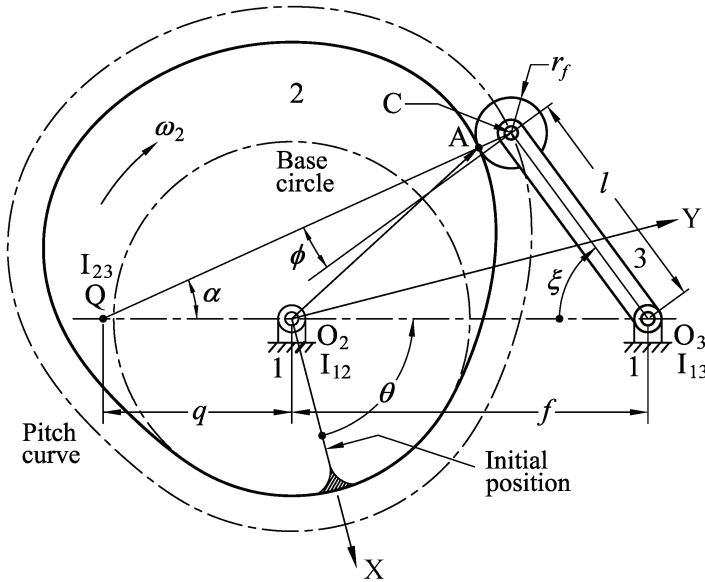
## 2.5 DISK CAM WITH AN OSCILLATING ROLLER FOLLOWER

Figure 2.6 shows a disk cam mechanism with an oscillating roller follower. In this case,  $f$  represents the distance from the cam center to the follower pivot point, and  $l$  represents the arm length of the follower. By setting up a Cartesian coordinate system X-Y fixed on the cam and with its origin at the fixed pivot  $O_2$ , the cam profile coordinates may be expressed in terms of  $\theta$ , which is measured against the direction of cam rotation from the reference radial on the cam to the line between the cam center and the follower pivot point. The speed of point Q, instant center  $I_{23}$ , on the cam can be expressed as

$$V_Q = q\omega_2 \quad (2.36)$$

where  $q = O_2Q$  and  $\omega_2$  is the angular velocity of the cam. On the other hand, the speed of point Q on the follower can be expressed as

$$V_Q = (f + q) \frac{d\xi(\theta)}{dt} = (f + q) \frac{d\xi(\theta)}{d\theta} \omega_2 \quad (2.37)$$



**Figure 2.6** Disk cam with an oscillating roller follower.

where  $\xi(\theta)$  is the angular displacement function of the follower:

$$\xi(\theta) = \cos^{-1} \left[ \frac{l^2 + f^2 - (r_b + r_f)^2}{2lf} \right] + S(\theta) \quad (2.38)$$

where  $r_b$  is the radius of the base circle,  $r_f$  is the radius of the follower roller, and  $S(\theta)$  is the angular motion program (the angular displacement curve) of the follower. It can be seen that  $\psi(\theta) \equiv \xi(\theta)$  in this case. When  $\theta = 0^\circ$ ,  $S(0) = 0$ , the initial value of the angular displacement function will be

$$\xi(0) = \cos^{-1} \left[ \frac{l^2 + f^2 - (r_b + r_f)^2}{2lf} \right] \quad (2.39)$$

which is independent of the cam rotation angle  $\theta$ . From Eqs. (2.36) and (2.37) and after some algebraic manipulation,

$$q = \frac{f \frac{d\xi(\theta)}{d\theta}}{1 - \frac{d\xi(\theta)}{d\theta}} = \frac{f \frac{dS(\theta)}{d\theta}}{1 - \frac{dS(\theta)}{d\theta}} = \frac{fv(\theta)}{1-v(\theta)} \quad (2.40)$$

where  $v(\theta)$  is the angular velocity program of the follower. From  $\triangle O_3QC$  and the cosine

law,

$$QC = \sqrt{l^2 + (f+q)^2 - 2l(f+q)\cos\xi(\theta)} \quad (2.41)$$

From  $\triangle O_3QC$  and the sine law,

$$\alpha = \sin^{-1} \left[ \frac{l \sin \xi(\theta)}{QC} \right] \quad (2.42)$$

Therefore, the vectors of the theoretical cam profile coordinates are

$$\mathbf{O}_2\mathbf{A} = \mathbf{O}_2\mathbf{Q} + \mathbf{QA} \quad (2.43)$$

where

$$\mathbf{O}_2\mathbf{Q} = q \begin{Bmatrix} \cos(\theta + 180^\circ) \\ \sin(\theta + 180^\circ) \end{Bmatrix} = -q \begin{Bmatrix} \cos\theta \\ \sin\theta \end{Bmatrix} \quad (2.44)$$

$$\mathbf{QA} = (QC - r_f) \begin{Bmatrix} \cos(\theta + \alpha) \\ \sin(\theta + \alpha) \end{Bmatrix} \quad (2.45)$$

As a result, the parametric vector equations of the theoretical cam profile coordinates are

$$\mathbf{R}(\theta) = \mathbf{O}_2\mathbf{A} = \begin{Bmatrix} (QC - r_f)\cos(\theta + \alpha) - q\cos\theta \\ (QC - r_f)\sin(\theta + \alpha) - q\sin\theta \end{Bmatrix} \quad (2.46)$$

From  $\triangle O_3QC$ , the pressure angle  $\phi$  can be expressed as

$$\phi = 90^\circ - \alpha - \xi(\theta) \quad (2.47)$$

The common normal at the contact point must always pass through points Q, A, and C. Therefore, from Eqs. (2.45) and (2.47), the unit normal vector to the theoretical cam profile can be expressed as

$$\mathbf{n}(\theta) = -\frac{\mathbf{QA}}{\|\mathbf{QA}\|} = \begin{Bmatrix} -\cos(\theta + \alpha) \\ -\sin(\theta + \alpha) \end{Bmatrix} = \begin{Bmatrix} \sin[\theta - \xi(\theta) - \phi] \\ -\cos[\theta - \xi(\theta) - \phi] \end{Bmatrix} \quad (2.48)$$

## 2.6 DISK CAM WITH AN OSCILLATING FLAT-FACED FOLLOWER

Figure 2.7 shows a disk cam mechanism with an oscillating flat-faced follower. In this case,  $f$  represents the distance from the cam center to the follower pivot point, and  $e$  represents the follower face offset from the follower pivot point. (If the follower face is offset from the pivot point towards the cam center, it is negative. The quantity  $e$  is positive in Fig. 2.7.) By setting up a Cartesian coordinate system X-Y fixed on the cam and with its origin at the fixed pivot  $O_2$ , the cam profile coordinates may be expressed in terms of  $\theta$ , which is measured against the direction of cam rotation from the reference radial on the cam to the line between the cam center and the follower pivot point. The speed of point Q, instant center  $I_{23}$ , on the cam can be expressed as

$$V_Q = q\omega_2 \quad (2.49)$$

where  $q = O_2Q$  and  $\omega_2$  is the angular velocity of the cam. On the other hand, the speed of point Q on the follower can be expressed as

$$V_Q = (f + q) \frac{d\xi(\theta)}{dt} = (f + q) \frac{d\xi(\theta)}{d\theta} \omega_2 \quad (2.50)$$

where  $\xi(\theta)$  is the angular displacement function of the follower:

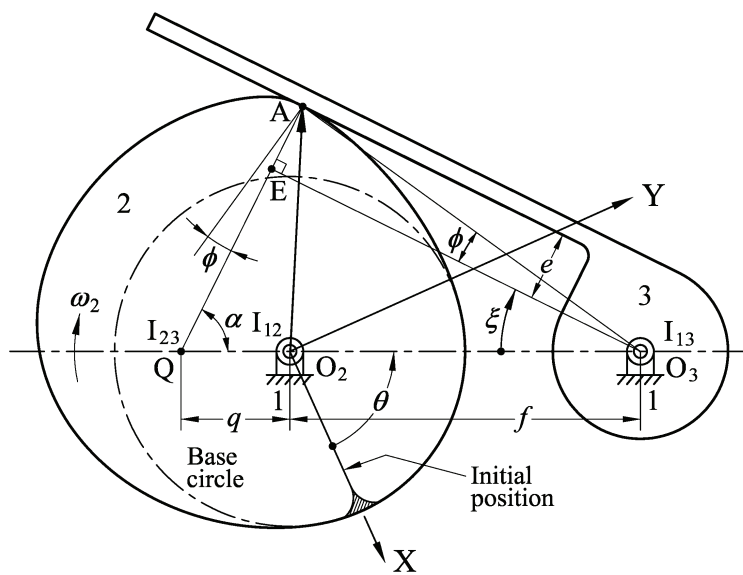


**Figure 2.7** Disk cam with an oscillating flat-faced follower.

$$\xi(\theta) = \sin^{-1} \left( \frac{r_b - e}{f} \right) + S(\theta) \quad (2.51)$$

Here,  $r_b$  is the radius of the base circle,  $e$  is the offset of the follower, and  $S(\theta)$  is the angular motion program (the angular displacement curve) of the follower. It can be seen that  $\psi(\theta) \equiv \xi(\theta)$  in this case. When  $\theta = 0^\circ$ ,  $S(0) = 0$ , the initial value of the angular displacement function will be

$$\xi(0) = \sin^{-1} \left( \frac{r_b - e}{f} \right) \quad (2.52)$$

which is independent of the cam rotation angle  $\theta$ . From Eqs. (2.49) and (2.50) and after some algebraic manipulation,

$$q = \frac{f \frac{d\xi(\theta)}{d\theta}}{1 - \frac{d\xi(\theta)}{d\theta}} = \frac{f \frac{dS(\theta)}{d\theta}}{1 - \frac{dS(\theta)}{d\theta}} = \frac{fv(\theta)}{1 - v(\theta)} \quad (2.53)$$

where  $v(\theta)$  is the angular velocity program of the follower. From  $\triangle O_3QE$ ,

$$QE = (f + q) \sin \xi(\theta) \quad (2.54)$$

$$\alpha = 90^\circ - \xi(\theta) \quad (2.55)$$

Therefore, the vectors of the theoretical cam profile coordinates are

$$\mathbf{O}_2\mathbf{A} = \mathbf{O}_2\mathbf{Q} + \mathbf{Q}\mathbf{A} \quad (2.56)$$

where

$$\mathbf{O}_2\mathbf{Q} = q \begin{Bmatrix} \cos(\theta + 180^\circ) \\ \sin(\theta + 180^\circ) \end{Bmatrix} = -q \begin{Bmatrix} \cos \theta \\ \sin \theta \end{Bmatrix} \quad (2.57)$$

$$\mathbf{Q}\mathbf{A} = (QE + e) \begin{Bmatrix} \cos(\theta + \alpha) \\ \sin(\theta + \alpha) \end{Bmatrix} \quad (2.58)$$

As a result, the parametric vector equations of the theoretical cam profile coordinates are

$$\mathbf{R}(\theta) = \mathbf{O}_2 \mathbf{A} = \begin{cases} (\text{QE} + e) \cos(\theta + \alpha) - q \cos \theta \\ (\text{QE} + e) \sin(\theta + \alpha) - q \sin \theta \end{cases} \quad (2.59)$$

From Eqs. (2.55) and (2.58), the unit normal vector to the theoretical cam profile can be expressed as

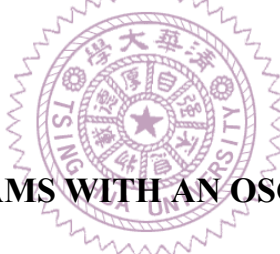
$$\mathbf{n}(\theta) = -\frac{\mathbf{QA}}{\|\mathbf{QA}\|} = \begin{cases} -\cos(\theta + \alpha) \\ -\sin(\theta + \alpha) \end{cases} = \begin{cases} \sin(\theta - \xi) \\ -\cos(\theta - \xi) \end{cases} \quad (2.60)$$

From  $\triangle O_3AE$ , the pressure angle  $\phi$  can be expressed as

$$\phi = \tan^{-1} \left( \frac{e}{O_3E} \right) \quad (2.61)$$

where

$$O_3E = (f + q) \cos \xi(\theta) \quad (2.62)$$



## 2.7 CONJUGATE DISK CAMS WITH AN OSCILLATING ROLLER FOLLOWER

Figure 2.8 shows a conjugate cam mechanism with an oscillating roller follower. There are two disk cams A and B, fixed on a common shaft. Two follower rollers C and D, mounted to a common follower, are each pushed in opposite directions by the conjugate cams. In this case,  $f$  represents the distance from the cam center  $O_2$  to the follower pivot point  $O_3$ , and  $l_A$  and  $l_B$  represents the arm lengths of the follower. By setting up a Cartesian coordinate system X-Y fixed on cam A and with its origin at the fixed pivot  $O_2$ , the cam profile coordinates may be expressed in terms of  $\theta$ , which is measured against the direction of cam rotation from the reference radial on the cam to the line between the cam center and the follower pivot point.

A conjugate cam mechanism may be considered as a permanent critical form and must always have three velocity instant centers [37]. As shown in Fig. 2.8, this means that the

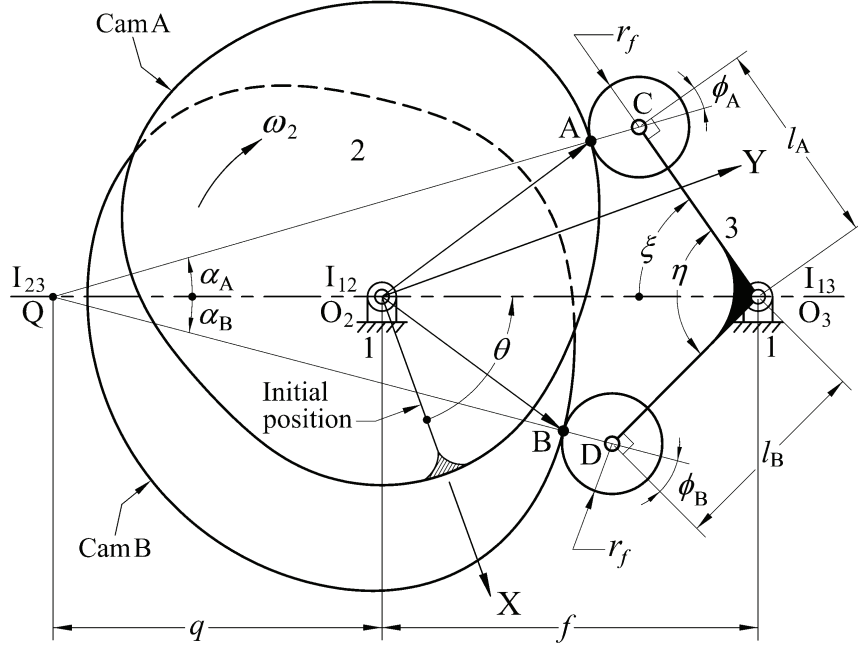


**Figure 2.8** Conjugate disk cams with an oscillating roller follower.

two normal lines through the points of contact and line of centers must always intersect at a common point, the instant center  $I_{23}$ . By labeling instant center  $I_{23}$  as  $Q$  and  $O_2Q = q$ , the speed of point  $Q$  on the cam can be expressed as

$$V_Q = q\omega_2 \quad (2.63)$$

where  $\omega_2$  is the angular velocity of the cam. On the other hand, the speed of point  $Q$  on the follower can be expressed as

$$V_Q = (f + q) \frac{d\xi(\theta)}{dt} = (f + q) \frac{d\xi(\theta)}{d\theta} \omega_2 \quad (2.64)$$

where  $\xi(\theta)$  is the angular displacement function of the follower:

$$\xi(\theta) = \cos^{-1} \left[ \frac{l_A^2 + f^2 - (r_b + r_f)^2}{2l_A f} \right] + S(\theta) \quad (2.65)$$

where  $r_b$  is the radius of the base circle of cam A,  $r_f$  is the radius the follower roller, and  $S(\theta)$  is the angular motion program (the angular displacement curve) of the follower. It can be seen that  $\psi(\theta) \equiv \xi(\theta)$  in this case. When  $\theta = 0^\circ$ ,  $S(0) = 0$ , the initial value of the angular displacement function will be

$$\xi(0) = \cos^{-1} \left[ \frac{l_A^2 + f^2 - (r_b + r_f)^2}{2l_A f} \right] \quad (2.66)$$

which is independent of the cam rotation angle  $\theta$ . From Eqs. (2.63) and (2.64) and after some algebraic manipulation,

$$q = \frac{f \frac{d\xi(\theta)}{d\theta}}{1 - \frac{d\xi(\theta)}{d\theta}} = \frac{f \frac{dS(\theta)}{d\theta}}{1 - \frac{dS(\theta)}{d\theta}} = \frac{fv(\theta)}{1 - v(\theta)} \quad (2.67)$$

where  $v(\theta)$  is the angular velocity program of the follower. From  $\triangle O_3QC$  and the cosine law,

$$QC = \sqrt{l_A^2 + (f+q)^2 - 2l_A(f+q)\cos\xi(\theta)} \quad (2.68)$$

From  $\triangle O_3QD$  and the cosine law,

$$QD = \sqrt{l_B^2 + (f+q)^2 - 2l_B(f+q)\cos[\eta - \xi(\theta)]} \quad (2.69)$$

where  $\eta$  is the subtending angle of the follower arms. From  $\triangle O_3QC$  and the sine law,

$$\alpha_A = \sin^{-1} \left[ \frac{l_A \sin \xi(\theta)}{QC} \right] \quad (2.70)$$

From  $\triangle O_3QD$  and the sine law,

$$\alpha_B = \sin^{-1} \left\{ \frac{l_B \sin [\eta - \xi(\theta)]}{QD} \right\} \quad (2.71)$$

Therefore, the vectors for the theoretical profile coordinates of cam A are

$$\mathbf{O}_2\mathbf{A} = \mathbf{O}_2\mathbf{Q} + \mathbf{QA} \quad (2.72)$$

where

$$\mathbf{O}_2\mathbf{Q} = q \begin{Bmatrix} \cos(\theta + 180^\circ) \\ \sin(\theta + 180^\circ) \end{Bmatrix} = -q \begin{Bmatrix} \cos \theta \\ \sin \theta \end{Bmatrix} \quad (2.73)$$

$$\mathbf{QA} = (QC - r_f) \begin{Bmatrix} \cos(\theta + \alpha_A) \\ \sin(\theta + \alpha_A) \end{Bmatrix} \quad (2.74)$$

Similarly, the vectors for the theoretical profile coordinates of cam B are

$$\mathbf{O}_2\mathbf{B} = \mathbf{O}_2\mathbf{Q} + \mathbf{QB} \quad (2.75)$$

where

$$\mathbf{QB} = (QD - r_f) \begin{Bmatrix} \cos(\theta - \alpha_B) \\ \sin(\theta - \alpha_B) \end{Bmatrix} \quad (2.76)$$

Hence, the parametric vector equations of the theoretical cam profile coordinates are

$$\mathbf{R}_A(\theta) = \mathbf{O}_2\mathbf{A} = \begin{Bmatrix} (QC - r_f) \cos(\theta + \alpha_A) - q \cos \theta \\ (QC - r_f) \sin(\theta + \alpha_A) - q \sin \theta \end{Bmatrix} \quad (2.77)$$

$$\mathbf{R}_B(\theta) = \mathbf{O}_2\mathbf{B} = \begin{Bmatrix} (QD - r_f) \cos(\theta - \alpha_B) - q \cos \theta \\ (QD - r_f) \sin(\theta - \alpha_B) - q \sin \theta \end{Bmatrix} \quad (2.78)$$

The common normal at the contact point A must always pass through points Q, A, and C. Also, the common normal at the contact point B must always pass through points Q, B, and D. Therefore, from Eqs. (2.74) and (2.76), the unit normal vectors to the theoretical cam profiles can be expressed as

$$\mathbf{n}_A(\theta) = -\frac{\mathbf{QA}}{\|\mathbf{QA}\|} = \begin{Bmatrix} -\cos(\theta + \alpha_A) \\ -\sin(\theta + \alpha_A) \end{Bmatrix} \quad (2.79)$$

$$\mathbf{n}_B(\theta) = -\frac{\mathbf{QB}}{\|\mathbf{QB}\|} = \begin{Bmatrix} -\cos(\theta - \alpha_B) \\ -\sin(\theta - \alpha_B) \end{Bmatrix} \quad (2.80)$$

From  $\triangle O_3QC$ , the pressure angle  $\phi_A$  of cam A can be expressed as

$$\phi_A = 90^\circ - \alpha_A - \xi(\theta) \quad (2.81)$$

From  $\triangle O_3QD$ , the pressure angle  $\phi_B$  of cam B can be expressed as

$$\phi_B = 90^\circ - \alpha_B - [\eta - \xi(\theta)] \quad (2.82)$$

# CHAPTER 3

## EQUIVALENT LINKAGE AND MECHANICAL ERROR ANALYSIS OF DISK CAM MECHANISMS

### 3.1 INTRODUCTION

The mechanical error in a cam mechanism refers to the follower motion deviation of the cam mechanism mainly caused by deflections and thermal expansions of links, clearances in joints, and manufacturing and assembly tolerances of members. The main purpose of the mechanical error analysis of the cam mechanism is to establish the theoretical correlation between the tolerance of each design parameter and the follower motion deviation. The mechanical error analysis is thus the key element of designing precision cam mechanisms. A simple, systematic, and accurate method for analyzing mechanical errors of cam mechanisms must be established for cam designers. As mentioned in Sub-section 1.2.1, Giordana et al. [59, 60] considered a disk cam with an oscillating roller follower from its equivalent four-bar linkage to deal with the influence of construction, measurement, and assembly errors on the motion deviation of the follower. Their method requires locating the curvature center of the cam profile by dealing with the data of measured cam profile coordinates through approximating small pieces of cam contours as circular arcs. Then the link lengths of the equivalent four-bar linkage corresponding to each cam angle must be estimated to perform the kinematic analysis. It involves much computation and may have insufficient accuracy. This chapter, still employing the concept of equivalent linkage, demonstrates a relatively simple and accurate analytical method to analyze the mechanical errors of disk cam mechanisms. A systematic approach, called the equivalent linkage method, is introduced in this chapter. This developed method can be advantageously extended to perform the mechanical error analysis of planar mechanisms incorporating linkages and cams. Theoretical validations of

the equivalent linkage method are performed to show its feasibility. Examples and a practical case study are then given to illustrate the method presented.

In undertaking the mechanical error analysis described in this study, the following assumptions are made: all members in a mechanism are rigid bodies, clearances in joints are reduced to the minimum level by proper fit and applying preload, and any thermal expansion caused by temperature variation is ignored.

### 3.2 FUNDAMENTALS OF THE EQUIVALENT LINKAGE METHOD

The kinematic analysis for a three-link direct-contact mechanism can be simplified by replacing the mechanism by an equivalent four-bar linkage [10, 38, 100, 101]. Such a replacement also provides a convenient means for determining the mechanical error of a disk cam mechanism. Figure 3.1(a) shows a direct-contact mechanism, in which points  $O_2$  and  $O_3$  are the fixed pivots of the cam and the follower, respectively, and points  $K_2$  and  $K_3$  are the centers of curvature of the cam and the follower in contact at point A, respectively.

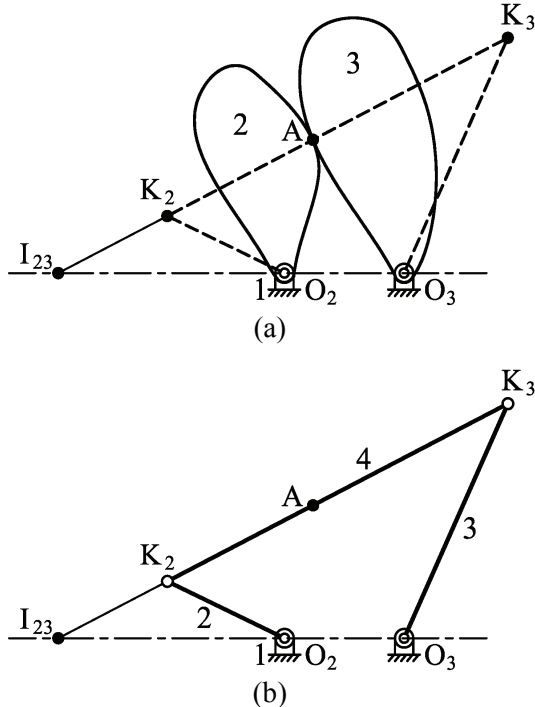


**Figure 3.1** Three-link direct-contact mechanism and its equivalent four-bar linkage.

The common normal at the contact point A must always pass through points  $K_2$ ,  $K_3$ , and the instant velocity center  $I_{23}$ . The equivalent linkage of this direct-contact mechanism is the four-bar linkage  $O_2K_2K_3O_3$  shown in Fig. 3.1(b), in which the coupler (link 4) of the linkage connects the centers of curvature of the cam,  $K_2$ , and of the follower,  $K_3$ . The instantaneous kinematic characteristics of links  $O_2K_2$  and  $O_3K_3$  are identical to those of the cam and the follower, respectively.

The actual profile of a machined cam may slightly deviate from the theoretical contour, and a deviation in the follower motion will thus be produced. Since the instantaneous kinematic characteristics of a cam mechanism are identical to those of its equivalent linkage, the mechanical error analysis of a cam mechanism can be performed through the aid of its equivalent linkage. In other words, if the profile error in the normal direction of a machined cam,  $\Delta n$ , equals the coupler-length error of the equivalent linkage,  $\Delta r_4$ , their output links will have the same motion deviations. Similarly, the dimensional errors of other theoretical design parameters of a cam mechanism arising from manufacturing and assembly errors can also be transformed into their corresponding link-length errors of the equivalent linkage. For a mechanism or mechanical device including more than one cam-follower systems, all cam-and-follower pairs in the mechanism or mechanical device can thus be simultaneously transformed into their equivalent four-bar linkages for performing the mechanical error analysis. As a result, the procedure developed by Hartenberg and Denavit [10], based on the concept of sensitivity analysis [62, 102], can be applied to calculate the output motion deviation of the equivalent four-bar linkage. A general form of the sensitivity analysis method for equivalent linkages is provided here.

### 3.2.1 Sensitivity Analysis Method for Equivalent linkages

For an  $N$  degree-of-freedom closed-loop linkage with  $m$  specified functional outputs, its implicit constraint or displacement equations, relating the constant link-length parameters  $r_1, r_2, \dots, r_n$  to the input variables  $\hat{\theta}_1, \hat{\theta}_2, \dots, \hat{\theta}_N$  and the functional output variables  $\psi_1, \psi_2, \dots, \psi_m$  may be written as

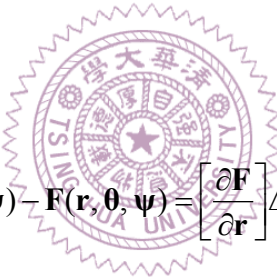
$$\mathbf{F}(\mathbf{r}, \boldsymbol{\theta}, \boldsymbol{\psi}) = \begin{Bmatrix} F_1(\mathbf{r}, \boldsymbol{\theta}, \boldsymbol{\psi}) \\ F_2(\mathbf{r}, \boldsymbol{\theta}, \boldsymbol{\psi}) \\ \vdots \\ F_m(\mathbf{r}, \boldsymbol{\theta}, \boldsymbol{\psi}) \end{Bmatrix} = \begin{Bmatrix} 0 \\ 0 \\ \vdots \\ 0 \end{Bmatrix} \quad (3.1)$$

where  $\mathbf{F}$  is an  $m$ -dimensional implicit function of vectors  $\mathbf{r}$ ,  $\boldsymbol{\theta}$ , and  $\boldsymbol{\psi}$ ; in which,  $\mathbf{r} = \{r_1 \ r_2 \ \cdots \ r_n\}^T$ ,  $\boldsymbol{\theta} = \{\hat{\theta}_1 \ \hat{\theta}_2 \ \cdots \ \hat{\theta}_N\}^T$ , and  $\boldsymbol{\psi} = \{\psi_1 \ \psi_2 \ \cdots \ \psi_m\}^T$ . Through kinematic analysis, the  $m$ -by-1 unknown vector  $\boldsymbol{\psi}$  would be solved analytically or numerically if vectors  $\mathbf{r}$  and  $\boldsymbol{\theta}$  are given. If the link-length parameters and the variables have slight deviations  $\Delta\mathbf{r}$ ,  $\Delta\boldsymbol{\theta}$ , and  $\Delta\boldsymbol{\psi}$ , the Taylor expansion of Eq. (3.1) can be written as

$$\mathbf{F}(\mathbf{r} + \Delta\mathbf{r}, \boldsymbol{\theta} + \Delta\boldsymbol{\theta}, \boldsymbol{\psi} + \Delta\boldsymbol{\psi}) \approx \mathbf{F}(\mathbf{r}, \boldsymbol{\theta}, \boldsymbol{\psi}) + \left[ \frac{\partial \mathbf{F}}{\partial \mathbf{r}} \right] \Delta\mathbf{r} + \left[ \frac{\partial \mathbf{F}}{\partial \boldsymbol{\theta}} \right] \Delta\boldsymbol{\theta} + \left[ \frac{\partial \mathbf{F}}{\partial \boldsymbol{\psi}} \right] \Delta\boldsymbol{\psi} = \mathbf{0} \quad (3.2)$$

The differential of the function  $\mathbf{F}$  may be written in terms of the Jacobian matrices of its partial derivatives as

$$d\mathbf{F} \approx \Delta\mathbf{F} \\ = \mathbf{F}(\mathbf{r} + \Delta\mathbf{r}, \boldsymbol{\theta} + \Delta\boldsymbol{\theta}, \boldsymbol{\psi} + \Delta\boldsymbol{\psi}) - \mathbf{F}(\mathbf{r}, \boldsymbol{\theta}, \boldsymbol{\psi}) = \left[ \frac{\partial \mathbf{F}}{\partial \mathbf{r}} \right] \Delta\mathbf{r} + \left[ \frac{\partial \mathbf{F}}{\partial \boldsymbol{\theta}} \right] \Delta\boldsymbol{\theta} + \left[ \frac{\partial \mathbf{F}}{\partial \boldsymbol{\psi}} \right] \Delta\boldsymbol{\psi} = \mathbf{0} \quad (3.3)$$



For a given vector of the input variables  $\boldsymbol{\theta}$  and letting  $\Delta\boldsymbol{\theta} = \mathbf{0}$ , the overall mechanical errors of the functional output variables will be

$$\Delta\boldsymbol{\psi} = - \left[ \frac{\partial \mathbf{F}}{\partial \boldsymbol{\psi}} \right]^{-1} \left[ \frac{\partial \mathbf{F}}{\partial \mathbf{r}} \right] \Delta\mathbf{r} = \mathbf{J} \Delta\mathbf{r} \quad (3.4)$$

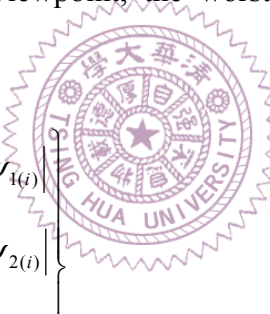
where,  $\mathbf{J}$  is called the sensitivity Jacobian matrix [102]. (Note that, in general,  $\hat{\theta}_1, \hat{\theta}_2, \dots, \hat{\theta}_N$  are inputs that are not subject to deviations or tolerances unless they are derived from the outputs of previous mechanisms or other devices [11]. Thus, the assumption of  $\Delta\boldsymbol{\theta} = \mathbf{0}$  could be given when considering that  $\boldsymbol{\theta}$  is an independent input vector.) Furthermore, the mechanical errors of the functional output variables caused by each link-length error can be expressed as

$$\Delta \boldsymbol{\psi}_{(i)} = \begin{Bmatrix} \Delta \psi_{1(i)} \\ \Delta \psi_{2(i)} \\ \vdots \\ \Delta \psi_{m(i)} \end{Bmatrix} = - \left[ \frac{\partial \mathbf{F}}{\partial \boldsymbol{\psi}} \right]^{-1} \left\{ \frac{\partial \mathbf{F}}{\partial \mathbf{r}} \right\}_i \Delta r_i = \mathbf{J}_i \Delta r_i \text{ for } i = 1, 2, \dots, n \quad (3.5)$$

where

$$\left\{ \frac{\partial \mathbf{F}}{\partial \mathbf{r}} \right\}_i = \left\{ \frac{\partial \mathbf{F}}{\partial r_i} \right\} = \begin{Bmatrix} \partial F_1 / \partial r_i \\ \partial F_2 / \partial r_i \\ \vdots \\ \partial F_m / \partial r_i \end{Bmatrix} \text{ for } i = 1, 2, \dots, n \quad (3.6)$$

and  $\mathbf{J}_i$  is called the sensitivity vector relating of the functional output variables and the  $i$ -th link-length parameter. In Eq. (3.5), the scalar  $\Delta \psi_{j(i)}$  represents the mechanical error of the  $j$ -th functional output variable caused by the dimensional error of the  $i$ -th link-length parameter. From the stochastic viewpoint, the worst-case deviations of the functional outputs will be [10, 11, 62]



$$\Delta \boldsymbol{\psi}_{\text{wor}} = \begin{Bmatrix} \Delta \psi_{1,\text{wor}} \\ \Delta \psi_{2,\text{wor}} \\ \vdots \\ \Delta \psi_{m,\text{wor}} \end{Bmatrix} = \begin{Bmatrix} \sum_{i=1}^n |\Delta \psi_{1(i)}| \\ \sum_{i=1}^n |\Delta \psi_{2(i)}| \\ \vdots \\ \sum_{i=1}^n |\Delta \psi_{m(i)}| \end{Bmatrix} \quad (3.7)$$

in which the scalars represent the worst combinations of the output deviation caused by each link-length error. The maximum expected deviations of the functional outputs will be [10, 11, 62, 103]

$$\Delta \boldsymbol{\psi}_{\text{rss}} = \begin{Bmatrix} \Delta \psi_{1,\text{rss}} \\ \Delta \psi_{2,\text{rss}} \\ \vdots \\ \Delta \psi_{m,\text{rss}} \end{Bmatrix} = \begin{Bmatrix} \sqrt{\sum_{i=1}^n (\Delta \psi_{1(i)})^2} \\ \sqrt{\sum_{i=1}^n (\Delta \psi_{2(i)})^2} \\ \vdots \\ \sqrt{\sum_{i=1}^n (\Delta \psi_{m(i)})^2} \end{Bmatrix} \quad (3.8)$$

in which the scalars are obtained by the widely used root sum of squares (RSS) approach [62]. Assuming a mechanism is manufactured and assembled under a normal distribution condition, Eq. (3.8) can give statistical tolerances of the functional outputs of the mechanism on the basis of three standard deviations. In other words, when the tolerances of the link-length parameters,  $\pm \Delta r_1$ ,  $\pm \Delta r_2$ , ...,  $\pm \Delta r_n$ , are allocated, the output deviations will fall inside the range of  $\pm \Delta \psi_{\text{rss}}$  with probability of 99.73% [11, 62]. To perform the mechanical error analysis, the data of input variables  $\theta$ , link-length parameters  $r$  and their deviations (or tolerance)  $\Delta r$  must be given to estimate the corresponding error functions  $\Delta\psi(\theta)$ ,  $\Delta\psi_{\text{wor}}(\theta)$ , and  $\Delta\psi_{\text{rss}}(\theta)$ .

### 3.2.2 Radial Profile Error and Normal-Direction Error of Disk Cams

In practice, the accuracy of a machined cam can be controlled through a properly specified tolerance of the radial dimension of the actual cam profile. Recall from Figs. 1.3 and 1.4 that the radial-dimensional tolerances of the cam profiles in the illustrated manufacturing drawings are specified to be 0.02 mm in the form of either a bilateral or unilateral tolerance. In other words, the radial dimension of the actual cam profile with respect to each cam angle must lie within a specified zone along the ideal profile. In order to find how the radial-dimension errors of the actual cam profile affect the motion deviation of the follower, the correlation between the radial-dimension error and the normal-direction error of the cam profile must be established.

Figures 3.2(a) and 3.2(b) respectively show a disk cam in contact with its roller follower or flat-faced follower, in which the theoretical cam profiles are shown in solid lines and the actual cam profiles in dashed lines, and the profile deviations are exaggerated for clarity. The theoretical contact point is designated by A, and its normal to the cam profile intersects the actual cam profile at point  $A_n$ ; line  $O_2A$  intersects the actual cam profile at point  $A_r$ . For a sufficiently small value of normal-direction profile error  $AA_n$ , since  $A_nA_r$  will be tangent to the actual cam profile and  $A_nA$  will be normal to the profile,

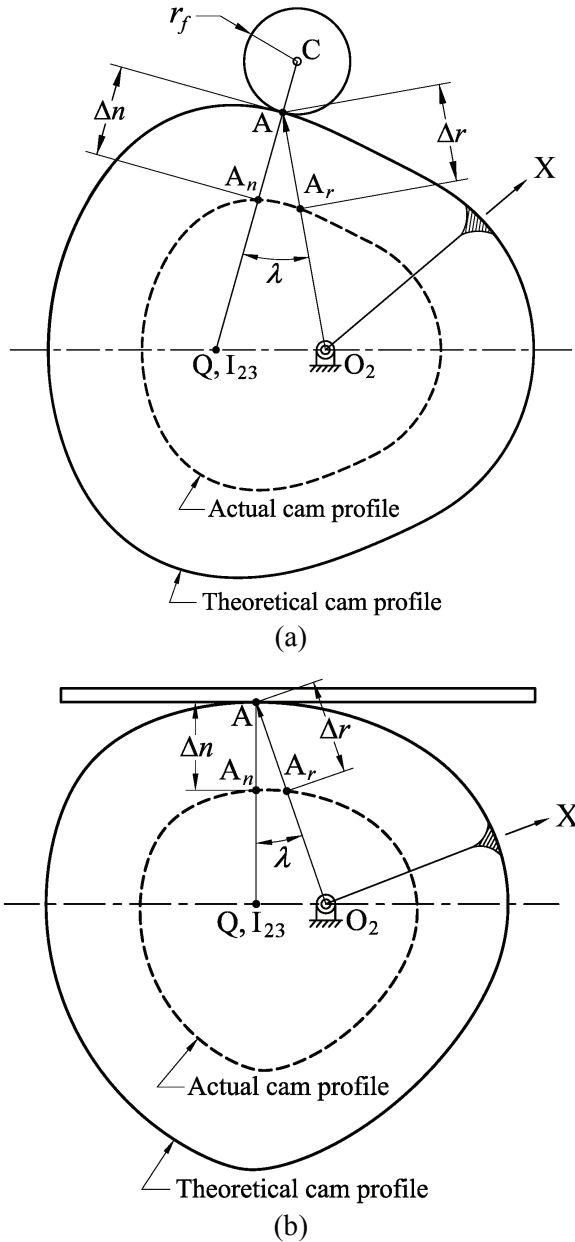


**Figure 3.2** Actual and theoretical profiles of disk cams.

$\triangle AA_n A_r$  can be considered as a right-angled triangle, and thus

$$\Delta n \approx \Delta r \cos \lambda \quad (3.9)$$

where  $\Delta n = AA_n$ ,  $\Delta r = AA_r$  and  $\lambda = \angle A_r A A_n$ . (The quantity  $\Delta n$  and  $\Delta r$  are negative if the actual cam profile is smaller than the theoretical one; in the figure shown they are negative.) The subtending angle between lines  $AA_n$  and  $AA_r$ ,  $\lambda$ , is called the shift angle in this dissertation. In addition, the common normal at the contact point A must always pass through point Q, which is also the instant center  $I_{23}$ , and so

$$\lambda = \angle O_2AQ \quad (3.10)$$

From  $\triangle O_2AQ$ ,

$$\lambda = \sin^{-1} \left( \frac{\mathbf{QA} \times \mathbf{O}_2\mathbf{A}}{\|\mathbf{QA}\| \cdot \|\mathbf{O}_2\mathbf{A}\|} \right) = \sin^{-1} \left[ \frac{\mathbf{QA} \times \mathbf{R}(\theta)}{\|\mathbf{QA}\| \cdot \|\mathbf{R}(\theta)\|} \right] \quad (3.11)$$

This is a general expression for the shift angle  $\lambda$  and is applicable to all types of disk cam mechanisms. Equation (3.9) shows how to transform the radial profile error of a cam into its corresponding normal-direction error, i.e., the coupler-length error of the equivalent linkage, by applying the shift angle. In practice, the use of the shift angle should be applicable when the following conditions are satisfied as far as possible: (1) the profile deviations are small enough (i.e., small tolerance amounts of the radial dimensions of the cam profile are specified), and (2) the actual cam profile is continuous and smooth enough to avoid sudden changes of directions of normal vectors to the machined cam surface (namely, good surface finish of the machined cam is achieved). If the parametric vector equations and the radial dimensions of a cam profile are obtained, one may evaluate the follower motion deviations arising from the cam profile error (or tolerance) by combining the proposed analytical transformation of cam profile errors with the sensitivity analysis method introduced in Sub-section 3.2.1.

### 3.2.3 Analysis Procedure

Figure 3.3 shows the flowchart of the analysis procedure for applying the equivalent linkage method to disk cam mechanisms, where the analysis steps are demonstrated as follows:

Step 1. Select a disk cam mechanism as the analysis target whose parametric vector equation and radial dimensions of the cam profile have been obtained, and then identify its design parameters whose dimensional deviations would cause the kinematic error of the follower.

Step 2. Replace the selected disk cam mechanism by its equivalent linkage, and then

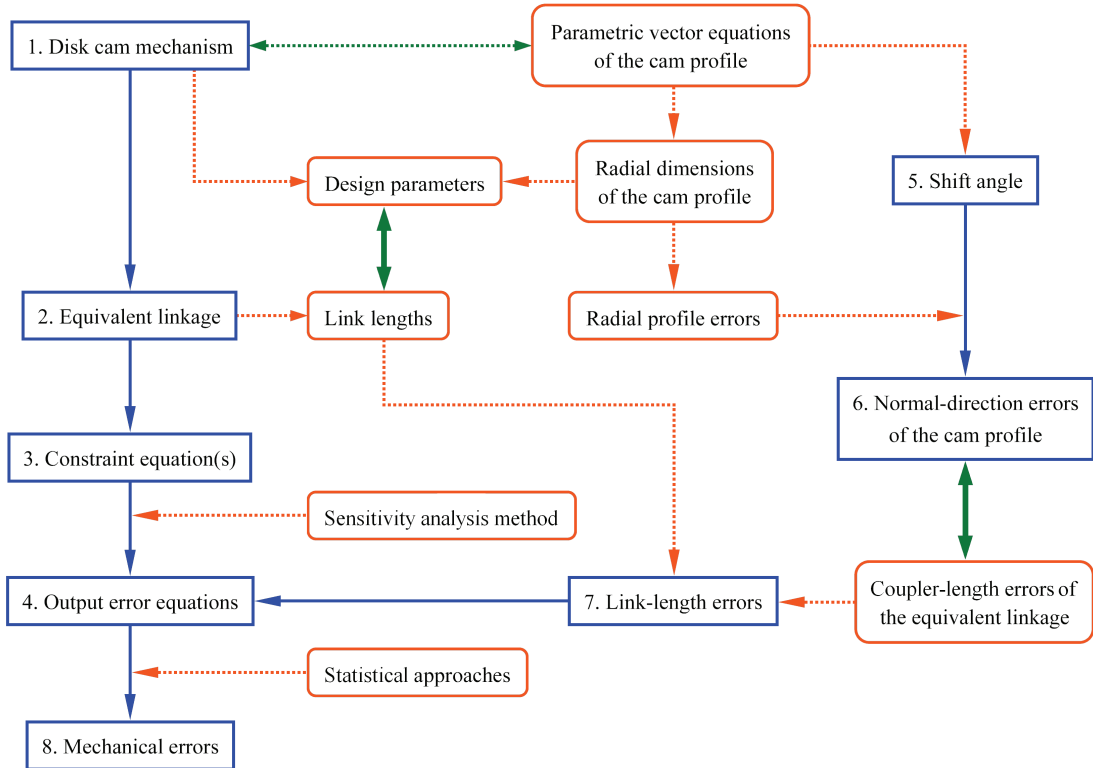


**Figure 3.3** Flowchart of the analysis procedure for the equivalent linkage method.

transform the design parameters identified in Step 1 into their corresponding link-length parameters of the equivalent linkage.

Step 3. Derive the constraint or displacement equation(s) of the equivalent linkage relating the link-length parameters to the input and output variables.

Step 4. Apply Eq. (3.5) to derive the kinematic error equations of the output link caused by each link-length error.

Step 5. Apply Eq. (3.10) to calculate the shift angle of the cam profile with the aid of the parametric vector equation of the cam profile.

Step 6. Apply Eq. (3.9) to estimate the normal-direction errors of the cam profile with specified radial profile errors, and then transform the normal-direction errors into their corresponding coupler-length errors of the equivalent linkage.

Step 7. Specify other link-length errors of the equivalent linkage, and then substitute them and the coupler-length errors obtained in Step 6 into the output error equations derived in Step 4.

Step 8. Calculate the mechanical errors of the follower output with the statistical approaches by applying Eqs. (3.7) and (3.8), and then evaluate the result.

The eight steps of the analysis procedure of the equivalent linkage method are equally applicable to planar mechanisms with multiple cam-follower systems included.

### 3.3 MECHANICAL ERRORS IN DISK CAM MECHANISMS

In this section, the proposed equivalent linkage method is applied to four types of commonly used disk cam mechanisms to derive the error functions of their follower outputs. Here, disk cams with an offset translating roller follower, an offset translating oblique flat-faced follower, an oscillating roller follower, and an oscillating flat-faced follower are demonstrated.

#### 3.3.1 Disk Cam with an Offset Translating Roller Follower

For the cam mechanism with an offset translating roller follower shown in Fig. 3.4(a), let point K be the center of curvature of the cam in contact with the follower [104] and point A be the contact point between the cam and the follower. Its equivalent linkage is the slider-crank linkage shown in Fig. 3.4(b), in which the coupler (link 4) of the linkage connects the center of curvature of the cam, K, and the roller center, C (i.e., the center of curvature of the roller). The instantaneous kinematic characteristics of the crank and the slider are identical to those of the cam and the follower. For the equivalent linkage shown in Fig. 3.4(b), the displacement equation, relating the parameters  $e$ ,  $r_2$ ,  $r_4$  to the input and output variables  $\theta_2$  and  $L(\theta)$ , may be written as

$$F(\mathbf{r}, \boldsymbol{\theta}, \boldsymbol{\psi}) = F(e, r_2, r_4, \theta_2, L) = 0 \quad (3.12)$$

in which,  $\mathbf{r} = \{e \ r_2 \ r_4\}^T$ ,  $\boldsymbol{\theta} = \{\theta_2\}$ , and  $\boldsymbol{\psi} = \{L\}$ ; or [10]

$$F = 2r_2(L \sin \theta_2 - e \cos \theta_2) + r_4^2 - (r_2^2 + L^2 + e^2) = 0 \quad (3.13)$$

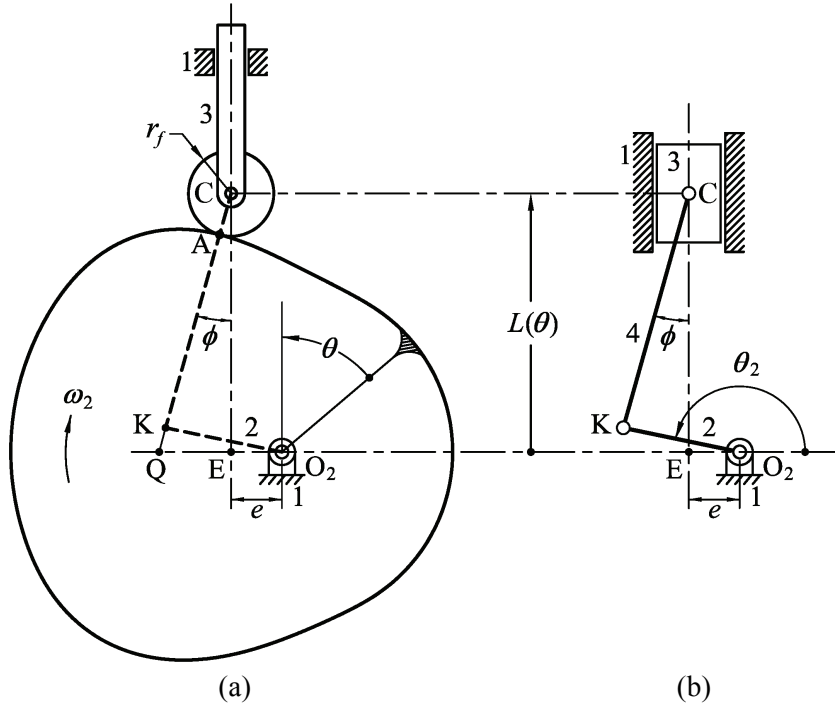


**Figure 3.4** Disk cam with an offset translating roller follower and its equivalent slider-crank linkage.

where  $e$  is the offset,  $r_2 = O_2K$ , and  $r_4 = KC$ . For small values of the errors  $\Delta e$ ,  $\Delta r_2$ ,  $\Delta r_4$ ,  $\Delta \theta_2$ , and  $\Delta L$ , the differential of the function  $F$  may be written in terms of its partial derivatives as

$$dF \approx \Delta F = \frac{\partial F}{\partial e} \Delta e + \frac{\partial F}{\partial r_2} \Delta r_2 + \frac{\partial F}{\partial r_4} \Delta r_4 + \frac{\partial F}{\partial \theta_2} \Delta \theta_2 + \frac{\partial F}{\partial L} \Delta L = 0 \quad (3.14)$$

#### Error caused only by $\Delta r_4$ :

If only the error of the coupler-length  $\Delta r_4$  is considered to induce the output error  $\Delta L$ , all other parameters having exactly the same dimensions, the mechanical error at the output can be expressed as

$$\Delta L = -\frac{\partial F / \partial r_4}{\partial F / \partial L} \Delta r_4 \quad (3.15)$$

where

$$\frac{\partial F}{\partial r_4} = 2r_4 \quad (3.16)$$

$$\frac{\partial F}{\partial L} = 2(r_2 \sin \theta_2 - L) \quad (3.17)$$

The quantity  $\Delta r_4$  is the resultant deviation of the profile error of the cam,  $\Delta n$ , together with the radius error of roller C,  $\Delta r_f$ . That is,  $\Delta r_4 = \Delta n + \Delta r_f$ . Since the output error  $\Delta L$  is identical to the follower motion error  $\Delta S$ , after manipulation and reduction, the mechanical errors  $\Delta S_n$  and  $\Delta S_{rf}$  respectively caused by  $\Delta n$  and  $\Delta r_f$  are

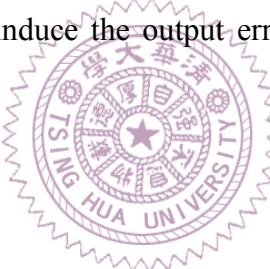
$$\Delta S_n = \Delta L = \frac{r_4}{L - r_2 \sin \theta_2} (\Delta r_4 - \Delta r_f) = \frac{\Delta r_4 - \Delta r_f}{\cos \phi} = \frac{\Delta n}{\cos \phi} \quad (3.18)$$

$$\Delta S_{rf} = \Delta L = \frac{r_4}{L - r_2 \sin \theta_2} (\Delta r_4 - \Delta n) = \frac{\Delta r_4 - \Delta n}{\cos \phi} = \frac{\Delta r_f}{\cos \phi} \quad (3.19)$$

### **Error caused only by $\Delta e$ :**

If only  $\Delta e$  is considered to induce the output error  $\Delta L$ , the mechanical error at the output can be expressed as

$$\Delta L = -\frac{\partial F / \partial e}{\partial F / \partial L} \Delta e \quad (3.20)$$



where

$$\frac{\partial F}{\partial e} = -2(r_2 \cos \theta_2 + e) \quad (3.21)$$

$$\frac{\partial F}{\partial L} = 2(r_2 \sin \theta_2 - L) \quad (3.22)$$

After some manipulation and reduction, the mechanical error  $\Delta S_e$  caused by  $\Delta e$  is

$$\Delta S_e = \Delta L = -\frac{r_2 \cos \theta_2 + e}{L - r_2 \sin \theta_2} \Delta e = \Delta e \tan \phi \quad (3.23)$$

Equations (3.18), (3.19), and (3.23) indicate that, as expected, the pressure angle,  $\phi$ , have a significant effect on the resulting errors; it appears in the form of  $(1/\cos \phi)$  to magnify them [10]. In addition, it is interesting to note that in the final expressions of Eqs.

(3.18), (3.19), and (3.23), the parameters  $r_2$  and  $r_4$  are not actually involved. In other words, locating the curvature center of the cam profile in the analysis process is not really essential, and this fact makes the analysis easier to perform.

### Error caused only by $\Delta r$ :

For the cam mechanism with an offset translating roller follower shown in Fig. 3.5, from the right-angled triangle QCE

$$\beta = 90^\circ - \phi \quad (3.24)$$

Applying the sine law to  $\triangle O_2AQ$  yields

$$\lambda = \sin^{-1} \left( \frac{q \sin \beta}{\|O_2A\|} \right) = \sin^{-1} \left[ \frac{v(\theta) \cos \phi}{\|\mathbf{R}(\theta)\|} \right] \quad (3.25)$$

From Eqs. (3.9), (3.18), and (3.25), the motion deviation of the translating roller follower caused by the radial-dimension error of the cam profile,  $\Delta r$ , is

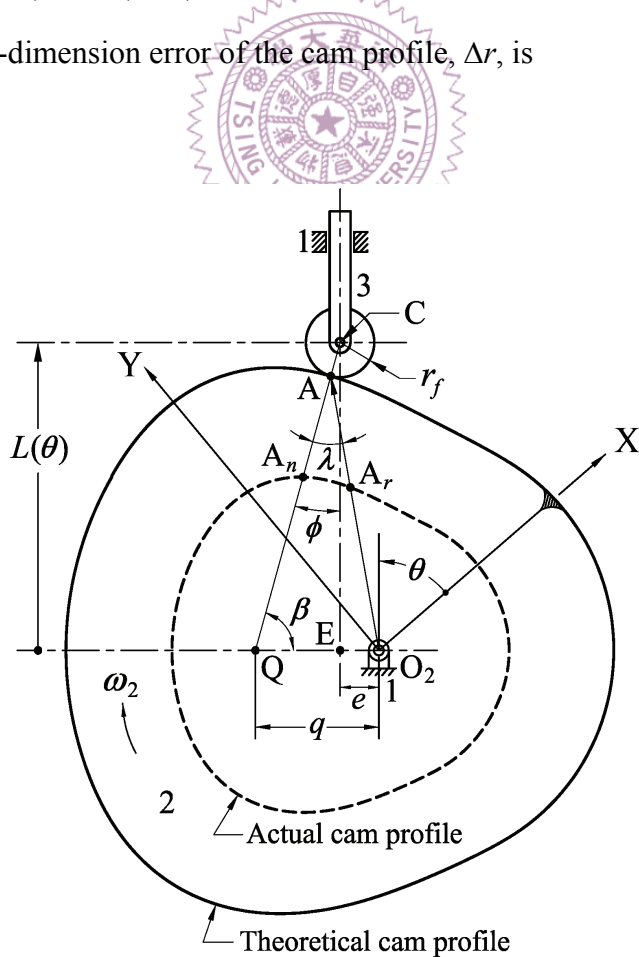


**Figure 3.5** Disk cam with an offset translating roller follower and its actual cam profile.

$$\Delta S_r = \Delta L \approx \frac{\Delta r \cos \lambda}{\cos \phi} \quad (3.26)$$

Note that the effect of the pressure angle  $\phi$  on the resulting error is here counteracted by the shift angle  $\lambda$  with the form of  $\cos \lambda$ .

### 3.3.2 Disk Cam with an Offset Translating Oblique Flat-Faced Follower

For the cam mechanism with an offset translating oblique flat-faced follower shown in Fig. 3.6(a), let point K be the center of curvature of the cam in contact with the follower and point A be the contact point between the cam and the follower. Its equivalent linkage is the Scotch yoke mechanism shown in Fig. 3.6(b), in which the additional link is a floating slider block (link 4). The floating slider block pivots on one end of the crank (link 2) at the center of curvature of the cam, K, and connects the yoke (link 3) by a prismatic joint whose relative translation is along line AP. The characteristic length of the floating slider block  $r_4$  is defined as KA, which is also the radius of curvature of the cam. The instantaneous kinematic characteristics of the crank and the yoke are identical to those of

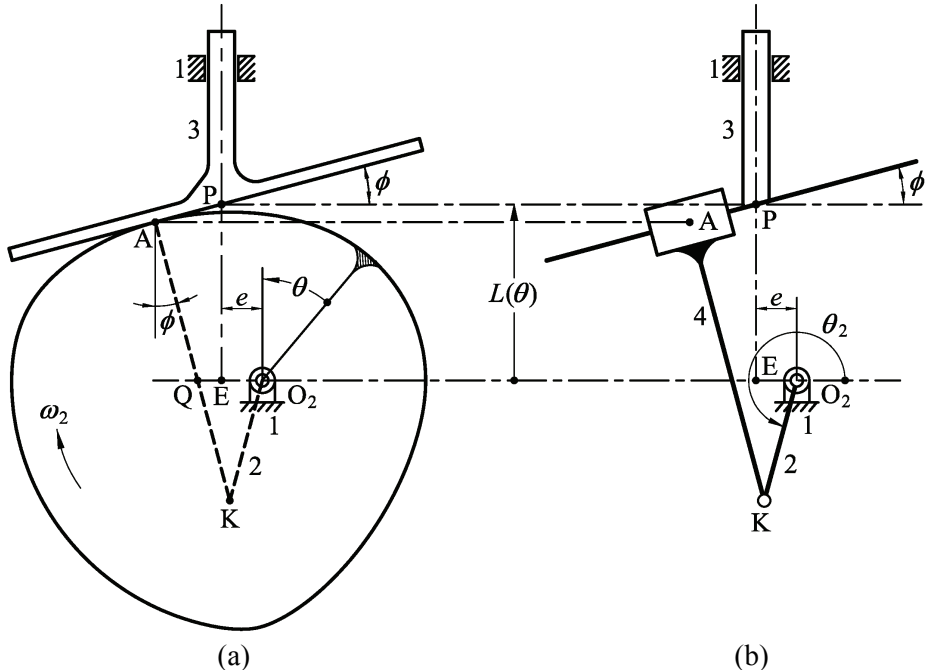


**Figure 3.6** Disk cam with an offset translating oblique flat-faced follower and its equivalent Scotch yoke mechanism.

the cam and the follower. For the equivalent linkage shown in Fig. 3.6(b), the displacement equation, relating the parameters  $\phi$ ,  $e$ ,  $r_2$ ,  $r_4$  to the input and output variables  $\theta_2$  and  $L(\theta)$ , may be written as

$$F(\mathbf{r}, \boldsymbol{\theta}, \boldsymbol{\psi}) = F(\phi, e, r_2, r_4, \theta_2, L) = 0 \quad (3.27)$$

in which,  $\mathbf{r} = \{\phi \ e \ r_2 \ r_4\}^T$ ,  $\boldsymbol{\theta} = \{\theta_2\}$ , and  $\boldsymbol{\psi} = \{L\}$ ; or

$$F = r_2 \sin(\theta_2 - \phi) + r_4 - e \sin \phi - L \cos \phi = 0 \quad (3.28)$$

where  $\phi$  is the oblique angle (the invariant pressure angle),  $e$  is the offset,  $r_2 = O_2K$ , and  $r_4 = KA$ . For small values of the errors  $\Delta\phi$ ,  $\Delta e$ ,  $\Delta r_2$ ,  $\Delta r_4$ ,  $\Delta\theta_2$ , and  $\Delta L$ , the differential of the function  $F$  may be written in terms of its partial derivatives as

$$dF \approx \Delta F = \frac{\partial F}{\partial \phi} \Delta \phi + \frac{\partial F}{\partial e} \Delta e + \frac{\partial F}{\partial r_2} \Delta r_2 + \frac{\partial F}{\partial r_4} \Delta r_4 + \frac{\partial F}{\partial \theta_2} \Delta \theta_2 + \frac{\partial F}{\partial L} \Delta L = 0 \quad (3.29)$$

#### **Error caused only by $\Delta r_4$ :**

If only the error of the cam profile  $\Delta r_4$  (or  $\Delta n$ ) is considered to induce the output error  $\Delta L$ , all other parameters having exactly the same dimensions, the mechanical error at the output can be expressed as

$$\Delta L = -\frac{\partial F / \partial r_4}{\partial F / \partial L} \Delta r_4 \quad (3.30)$$

where

$$\frac{\partial F}{\partial r_4} = 1 \quad (3.31)$$

$$\frac{\partial F}{\partial L} = -\cos \phi \quad (3.32)$$

Since the output error  $\Delta L$  is identical to the follower motion error  $\Delta S$ , after manipulation and reduction, the mechanical error  $\Delta S_n$  caused by  $\Delta n$  is

$$\Delta S_n = \Delta L = \frac{\Delta r_4}{\cos \phi} = \frac{\Delta n}{\cos \phi} \quad (3.33)$$

**Error caused only by  $\Delta\phi$ :**

If only  $\Delta\phi$  is considered to induce the output error  $\Delta L$ , the mechanical error at the output can be expressed as

$$\Delta L = -\frac{\partial F/\partial\phi}{\partial F/\partial L} \Delta\phi \quad (3.34)$$

where

$$\frac{\partial F}{\partial \phi} = L \sin \phi - e \cos \phi - r_2 \cos(\theta_2 - \phi) \quad (3.35)$$

$$\frac{\partial F}{\partial L} = -\cos \phi \quad (3.36)$$

After some manipulation and reduction, the mechanical error  $\Delta S_\phi$  caused by  $\Delta\phi$  is

$$\Delta S_\phi = \Delta L = \frac{L \sin \phi - e \cos \phi - r_2 \cos(\theta_2 - \phi)}{\cos \phi} \Delta\phi = \frac{u}{\cos \phi} \Delta\phi \quad (3.37)$$

where

$$u = PA = L \sin \phi + (q - e) \cos \phi \quad (3.38)$$

Here,  $u$  is the varying distance from the follower reference point P to the contact point A. (It should be noted that, in order to have consistent units,  $\Delta\phi$  must be in radians. Then a quantity with ‘length’ times ‘angle in radian’, such as  $\Delta S_\phi$ , may be regarded to have a dimension of ‘length’.)

**Error caused only by  $\Delta e$ :**

If only  $\Delta e$  is considered to induce the output error  $\Delta L$ , the mechanical error at the output can be expressed as

$$\Delta L = -\frac{\partial F/\partial e}{\partial F/\partial L} \Delta e \quad (3.39)$$

where

$$\frac{\partial F}{\partial e} = -\sin \phi \quad (3.40)$$

$$\frac{\partial F}{\partial L} = -\cos \phi \quad (3.41)$$

After some manipulation and reduction, the mechanical error  $\Delta S_e$  caused by  $\Delta e$  is

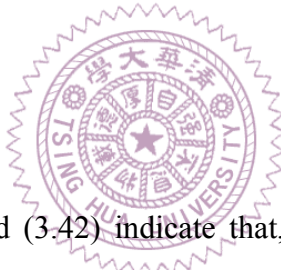
$$\Delta S_e = \Delta L = -\frac{\sin \phi}{\cos \phi} \Delta e = -\Delta e \tan \phi \quad (3.42)$$

For a translating flat-faced follower with zero oblique angle,  $\phi = 0^\circ$  and Eq. (3.38) yields  $u = PA = (q - e)$ , then Eqs. (3.33), (3.37) and (3.42) yield

$$\Delta S_n = \Delta n \quad (3.43)$$

$$\Delta S_\phi = (q - e) \Delta \phi \quad (3.44)$$

$$\Delta S_e = 0 \quad (3.45)$$



Equations (3.33), (3.37), and (3.42) indicate that, again, the pressure angle have a significant effect on the resulting errors; it appears in the form of  $(1/\cos \phi)$  to magnify them. It is also interesting to note that in the final expressions of Eqs. (3.33), (3.37), and (3.42), the parameters  $r_2$  and  $r_4$  are not actually involved. Thus, locating the curvature center of the cam profile in the analysis process is not really essential, and this fact makes the analysis easier to perform.

### **Error caused only by $\Delta r$ :**

For the cam mechanism with an translating oblique flat-faced follower shown in Fig. 3.7, applying the sine law to  $\triangle O_2AQ$  yields

$$\lambda = \sin^{-1} \left[ \frac{q \sin(\phi + 90^\circ)}{\|O_2A\|} \right] = \sin^{-1} \left[ \frac{v(\theta) \cos \phi}{\|\mathbf{R}(\theta)\|} \right] \quad (3.46)$$

where  $\angle O_2QA = \phi + 90^\circ$ . From Eqs. (3.9), (3.33), and (3.46), the motion deviation of the

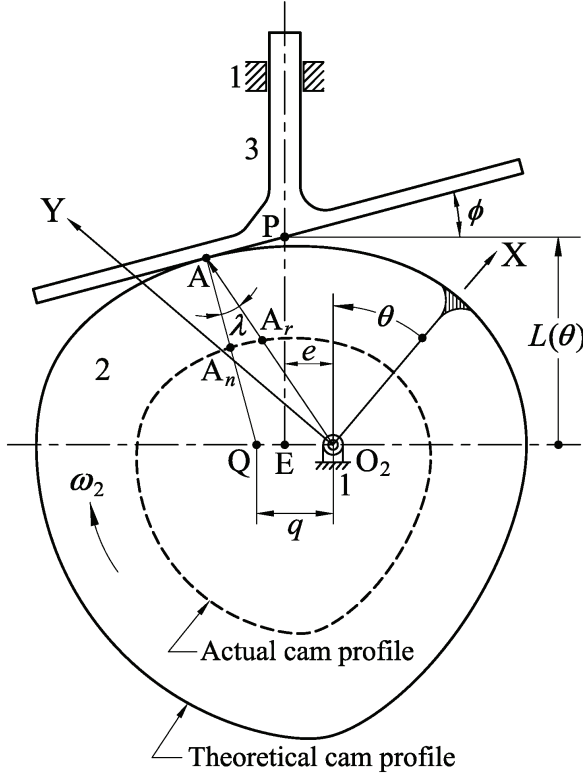


**Figure 3.7** Disk cam with an offset translating oblique flat-faced follower and its actual cam profile.

translating flat-faced follower caused by the radial-dimension error of the cam profile,  $\Delta r$ , is

$$\Delta S_r = \Delta L \approx \frac{\Delta r \cos \lambda}{\cos \phi} \quad (3.47)$$

Note that the follower motion deviation  $\Delta S_r$  is dominated by the shift angle  $\lambda$  with the form of  $\cos \lambda$ , since the pressure angle  $\phi$  is a constant.

### 3.3.3 Disk Cam with an Oscillating Roller Follower

For the cam mechanism with an oscillating roller follower shown in Fig. 3.8(a), let point K be the center of curvature of the cam in contact with the follower and point A be the contact point between the cam and the follower. Its equivalent linkage is the four-bar linkage shown in Fig. 3.8(b), in which the coupler (link 4) of the linkage connects the center of curvature of the cam, K, and the roller center, C (i.e., the center of curvature of

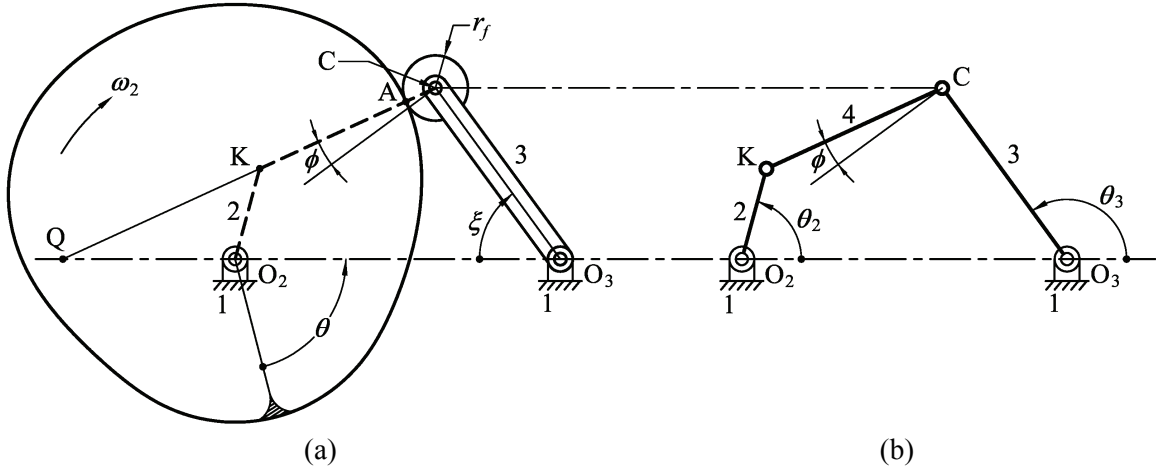


**Figure 3.8** Disk cam with an oscillating roller follower and its equivalent four-bar linkage.

the roller). The instantaneous kinematic characteristics of the crank and the rocker are identical to those of the cam and the follower. For the equivalent linkage shown in Fig. 3.8(b), the displacement equation, relating the parameters  $r_1, r_2, r_3, r_4$  to the input and output variables  $\theta_2$  and  $\theta_3$ , may be written as

$$F(\mathbf{r}, \boldsymbol{\theta}, \boldsymbol{\psi}) = F(r_1, r_2, r_3, r_4, \theta_2, \theta_3) = 0 \quad (3.48)$$

in which,  $\mathbf{r} = \{r_1 \ r_2 \ r_3 \ r_4\}^T$ ,  $\boldsymbol{\theta} = \{\theta_2\}$ , and  $\boldsymbol{\psi} = \{\theta_3\}$ ; or [10, 105]

$$F = 2[r_1(r_3 \cos \theta_3 - r_2 \cos \theta_2) - r_2 r_3 \cos(\theta_2 - \theta_3)] + r_1^2 + r_2^2 + r_3^2 - r_4^2 = 0 \quad (3.49)$$

where  $r_1 = O_2O_3 = f$ ,  $r_2 = O_2K$ ,  $r_3 = O_3C = l$ , and  $r_4 = KC$ . Equation (3.49) is also known as the Freudenstein equation [10, 105]. For small values of the errors  $\Delta r_1, \Delta r_2, \Delta r_3, \Delta r_4, \Delta \theta_2$ , and  $\Delta \theta_3$ , the differential of the function  $F$  may be written in terms of its partial derivatives as

$$dF \approx \Delta F = \frac{\partial F}{\partial r_1} \Delta r_1 + \frac{\partial F}{\partial r_2} \Delta r_2 + \frac{\partial F}{\partial r_3} \Delta r_3 + \frac{\partial F}{\partial r_4} \Delta r_4 + \frac{\partial F}{\partial \theta_2} \Delta \theta_2 + \frac{\partial F}{\partial \theta_3} \Delta \theta_3 = 0 \quad (3.50)$$

#### Error caused only by $\Delta r_4$ :

If only the error of the coupler-length  $\Delta r_4$  is considered to induce the output error  $\Delta \theta_3$ , the mechanical error at the output can be expressed as

$$\Delta\theta_3 = -\frac{\partial F/\partial r_4}{\partial F/\partial\theta_3} \Delta r_4 \quad (3.51)$$

where

$$\frac{\partial F}{\partial r_4} = -2r_4 \quad (3.52)$$

$$\frac{\partial F}{\partial\theta_3} = -2r_3[r_1 \sin\theta_3 + r_2 \sin(\theta_2 - \theta_3)] \quad (3.53)$$

The quantity  $\Delta r_4$  is the resultant deviation of the profile error of the cam,  $\Delta n$ , together with the radius error of roller C,  $\Delta r_f$ . That is,  $\Delta r_4 = \Delta n + \Delta r_f$ . Recall from Fig. 3.8 that  $\xi(\theta) = 180^\circ - \theta_3$ , and thus  $\Delta S = \Delta\xi = -\Delta\theta_3$ . After some manipulation and reduction, the mechanical errors  $\Delta S_n$  and  $\Delta S_{rf}$  respectively caused by  $\Delta n$  and  $\Delta r_f$  are

$$\Delta S_n = -\Delta\theta_3 = \frac{r_4}{r_3[r_1 \sin\theta_3 + r_2 \sin(\theta_2 - \theta_3)]} (\Delta r_4 + \Delta r_f) = \frac{\Delta r_4 - \Delta r_f}{r_3 \cos\phi} = \frac{\Delta n}{l \cos\phi} \quad (3.54)$$

$$\Delta S_{rf} = -\Delta\theta_3 = \frac{r_4}{r_3[r_1 \sin\theta_3 + r_2 \sin(\theta_2 - \theta_3)]} (\Delta r_4 - \Delta n) = \frac{\Delta r_f - \Delta n}{r_3 \cos\phi} = \frac{\Delta r_f}{l \cos\phi} \quad (3.55)$$

### **Error caused only by $\Delta r_i$ :**

If only  $\Delta r_1$  (or  $\Delta f$ ) is considered to induce the output error  $\Delta\theta_3$ , the mechanical error at the output can be expressed as

$$\Delta\theta_3 = -\frac{\partial F/\partial r_1}{\partial F/\partial\theta_3} \Delta r_1 \quad (3.56)$$

where

$$\frac{\partial F}{\partial r_1} = 2(r_1 + r_3 \cos\theta_3 - r_2 \cos\theta_2) \quad (3.57)$$

$$\frac{\partial F}{\partial\theta_3} = -2r_3[r_1 \sin\theta_3 + r_2 \sin(\theta_2 - \theta_3)] \quad (3.58)$$

After some manipulation and reduction, the mechanical error  $\Delta S_f$  caused by  $\Delta f$  is

$$\begin{aligned}\Delta S_f = -\Delta\theta_3 &= -\frac{r_1 + r_3 \cos\theta_3 - r_2 \cos\theta_2}{r_3[r_1 \sin\theta_3 + r_2 \sin(\theta_2 - \theta_3)]} \Delta r_1 = -\frac{\Delta r_1 \sin(\theta_3 - \phi)}{r_3 \cos\phi} \\ &= -\frac{\Delta f \sin(\xi + \phi)}{l \cos\phi} = -\frac{\Delta f \cos\alpha}{l \cos\phi}\end{aligned}\quad (3.59)$$

where  $\alpha$  is defined in Eq. (2.42).

### **Error caused only by $\Delta r_3$ :**

If only  $\Delta r_3$  (or  $\Delta l$ ) is considered to induce the output error  $\Delta\theta_3$ , the mechanical error at the output can be expressed as

$$\Delta\theta_3 = -\frac{\partial F/\partial r_3}{\partial F/\partial\theta_3} \Delta r_3 \quad (3.60)$$

where

$$\frac{\partial F}{\partial r_3} = 2[r_3 + r_1 \cos\theta_3 - r_2 \cos(\theta_2 - \theta_3)] \quad (3.61)$$

$$\frac{\partial F}{\partial\theta_3} = -2r_3[r_1 \sin\theta_3 + r_2 \sin(\theta_2 - \theta_3)] \quad (3.62)$$

After some manipulation and reduction, the mechanical error  $\Delta S_l$  caused by  $\Delta l$  is

$$\Delta S_l = -\Delta\theta_3 = -\frac{r_3 + r_1 \cos\theta_3 - r_2 \cos(\theta_2 - \theta_3)}{r_3[r_1 \sin\theta_3 + r_2 \sin(\theta_2 - \theta_3)]} \Delta r_3 = \frac{\Delta r_3 \tan\phi}{r_3} = \frac{\Delta l \tan\phi}{l} \quad (3.63)$$

Equations (3.54), (3.55), (3.59), and (3.63) again indicate that the pressure angle appears in the form of  $(1/\cos\phi)$  to magnify the resulting errors. Also, in the final expressions of Eqs. (3.54), (3.55), (3.59), and (3.63), the parameters  $r_2$  and  $r_4$  are not actually involved, and thus locating the curvature center of the cam profile is not really essential.

### **Error caused only by $\Delta r$ :**

For the cam mechanism with an oscillating roller follower shown in Fig. 3.9, applying the sine law to  $\triangle O_2AQ$  yields

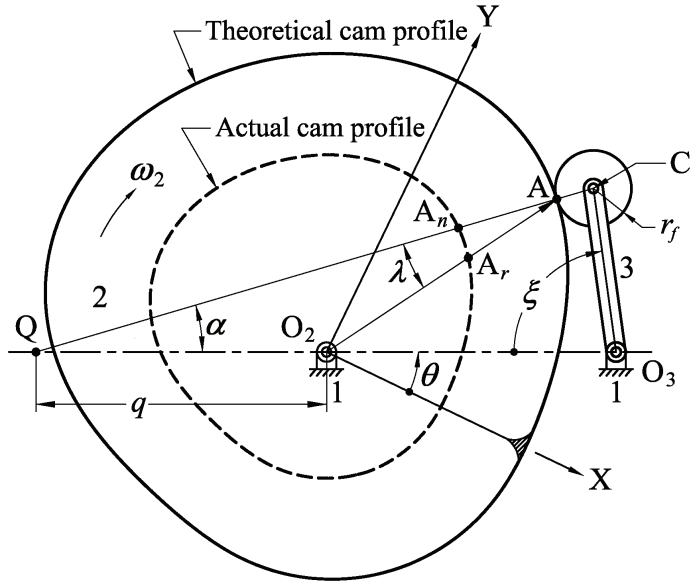


**Figure 3.9** Disk cam with an oscillating roller follower and its actual cam profile.

$$\lambda = \sin^{-1} \left( \frac{q \sin \alpha}{\|\mathbf{O}_2 \mathbf{A}\|} \right) = \sin^{-1} \left\{ \frac{f v(\theta) \sin \alpha}{[1 - v(\theta)] \|\mathbf{R}(\theta)\|} \right\} \quad (3.64)$$

From equations (3.9), (3.54), and (3.64), the motion deviation of the oscillating roller follower caused by the radial-dimension error of the cam profile,  $\Delta r$ , is

$$\Delta S_r = -\Delta \theta_3 \approx \frac{\Delta r \cos \lambda}{l \cos \phi} \quad (3.65)$$

Similarly, in this case, the effect of the pressure angle is counteracted by the shift angle.

### 3.3.4 Disk Cam with an Oscillating Flat-faced Follower

For the cam mechanism with an oscillating flat-faced follower shown in Fig. 3.10(a), let point K be the center of curvature of the cam in contact with the follower and point A be the contact point between the cam and the follower. Its equivalent linkage is the Whithworth or crank-shaper mechanism (i.e., the turning-block linkage, a slider-crank inversion) shown in Fig. 3.10(b), in which the additional link is a floating slider block (link 4). The floating slider block pivots on one end of the crank (link 2) at the center of curvature of the cam, K, and connects the shaper (link 3) by a prismatic joint whose

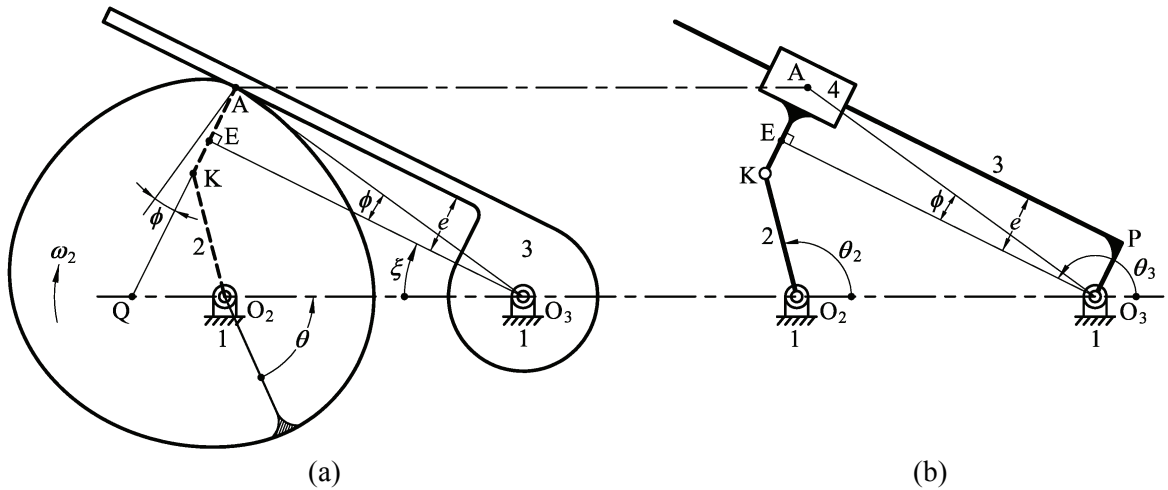


**Figure 3.10** Disk cam with an oscillating flat-faced follower and its equivalent Whithworth mechanism.

relative translation is along line AP; where quadrangle  $O_3EAP$  is a rectangle and  $O_3P = EA = e$ . The floating slider block has a characteristic length of  $r_4 = KA$ , which is also the radius of curvature of the cam. The instantaneous kinematic characteristics of the crank and the shaper are identical to those of the cam and the follower. For the equivalent linkage shown in Fig. 3.10(b), the displacement equation, relating the parameters  $e, r_1, r_2, r_4$  to the input and output variables  $\theta_2$  and  $\theta_3$ , may be written as

$$F(\mathbf{r}, \boldsymbol{\theta}, \boldsymbol{\psi}) = F(e, r_1, r_2, r_4, \theta_2, \theta_3) = 0 \quad (3.66)$$

in which,  $\mathbf{r} = \{e \ r_1 \ r_2 \ r_4\}^T$ ,  $\boldsymbol{\theta} = \{\theta_2\}$ , and  $\boldsymbol{\psi} = \{\theta_3\}$ ; or

$$F = r_1 \sin \theta_3 + r_2 \sin(\theta_2 - \theta_3) - r_4 + e = 0 \quad (3.67)$$

where  $e$  is the follower offset,  $r_1 = O_2O_3 = f$ ,  $r_2 = O_2K$ , and  $r_4 = KA$ . For small values of the errors  $\Delta e$ ,  $\Delta r_1$ ,  $\Delta r_2$ ,  $\Delta r_4$ ,  $\Delta \theta_2$ , and  $\Delta \theta_3$ , the differential of the function  $F$  may be written in terms of its partial derivatives as

$$dF \approx \Delta F = \frac{\partial F}{\partial e} \Delta e + \frac{\partial F}{\partial r_1} \Delta r_1 + \frac{\partial F}{\partial r_2} \Delta r_2 + \frac{\partial F}{\partial r_4} \Delta r_4 + \frac{\partial F}{\partial \theta_2} \Delta \theta_2 + \frac{\partial F}{\partial \theta_3} \Delta \theta_3 = 0 \quad (3.68)$$

#### Error caused only by $\Delta r_4$ :

If only the error of the cam profile  $\Delta r_4$  (or  $\Delta n$ ) is considered to induce the output error

$\Delta\theta_3$ , all other parameters having exactly the same dimensions, the mechanical error at the output can be expressed as

$$\Delta\theta_3 = -\frac{\partial F/\partial r_4}{\partial F/\partial\theta_3} \Delta r_4 \quad (3.69)$$

where

$$\frac{\partial F}{\partial r_4} = -1 \quad (3.70)$$

$$\frac{\partial F}{\partial\theta_3} = r_1 \cos\theta_3 - r_2 \cos(\theta_2 - \theta_3) \quad (3.71)$$

Recall from Fig. 3.10 that  $\xi(\theta) = 180^\circ - \theta_3$ , and thus  $\Delta S = \Delta\xi = -\Delta\theta_3$ . After some manipulation and reduction, the mechanical error  $\Delta S_n$  caused by  $\Delta n$  is

$$\Delta S_n = -\Delta\theta_3 = \frac{-\Delta r_4}{r_1 \cos\theta_3 - r_2 \cos(\theta_2 - \theta_3)} = \frac{\Delta n}{u} = \frac{\Delta n \tan\phi}{e} \quad (3.72)$$

where

$$u = PA = O_3E = \frac{e}{\tan\phi} = (f + q) \cos\xi \quad (3.73)$$

Here,  $u$  is the varying distance from the follower reference point P, as shown in Fig. 3.10(b), to the contact point A.

### **Error caused only by $\Delta r_i$ :**

If only  $\Delta r_1$  (or  $\Delta f$ ) is considered to induce the output error  $\Delta\theta_3$ , the mechanical error at the output can be expressed as

$$\Delta\theta_3 = -\frac{\partial F/\partial r_1}{\partial F/\partial\theta_3} \Delta r_1 \quad (3.74)$$

where

$$\frac{\partial F}{\partial r_1} = \sin\theta_3 \quad (3.75)$$

$$\frac{\partial F}{\partial \theta_3} = r_1 \cos \theta_3 - r_2 \cos(\theta_2 - \theta_3) \quad (3.76)$$

After some manipulation and reduction, the mechanical error  $\Delta S_f$  caused by  $\Delta f$  is

$$\Delta S_f = -\Delta \theta_3 = \frac{\sin \theta_3}{r_1 \cos \theta_3 - r_2 \cos(\theta_2 - \theta_3)} \Delta r_1 = -\frac{\Delta f \sin \xi}{u} = -\frac{\Delta f \sin \xi \tan \phi}{e} \quad (3.77)$$

### **Error caused only by $\Delta e$ :**

If only  $\Delta e$  is considered to induce the output error  $\Delta \theta_3$ , the mechanical error at the output can be expressed as

$$\Delta \theta_3 = -\frac{\partial F / \partial e}{\partial F / \partial \theta_3} \Delta e \quad (3.78)$$

where

$$\frac{\partial F}{\partial e} = 1 \quad (3.79)$$



$$\frac{\partial F}{\partial \theta_3} = r_1 \cos \theta_3 - r_2 \cos(\theta_2 - \theta_3) \quad (3.80)$$

After some manipulation and reduction, the mechanical error  $\Delta S_e$  caused by  $\Delta e$  is

$$\Delta S_e = -\Delta \theta_3 = \frac{\Delta e}{r_1 \cos \theta_3 - r_2 \cos(\theta_2 - \theta_3)} = -\frac{\Delta e}{u} = -\frac{\Delta e \tan \phi}{e} \quad (3.81)$$

Equations (3.72), (3.77), and (3.81) indicate that the pressure angle appears in the form of  $\tan \phi$  to magnify the resulting errors. Also, in the final expressions of Eqs. (3.72), (3.77), and (3.81), the parameters  $r_2$  and  $r_4$  are not actually involved, and thus locating the curvature center of the cam profile is not really essential.

### **Error caused only by $\Delta r$ :**

For the cam mechanism with an oscillating flat-faced follower shown in Fig. 3.11, applying the sine law to  $\triangle O_2AQ$  yields

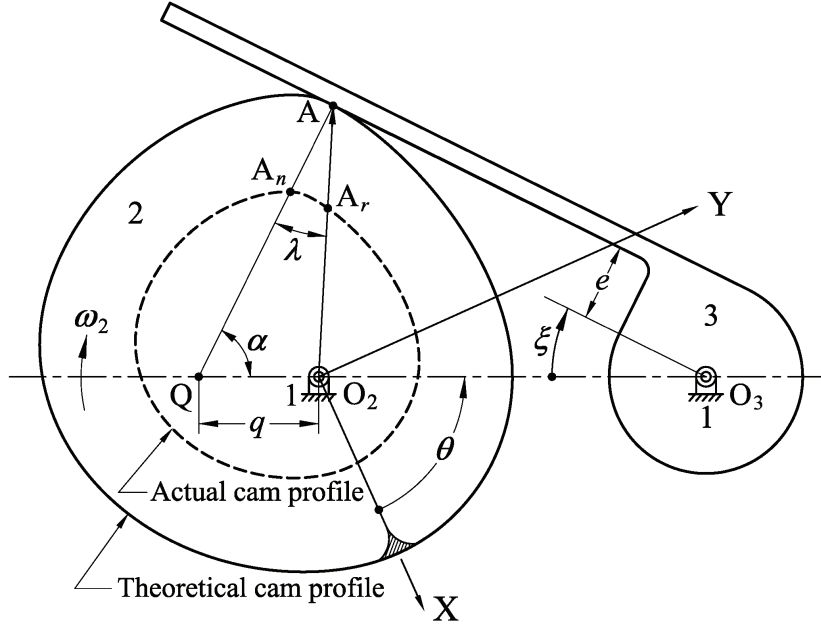


**Figure 3.11** Disk cam with an oscillating flat-faced follower and its actual cam profile.

$$\lambda = \sin^{-1} \left( \frac{q \sin \alpha}{\|O_2 A\|} \right) = \sin^{-1} \left\{ \frac{f v(\theta) \cos \xi(\theta)}{[1 - v(\theta)] \|R(\theta)\|} \right\} \quad (3.82)$$

where  $\alpha$  is defined in Eq. (2.55). From Eqs. (3.9), (3.72), and (3.82), the motion deviation of the oscillating flat-faced follower caused by the radial-dimension error of the cam profile,  $\Delta r$ , is

$$\Delta S_r = -\Delta \theta_3 \approx \frac{\Delta r \cos \lambda}{u} = \frac{\Delta r \cos \lambda \tan \phi}{e} \quad (3.83)$$

In this case, the effect of the pressure angle (in the form of  $\tan \phi$ ) is multiplied by the shift angle (in the form of  $\cos \lambda$ ).

### 3.4 VELOCITY AND ACCELERATION ERROR FUNCTIONS

The surface irregularity of the cam profile is one of the primary sources of vibratory noise [6], and it was experimentally proved that a non-uniform manufacturing error can cause an appreciable dynamic disturbed acceleration curve [7]. However, even a uniform

manufacturing error, as well as the deviation of each link length, can certainly produce additional disturbance of the actual acceleration of the follower, and this could be another concern of the designer. Because the equivalent linkage model provides the closed-form solutions for the error function, this acceleration disturbance arising from a uniform manufacturing error can be expressed analytically.

Since the equivalent linkage method provides the closed-form solutions for the displacement error functions of the follower, its corresponding velocity and acceleration error functions can also be expressed analytically. The velocity and acceleration error analysis is straightforwardly performed by differentiating the obtained displacement error functions with respect to time once and twice. Thus, the velocity and acceleration errors of the follower can be expressed as

$$\Delta V(t) = \frac{d(\Delta S(\theta))}{dt} = \frac{d(\Delta S(\theta))}{d\theta} \frac{d\theta}{dt} = \frac{d(\Delta S(\theta))}{d\theta} \omega_2 = \Delta v(\theta) \omega_2 \quad (3.84)$$

$$\Delta A(t) = \frac{d^2(\Delta S(\theta))}{dt^2} = \frac{d^2(\Delta S(\theta))}{d\theta^2} \omega_2^2 + \frac{d(\Delta S(\theta))}{d\theta} \alpha_2 = \Delta a(\theta) \omega_2^2 + \Delta v(\theta) \alpha_2, \quad (3.85)$$

where  $\alpha_2$  is the angular acceleration of the cam. The analytical expressions are tedious and shown in Appendix A. The velocity and acceleration error functions for cams with an offset translating roller follower are given in Appendix A.1, those for cams with an offset translating oblique flat-faced follower are given in Appendix A.2, those for cams with an oscillating roller follower are given in Appendix A.3, and those for cams with an oscillating flat-faced follower are given in Appendix A.4.

### 3.5 THEORETICAL VALIDATIONS OF THE METHOD

In this section, theoretical validations are performed to verify the accuracy and feasibility of the equivalent linkage method. Firstly, the mechanical error analysis of an eccentric circular cam mechanism, whose exact solution is available, is undertaken. Through using the presented method, an approximate form of the follower motion error is

obtained and compared with the exact solution by means of an example. Secondly, through an exaggerated case of a disk cam whose profile coordinates are assumed to be computed with adopting an incorrect follower motion program, the cam profile errors evaluated by using the shift angle are compared with their exact values calculated numerically.

### 3.5.1 Validity of the Equivalent Linkage Method

The validity of the equivalent linkage method may be recognized by analyzing the cam mechanism shown in Fig. 3.12, an eccentric circular cam with an oscillating roller follower. The cam mechanism has an invariant equivalent four-bar linkage  $O_2KCO_3$ , and thus an exact solution is available. For the equivalent linkage  $O_2KCO_3$ , the displacement equation, relating the parameters  $f, l, r_2, r_f, R$  to the input and output variables  $\theta$  and  $\xi(\theta)$ , may be written as

$$F = 2[r_2 l \cos(\theta + \xi) - f(r_2 \cos \theta + l \cos \xi)] + r_2^2 + f^2 - (R + r_f)^2 = 0 \quad (3.86)$$

where  $r_2 = O_2K$  is the amount of eccentricity,  $R$  is the radius of the circular cam,  $r_f$  is the radius of the follower roller,  $f = O_2O_3$  is the distance between fixed pivots,  $l = O_3C$  is the follower arm length,  $\theta$  is the cam rotation angle, and  $\xi$  is the angular displacement of the

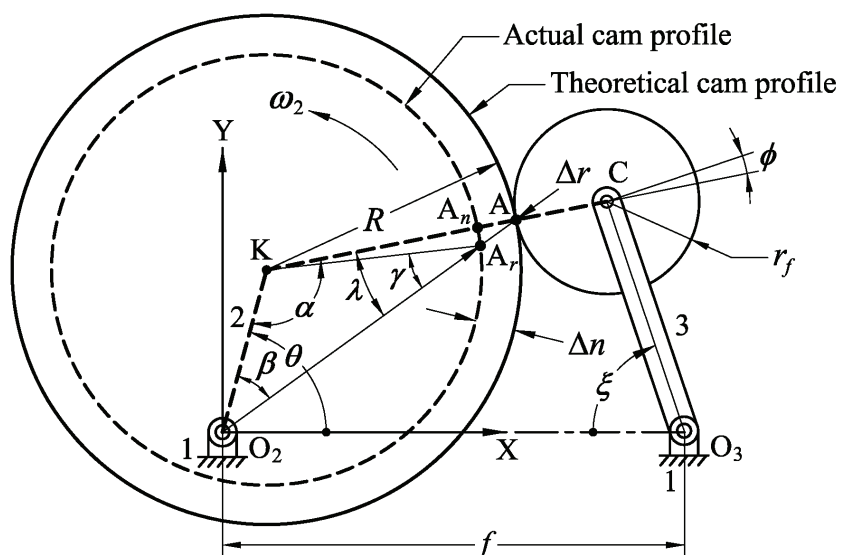


**Figure 3.12** Eccentric circular cam with an oscillating roller follower and its invariant equivalent four-bar linkage.

follower arm. (Note that  $KC = R + r_f$  is the invariant coupler length.) Also,  $\xi(\theta)$  can be expressed as

$$\xi(\theta) = \sin^{-1} \left( \frac{r_2 \sin \theta}{O_3 K} \right) + \cos^{-1} \left[ \frac{l^2 + (O_3 K)^2 - (R + r_f)^2}{2l(O_3 K)} \right] \quad (3.87)$$

where

$$O_3 K = \sqrt{r_2^2 + f^2 - 2r_2 f \cos \theta} \quad (3.88)$$

The pressure angle can be expressed as

$$\phi = \cos^{-1} \left[ \frac{(R + r_f)^2 + l^2 - (O_3 K)^2}{2l(R + r_f)} \right] - 90^\circ \quad (3.89)$$

The contact point is designated by A. Applying the cosine law to  $\triangle O_2 KA$  yields

$$O_2 A = \sqrt{r_2^2 + R^2 - 2r_2 R \cos \alpha} \quad (3.90)$$

where

$$\alpha = \angle O_2 KA = 270^\circ - (\theta + \xi + \phi) \quad (3.91)$$

Applying the sine law to  $\triangle O_2 KA$  yields

$$\lambda = \angle O_2 AK = \sin^{-1} \left( \frac{r_2 \sin \alpha}{O_2 A} \right) \quad (3.92)$$

Assuming the profile error in the normal direction of the cam profile has a constant magnitude of  $\Delta n$ , the actual cam profile will also be a circular cam and have a radius of  $R + \Delta n$ . (The quantity  $\Delta n$  is negative if the actual cam profile is smaller than the theoretical one; in the figure shown it is negative.) Line AK intersects the actual cam profile at point  $A_n$ , and line  $AO_2$  intersects the actual cam profile at point  $A_r$ . Then

$$KA_n = KA_r = R + \Delta n \quad (3.93)$$

Applying the sine law to  $\triangle O_2 KA_r$  yields

$$\gamma = \angle O_2 A_r K = \sin^{-1} \left( \frac{r_2 \sin \beta}{KA_r} \right) = \sin^{-1} \left( \frac{r_2 \sin \beta}{R + \Delta n} \right) \quad (3.94)$$

where

$$\beta = \angle A_r O_2 K = 180^\circ - (\alpha + \lambda) \quad (3.95)$$

Therefore,

$$O_2 A_r = r_2 \frac{\sin(\beta + \gamma)}{\sin \gamma} \quad (3.96)$$

From Eqs. (3.90) and (3.96), the exact solution of the radial profile error can be expressed as

$$\Delta r_{ex} = AA_r = O_2 A_r - O_2 A = r_2 \frac{\sin(\beta + \gamma)}{\sin \gamma} - \sqrt{r_2^2 + R^2 - 2r_2 R \cos \alpha} \quad (3.97)$$

From Eqs. (3.87) and (3.88), the exact solution of the follower motion error can be expressed as

$$\begin{aligned} \Delta S_{ex} &= \Delta \xi \\ &= \cos^{-1} \left\{ \frac{l^2 + (O_3 K)^2 - [(R + \Delta n) + r_f]^2}{2l(O_3 K)} \right\} - \cos^{-1} \left[ \frac{l^2 + (O_3 K)^2 - (R + r_f)^2}{2l(O_3 K)} \right] \end{aligned} \quad (3.98)$$

On the other hand, from Eq. (3.9), the approximate form of the radial profile error obtained from the presented method is

$$\Delta r_{ap} \approx \frac{\Delta n}{\cos \lambda} = \frac{O_2 A}{\sqrt{(O_2 A)^2 - (r_2 \sin \alpha)^2}} \Delta n \quad (3.99)$$

From Eqs. (3.9) and (3.86), the approximate form of the follower motion error obtained from the presented method is

$$\Delta S_{ap} = \Delta \xi = - \frac{\partial F / \partial R}{\partial F / \partial \xi} \Delta n = \frac{\Delta n}{l \cos \phi} \approx \frac{\Delta r_{ex} \cos \lambda}{l \cos \phi} \quad (3.100)$$

Here, the value of the shift angle  $\lambda$  can be determined from either Eq. (3.64) or Eq. (3.92), because they have exactly the same result.

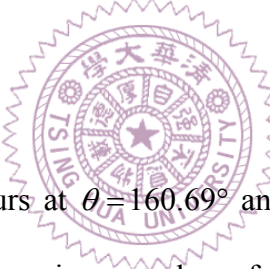
For comparison of the results, the following values are substituted into the related equations derived above:  $r_2 = 60$  mm,  $f = 140$  mm,  $l = 130$  mm,  $R = 100$  mm,  $r_f = 20$  mm and  $\Delta n = 22 \mu\text{m}$  (a corresponding tolerance of IT6). Figure 3.13(a) shows the exact solutions of  $\Delta r_{\text{ex}}$  and  $\Delta S_{\text{ex}}$ , with respect to  $\theta$ , and Fig. 3.13(b) shows the approximate solutions of  $\Delta r_{\text{ap}}$  and  $\Delta S_{\text{ap}}$ . Since the curves cannot be distinguished by inspection, their differences  $\delta_r$  and  $\delta_s$  are shown in Fig. 3.13(c), also, their relative deviations  $\varepsilon_r$  and  $\varepsilon_s$  are shown in Fig. 3.13(d), where

$$\delta_r = \Delta r_{\text{ap}} - \Delta r_{\text{ex}} \quad (3.101)$$

$$\delta_s = \Delta S_{\text{ap}} - \Delta S_{\text{ex}} \quad (3.102)$$

$$\varepsilon_r = \frac{\Delta r_{\text{ap}} - \Delta r_{\text{ex}}}{\Delta r_{\text{ex}}} \times 100\% \quad (3.103)$$

$$\varepsilon_s = \frac{\Delta S_{\text{ap}} - \Delta S_{\text{ex}}}{\Delta S_{\text{ex}}} \times 100\% \quad (3.104)$$



The maximum value of  $\Delta r_{\text{ex}}$  occurs at  $\theta = 160.69^\circ$  and  $\theta = 326.45^\circ$ , both have the same magnitude of  $27.4983 \mu\text{m}$ . The maximum value of  $\delta_r$  also occurs at  $\theta = 160.69^\circ$  and  $\theta = 326.45^\circ$ , both have the same magnitude of  $0.0017 \mu\text{m}$ , a relative deviation of  $0.0062\%$ . The extreme value of  $\Delta S_{\text{ex}}$  occurs at  $\theta = 0^\circ$  (or  $360^\circ$ ) and has a magnitude of  $0.016092^\circ$ . The extreme value of  $\delta_s$  occurs at  $\theta = 333.48^\circ$  and has a magnitude of  $-0.004551^\circ$  [ $1'' = (1/3600)^\circ$ ]. Also, the extreme value of  $\varepsilon_s$  occurring at  $\theta = 325.7^\circ$  is only  $-0.009\%$ . In other words, for a tolerance grade of IT6, the predicted results have at least a relative accuracy of 99.99%.

In addition, when the cam profile error  $\Delta n$  is discretely raised from a tolerance grade of IT6 ( $22 \mu\text{m}$ ) to IT13 ( $540 \mu\text{m}$ ), the corresponding difference  $\delta_s$  and relative deviation  $\varepsilon_s$  are respectively shown in Figs. 3.14(a) and 3.14(b). It can be seen that the magnitudes of  $\delta_s$  and  $\varepsilon_s$  gradually increase with the increased tolerance grade. The accuracy of the equivalent linkage method definitely degrades with increased profile deviation. But, even

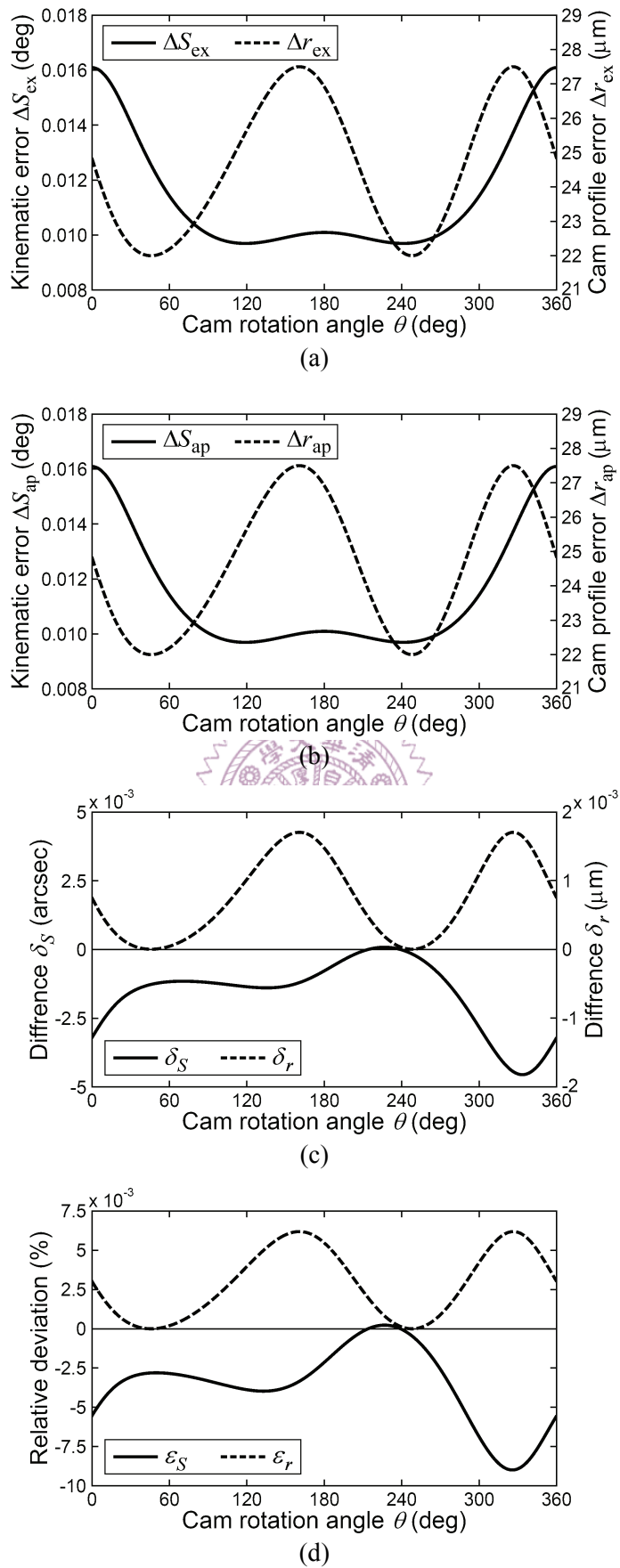


**Figure 3.13** Exact and approximate solutions and their comparisons for a circular cam profile with a tolerance grade of IT6.

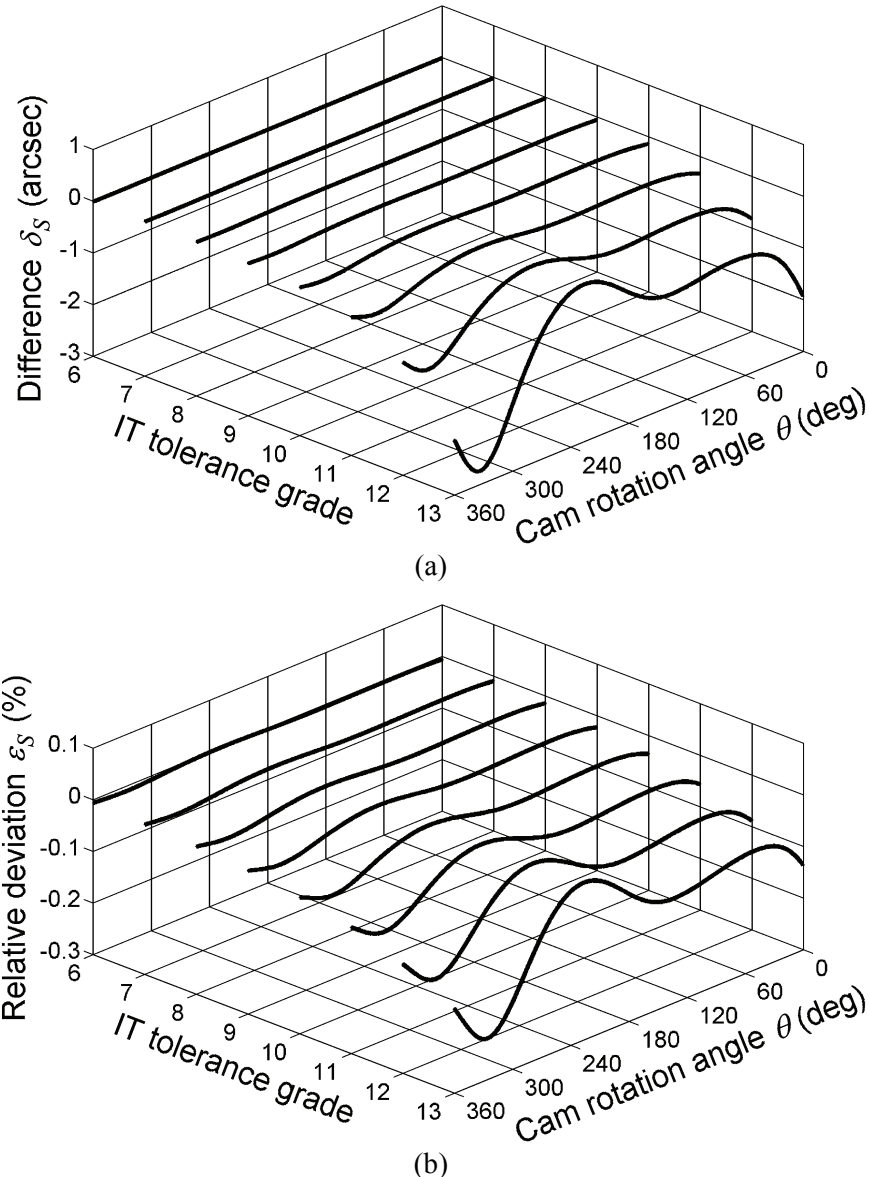


**Figure 3.14** Comparisons between exact and approximate solutions for a circular cam profile with a tolerance grade raised from IT6 to IT13.

the cam profile has a very large tolerance grade of IT13, the extreme difference  $\delta_s$  and relative deviation  $\varepsilon_s$  are only  $-2.7323''$  ( $\approx -0.000759^\circ$ ) or  $-0.2196\%$ . That is, the equivalent linkage method can provide sufficient accuracy from an engineering viewpoint.

The combined effects of the approximated results of the shift angle and the sensitivity analysis method cause the inaccuracy of the equivalent linkage method. Such an inaccuracy may be reduced by adopting some modifications, as introduced below. Figure 3.15 shows the geometric correlation between the radial profile error and the normal-direction error of a circular cam, in which, by applying the sine law to  $\triangle KA_A$  yields

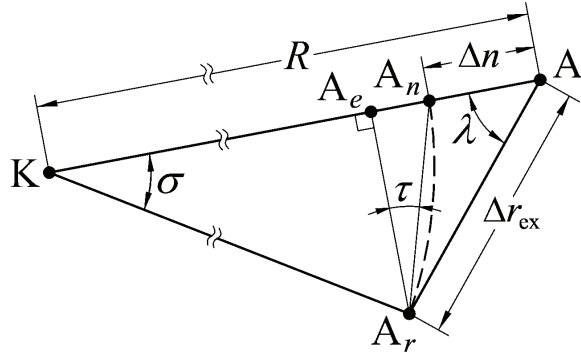


**Figure 3.15** Geometric correlation between the radial profile error and the normal-direction error of a circular cam.

$$\sigma = \angle \text{AKA}_r = \sin^{-1} \left( \frac{\text{AA}_r \sin \lambda}{\text{KA}_r} \right) = \sin^{-1} \left( \frac{\Delta r_{\text{ex}} \sin \lambda}{\text{KA}_r} \right) \quad (3.105)$$

Figure 3.15 shows that point  $A_e$ , rather than point  $A_n$ , is the projection point of point  $A$ , on line  $KA$ . Thus,  $\angle A_e A_r A_n = \tau = \sigma/2$  and

$$\begin{aligned} \Delta n &= \text{AA}_e + \text{AA}_n \\ &= \Delta r_{\text{ex}} \cos \lambda + \Delta r_{\text{ex}} \sin \lambda \tan \tau = \Delta r_{\text{ex}} (\cos \lambda + \sin \lambda \tan \tau) \\ &= \Delta r_{\text{ex}} \left( \cos \lambda + \sin \lambda \tan \frac{\sigma}{2} \right) \end{aligned} \quad (3.106)$$

Equation (3.106) shows an exact correlation between the radial profile error and the normal-direction error of eccentric circular cams. (The quantities  $\Delta n$  and  $\text{AA}_e$  are negative if the actual cam profile is smaller than the theoretical one; in the figure shown, they are negative.) The equation may also be applicable to all types of disk cams by assuming  $\angle A_e A_r A_n = \tau \approx \sigma/2$ . In the following context, the subtending angle between lines  $KA_r$  and  $KA$ ,  $\sigma$ , is called the compensated shift angle, and the subtending angle between lines  $A_r A_n$  and  $A_r A_e$ ,  $\tau$ , is called the tangential deviation angle. Then expanding Eq. (3.86) in its Taylor series form and considering only  $\Delta\xi$  and  $\Delta n$  gives

$$dF \approx \Delta F = \frac{\partial F}{\partial \xi} \Delta \xi + \frac{\partial F}{\partial R} \Delta n + \frac{1}{2} \left( \frac{\partial^2 F}{\partial \xi^2} \Delta \xi^2 + 2 \frac{\partial^2 F}{\partial \xi \partial R} \Delta \xi \Delta n + \frac{\partial^2 F}{\partial R^2} \Delta n^2 \right) + R_F = 0 \quad (3.107)$$

where  $R_F$  represents the reminder higher-order terms. Because the deviations  $\Delta\xi$  and  $\Delta n$  are

small, the higher-order terms may be neglected. Accordingly, function  $\Delta S_{ap}$  may be expressed as

$$\begin{aligned}\Delta S_{ap} &= \Delta\xi \\ &= \frac{\sqrt{\left(\frac{\partial F}{\partial\xi} + \frac{\partial^2 F}{\partial\xi\partial R}\Delta n\right)^2 - \frac{\partial^2 F}{\partial\xi^2}\left(2\frac{\partial F}{\partial R}\Delta n + \frac{\partial^2 F}{\partial R^2}\Delta n^2\right)} - \left(\frac{\partial F}{\partial\xi} + \frac{\partial^2 F}{\partial\xi\partial R}\Delta n\right)}{\frac{\partial^2 F}{\partial\xi^2}}\end{aligned}\quad (3.108)$$

After some manipulation and reduction, it follows that

$$\Delta S_{ap} = \sqrt{\frac{(R+r_f+\Delta n)^2 - (R+r_f)^2}{l(R+r_f)\sin\phi+l^2} + \left[\frac{(R+r_f)\cos\phi}{(R+r_f)\sin\phi+l}\right]^2} - \frac{(R+r_f)\cos\phi}{(R+r_f)\sin\phi+l} \quad (3.109)$$

or

$$\begin{aligned}\Delta S_{ap} &= \sqrt{\frac{\{R+r_f+\Delta r_{ex}[\cos\lambda+\sin\lambda\tan(\sigma/2)]\}^2 - (R+r_f)^2}{l(R+r_f)\sin\phi+l^2} + \left[\frac{(R+r_f)\cos\phi}{(R+r_f)\sin\phi+l}\right]^2} \\ &\quad - \frac{(R+r_f)\cos\phi}{(R+r_f)\sin\phi+l}\end{aligned}\quad (3.110)$$

Equation (3.110) shows the modified form of the follower motion error obtained from the presented method, taking into consideration the compensated shift angle and the second-order terms of the Taylor expansions of the displacement equation. By applying Eq. (3.110) to predict the follower output deviation, the difference  $\delta_s$  and the relative deviation  $\varepsilon_s$  are shown in Figs. 3.16(a) and 3.16(b), respectively. As can be seen, the magnitudes of  $\delta_s$  and  $\varepsilon_s$  still increase with the increased tolerance grade. But, even the cam profile has a very large tolerance grade of IT13 (540  $\mu\text{m}$ ), the extremes of the difference  $\delta_s$  and relative deviation  $\varepsilon_s$ , both occurring at  $\theta=0^\circ$  (or  $360^\circ$ ), are merely  $-0.011256''$  ( $\approx -0.000003^\circ$ ) or  $-0.00079\%$ . In other words, by considering the compensated shift angle and the second-order terms of the Taylor expansions of the displacement equation, the equivalent linkage method will still have at least a relative accuracy of 99.999% even for a very large tolerance grade of IT13. However, as shown in Eqs. (3.105) and (3.110), the modified form

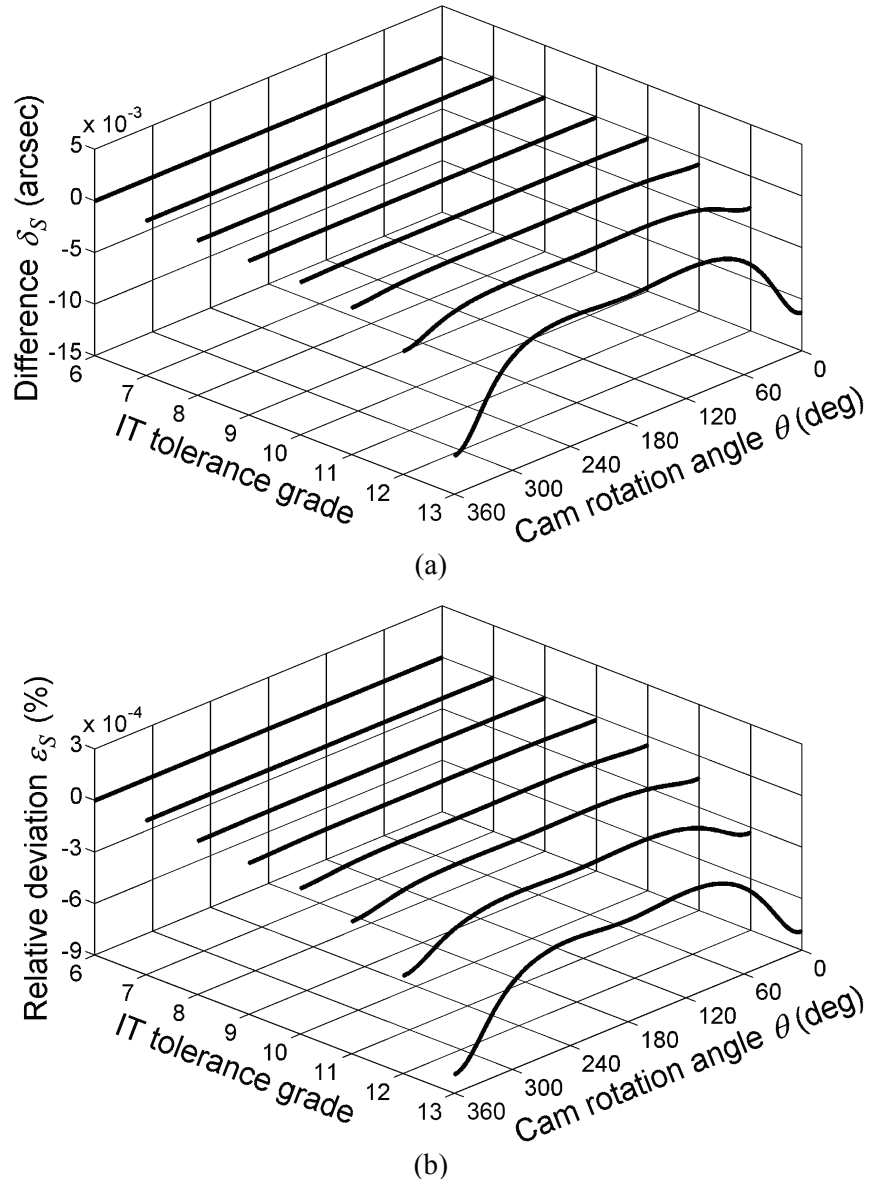


**Figure 3.16** Comparisons between exact and approximate solutions for a circular cam profile with a tolerance grade raised from IT6 to IT13 after considering the compensated shift angle and the second-order terms of the Taylor expansions of the displacement equation.

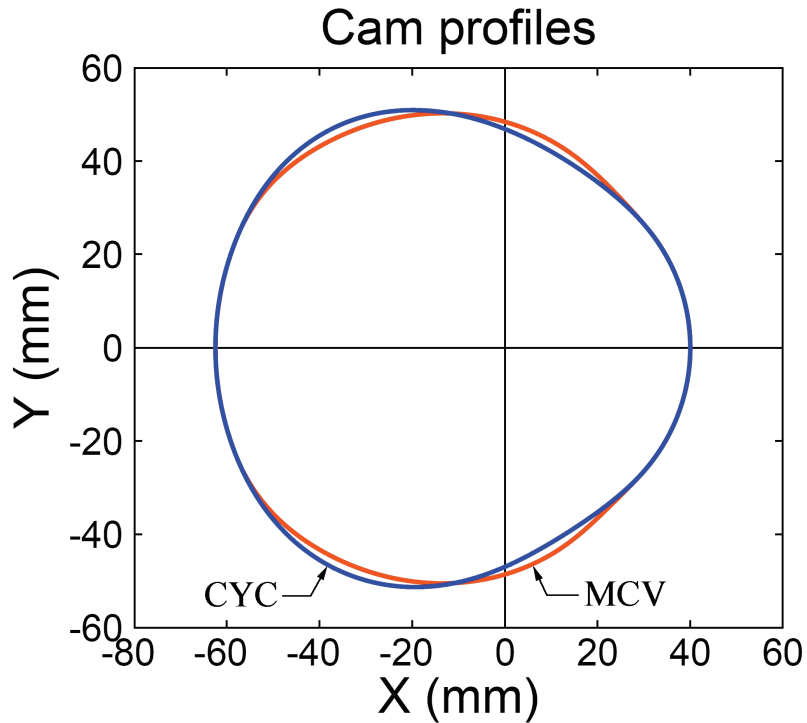
of the equivalent linkage method involves locating the curvature center of the cam profile, thus making the analysis more complicated to perform. From an engineering viewpoint, the original form of the equivalent linkage method is suggested instead because of its simplicity and sufficient accuracy.

### 3.5.2 Validity of the Shift Angle

The validity of the shift angle may be recognized by evaluating the cam profile errors

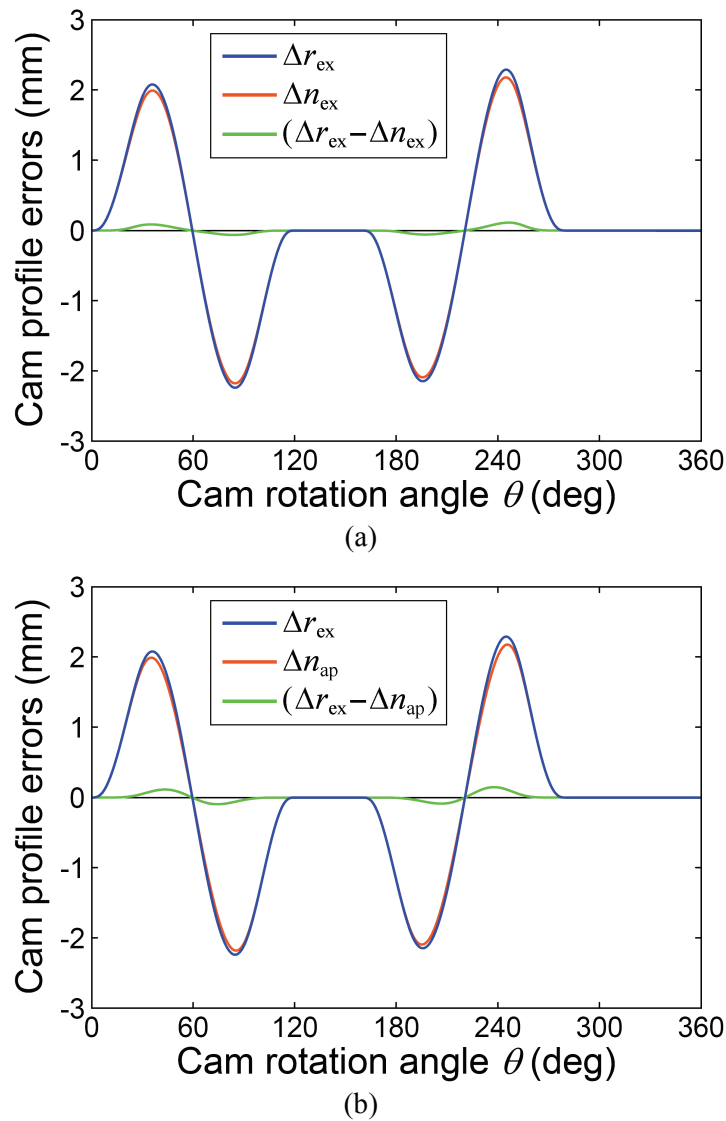
of an exaggerated case. A cam system is designed to drive the oscillating roller follower to oscillate  $25^\circ$  clockwise with cycloidal motion while the cam rotates clockwise from  $0^\circ$  to  $120^\circ$ , dwell for the next  $40^\circ$ , return with cycloidal motion for  $120^\circ$  cam rotation and dwell for the remaining  $80^\circ$ . The distance between pivots,  $f$ , is 80 mm; the length of the follower arm,  $l$ , is 52 mm. The base circle radius,  $r_b$ , is 40 mm and the radius of the follower roller,  $r_f$ , is 8 mm. Based on the above motion program and constant design parameters, the theoretical cam profile labeled as ‘CYC’ is drawn in Fig. 3.17. If, exaggeratedly, the cam profile coordinates are incorrectly computed by using modified constant velocity (MCV) motion [5, 8] for both the rise and return regions, the incorrect cam profile labeled as ‘MCV’ is then regarded as the actual cam profile (see Fig. 3.17). As can be observed, the theoretical and actual cam profiles are totally different at the rise and return regions, while their contours overlap at both the high and low dwell regions. At the rise and return regions, the curvatures of the theoretical cam contour are quite different to those of the actual one, and the cam profile errors are considerably large and visible.

Figure 3.18 shows the cam profile errors versus the cam rotation angle  $\theta$ . The exact



**Figure 3.17** Theoretical and actual cam profiles of an exaggerated case.

radial profile error  $\Delta r_{\text{ex}}$ , the exact normal-direction error  $\Delta n_{\text{ex}}$ , and their difference are shown in Fig. 3.18(a). The exact value of  $\Delta r_{\text{ex}}$  is obtained using the Newton-Raphson method by calculating the intersection of the actual cam profile and the radial line, which passes through the contour point at the theoretical cam profile with respect to each cam rotation angle. The exact value of the normal-direction error  $\Delta n_{\text{ex}}$  is obtained in a similar manner, that is, the intersection of the actual cam profile and the normal line passing through the contour point at the theoretical cam profile is calculated numerically. The distances between the intersections and the theoretical contour points are the corresponding profile errors. As can be seen,  $\Delta r_{\text{ex}}$  and  $\Delta n_{\text{ex}}$  have quite similar trends. The extreme values



**Figure 3.18** Cam profile errors of an exaggerated case.

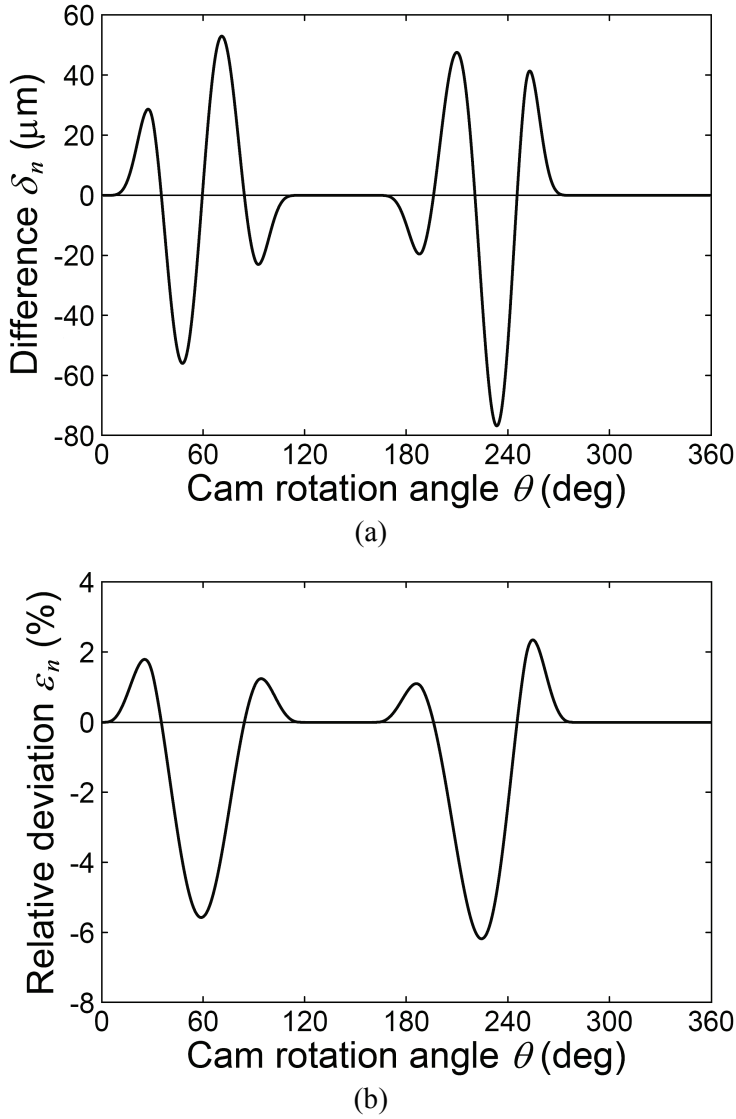


**Figure 3.19** Comparisons between exact and approximate solutions of an exaggerated case.

of  $\Delta r_{\text{ex}}$  occur at  $\theta = 84.75^\circ$  and  $\theta = 244.89^\circ$  and have corresponding magnitudes of  $-2.2369$  and  $2.2909$  mm, respectively. The extreme values of  $\Delta n_{\text{ex}}$  occur at  $\theta = 84.8^\circ$  and  $\theta = 244.76^\circ$  and have corresponding magnitudes of  $-2.1745$  and  $2.1792$  mm, respectively. Considering that the theoretical cam profile has a maximum radial dimension of  $62.478$  mm, an extreme profile deviation of  $\Delta r_{\text{ex}} = 2.2909$  mm implies quite a large tolerance grade ranging from IT16 (1.9 mm) to IT17 (3 mm). When  $\theta = 59.5^\circ$  and  $\theta = 220.53^\circ$ , the magnitudes of  $\Delta r_{\text{ex}}$  and  $\Delta n_{\text{ex}}$  are both zero since the theoretical and actual cam contours intersect at the two positions. Figure 3.18(b) shows the exact radial profile error  $\Delta r_{\text{ex}}$ , the approximate normal-direction error  $\Delta n_{\text{ap}}$ , and their difference, where

$$\Delta n_{ap} \approx \Delta r_{ex} \cos \lambda \quad (3.111)$$

in which the value of the shift angle  $\lambda$  can be determined by using Eq. (3.64). The extreme values of  $\Delta n_{ap}$  occur at  $\theta = 85.32^\circ$  and  $\theta = 245.62^\circ$  and have corresponding magnitudes of  $-2.1781$  and  $2.1772$  mm, respectively. Since the curves of  $\Delta n_{ex}$  and  $\Delta n_{ap}$  cannot be easily distinguished by inspection, their difference  $\delta_n$  is shown in Fig. 3.19(a), also, their relative deviation  $\varepsilon_n$  is shown in Fig. 3.19(b), where

$$\delta_n = \Delta n_{ap} - \Delta n_{ex} \quad (3.112)$$

$$\varepsilon_n = \frac{\Delta n_{ap} - \Delta n_{ex}}{\Delta n_{ex}} \times 100\% \quad (3.113)$$

The extreme value of  $\delta_n$  occurs at  $\theta = 233.43^\circ$  and has a magnitude of  $-76.7021$   $\mu\text{m}$ , while the extreme value of  $\varepsilon_n$  occurring at  $\theta = 224.41^\circ$  is  $-6.1746\%$ . In other words, for such an exaggerated case, the use of the shift angle to correlate the radial-dimension error and the normal-direction error of the cam profile can still have at least a relative accuracy of  $93\%$ .

In addition, from a geometric viewpoint, the validity of the shift angle can also be evaluated by considering the extent of the tangential deviation angle  $\tau$  as shown in Fig. 3.15. In practice, since  $\triangle AA_e A_r$ , instead of  $\triangle AA_n A_r$ , is an exact right-angled triangle, then  $AA_n = \Delta n = \Delta n_{ex}$ ,  $AA_e = \Delta n_{ap}$  and  $\angle AA_n A_r = 90^\circ \pm \tau$ . Evidently, if the tangential deviation angle  $\tau$  is smaller, the correlation of  $\Delta n \approx \Delta r \cos \lambda$  will be more accurate and applicable. From Eq. (3.106), the exact correlation between  $\Delta n_{ex}$  and  $\Delta r_{ex}$  is

$$\Delta n_{ex} = \Delta r_{ex} (\cos \lambda + \sin \lambda \tan \tau) \quad (3.114)$$

Then the tangential deviation angle  $\tau$  can be expressed as

$$\tau = \tan^{-1} \left( \frac{\Delta n_{ex}}{\Delta r_{ex} \sin \lambda} - \cot \lambda \right) = \tan^{-1} \left[ \left( \frac{\Delta n_{ex}}{\Delta n_{ap}} - 1 \right) \cot \lambda \right] \quad (3.115)$$

For this exaggerated case, the tangential deviation angle  $\tau$  versus the cam rotation angle  $\theta$

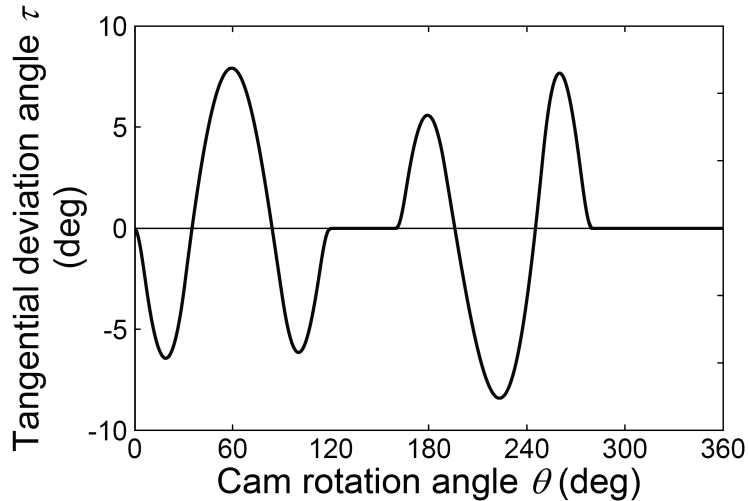


**Figure 3.20** Tangential deviation angle of an exaggerated case.

is shown in Fig. 3.20. The extreme values of  $\tau$  occur at  $\theta = 59.56^\circ$  and  $\theta = 223.38^\circ$  and have corresponding magnitudes of  $7.919^\circ$  and  $-8.403^\circ$ , respectively. It is found that the trends of  $\tau$  and  $\varepsilon_n$  are quite similar if their signs are ignored, that is, the relative deviation  $\varepsilon_n$  is proportional to the tangential deviation angle  $\tau$ . Considering that the variation range of the tangential deviation angle is estimated at  $\pm 8^\circ$ , the use of the shift angle to correlate the radial-dimension error and the normal-direction error of the cam profile having a relative deviation less than 7% implies acceptable accuracy from an engineering viewpoint.

## 3.6 EXAMPLES

The equivalent linkage method presented above is illustrated by the following four examples. For disk cams with an offset translating roller follower, an offset translating oblique flat-faced follower, an oscillating roller follower, and an oscillating flat-faced follower, the displacement, velocity, and acceleration errors of the followers with cycloidal motions are computed and analyzed.

### 3.6.1 Disk Cam with an Offset Translating Roller Follower

A cam system requires the offset translating roller follower to rise 24 mm with

cycloidal motion while the cam rotates clockwise from  $0^\circ$  to  $100^\circ$ , dwell for the next  $50^\circ$ , return with cycloidal motion for  $100^\circ$  cam rotation and dwell for the remaining  $110^\circ$ . The offset  $e$  is 12 mm. The radii of the base circle and the follower roller are 40 and 10 mm, respectively.

The cam profile, which has a maximum radial dimension of 63.525 mm, is shown in Fig. 2.4. For a tolerance grade of IT6, the cam profile may have a deviation of  $\Delta r = 19 \mu\text{m}$  and the offset may have a deviation of  $\Delta e = 11 \mu\text{m}$ , respectively. (The radius error of the roller,  $\Delta r_f$ , may be ignored since it generally has a smaller tolerance grade and may have a magnitude of  $2 \mu\text{m}$  at most if precision roller is used.) The motion of the follower will then have deviations result from them,  $\Delta S_r$  caused by  $\Delta r$  and  $\Delta S_e$  caused by  $\Delta e$ , respectively. The worst-case deviation of the follower motion will be

$$\Delta S_{\text{wor}} = |\Delta S_r| + |\Delta S_e| \quad (3.116)$$

The maximum expected deviation of the follower motion will be

$$\Delta S_{\text{rss}} = \sqrt{\Delta S_r^2 + \Delta S_e^2} \quad (3.117)$$

All functions that might be of interest are shown in Fig. 3.21, and their extreme values are also listed in Table 3.1. Figure 3.21(a) shows that the pressure angle  $\phi$  and the shift angle  $\lambda$  have quite similar trends. Therefore, the variation of  $(1/\cos\phi)$  is flattened by  $\cos\lambda$ . As shown in Fig. 3.21(b), since  $0.885 \leq (\cos\lambda / \cos\phi) \leq 1.0809$ , the magnitude of  $\Delta S_r$  has only slight variation.

The extreme value of  $\Delta S_{\text{wor}}$  occurs at  $\theta = 206.9^\circ$ , very close to  $\theta = 205.84^\circ$ , where, in absolute value, the extreme pressure angle  $\phi$  occurs. In addition,  $\Delta S_{\text{wor}}$  has an extreme value of  $27.84 \mu\text{m}$ . From the viewpoint of the position accuracy of the follower motion, for a total follower travel of 24 mm, a position deviation of  $\Delta S_{\text{max}} = 27.84 \mu\text{m}$  implies a lower accuracy. That is, if the worst situation occurs, the follower motion will have a degraded accuracy ranging from IT7 (21  $\mu\text{m}$ ) to IT8 (33  $\mu\text{m}$ ).

The velocity error functions  $\Delta V_r$  caused by  $\Delta r$  and  $\Delta V_e$  caused by  $\Delta e$  are shown in Fig.

3.22(a). The acceleration error functions  $\Delta A_r$  caused by  $\Delta r$  and  $\Delta A_e$  caused by  $\Delta e$  are shown in Fig. 3.22(b). (The angular velocity and acceleration of the cam are respectively

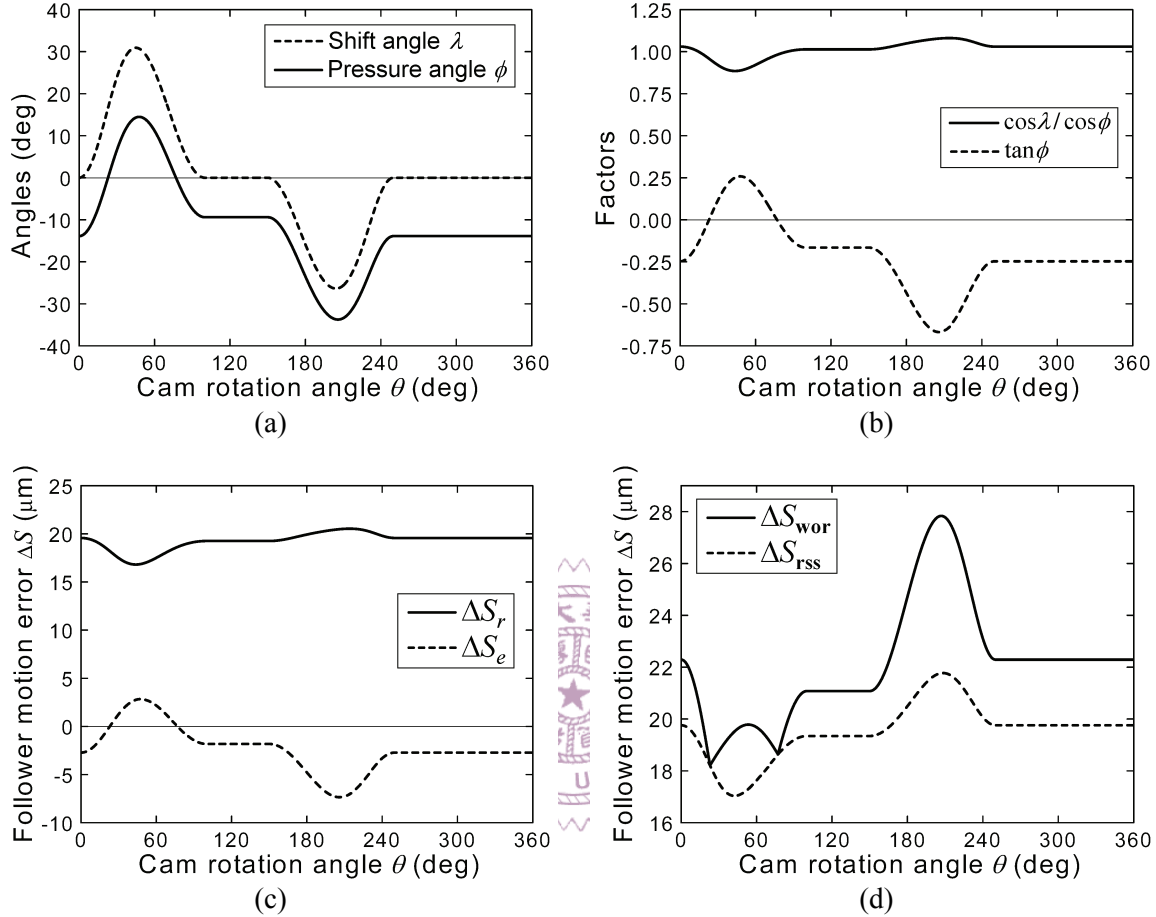


**Figure 3.21** Mechanical error analysis results of a disk cam with an offset translating roller follower.

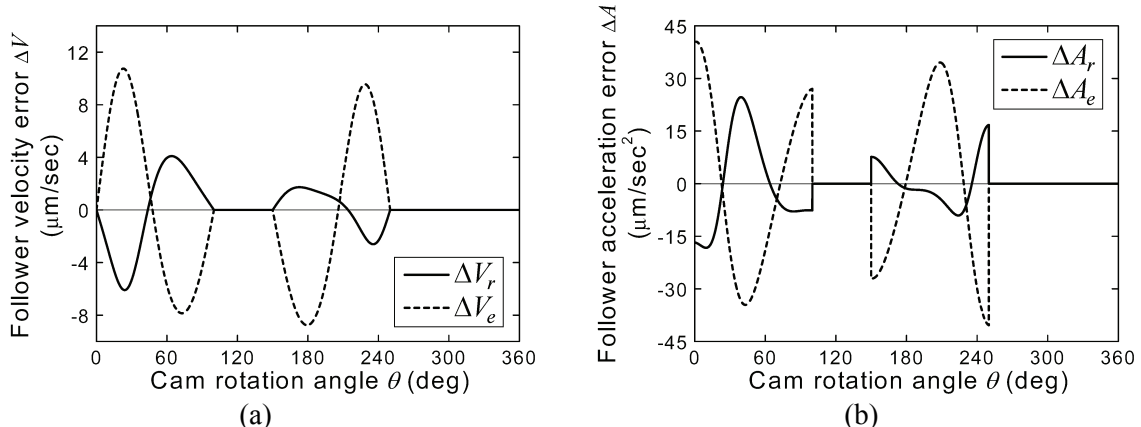


**Figure 3.22** Velocity and acceleration error functions of a disk cam with an offset translating roller follower.

**Table 3.1** Input angles and extreme values of the example for the mechanical error analysis of a disk cam with an offset translating roller follower.

Input angle	Extreme value
$\theta = 22.97^\circ$	$(\Delta S_{wor})_{min} = 18.21 \mu\text{m}$
$\theta = 42.48^\circ$	$(\Delta S_{rss})_{min} = 17.04 \mu\text{m}$
$\theta = 43.71^\circ$	$(\cos \lambda / \cos \phi)_{min} = 0.885$
$\theta = 43.71^\circ$	$(\Delta S_r)_{min} = 16.81 \mu\text{m}$
$\theta = 45.13^\circ$	$\lambda_{max} = 30.93^\circ$
$\theta = 47.72^\circ$	$\phi_{max} = 14.49^\circ$
$\theta = 47.72^\circ$	$(\tan \phi)_{max} = 0.2584$
$\theta = 47.72^\circ$	$(\Delta S_e)_{max} = 2.84 \mu\text{m}$
$\theta = 204.27^\circ$	$\lambda_{min} = -26.37^\circ$
$\theta = 205.84^\circ$	$\phi_{min} = -33.74^\circ$
$\theta = 205.84^\circ$	$(\tan \phi)_{min} = -0.6679$
$\theta = 205.84^\circ$	$(\Delta S_e)_{min} = -7.35 \mu\text{m}$
$\theta = 206.9^\circ$	$(\Delta S_{wor})_{max} = 27.84 \mu\text{m}$
$\theta = 208.32^\circ$	$(\Delta S_{rss})_{max} = 21.77 \mu\text{m}$
$\theta = 214.17^\circ$	$(\cos \lambda / \cos \phi)_{max} = 1.0809$
$\theta = 214.17^\circ$	$(\Delta S_r)_{max} = 20.54 \mu\text{m}$

given as  $\omega_2 = 1 \text{ rad/s}$  cw and  $\alpha_2 = 0 \text{ rad/s}^2$ ). Note that in the acceleration error functions, there is a sudden change at each beginning and at each end of the motion, although the theoretical follower displacement is cycloidal motion.

### 3.6.2 Disk Cam with an Offset Translating Oblique Flat-faced Follower

A cam system requires the offset translating oblique flat-faced follower to rise 22 mm with cycloidal motion while the cam rotates clockwise from  $0^\circ$  to  $120^\circ$ , dwell for the next  $70^\circ$ , return with cycloidal motion for  $100^\circ$  cam rotation and dwell for the remaining  $70^\circ$ . The offset,  $e$ , is 10 mm; the oblique angle of the follower,  $\phi$ , is  $15^\circ$ . The radius of the base circle,  $r_b$ , is 40 mm.

The cam profile, which has a maximum radial dimension of 61.25 mm, is shown in Fig. 2.5. For a tolerance grade of IT6, the cam profile may have a deviation of  $\Delta r = 19 \mu\text{m}$ ,

the offset may have a deviation of  $\Delta e = 9 \mu\text{m}$ , and the oblique angle may have a deviation of  $\Delta\phi = 0.011^\circ = 1.92 \times 10^{-4} \text{ rad}$ . The motion of the follower will then have deviations result from them,  $\Delta S_r$  caused by  $\Delta r$ ,  $\Delta S_\phi$  caused by  $\Delta\phi$ , and  $\Delta S_e$  caused by  $\Delta e$ , respectively. The worst-case deviation of the follower motion will be

$$\Delta S_{\text{wor}} = |\Delta S_r| + |\Delta S_\phi| + |\Delta S_e| \quad (3.118)$$

The maximum expected deviation of the follower motion will be

$$\Delta S_{\text{rss}} = \sqrt{\Delta S_r^2 + \Delta S_\phi^2 + \Delta S_e^2} \quad (3.119)$$

All functions that might be of interest are shown in Fig. 3.23, and their extreme values are also listed in Table 3.2. Figure 3.23(a) shows that the shift angle  $\lambda$ , having quite similar trend to the varying distance  $u$ , is zero at the two dwell regions ( $\theta = 120^\circ \sim 190^\circ$  and  $\theta = 290^\circ \sim 360^\circ$ ). However, the shift angle  $\lambda$ , which appears in the form of  $\cos\lambda$ , is more non-sensitive than the varying distance  $u$  in essence to magnify the resulting errors. In Fig. 3.23(b), one non-dimensional factor  $(u/u_{\max}\cos\phi)$  rather than  $(u/\cos\phi)$  is given to compare with the other non-dimensional factor  $(\cos\lambda/\cos\phi)$ . As can be seen, since  $0.9297 \leq (\cos\lambda/\cos\phi) \leq 1.0353$ , its magnitude has only slight variation. Hence, the variation of  $\Delta S_r$  is flatter than that of  $\Delta S_\phi$ , as shown in Fig. 3.23(c). Since the variation of  $\Delta S_r$  is dominated by factor  $(\cos\lambda/\cos\phi)$ , it has an extreme value of  $19.67 \mu\text{m}$  at the two dwell regions. In addition, owing to that  $\tan\phi = 0.2679$  is a constant, the magnitude of  $\Delta S_e = -2.41 \mu\text{m}$  is invariant.

The extreme value of  $\Delta S_{\text{wor}}$  occurring at  $\theta = 71.5^\circ$  is  $25.57 \mu\text{m}$ . From the viewpoint of the position accuracy of the follower motion, for a total follower travel of 22 mm, a position deviation of  $\Delta S_{\max} = 25.57 \mu\text{m}$  implies a lower accuracy. That is, if the worst situation occurs, the follower motion will have a degraded accuracy ranging from IT7 (21  $\mu\text{m}$ ) to IT8 (33  $\mu\text{m}$ ).

The velocity error functions  $\Delta V_r$  caused by  $\Delta r$ ,  $\Delta V_\phi$  caused by  $\Delta\phi$ , and  $\Delta V_e$  caused by

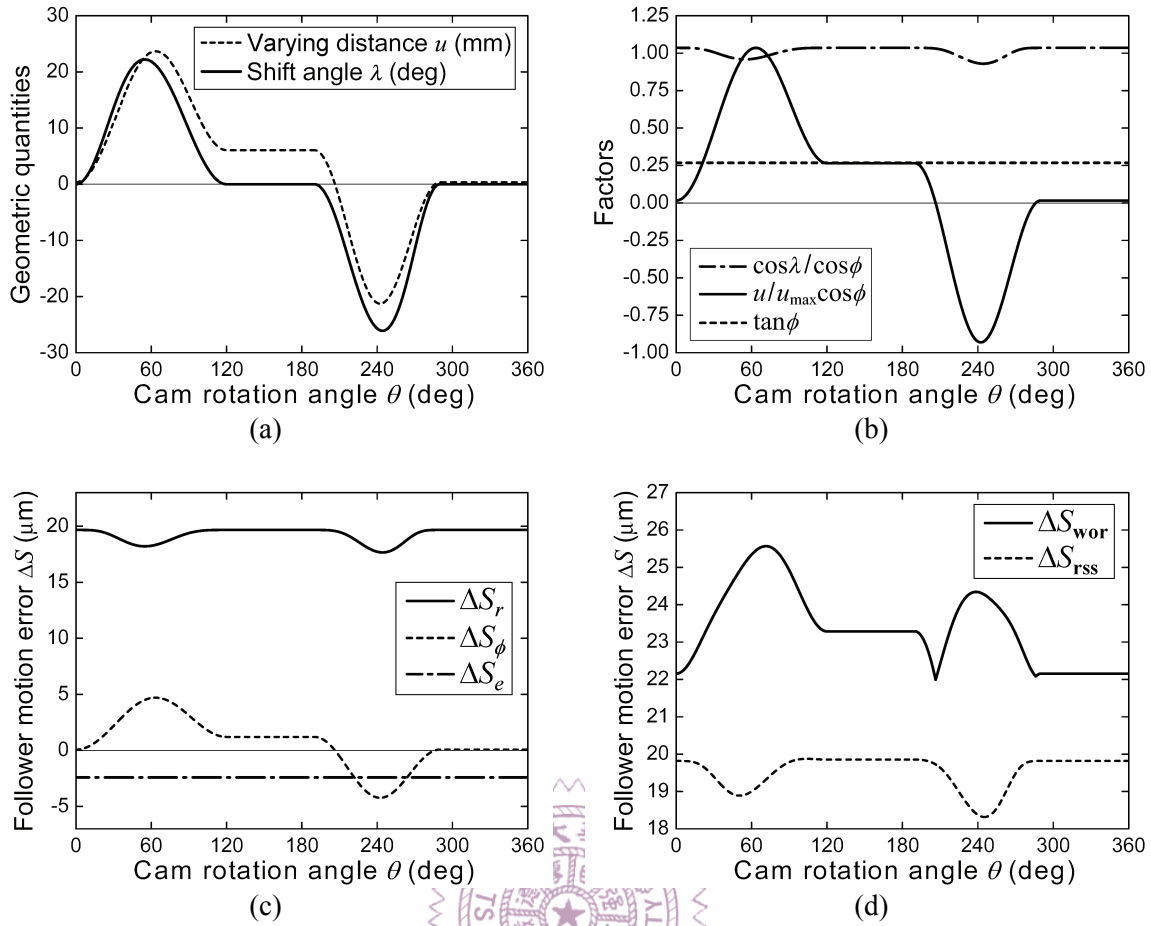


**Figure 3.23** Mechanical error analysis results of a disk cam with an offset translating oblique flat-faced follower.

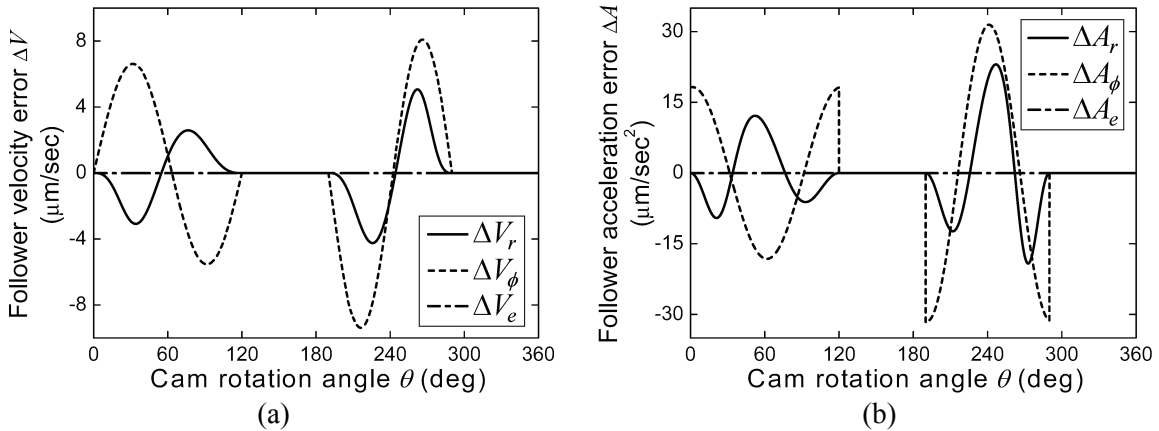


**Figure 3.24** Velocity and acceleration error functions of a disk cam with an offset translating oblique flat-faced follower.

$\Delta e$  are shown in Fig. 3.24(a). The acceleration error functions  $\Delta A_r$  caused by  $\Delta r$ ,  $\Delta A_\phi$  caused by  $\Delta \phi$ , and  $\Delta A_e$  caused by  $\Delta e$  are shown in Fig. 3.24(b). (The velocity and

**Table 3.2** Input angles and extreme values of the example for the mechanical error analysis of a disk cam with an offset translating oblique flat-faced follower.

Input angle	Extreme value
$\theta = 54.84^\circ$	$\lambda_{\max} = 22.21^\circ$
$\theta = 63.41^\circ$	$u_{\max} = 23.67 \text{ mm}$
$\theta = 63.41^\circ$	$(\Delta S_\phi)_{\max} = 4.704 \mu\text{m}$
$\theta = 71.5^\circ$	$(\Delta S_{\text{wor}})_{\max} = 25.57 \mu\text{m}$
$\theta = 103.89^\circ$	$(\Delta S_{\text{rss}})_{\max} = 19.87 \mu\text{m}$
$\theta = 120^\circ \sim 190^\circ$	$(\cos \lambda / \cos \phi)_{\max} = 1.0353$
$\theta = 120^\circ \sim 190^\circ$	$(\Delta S_r)_{\max} = 19.67 \mu\text{m}$
$\theta = 206.39^\circ$	$(\Delta S_{\text{wor}})_{\min} = 21.99 \mu\text{m}$
$\theta = 242.37^\circ$	$u_{\min} = -21.27 \text{ mm}$
$\theta = 242.37^\circ$	$(\Delta S_\phi)_{\min} = -4.23 \mu\text{m}$
$\theta = 244.31^\circ$	$(\cos \lambda / \cos \phi)_{\min} = 0.9297$
$\theta = 244.31^\circ$	$\lambda_{\min} = -26.1^\circ$
$\theta = 244.31^\circ$	$(\Delta S_r)_{\min} = 17.66 \mu\text{m}$
$\theta = 245.23^\circ$	$(\Delta S_{\text{rss}})_{\min} = 18.32 \mu\text{m}$
$\theta = 290^\circ \sim 360^\circ$	$(\cos \lambda / \cos \phi)_{\max} = 1.0353$
$\theta = 290^\circ \sim 360^\circ$	$(\Delta S_r)_{\max} = 19.67 \mu\text{m}$

acceleration of the cam are respectively given as  $\omega_2 = 1 \text{ rad/s}$  cw and  $\alpha_2 = 0 \text{ rad/s}^2$ .) As a result of that  $\Delta S_e$  is invariant, the corresponding  $\Delta V_e$  and  $\Delta A_e$  are both zero. Note that in the acceleration error functions, there is a sudden change at each beginning and at each end of  $\Delta A_\phi$ , although the theoretical follower displacement is cycloidal motion. On the contrary,  $\Delta A_r$  is a continuous and smooth function, since  $\cos \lambda$  may have continuous derivatives to the second order at least.

### 3.6.3 Disk Cam with an Oscillating Roller Follower

A cam system requires the oscillating roller follower to oscillate  $25^\circ$  clockwise with cycloidal motion while the cam rotates clockwise from  $0^\circ$  to  $120^\circ$ , dwell for the next  $40^\circ$ , return with cycloidal motion for  $120^\circ$  cam rotation and dwell for the remaining  $80^\circ$ . The distance between pivots,  $f$ , is 80 mm; the length of the follower arm,  $l$ , is 52 mm. The base

circle radius,  $r_b$ , is 40 mm and the radius of the follower roller,  $r_f$ , is 8 mm.

The cam profile, which has a maximum radial dimension of 62.478 mm, is shown in Fig. 2.6. For a tolerance grade of IT6, each of the three parameters ( $r$ ,  $f$ , and  $l$ ) happens to have the same tolerance of 19  $\mu\text{m}$ . (The radius error of the roller,  $\Delta r_f$ , may be ignored since it generally has a smaller tolerance grade and may have a magnitude of 2  $\mu\text{m}$  at most if a precision roller is used.) Then the motion of the follower will have deviations resulting from them,  $\Delta S_r$  caused by  $\Delta r$ ,  $\Delta S_f$  caused by  $\Delta f$ , and  $\Delta S_l$  caused by  $\Delta l$ , respectively. The worst-case deviation of the follower motion will be

$$\Delta S_{\text{wor}} = |\Delta S_r| + |\Delta S_f| + |\Delta S_l| \quad (3.120)$$

The maximum expected deviation of the follower motion will be

$$\Delta S_{\text{rss}} = \sqrt{\Delta S_r^2 + \Delta S_f^2 + \Delta S_l^2} \quad (3.121)$$

All functions that might be of interest are shown in Fig. 3.25, and their extreme values are also listed in Table 3.3. In this case, the pressure angle  $\phi$  ranges from  $-19.87^\circ$  to  $26.35^\circ$ . Figure 3.25(a) shows that the pressure angle  $\phi$  and the shift angle  $\lambda$  have quite similar trends. Therefore, the variation of  $(1/\cos\phi)$  is flattened by  $\cos\lambda$ , and  $0.9391 \leq (\cos\lambda / \cos\phi) \leq 1.0704$ . Partly due to the slight variation of the pressure angle and partly due to the counteraction of the shift angle, the resulting error of  $\Delta S_r$  has an even slighter variation.

The extreme value of  $\Delta S_{\text{wor}}$  occurs at  $\theta = 41.24^\circ$ , very close to  $\theta = 41.49^\circ$ , where the extreme pressure angle  $\phi$  occurs. The worst-case deviation has an extreme magnitude of  $\Delta S_{\text{wor}} = 0.0539^\circ$ . From the viewpoint of the position accuracy of the follower motion, for a total follower travel of  $25^\circ$ , an angular position deviation of  $\Delta S_{\text{max}} = 0.0539^\circ$  implies a quite low accuracy. In other words, if the worst situation occurs, the follower motion will have a degraded accuracy ranging from IT9 ( $0.052^\circ$ ) to IT10 ( $0.084^\circ$ ).

The velocity error functions  $\Delta V_r$  caused by  $\Delta r$ ,  $\Delta V_l$  caused by  $\Delta l$ , and  $\Delta V_f$  caused by  $\Delta f$  are shown in Fig. 3.26(a). Their corresponding acceleration error functions are shown in

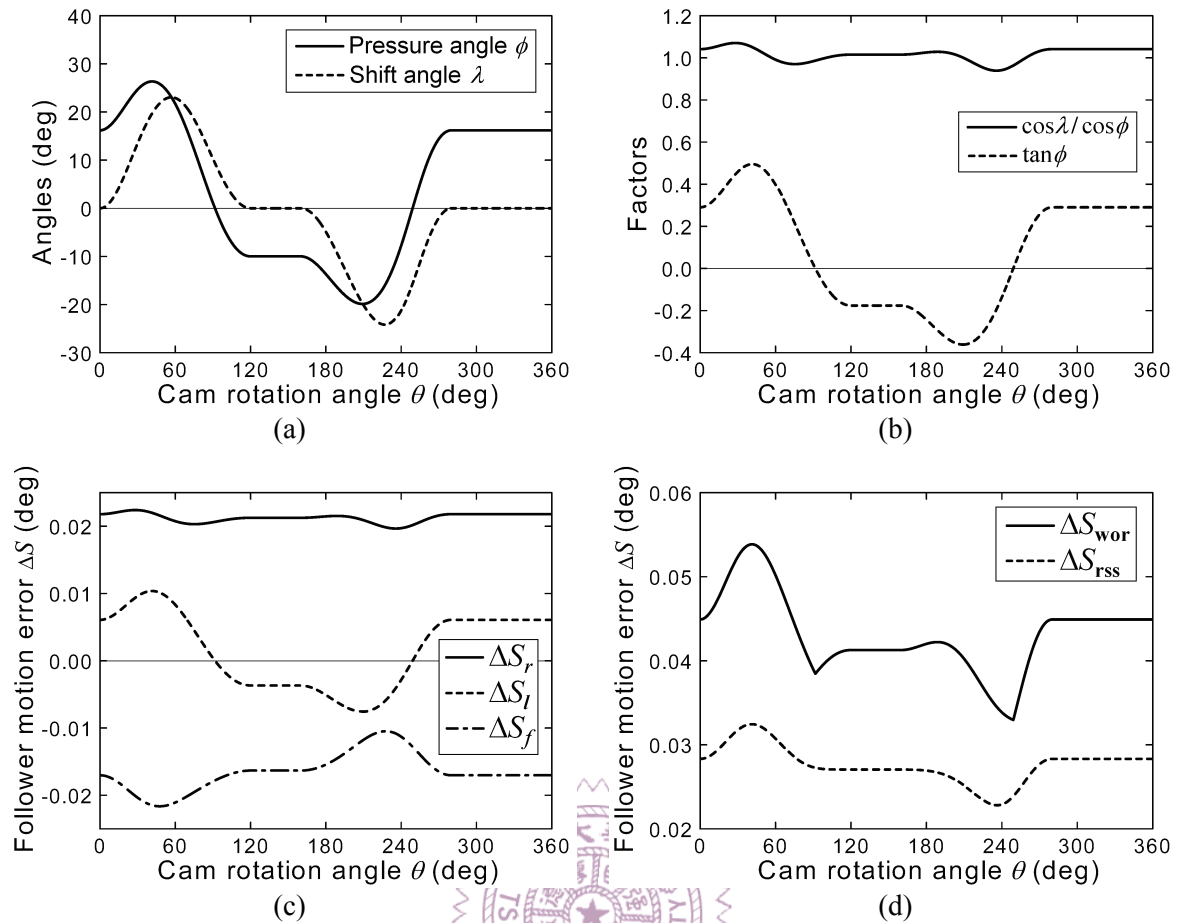


**Figure 3.25** Mechanical error analysis results of a disk cam with an oscillating roller follower.

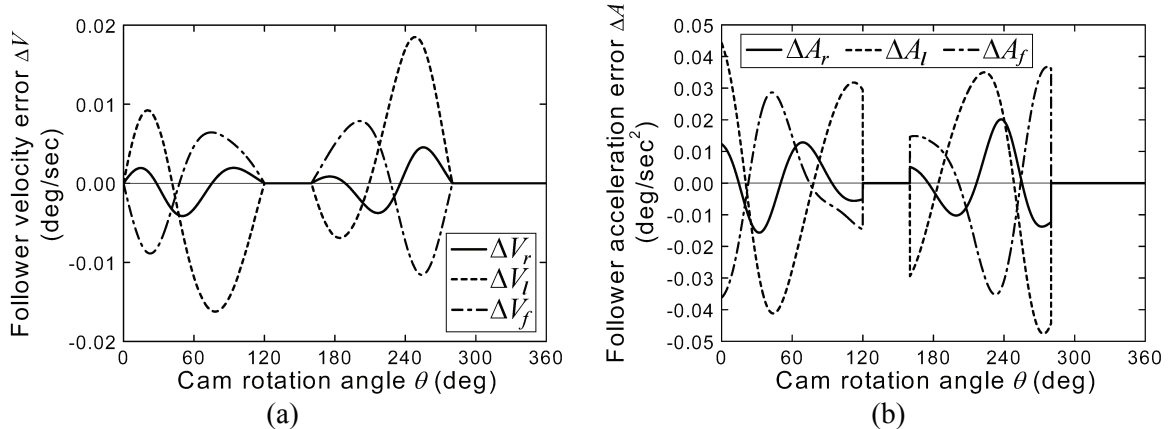


**Figure 3.26** Velocity and acceleration error functions of a disk cam with an oscillating roller follower.

Fig. 3.26(b). (The velocity and acceleration of the cam are respectively given as  $\omega_2 = 1$  rad/s cw and  $\alpha_2 = 0$  rad/s<sup>2</sup>.) In this case, they also have a sudden change at each beginning and end of the motion even though the theoretical follower displacement is cycloidal motion.

**Table 3.3** Input angles and extreme values of the example for the mechanical error analysis of a disk cam with an oscillating roller follower.

Input angle	Extreme value
$\theta = 28.06^\circ$	$(\cos \lambda / \cos \phi)_{\max} = 1.0704$
$\theta = 28.06^\circ$	$(\Delta S_r)_{\max} = 0.0224^\circ$
$\theta = 41.07^\circ$	$(\Delta S_{\text{rss}})_{\max} = 0.0325^\circ$
$\theta = 41.24^\circ$	$(\Delta S_{\text{wor}})_{\max} = 0.0539^\circ$
$\theta = 41.49^\circ$	$\phi_{\max} = 26.35^\circ$
$\theta = 41.49^\circ$	$(\tan \phi)_{\max} = 0.4953$
$\theta = 41.49^\circ$	$(\Delta S_l)_{\max} = 0.0104^\circ$
$\theta = 47.56^\circ$	$(\Delta S_f)_{\min} = -0.0216^\circ$
$\theta = 56.84^\circ$	$\lambda_{\max} = 23.05^\circ$
$\theta = 209.2^\circ$	$\phi_{\min} = -19.87^\circ$
$\theta = 209.2^\circ$	$(\tan \phi)_{\min} = -0.3614$
$\theta = 209.2^\circ$	$(\Delta S_l)_{\min} = 0.0076^\circ$
$\theta = 227^\circ$	$\lambda_{\min} = -24.17^\circ$
$\theta = 227.63^\circ$	$(\Delta S_f)_{\max} = -0.0105^\circ$
$\theta = 235.72^\circ$	$(\cos \lambda / \cos \phi)_{\min} = 0.9391$
$\theta = 235.72^\circ$	$(\Delta S_r)_{\min} = 0.0197^\circ$
$\theta = 236.24^\circ$	$(\Delta S_{\text{rss}})_{\min} = 0.0228^\circ$
$\theta = 249.1^\circ$	$(\Delta S_{\text{wor}})_{\min} = 0.033^\circ$

### 3.6.4 Disk Cam with an Oscillating Flat-Faced Follower

A cam system requires the oscillating flat-faced follower to oscillate  $15^\circ$  clockwise with cycloidal motion while the cam rotates clockwise from  $0^\circ$  to  $120^\circ$ , dwell for the next  $40^\circ$ , return with cycloidal motion for  $120^\circ$  cam rotation and dwell for the remaining  $80^\circ$ . The distance between pivots,  $f$ , is 80 mm; the offset of the follower face,  $e$ , is 16 mm. The base circle radius,  $r_b$ , is 40 mm.

The cam profile, which has a maximum radial dimension of 58.934 mm, is shown in Fig. 2.7. For a tolerance grade of IT6, the cam profile and the distance between pivots may have the same deviation of  $\Delta r = \Delta f = 19 \mu\text{m}$ , and the offset may have a deviation of  $\Delta e = 11 \mu\text{m}$ . Then the motion of the follower will have deviations result from them,  $\Delta S_r$  caused

by  $\Delta r$ ,  $\Delta S_f$  caused by  $\Delta f$ , and  $\Delta S_e$  caused by  $\Delta e$ , respectively. The worst-case deviation of the follower motion will be

$$\Delta S_{\text{wor}} = |\Delta S_r| + |\Delta S_f| + |\Delta S_e| \quad (3.122)$$

The maximum expected deviation of the follower motion will be

$$\Delta S_{\text{rss}} = \sqrt{\Delta S_r^2 + \Delta S_f^2 + \Delta S_e^2} \quad (3.123)$$

All functions that might be of interest are shown in Fig. 3.27, and their extreme values are also listed in Table 3.4. Figure 3.27(a) shows that the range of the pressure angle is  $9.355^\circ \leq \phi \leq 15.535^\circ$ ; its variation is much slighter than that of the shift angle  $\lambda$  ( $-16.751^\circ \leq \lambda \leq 26.355^\circ$ ). Hence, the factors  $(\cos \lambda \tan \phi)$  and  $\tan \phi$  shown in Fig. 3.27(b) will

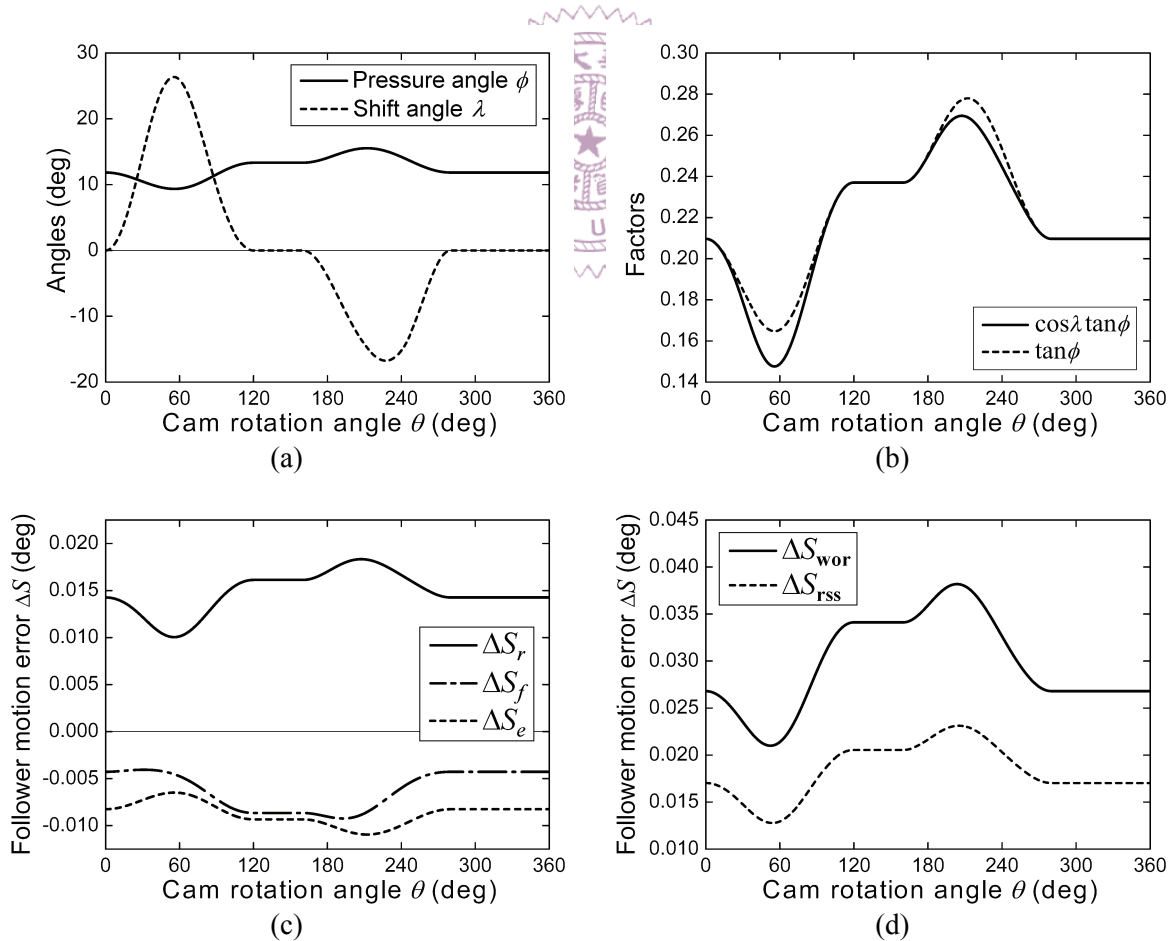


**Figure 3.27** Mechanical error analysis results of a disk cam with an oscillating flat-faced follower.

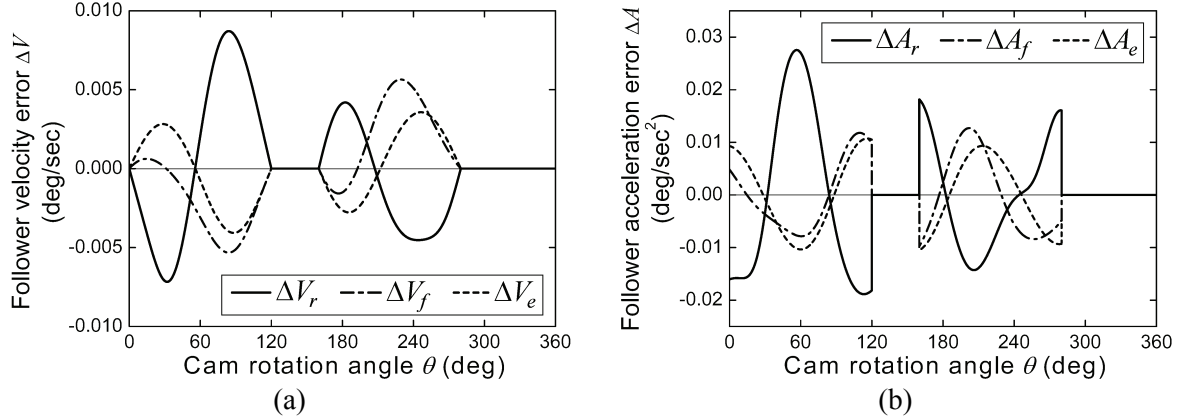


**Figure 3.28** Velocity and acceleration error functions of a disk cam with an oscillating flat-faced follower.

**Table 3.4** Input angles and extreme values of the example for the mechanical error analysis of a disk cam with an oscillating flat-faced follower.

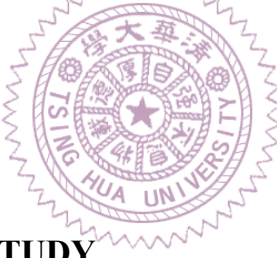
Input angle	Extreme value
$\theta = 31.18^\circ$	$(\Delta S_f)_{\max} = -0.0041^\circ$
$\theta = 52.42^\circ$	$(\Delta S_{\text{wor}})_{\min} = 0.021^\circ$
$\theta = 53.92^\circ$	$(\Delta S_{\text{rss}})_{\min} = 0.0128^\circ$
$\theta = 55.4^\circ$	$\lambda_{\max} = 26.355^\circ$
$\theta = 55.61^\circ$	$(\cos \lambda \tan \phi)_{\min} = 0.1476$
$\theta = 55.61^\circ$	$(\Delta S_r)_{\min} = 0.01^\circ$
$\theta = 55.77^\circ$	$\phi_{\min} = 9.355^\circ$
$\theta = 55.77^\circ$	$(\tan \phi)_{\min} = 0.1647$
$\theta = 55.77^\circ$	$(\Delta S_e)_{\max} = -0.0065^\circ$
$\theta = 192.72^\circ$	$(\Delta S_f)_{\min} = -0.0092^\circ$
$\theta = 203.54^\circ$	$(\Delta S_{\text{wor}})_{\max} = 0.0382^\circ$
$\theta = 204.96^\circ$	$(\Delta S_{\text{rss}})_{\max} = 0.0231^\circ$
$\theta = 207.4^\circ$	$(\cos \lambda \tan \phi)_{\max} = 0.2695$
$\theta = 207.4^\circ$	$(\Delta S_r)_{\max} = 0.0183^\circ$
$\theta = 212.11^\circ$	$\phi_{\max} = 15.535^\circ$
$\theta = 212.11^\circ$	$(\tan \phi)_{\max} = 0.278$
$\theta = 212.11^\circ$	$(\Delta S_e)_{\min} = -0.0109^\circ$
$\theta = 227.43^\circ$	$\lambda_{\min} = -16.751^\circ$

have quite similar trends. This situation results in that the occurrence of extreme values of  $\Delta S_r$  (occurring at  $\theta = 55.61^\circ$  and  $\theta = 207.4^\circ$ ) are close to those of  $\Delta S_e$  (occurring at  $\theta =$

$55.77^\circ$  and  $\theta = 212.11^\circ$ ).

The extreme value of  $\Delta S_{\text{wor}}$  occurs at  $\theta = 203.54^\circ$ , close to  $\theta = 212.11^\circ$ , where the extreme pressure angle  $\phi$  occurs. The worst-case deviation has an extreme magnitude of  $\Delta S_{\text{wor}} = 0.0382^\circ$ . From the viewpoint of the position accuracy of the follower motion, for a total follower travel of  $15^\circ$ , an angular position deviation of  $\Delta S_{\text{max}} = 0.0382^\circ$  implies a quite low accuracy. In other words, if the worst situation occurs, the follower motion will have a degraded accuracy ranging from IT8 ( $0.027^\circ$ ) to IT9 ( $0.043^\circ$ ).

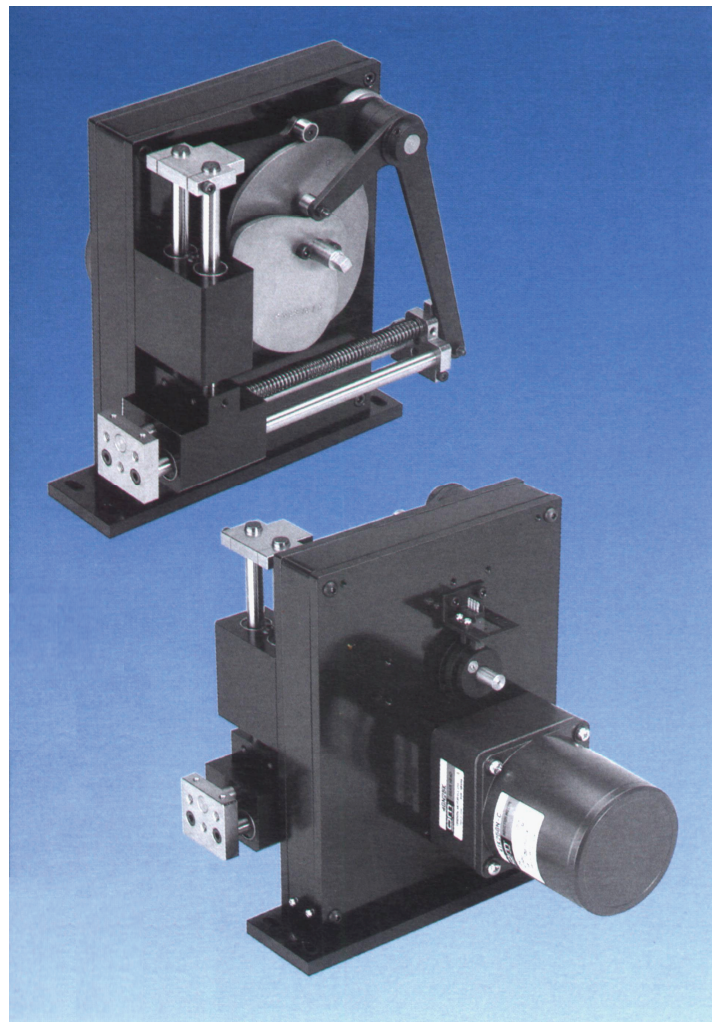
The velocity error functions  $\Delta V_r$  caused by  $\Delta r$ ,  $\Delta V_f$  caused by  $\Delta f$ , and  $\Delta V_e$  caused by  $\Delta e$  are shown in Fig. 3.28(a). Their corresponding acceleration error functions are shown in Fig. 3.28(b). (The velocity and acceleration of the cam are respectively given as  $\omega_2 = 1$  rad/s cw and  $\alpha_2 = 0$  rad/s<sup>2</sup>.) Similar to above examples, in this case, they all have a sudden change at each beginning and end of the motion even though the theoretical follower displacement is cycloidal motion.



### 3.7 A PRACTICAL CASE STUDY

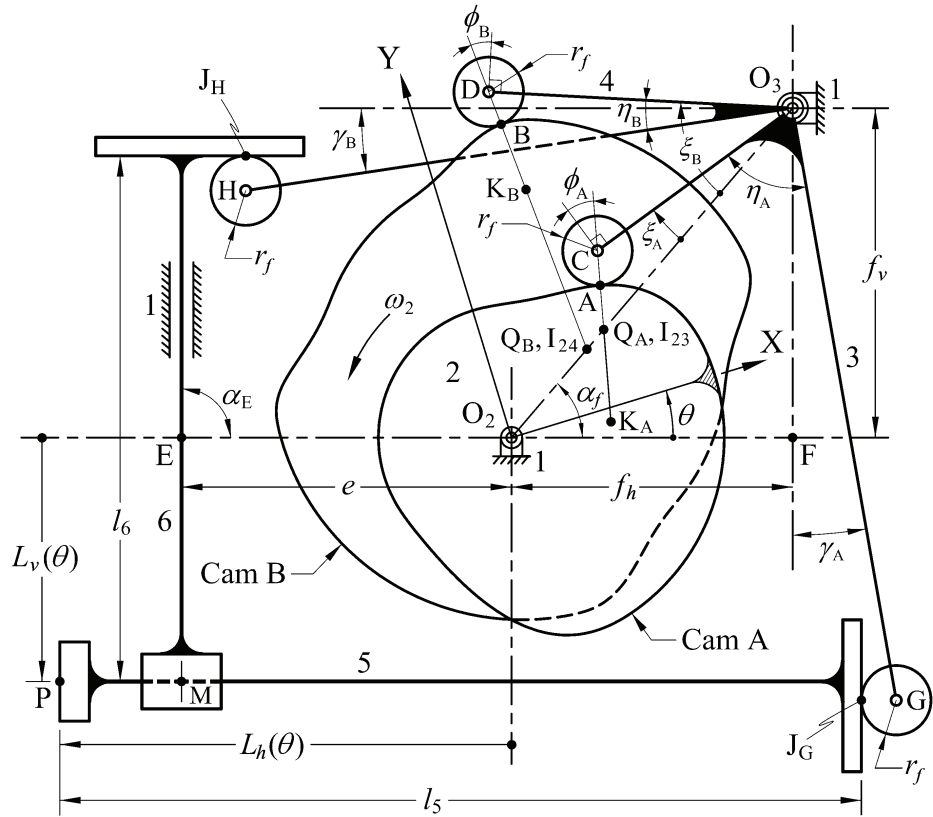
In this section, the equivalent linkage method is applied to a practical case to further show its feasibility and effectiveness of analyzing mechanical errors in cam-linkage combined mechanisms.

Figure 3.29 shows the MEG X6061 mechanism [106], an existing pick-and-place device of planar cam-follower type, and Fig. 3.30(a) shows the kinematic diagram of this device. In practice, return springs are used in the device to retain the intended contact of every high pair, but for clarity they are not shown in the figure. It utilizes dual cams and dual primary followers to generate the end-effector motion of the follower train. The dual cams A and B are fixed on a common shaft, which rotates with respect to the frame and serves as the driving link of the mechanism. The frame is consistently numbered as 1, the driving link as 2, and other links are successively numbered. Cam A drives an oscillating

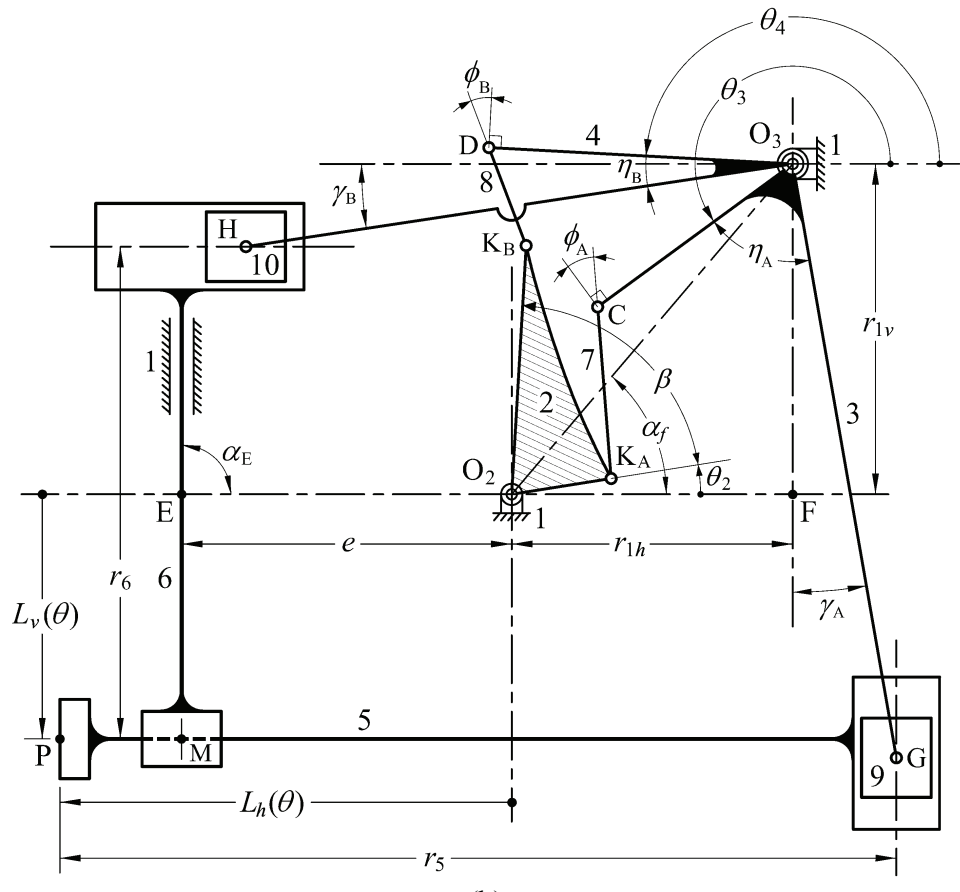


**Figure 3.29** The MEG X6061 planar cam-follower type pick-and-place device [106].

follower (link 3) which in turn drives the end-effector (link 5), a floating secondary follower, to generate the desired horizontal motion of the end-effector. Similarly, cam B drives the other oscillating follower (link 4) which in turn drives a secondary translating follower (link 6) to generate the desired vertical motion of the end-effector. Finally, a clamping device is attached at the left end of the end-effector to effectively pick and place target objects. Because the direction of link 5 remains unchanged, the clamping device attached on the end-effector produces a curvilinear translation, and all points on it will trace congruent paths. In order to perform safely and reliably its intended function, the kinematic accuracy of the end-effector must be evaluated through the mechanical error analysis of the mechanism.



(a)



(b)

**Figure 3.30** Planar cam-follower type pick-and-place device and its equivalent ten-bar linkage.

### 3.7.1 Cam Profiles Determination

As shown in Fig. 3.30(a), dual cams A and B are both pivoted at  $O_2$ , and dual oscillating follower arms (links 3 and 4) are both pivoted at  $O_3$ . The center distance  $O_2O_3$  can be expressed as  $f = O_2O_3 = (f_h^2 + f_v^2)^{1/2}$  where  $f_h$  ( $= O_2F$ ) and  $f_v$  ( $= O_3F$ ) are the horizontal and vertical distances between the centers of pivots, respectively. Then the subtending angle  $\alpha_f$  is  $\tan^{-1}(f_v/f_h)$ . The base circle of cam A is  $r_{bA}$  and that of cam B is  $r_{bB}$ . Rollers C and G, which are mounted on link 3, and rollers D and H, which are mounted on link 4, are all have the same radius of  $r_f$ . The dimensions of link 3 are  $l_C = O_3C$ ,  $l_G = O_3G$ , and  $\eta_A = \angle CO_3G$ ; the dimensions of link 4 are  $l_D = O_3D$ ,  $l_H = O_3H$ , and  $\eta_B = \angle DO_3H$ . The distance from the right-end plate of link 5 to its reference point P is  $l_5$ ; the distance from the top-end plate of link 6 to its reference point M is  $l_6$ . The central axis of link 5, line PM, remains in the horizontal direction, the central axis of link 6, line EM, remains in the vertical direction, and thus  $\alpha_E = 90^\circ$ . The central axis of link 6 has an offset of  $e$  ( $= O_2E$ ) from the cam center. The cams rotate counterclockwise with a constant angular velocity of  $\omega_2$  rad/s. By setting up a Cartesian coordinate system X-Y fixed on the driving link and with its origin at the fixed pivot  $O_2$ , after the desired motions of the end-effector have been specified, the profile coordinates of both cams may be expressed in terms of the cam rotation angle  $\theta$ , which is measured counterclockwise from the horizontal line to the X-axis.

Since all points on link 5 will trace congruent paths, the desired motion of this link may be described by the path of any convenient point such as point P, the left end of this link. After the horizontal motion program  $S_h(\theta)$  and the vertical motion program  $S_v(\theta)$  of the reference point P have been specified, the position functions of point P relative to the cam center  $O_2$  can consequently be expressed as the following two functions:

$$L_h(\theta) = l_5 + r_f - f_h + l_G \cos \left\{ \alpha_f + \eta_A - \cos^{-1} \left[ \frac{l_C^2 + f^2 - (r_{bA} + r_f)^2}{2l_C f} \right] \right\} + S_h(\theta) \quad (3.124)$$

and

$$L_v(\theta) = l_6 - r_f - f_v + l_H \sin \left\{ \alpha_f + \eta_B - \cos^{-1} \left[ \frac{l_D^2 + f^2 - (r_{bB} + r_f)^2}{2l_D f} \right] \right\} + S_v(\theta) \quad (3.125)$$

where  $L_h(\theta)$  is the horizontal displacement function and  $L_v(\theta)$  is the vertical displacement function of point P. When  $\theta = 0^\circ$ ,  $S_h(0) = 0$ ,  $S_v(0) = 0$ , the initial value of the horizontal displacement function will be

$$L_h(0) = l_5 + r_f - f_h + l_G \cos \left\{ \alpha_f + \eta_A - \cos^{-1} \left[ \frac{l_C^2 + f^2 - (r_{bA} + r_f)^2}{2l_C f} \right] \right\} \quad (3.126)$$

and that of the vertical displacement function will be

$$L_v(0) = l_6 - r_f - f_v + l_H \sin \left\{ \alpha_f + \eta_B - \cos^{-1} \left[ \frac{l_D^2 + f^2 - (r_{bB} + r_f)^2}{2l_D f} \right] \right\} \quad (3.127)$$

Both initial values are independent of the cam rotation angle  $\theta$ . Here, functions  $S_h(\theta)$  and  $L_h(\theta)$  increase positively when point P moves leftward, and functions  $S_v(\theta)$  and  $L_v(\theta)$  increase positively when point P move downward; all of them are positive in Fig. 3.30(a). After some algebraic manipulation, the angular displacement functions of dual primary oscillating followers, O<sub>3</sub>C and O<sub>3</sub>D, can be respectively expressed as

$$\xi_A(\theta) = \alpha_f + \eta_A - \gamma_A(\theta) - 90^\circ = \alpha_f + \eta_A - \cos^{-1} \left[ \frac{L_h(\theta) - l_5 - r_f + f_h}{l_G} \right] \quad (3.128)$$

and

$$\xi_B(\theta) = \alpha_f + \eta_B - \gamma_B(\theta) = \alpha_f + \eta_B - \sin^{-1} \left[ \frac{L_v(\theta) - l_6 + r_f + f_v}{l_H} \right] \quad (3.129)$$

where  $\gamma_A(\theta)$  [ $= \alpha_f + \eta_A - \xi_A(\theta) - 90^\circ$ ] and  $\gamma_B(\theta)$  [ $= \alpha_f + \eta_B - \xi_B(\theta)$ ] are the angular displacement functions of oscillating arms O<sub>3</sub>G and O<sub>3</sub>H, respectively. Then by following the analytical approach shown in Section 2.5, the profile coordinates of cams A and B can

be derived and expressed as

$$\mathbf{R}_A(\theta) = \mathbf{O}_2 \mathbf{A} = \begin{cases} q_A \cos(\alpha_f - \theta) + (Q_A C - r_f) \cos(\alpha_f + \alpha_A - \theta) \\ q_A \sin(\alpha_f - \theta) + (Q_A C - r_f) \sin(\alpha_f + \alpha_A - \theta) \end{cases} \quad (3.130)$$

and

$$\mathbf{R}_B(\theta) = \mathbf{O}_2 \mathbf{B} = \begin{cases} q_B \cos(\alpha_f - \theta) + (Q_B D - r_f) \cos(\alpha_f + \alpha_B - \theta) \\ q_B \sin(\alpha_f - \theta) + (Q_B D - r_f) \sin(\alpha_f + \alpha_B - \theta) \end{cases} \quad (3.131)$$

where, by labeling instant centers  $I_{23}$  and  $I_{24}$  as  $Q_A$  and  $Q_B$ , respectively,

$$q_A = O_2 Q_A = O_2 I_{23} = \frac{f \frac{d\xi_A(\theta)}{d\theta}}{1 + \frac{d\xi_A(\theta)}{d\theta}} = \frac{f v_h(\theta)}{v_h(\theta) + \sqrt{l_G^2 - [L_h(\theta) - l_5 - r_f + f_h]^2}} \quad (3.132)$$

$$q_B = O_2 Q_B = O_2 I_{24} = \frac{f \frac{d\xi_B(\theta)}{d\theta}}{1 + \frac{d\xi_B(\theta)}{d\theta}} = \frac{f v_v(\theta)}{v_v(\theta) + \sqrt{l_H^2 - [L_v(\theta) - l_6 + r_f + f_v]^2}} \quad (3.133)$$

in which,  $v_h(\theta) = dL_h(\theta)/d\theta = dS_h(\theta)/d\theta$  and  $v_v(\theta) = dL_v(\theta)/d\theta = dS_v(\theta)/d\theta$ ; and

$$Q_A C = \sqrt{l_C^2 + (f - q_A)^2 - 2l_C(f - q_A)\cos\xi_A(\theta)} \quad (3.134)$$

$$Q_B D = \sqrt{l_D^2 + (f - q_B)^2 - 2l_D(f - q_B)\cos\xi_B(\theta)} \quad (3.135)$$

$$\alpha_A = \angle C Q_A O_3 = \sin^{-1} \left[ \frac{l_C \sin \xi_A(\theta)}{Q_A C} \right] \quad (3.136)$$

$$\alpha_B = \angle D Q_B O_3 = \sin^{-1} \left[ \frac{l_D \sin \xi_B(\theta)}{Q_B D} \right] \quad (3.137)$$

In this case, the specified motion programs,  $S_h(\theta)$  and  $S_v(\theta)$ , are shown in Fig. 3.31(a).

Such motion programs can lead to the resulting path of point P as shown in Fig. 3.31(b); that is, point P will successively occupy positions  $P_0, P_1, P_2, P_3, \dots$  with  $P_0$  being the initial position. In addition, the path positions of point P are correlated with cam rotation

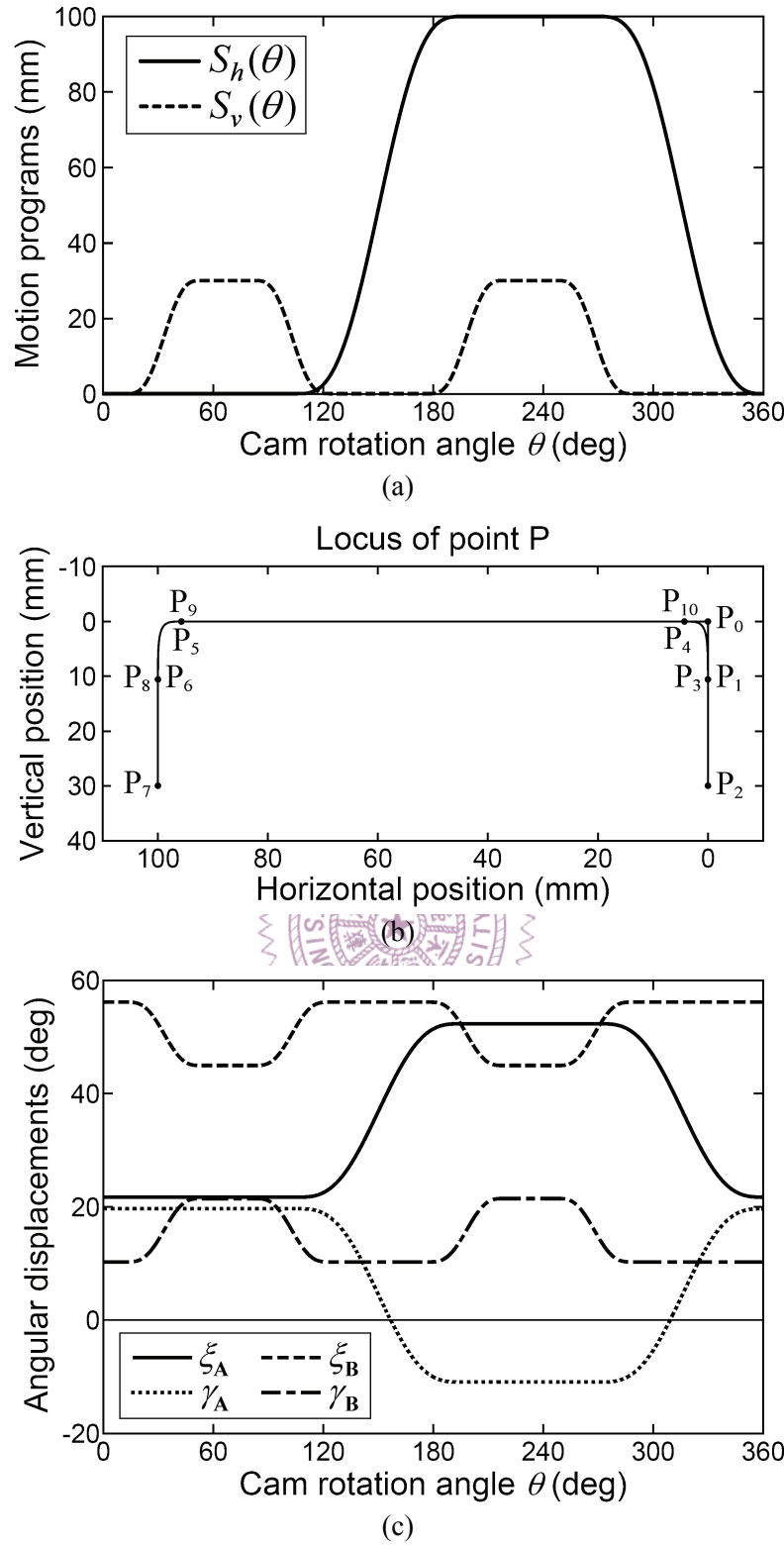


**Figure 3.31** Functional requirements of a planar cam-follower type pick-and-place device:  
 (a) motion programs;  
 (b) locus of the functional output (the reference point P);  
 (c) angular displacements of the dual primary oscillating followers.

angles. In other words, point P stays at its initial position  $P_0$  while the cams rotate counterclockwise from  $0^\circ$  to  $13^\circ$ , then moves downward via  $P_1$  to its first working position

$P_2$  for  $40^\circ$  cam rotation and then dwells for the next  $30^\circ$ . When the cams rotate from  $83^\circ$  to  $123^\circ$ , point P moves upward from position  $P_2$  via  $P_3$  to position  $P_4$ ; during this period, when  $\theta = 106^\circ$ , point P also simultaneously starts its leftward motion at position  $P_3$ . When the cams rotate from  $123^\circ$  to  $178^\circ$ , point P moves leftward from position  $P_4$  to position  $P_5$ . From  $178^\circ$  to  $218^\circ$ , point P moves downward again from position  $P_5$  via  $P_6$  to position  $P_7$ , its second working position, and then dwells for the next  $30^\circ$ ; during this period, when  $\theta = 195^\circ$ , point P complete its leftward motion at  $P_6$ . From  $248^\circ$  to  $288^\circ$ , tracing the former path, point P moves upward from position  $P_7$  via  $P_8$  to position  $P_9$ ; then from position  $P_9$ , it moves rightward to position  $P_0$  for the next  $72^\circ$ . During this period, when  $\theta = 271^\circ$ , it must occupy position  $P_8$ . The horizontal and vertical travel lengths of point P are 100 and 30 mm, respectively, both with cycloidal motions.

Other dimensions of the design parameters are:  $f_h = 60$  mm,  $f_v = 75$  mm,  $l_C = l_D = 60$  mm,  $l_G = 190$  mm,  $l_H = 160$  mm,  $\eta_A = 80^\circ$ ,  $\eta_B = 15^\circ$ ,  $r_f = 8$  mm,  $r_{bA} = 38$  mm,  $r_{bB} = 72$  mm,  $l_s = 230$  mm,  $l_6 = 200$  mm,  $e = 100$  mm, and  $\alpha_E = 90^\circ$ . The magnitude of offset  $e$  will not affect cam profiles. Figure 3.31(c) shows the angular displacements of the oscillating

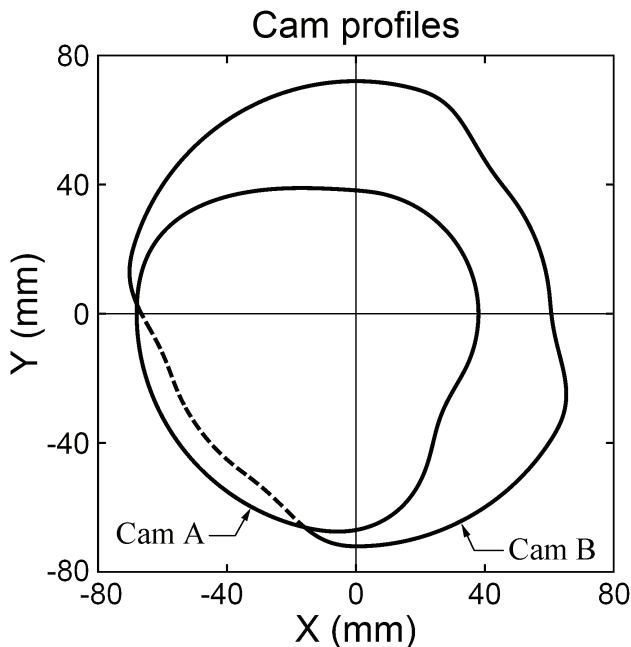


**Figure 3.32** Profiles of the dual cams A and B in a planar cam-follower type pick-and-place device.

followers. The determined cam profiles and their corresponding pressure angles  $\phi_A$ ,  $\phi_B$  together with shift angles  $\lambda_A$ ,  $\lambda_B$  are shown in Figs. 3.32, 3.33(a) and 3.33(b), respectively, while the pressure angles can be found by

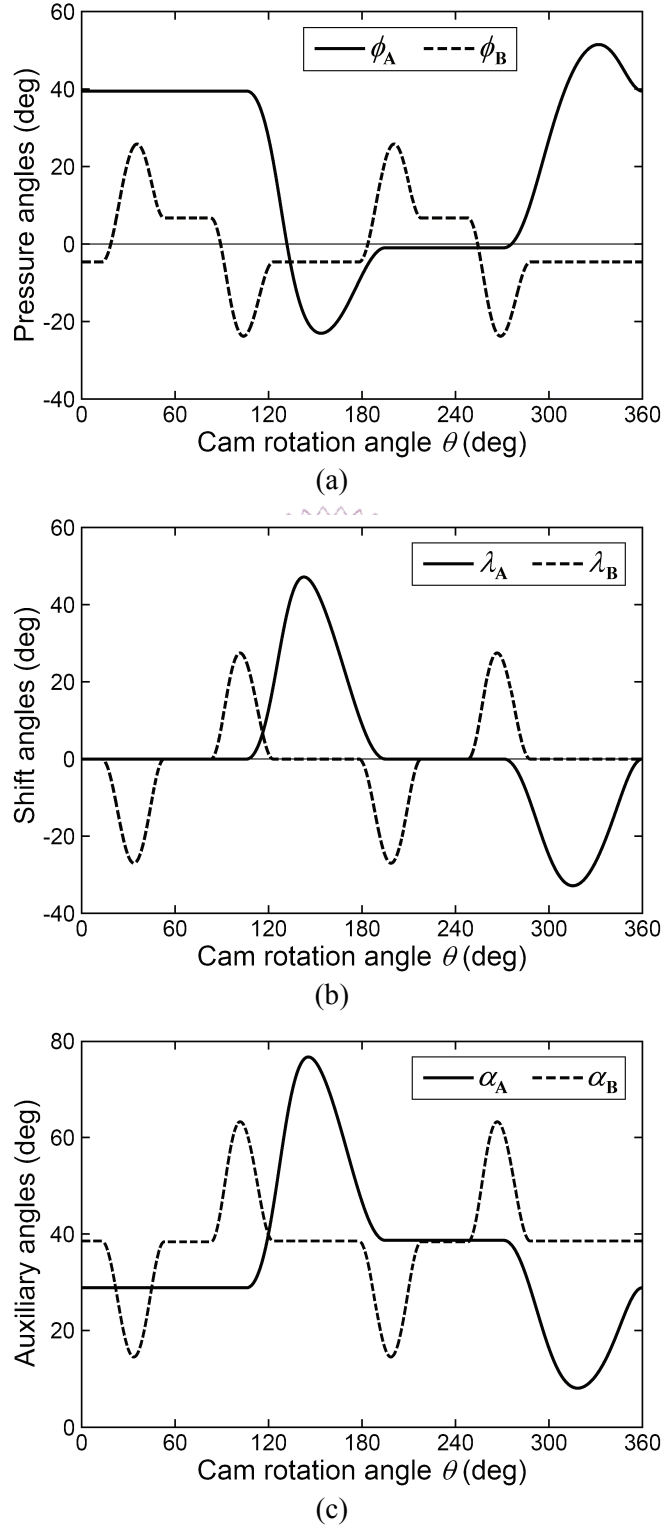


**Figure 3.33** Angles of a planar cam-follower type pick-and-place device.

**Table 3.5** Input angles and extreme values of angles of a planar cam-follower type pick-and-place device.

Input angle	Extreme value	Input angle	Extreme value
$\theta = 33.52^\circ$	$(\alpha_B)_{\min} = 14.47^\circ$	$\theta = 198.52^\circ$	$(\alpha_B)_{\min} = 14.47^\circ$
$\theta = 33.75^\circ$	$(\lambda_B)_{\min} = -27^\circ$	$\theta = 198.57^\circ$	$(\lambda_B)_{\min} = -27^\circ$
$\theta = 35.63^\circ$	$(\phi_B)_{\max} = 25.81^\circ$	$\theta = 200.63^\circ$	$(\phi_B)_{\max} = 25.81^\circ$
$\theta = 101.71^\circ$	$(\lambda_B)_{\max} = 27.48^\circ$	$\theta = 266.71^\circ$	$(\lambda_B)_{\max} = 27.48^\circ$
$\theta = 101.83^\circ$	$(\alpha_B)_{\max} = 63.25^\circ$	$\theta = 266.83^\circ$	$(\alpha_B)_{\max} = 63.25^\circ$
$\theta = 103.92^\circ$	$(\phi_B)_{\min} = -23.77^\circ$	$\theta = 268.92^\circ$	$(\phi_B)_{\min} = -23.77^\circ$
$\theta = 142.72^\circ$	$(\lambda_A)_{\max} = 47.17^\circ$	$\theta = 315.36^\circ$	$(\lambda_A)_{\min} = -32.86^\circ$
$\theta = 145.58^\circ$	$(\alpha_A)_{\max} = 76.67^\circ$	$\theta = 318.43^\circ$	$(\alpha_A)_{\min} = 8^\circ$
$\theta = 153.75^\circ$	$(\phi_A)_{\min} = -23.02^\circ$	$\theta = 331.91^\circ$	$(\phi_A)_{\max} = 51.5^\circ$

$$\phi_A = 90^\circ - \alpha_A - \xi_A(\theta) \quad (3.138)$$

$$\phi_B = 90^\circ - \alpha_B - \xi_B(\theta) \quad (3.139)$$

and the shift angles can be found by

$$\lambda_A = \angle O_2 A Q_A = \sin^{-1} \left( \frac{q_A \sin \alpha_A}{\|O_2 A\|} \right) = \sin^{-1} \left( \frac{q_A \sin \alpha_A}{\|\mathbf{R}_A(\theta)\|} \right) \quad (3.140)$$

$$\lambda_B = \angle O_2 B Q_B = \sin^{-1} \left( \frac{q_B \sin \alpha_B}{\|O_2 B\|} \right) = \sin^{-1} \left( \frac{q_B \sin \alpha_B}{\|\mathbf{R}_B(\theta)\|} \right) \quad (3.141)$$

Also, the subtending angles between  $O_2 O_3$  and the contact normals,  $\alpha_A$  and  $\alpha_B$ , are both shown in Fig. 3.33(c). The cams A and B have their maximum radial dimensions of 68.008 and 72 mm, respectively, while the extremes of the angles are listed in Table 3.5.

### 3.7.2 Output Error Equations

The equivalent ten-bar linkage of this mechanism is shown in Fig. 3.30(b), in which the couplers are the added links 7 and 8 of the linkage and they respectively connect the centers of curvature of cams A and B ( $K_A$  and  $K_B$ ) and the roller centers (C and D). Also, the half joint  $J_G$  is replaced by slider 9 which connects links 3 and 5, and the half joint  $J_H$  is

replaced by slider 10 which connects links 4 and 6. Since an equivalent linkage and its original mechanism should have the same instantaneous kinematic characteristics, the instantaneous kinematic characteristics of the rockers (links 3 and 4) with respect to the driving link (link 2) shown in Fig. 3.30(b) will be identical to those of the dual primary follower with respect to the dual cams shown in Fig. 3.30(a).

For the equivalent linkage shown in Fig. 3.30(b), the input variable  $\theta_2$  is the angular displacement of the driving link; it is measured counterclockwise from the horizontal line to  $O_2K_A$ . After points  $K_A$  and  $K_B$ , the curvature centers of cams A and B, have been located, the magnitude of angle  $\theta_2$  together with the subtending angle  $\beta = \angle K_A O_2 K_B$  can be found. Also, the variables  $\theta_3$  and  $\theta_4$  can be directly determined by  $\theta_3 = 180^\circ + \alpha_f - \xi_A$  and  $\theta_4 = 180^\circ + \alpha_f - \xi_B$ . It must be emphasized that generally the magnitude of angle  $\theta_2$  is not equal to that of angle  $\theta$ , the cam rotation angle of the original mechanism. Fortunately, from the results of Section 3.3, the resulting error equations of the follower motion do not really involve the magnitudes of angles  $\theta_2$  and  $\beta$ , and thus locating the curvature centers of the cam profiles are not essential.

From the four-bar loops  $O_2K_ACO_3$  and  $O_2K_BDO_3$  of the equivalent linkage shown in Fig. 3.30(b), the constraint equations that relate design parameters  $r_{1h}$ ,  $r_{1v}$ ,  $r_{2A}$ ,  $r_{2B}$ ,  $r_{3C}$ ,  $r_{4D}$ ,  $r_7$ ,  $r_8$ , and  $\beta$  to the variables  $\theta_2$ ,  $\theta_3$ , and  $\theta_4$  may be respectively written as [10, 105]

$$G_A = 2[r_{1h}(r_{3C} \cos \theta_3 - r_{2A} \cos \theta_2) + r_{1v}(r_{3C} \sin \theta_3 - r_{2A} \sin \theta_2) - r_{2A}r_{3C} \cos(\theta_2 - \theta_3)] + r_{1h}^2 + r_{1v}^2 + r_{2A}^2 + r_{3C}^2 - r_7^2 = 0 \quad (3.142)$$

and

$$G_B = 2\{r_{1h}[r_{4D} \cos \theta_4 - r_{2B} \cos(\theta_2 + \beta)] + r_{1v}[r_{4D} \sin \theta_4 - r_{2B} \sin(\theta_2 + \beta)] - r_{2B}r_{4D} \cos(\theta_2 + \beta - \theta_4)\} + r_{1h}^2 + r_{1v}^2 + r_{2B}^2 + r_{4D}^2 - r_8^2 = 0 \quad (3.143)$$

where  $r_{1h} = O_2F = f_h$ ,  $r_{1v} = O_3F = f_v$ ,  $r_{2A} = O_2K_A$ ,  $r_{2B} = O_2K_B$ ,  $r_{3C} = O_3C = l_C$ ,  $r_{4D} = O_3D = l_D$ ,  $r_7 = K_AC$ ,  $r_8 = K_BD$ , and  $\beta = \angle K_A O_2 K_B$ . Further, by dealing with the loop closure equation of  $\mathbf{O}_2\mathbf{O}_3 + \mathbf{O}_3\mathbf{P} - \mathbf{O}_2\mathbf{P} = \mathbf{0}$ , the constraint equations relating parameters  $r_{1h}$ ,  $r_{1v}$ ,  $r_{3G}$ ,  $r_{4H}$ ,  $r_5$ ,  $r_6$ ,  $e$ ,

$\eta_A$ ,  $\eta_B$ , and  $\alpha_E$  to the dependent and output variables  $\theta_3$ ,  $\theta_4$ ,  $L_h$ , and  $L_v$  can be derived and expressed as

$$\begin{aligned}\mathbf{F} &= \begin{cases} L_h - r_5 \csc \alpha_E + r_{1h} + r_{3G} \cos(\theta_3 + \eta_A) - [L_v + r_{1v} + r_{3G} \sin(\theta_3 + \eta_A)] \cot \alpha_E \\ L_v - r_6 \csc \alpha_E + r_{1v} + r_{4H} \sin(\theta_4 + \eta_B) + [L_h + r_{1h} + r_{4H} \cos(\theta_4 + \eta_B)] \cot \alpha_E \end{cases} \\ &= \begin{pmatrix} 0 \\ 0 \end{pmatrix}\end{aligned}\quad (3.144)$$

where  $r_{3G} = O_3G = l_G$ ,  $r_{4H} = O_3H = l_H$ ,  $r_5 = l_5 + r_f$ , and  $r_6 = l_6 - r_f$ . For convenient expressions, the displacement functions of point P are designated as  $\Psi$  and defined by

$$\Psi = \begin{pmatrix} L_h(\theta) \\ L_v(\theta) \end{pmatrix}\quad (3.145)$$

The 14 design parameters  $r_{1h}$ ,  $r_{1v}$ ,  $r_{3C}$ ,  $r_{4D}$ ,  $r_{3G}$ ,  $r_{4H}$ ,  $r_5$ ,  $r_6$ ,  $r_7$ ,  $r_8$ ,  $e$ ,  $\eta_A$ ,  $\eta_B$ , and  $\alpha_E$  in the equivalent ten-bar linkage as shown in Fig. 3.30(b) are considered to have deviations. Then by applying Eq. (3.5) and recalling that  $\alpha_E = 90^\circ$ , the mechanical errors of the functional output variables,  $\Delta L_h$  and  $\Delta L_v$ , caused by the deviation of each design parameter can be expressed as

$$\begin{aligned}\Delta \Psi_{(1)} &= \begin{pmatrix} \Delta L_{h(1)} \\ \Delta L_{v(1)} \end{pmatrix} = -\left[ \frac{\partial \mathbf{F}}{\partial \Psi} \right]^{-1} \left\{ \frac{\partial \mathbf{F}}{\partial r_{1h}} \right\} \Delta r_{1h} = \begin{cases} -r_{3G} \sin(\theta_3 + \eta_A) \frac{\partial G_A / \partial r_{1h}}{\partial G_A / \partial \theta_3} - 1 \\ r_{4H} \cos(\theta_4 + \eta_B) \frac{\partial G_B / \partial r_{1h}}{\partial G_B / \partial \theta_4} \end{cases} \Delta r_{1h} \\ &= \begin{cases} -\frac{l_G \cos \gamma_A \cos(\alpha_A + \alpha_f)}{l_C \cos \phi_A} - 1 \\ \frac{l_H \cos \gamma_B \cos(\alpha_B + \alpha_f)}{l_D \cos \phi_B} \end{cases} \Delta f_h\end{aligned}\quad (3.146)$$

$$\begin{aligned}\Delta \Psi_{(2)} &= \begin{pmatrix} \Delta L_{h(2)} \\ \Delta L_{v(2)} \end{pmatrix} = -\left[ \frac{\partial \mathbf{F}}{\partial \Psi} \right]^{-1} \left\{ \frac{\partial \mathbf{F}}{\partial r_{1v}} \right\} \Delta r_{1v} = \begin{cases} -r_{3G} \sin(\theta_3 + \eta_A) \frac{\partial G_A / \partial r_{1v}}{\partial G_A / \partial \theta_3} \\ r_{4H} \cos(\theta_4 + \eta_B) \frac{\partial G_B / \partial r_{1v}}{\partial G_B / \partial \theta_4} - 1 \end{cases} \Delta r_{1v} \\ &= \begin{cases} -\frac{l_G \cos \gamma_A \sin(\alpha_A + \alpha_f)}{l_C \cos \phi_A} \\ \frac{l_H \cos \gamma_B \sin(\alpha_B + \alpha_f)}{l_D \cos \phi_B} - 1 \end{cases} \Delta f_v\end{aligned}\quad (3.147)$$

$$\Delta\boldsymbol{\Psi}_{(3)} = \begin{Bmatrix} \Delta L_{h(3)} \\ \Delta L_{v(3)} \end{Bmatrix} = - \left[ \frac{\partial \mathbf{F}}{\partial \boldsymbol{\Psi}} \right]^{-1} \left\{ \frac{\partial \mathbf{F}}{\partial r_{3C}} \right\} \Delta r_{3C} = \begin{Bmatrix} -r_{3G} \sin(\theta_3 + \eta_A) \frac{\partial G_A / \partial r_{3C}}{\partial G_A / \partial \theta_3} \\ 0 \end{Bmatrix} \Delta r_{3C} \quad (3.148)$$

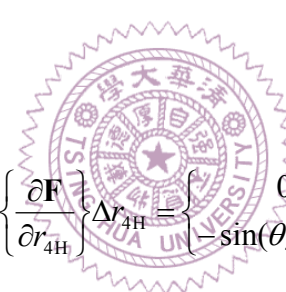
$$= \begin{Bmatrix} l_G \cos \gamma_A \tan \phi_A / l_C \\ 0 \end{Bmatrix} \Delta l_C$$

$$\Delta\boldsymbol{\Psi}_{(4)} = \begin{Bmatrix} \Delta L_{h(4)} \\ \Delta L_{v(4)} \end{Bmatrix} = - \left[ \frac{\partial \mathbf{F}}{\partial \boldsymbol{\Psi}} \right]^{-1} \left\{ \frac{\partial \mathbf{F}}{\partial r_{4D}} \right\} \Delta r_{4D} = \begin{Bmatrix} 0 \\ r_{4H} \cos(\theta_4 + \eta_B) \frac{\partial G_B / \partial r_{4D}}{\partial G_B / \partial \theta_4} \end{Bmatrix} \Delta r_{4D} \quad (3.149)$$

$$= \begin{Bmatrix} 0 \\ -l_H \cos \gamma_B \tan \phi_B / l_D \end{Bmatrix} \Delta l_D$$

$$\Delta\boldsymbol{\Psi}_{(5)} = \begin{Bmatrix} \Delta L_{h(5)} \\ \Delta L_{v(5)} \end{Bmatrix} = - \left[ \frac{\partial \mathbf{F}}{\partial \boldsymbol{\Psi}} \right]^{-1} \left\{ \frac{\partial \mathbf{F}}{\partial r_{3G}} \right\} \Delta r_{3G} = \begin{Bmatrix} -\cos(\theta_3 + \eta_A) \\ 0 \end{Bmatrix} \Delta r_{3G} \quad (3.150)$$

$$= \begin{Bmatrix} -\sin \gamma_A \\ 0 \end{Bmatrix} \Delta l_G$$



$$\Delta\boldsymbol{\Psi}_{(6)} = \begin{Bmatrix} \Delta L_{h(6)} \\ \Delta L_{v(6)} \end{Bmatrix} = - \left[ \frac{\partial \mathbf{F}}{\partial \boldsymbol{\Psi}} \right]^{-1} \left\{ \frac{\partial \mathbf{F}}{\partial r_{4H}} \right\} \Delta r_{4H} = \begin{Bmatrix} 0 \\ -\sin(\theta_4 + \eta_B) \end{Bmatrix} \Delta r_{4H} \quad (3.151)$$

$$= \begin{Bmatrix} 0 \\ \sin \gamma_B \end{Bmatrix} \Delta l_H$$

$$\Delta\boldsymbol{\Psi}_{(7)} = \begin{Bmatrix} \Delta L_{h(7)} \\ \Delta L_{v(7)} \end{Bmatrix} = - \left[ \frac{\partial \mathbf{F}}{\partial \boldsymbol{\Psi}} \right]^{-1} \left\{ \frac{\partial \mathbf{F}}{\partial r_5} \right\} \Delta r_5 = \begin{Bmatrix} 1 \\ 0 \end{Bmatrix} \Delta r_5 = \begin{Bmatrix} 1 \\ 0 \end{Bmatrix} \Delta l_5 \quad (3.152)$$

$$\Delta\boldsymbol{\Psi}_{(8)} = \begin{Bmatrix} \Delta L_{h(8)} \\ \Delta L_{v(8)} \end{Bmatrix} = - \left[ \frac{\partial \mathbf{F}}{\partial \boldsymbol{\Psi}} \right]^{-1} \left\{ \frac{\partial \mathbf{F}}{\partial r_6} \right\} \Delta r_6 = \begin{Bmatrix} 0 \\ 1 \end{Bmatrix} \Delta r_6 = \begin{Bmatrix} 0 \\ 1 \end{Bmatrix} \Delta l_6 \quad (3.153)$$

$$\Delta\boldsymbol{\Psi}_{(9)} = \begin{Bmatrix} \Delta L_{h(9)} \\ \Delta L_{v(9)} \end{Bmatrix} = - \left[ \frac{\partial \mathbf{F}}{\partial \boldsymbol{\Psi}} \right]^{-1} \left\{ \frac{\partial \mathbf{F}}{\partial r_7} \right\} \Delta r_7 = \begin{Bmatrix} -r_{3G} \sin(\theta_3 + \eta_A) \frac{\partial G_A / \partial r_7}{\partial G_A / \partial \theta_3} \\ 0 \end{Bmatrix} \Delta r_7 \quad (3.154)$$

$$= \begin{Bmatrix} l_G \cos \gamma_A / (l_C \cos \phi_A) \\ 0 \end{Bmatrix} \Delta n_A$$

$$\Delta\boldsymbol{\Psi}_{(10)} = \begin{Bmatrix} \Delta L_{h(10)} \\ \Delta L_{v(10)} \end{Bmatrix} = - \left[ \frac{\partial \mathbf{F}}{\partial \boldsymbol{\Psi}} \right]^{-1} \left\{ \frac{\partial \mathbf{F}}{\partial r_8} \right\} \Delta r_8 = \begin{Bmatrix} 0 \\ r_{4H} \cos(\theta_4 + \eta_B) \frac{\partial G_B / \partial r_8}{\partial G_B / \partial \theta_4} \end{Bmatrix} \Delta r_8 \\ = \begin{Bmatrix} 0 \\ -l_H \cos \gamma_B / (l_D \cos \phi_B) \end{Bmatrix} \Delta n_B \quad (3.155)$$

$$\Delta\boldsymbol{\Psi}_{(11)} = \begin{Bmatrix} \Delta L_{h(11)} \\ \Delta L_{v(11)} \end{Bmatrix} = - \left[ \frac{\partial \mathbf{F}}{\partial \boldsymbol{\Psi}} \right]^{-1} \left\{ \frac{\partial \mathbf{F}}{\partial e} \right\} \Delta e = \begin{Bmatrix} 0 \\ 0 \end{Bmatrix} \Delta e \quad (3.156)$$

$$\Delta\boldsymbol{\Psi}_{(12)} = \begin{Bmatrix} \Delta L_{h(12)} \\ \Delta L_{v(12)} \end{Bmatrix} = - \left[ \frac{\partial \mathbf{F}}{\partial \boldsymbol{\Psi}} \right]^{-1} \left\{ \frac{\partial \mathbf{F}}{\partial \eta_A} \right\} \Delta \eta_A = \begin{Bmatrix} r_{3G} \sin(\theta_3 + \eta_A) \\ 0 \end{Bmatrix} \Delta \eta_A \\ = \begin{Bmatrix} -l_G \cos \gamma_A \\ 0 \end{Bmatrix} \Delta \eta_A \quad (3.157)$$

$$\Delta\boldsymbol{\Psi}_{(13)} = \begin{Bmatrix} \Delta L_{h(13)} \\ \Delta L_{v(13)} \end{Bmatrix} = - \left[ \frac{\partial \mathbf{F}}{\partial \boldsymbol{\Psi}} \right]^{-1} \left\{ \frac{\partial \mathbf{F}}{\partial \eta_B} \right\} \Delta \eta_B = \begin{Bmatrix} 0 \\ -r_{4H} \cos(\theta_4 + \eta_B) \end{Bmatrix} \Delta \eta_B \\ = \begin{Bmatrix} 0 \\ l_H \cos \gamma_B \end{Bmatrix} \Delta \eta_B \quad (3.158)$$

$$\Delta\boldsymbol{\Psi}_{(14)} = \begin{Bmatrix} \Delta L_{h(14)} \\ \Delta L_{v(14)} \end{Bmatrix} = - \left[ \frac{\partial \mathbf{F}}{\partial \boldsymbol{\Psi}} \right]^{-1} \left\{ \frac{\partial \mathbf{F}}{\partial \alpha_E} \right\} \Delta \alpha_E = \begin{Bmatrix} -L_v - r_{1v} - r_{3G} \sin(\theta_3 + \eta_A) \\ L_h + r_{1h} + r_{4H} \cos(\theta_4 + \eta_B) \end{Bmatrix} \Delta \alpha_E \\ = \begin{Bmatrix} -L_v - f_v + l_G \cos \gamma_A \\ L_h + f_h - l_H \cos \gamma_B \end{Bmatrix} \Delta \alpha_E \quad (3.159)$$

The radius errors of the follower rollers may be ignored since they generally have a small tolerance grade if precision rollers are used. As can be seen from Eq. (3.156), the variation of the offset ( $\Delta e$ ) does not appear in the equation and thus will not affect the mechanical errors. By substituting Eqs. (3.9), (3.140), and (3.141) into Eqs. (3.154) and (3.155) and ignoring the radius errors of the follower rollers, the respective mechanical errors caused by the radial profile errors of cams A and B are

$$\Delta\boldsymbol{\Psi}_{(9)} = \begin{Bmatrix} \Delta L_{h(9)} \\ \Delta L_{v(9)} \end{Bmatrix} = \begin{Bmatrix} l_G \cos \gamma_A / (l_C \cos \phi_A) \\ 0 \end{Bmatrix} \Delta r_A \cos \lambda_A \quad (3.160)$$

$$\Delta \Psi_{(10)} = \begin{Bmatrix} \Delta L_{h(10)} \\ \Delta L_{v(10)} \end{Bmatrix} = \begin{Bmatrix} 0 \\ -l_H \cos \gamma_B / (l_D \cos \phi_B) \end{Bmatrix} \Delta r_B \cos \lambda_B \quad (3.161)$$

Thus, by Eqs. (3.146)~(3.153) and (3.156)~(3.161), the worst case deviations of the functional outputs will be

$$\Delta \Psi_{\text{wor}} = \begin{Bmatrix} \Delta L_{h, \text{wor}} \\ \Delta L_{v, \text{wor}} \end{Bmatrix} = \begin{Bmatrix} \sum_{i=1}^{14} |\Delta L_{h(i)}| \\ \sum_{i=1}^{14} |\Delta L_{v(i)}| \end{Bmatrix} \quad (3.162)$$

and the maximum expected deviations of the functional outputs will be

$$\Delta \Psi_{\text{rss}} = \begin{Bmatrix} \Delta L_{h, \text{rss}} \\ \Delta L_{v, \text{rss}} \end{Bmatrix} = \begin{Bmatrix} \sqrt{\sum_{i=1}^{14} (\Delta L_{h(i)})^2} \\ \sqrt{\sum_{i=1}^{14} (\Delta L_{v(i)})^2} \end{Bmatrix} \quad (3.163)$$

### 3.7.3 Mechanical Error Analysis Results



The error equations of the planar cam-follower type pick-and-place device derived in Sub-section 3.7.2 are applied for actually predicting motion deviations of its functional outputs with specified deviations of the design parameters. For a tolerance grade of IT6, the 14 design parameters may have deviations of  $\Delta f_h = \Delta f_v = \Delta l_C = \Delta l_D = \Delta r_A = \Delta r_B = 19 \mu\text{m}$ ,  $\Delta l_G = \Delta l_5 = \Delta l_6 = 29 \mu\text{m}$ ,  $\Delta l_H = 25 \mu\text{m}$ ,  $\Delta e = 22 \mu\text{m}$ ,  $\Delta \eta_A = 0.019^\circ = 3.32 \times 10^{-4} \text{ rad}$ ,  $\Delta \eta_B = 0.011^\circ = 1.92 \times 10^{-4} \text{ rad}$ , and  $\Delta \alpha_E = 0.022^\circ = 3.84 \times 10^{-4} \text{ rad}$ . Based on the derived error equations, only  $\Delta f_h$ ,  $\Delta f_v$ , and  $\Delta \alpha_E$  will lead to both horizontal and vertical output errors simultaneously. The deviations  $\Delta r_A$ ,  $\Delta l_C$ ,  $\Delta l_G$ ,  $\Delta l_5$ , and  $\Delta \eta_A$  will only lead to the horizontal output error, and the deviations  $\Delta r_B$ ,  $\Delta l_D$ ,  $\Delta l_H$ ,  $\Delta l_6$ , and  $\Delta \eta_B$  will only lead to the vertical output error. The deviation of the offset ( $\Delta e$ ) has no effect on the mechanical errors.

All functions of the prediction results that might be of interest are shown in Fig. 3.34. Figure 3.34(a) shows the resultant mechanical errors of the horizontal displacement of

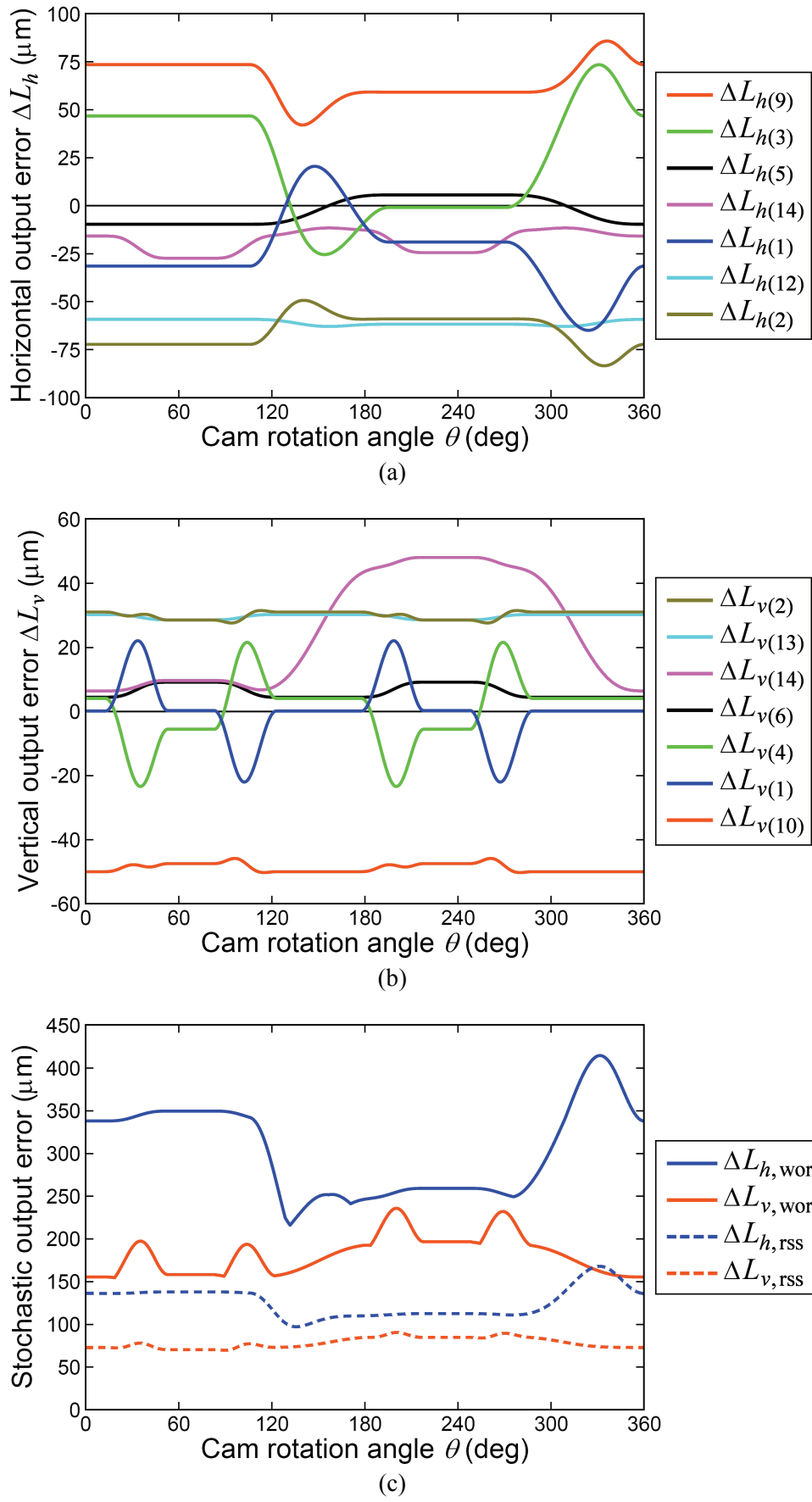


**Figure 3.34** Mechanical error analysis results of a planar cam-follower type pick-and-place device.

point P arising from each dimensional deviation. Because  $\Delta L_{h(4)} = \Delta L_{h(6)} = \Delta L_{h(8)} = \Delta L_{h(10)} = \Delta L_{h(11)} = \Delta L_{h(13)} = 0$  and  $\Delta L_{h(7)} = \Delta l_5 = 29 \mu\text{m}$  are invariant, they are not shown in Fig. 3.34(a). The seven error functions shown in Fig. 3.34(a) can be further divided into six types by their trends. Firstly,  $\Delta L_{h(12)}$  (caused by  $\Delta \eta_A$ ) apparently has only slight variation. Since from Eq. (3.157), the trend of  $\Delta L_{h(12)}$  is dominated by  $\cos \gamma_A$ , which also has only slight variation while  $\gamma_A$  varies only from about  $-10^\circ$  to  $20^\circ$  as shown in Fig. 3.31(c). That is, other error equations involving  $\cos \gamma_A$  are also slightly influenced by this factor. Secondly,  $\Delta L_{h(2)}$  (caused by  $\Delta f_v$ ) and  $\Delta L_{h(9)}$  (caused by  $\Delta r_A$ ) have almost the same trend and extreme position when their signs are ignored. As shown in Figs. 3.33(b) and 3.33(c),  $\alpha_A$  and  $\lambda_A$  have quite similar trends. Thus, from Eqs. (3.147) and (3.160),  $[\sin(\alpha_A + \alpha_f)/\cos \phi_A]$  and  $(\cos \lambda_A/\cos \phi_A)$  are proportional to each other. Thirdly, the trend of  $\Delta L_{h(1)}$  (caused by  $\Delta f_h$ ) mainly dominated by  $[\cos(\alpha_A + \alpha_f)/\cos \phi_A]$  is similar to that of  $\alpha_A$  as shown in Fig. 3.33(c). Fourthly,  $\Delta L_{h(3)}$  (caused by  $\Delta l_C$ ) mainly dominated by  $\tan \phi_A$  is proportional to pressure angle  $\phi_A$ . Fifthly, the trend of  $\Delta L_{h(5)}$  (caused by  $\Delta l_G$ ) is proportional to that of  $\sin \gamma_A$ . Finally, the trend of  $\Delta L_{h(14)}$  (caused by  $\Delta \alpha_E$ ) mainly dominated by the vertical displacement function  $L_v$  is similar to that of  $S_v$  as shown in Fig. 3.31(a) when their signs are ignored. An important effect of  $\Delta L_{h(14)}$  is that it appears variant motion error during horizontal dwells, while the others appear invariant ones. As can be seen,  $\Delta r_A$ ,  $\Delta f_v$ , and  $\Delta \eta_A$  have the most effects on the output error  $\Delta L_h$ , while  $\Delta f_h$  and  $\Delta l_C$  have the secondary effects.

Similarly, Fig. 3.34(b) shows the resultant mechanical errors of the vertical displacement of point P arising from each dimensional deviation. Because  $\Delta L_{v(3)} = \Delta L_{v(5)} = \Delta L_{v(7)} = \Delta L_{v(9)} = \Delta L_{v(11)} = \Delta L_{v(12)} = 0$  and  $\Delta L_{v(8)} = \Delta l_6 = 29 \mu\text{m}$  are invariant, they are not shown in Fig. 3.34(b). The seven error functions shown in Fig. 3.34(b) can also be further divided into six types by their trends, just like those shown in Fig. 3.34(a). Firstly,  $\Delta L_{v(13)}$  (caused by  $\Delta \eta_B$ ) obviously has only slight variation. Since from Eq. (3.158), the trend of  $\Delta L_{v(13)}$  is dominated by  $\cos \gamma_B$ , which also has only slight variation while  $\gamma_B$  varies only from about  $10^\circ$  to  $20^\circ$  as shown in Fig. 3.31(c). Hence, other error equations involving

$\cos\gamma_B$  are also slightly influenced by this factor. Secondly,  $\Delta L_{v(2)}$  (caused by  $\Delta f_v$ ) and  $\Delta L_{v(10)}$  (caused by  $\Delta r_B$ ) have almost the same trend and extreme position when their signs are ignored. As shown in Figs. 3.33(b) and 3.33(c),  $\alpha_B$  and  $\lambda_B$  have quite similar trends. Thus, from Eqs. (3.146) and (3.161),  $[\sin(\alpha_B + \alpha_f)/\cos\phi_B]$  and  $(\cos\lambda_B/\cos\phi_B)$  are proportional to each other. Also, because the variations of  $\sin(\alpha_B + \alpha_f)$  and  $\cos\lambda_B$  are both flattened by  $(1/\cos\phi_B)$ , the magnitudes of  $\Delta L_{v(2)}$  and  $\Delta L_{v(10)}$  have only slight variations. Thirdly, the trend of  $\Delta L_{v(1)}$  (caused by  $\Delta f_h$ ) mainly dominated by  $[\cos(\alpha_B + \alpha_f)/\cos\phi_B]$  is similar to that of  $\alpha_B$  as shown in Fig. 3.33(c). Fourthly,  $\Delta L_{v(4)}$  (caused by  $\Delta l_D$ ) mainly dominated by  $\tan\phi_B$  is proportional to pressure angle  $\phi_B$ . Fifthly,  $\Delta L_{v(6)}$  (caused by  $\Delta l_H$ ) is proportional to that of  $\sin\gamma_B$ . Finally, the trend of  $\Delta L_{v(14)}$  (caused by  $\Delta \alpha_E$ ) mainly dominated by the horizontal displacement function  $L_h$  is similar to that of  $S_h$  as shown in Fig. 3.31(a) when their signs are ignored. An important effect of  $\Delta L_{v(14)}$  is that it appears variant motion error during vertical dwells, while the others appear invariant ones. As can be seen,  $\Delta r_B$  has the most effect on the output error  $\Delta L_v$ , while  $\Delta f_v$ ,  $\Delta \eta_B$ , and  $\Delta \alpha_E$  have the secondary effects.

Interestingly, the mechanical error  $\Delta L_{h(9)}$  caused by the cam profile error  $\Delta r_A$  may be compensated by the mechanical error  $\Delta L_{h(2)}$  caused by the vertical center distance error  $\Delta f_v$ . The mechanical error  $\Delta L_{v(10)}$  caused by the cam profile error  $\Delta r_B$  may also be compensated by the mechanical error  $\Delta L_{v(2)}$  caused by  $\Delta f_v$ . That is, the mechanical errors caused by the cam profile errors may be reduced to the smallest by properly adjusting the vertical center distance error to an optimal value by some center distance adjustment means.

As shown in Fig. 3.34(c), the extreme value of  $\Delta L_{h,wor}$  occurring at  $\theta = 331.68^\circ$  is 414.47  $\mu\text{m}$ , the extreme value of  $\Delta L_{h,rss}$  occurring at  $\theta = 331.42^\circ$  is 167.81  $\mu\text{m}$ ; both are very close to  $\theta = 331.91^\circ$ , where the extreme pressure angle  $\phi_A$  occurs. Also, the extreme value of  $\Delta L_{v,wor}$  occurring at  $\theta = 200.42^\circ$  is 235.69  $\mu\text{m}$ , and the extreme value of  $\Delta L_{v,rss}$  occurring at  $\theta = 200.72^\circ$  is 90.4  $\mu\text{m}$ ; both are very close to 200.63 $^\circ$ , where the extreme pressure angle  $\phi_B$  occurs. From the viewpoint of the position accuracy of the functional

outputs, for total end-effector travels of 100 mm in horizontal direction and 30 mm in vertical direction, position deviations of  $\Delta L_{h,\max} = 414.47 \mu\text{m}$  and  $\Delta L_{v,\max} = 235.69 \mu\text{m}$  imply a quite low accuracy. That is, if the worst situation occurs, although the design parameters are specified to have a small tolerance grade of IT6, the horizontal functional output will have a degraded accuracy ranging from IT12 (350  $\mu\text{m}$ ) to IT13 (540  $\mu\text{m}$ ), and the vertical functional output will also have a degraded accuracy ranging from IT12 (210  $\mu\text{m}$ ) to IT13 (330  $\mu\text{m}$ ). Even for better, the maximum expected deviations of the horizontal and vertical functional outputs will still lead to a degraded accuracy ranging from IT10 (140 and 84  $\mu\text{m}$  for each direction) to IT11 (220 and 130  $\mu\text{m}$  for each direction).

In addition, the relative accuracy of the expected positions between the low and high dwells of the end-effector, i.e., the operating accuracy of the mechanism, dominates the operating performance of the pick-and-place device. To maintain and improve operating accuracy of the pick-and-place device should be of concern for designers. When considering the maximum expected deviations, the relative deviations between the low and high dwells of the horizontal and vertical functional outputs are merely 25.41 and 14.13  $\mu\text{m}$ , respectively. Such slight deviations imply an acceptable operating accuracy of the mechanism ranging from IT6 (22 and 13  $\mu\text{m}$  for each direction) to IT7 (35 and 21  $\mu\text{m}$  for each direction). The operating performance of the pick-and-place device can thus be maintained when its all design parameters are specified to have a tolerance grade of IT6.

### 3.8 CONCLUDING REMARKS

The displacement, velocity, and acceleration errors of the follower motion arising from the variation in each design parameter can be determined analytically. The resulting error equations do not really involve the location of the curvature center of the cam profile, and thus locating the curvature center of the cam profile is not essential. The method is validated through analyzing a cam mechanism that has an invariant equivalent linkage, and

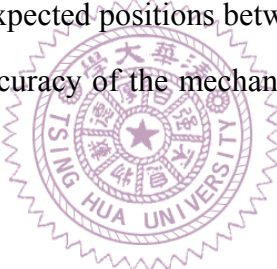
thus an exact solution is available. As compared to the exact solutions, the results predicted by the presented method can have at least a relative accuracy of 99.99% when the cam profile is specified to have a tolerance grade of IT6. Even the cam profile is specified to have a very large tolerance grade of IT13, the method can still provide at least a relative accuracy of 99%. Also, through an exaggerated case whose relatively large profile error is assumed to be caused by adopting an incorrect follower motion program, the cam profile errors evaluated by using the shift angle can have at least a relative accuracy of 93% when compared with their exact values calculated numerically. Although the extreme cam profile errors in the exaggerated case have a quite large tolerance grade ranging from IT16 to IT17, such a relative accuracy of 93% shows acceptable reliability of using the shift angle to correlate the radial-dimension error and the normal-direction error of the cam profile. That is, the equivalent linkage method can have sufficient accuracy from an engineering viewpoint.

For the roller follower cases, the pressure angle has the most dominating effect on the resulting error, and the larger pressure angle will result in the larger mechanical error. The pressure angle and the shift angle have quite similar trends. Owing to the counteraction of the shift angle, the resulting error caused by the error of the cam profile in the radial direction has relatively smaller variation. In the worst case, owing to the joined effects of various design parameters, the accuracy of the follower motion may degrade considerably. The extreme values of the worst-case and maximum-expected position deviations occur very close to where the extreme pressure angle occurs. The acceleration error functions have a sudden change at each beginning and end of the motion even though the theoretical follower displacement is cycloidal motion.

For the flat-faced follower cases, the resulting errors are also significantly affected by the pressure angle, and the larger pressure angle will result in the larger mechanical error. In the worst case, owing to the joined effects of various design parameters, the accuracy of the follower motion may also degrade considerably. For the oscillating flat-faced follower case, all acceleration error functions have a sudden change at each beginning and end of

the motion even though the theoretical follower displacement is cycloidal motion. However, for the translating flat-faced follower case, neither the error of the cam profile nor the variation of offset amount will cause sudden change of the acceleration error function. This implies that a translating flat-faced follower is a potentially superior choice to the other types of followers for generating smoother motions.

A practical case study of analyzing the mechanical errors of the MEG X6061 planar cam-follower type pick-and-place device, a planar six-link cam-linkage combined mechanism, is successfully performed. It is again found that the extreme values of the worst-case and maximum expected deviations of the functional outputs occur very close to where the extreme pressure angles occur. In the worst case, owing to the joined effects of various design parameters, the accuracy of the functional outputs may degrade considerably when the design parameters are specified to have a tolerance grade of IT6. But, the relative accuracy of the expected positions between the low and high dwells of the end-effector, i.e., the operating accuracy of the mechanism, can maintain at an acceptable level.



# CHAPTER 4

## OPTIMAL TOLERANCE ALLOCATION FOR DISK CAM MECHANISMS

### 4.1 INTRODUCTION

Once the theoretical model for the mechanical error analysis of a disk cam mechanism is established, its tolerance allocation can be dealt with by using optimal procedures. As mentioned in Sub-section 1.2.1, several procedures for the optimal tolerance allocation of cam mechanisms have been suggested by considering the minimum production cost [17, 18, 65, 66, 72]. As compared to employing the production cost as the criterion for searching the optimal tolerance combination for cam mechanisms, considering the concept of design for manufacture and assembly (DFMA) [95-98] should be more appropriate in the theoretical design phase. Generally, lowering the production cost and improving the manufacturability and assembly of parts are similar concepts in essence. Based on the concept of DFMA, the modeling of manufacturability-tolerance and assembly-tolerance relationships may be more easily and explicitly performed by designers. Hence, to help designers in more appropriately allocating tolerances, an alternative means for optimal tolerance allocation with maximization of the manufacturability and assembly of disk cam mechanisms as the objective is introduced in this chapter. A practical case study is correspondingly given to illustrate the optimal procedure presented.

### 4.2 FUNDAMENTALS OF THE OPTIMAL TOLERANCE ALLOCATION

One of the practical considerations in designing a cam mechanism is the optimal tolerance allocation of each design parameter to achieve the desired kinematic accuracy of

the follower motion [17, 18, 65, 66, 72]. The optimal objective can either be the minimum production cost or the maximum manufacturability and assembly. The latter is based on the consideration of DFMA and aims to achieve the lowest level of difficulty of manufacturing and assembling cam mechanisms at the design stage. By incorporating the equivalent linkage method presented in Chapter 3 and the concept of DFMA, the procedure for optimal tolerance allocation with maximization of the manufacturability and assembly of disk cam mechanisms as the objective is developed in this section.

#### 4.2.1 The Manufacturability and Assembly Indices

Every manufacturing and assembly error may affect the accuracy of the follower motion, and the specified tolerance of each design parameter has its own respective cost. Lower costs imply a lower level of difficulty in the manufacture and assembly of cam mechanisms. In order to optimally allocate the tolerances of the design parameters of a disk cam mechanism, the cost of each manufacturing and assembly tolerance must be evaluated. Therefore, the deviations of the design parameters of a disk cam mechanism are classified as the errors arising from manufacturing and the errors arising from assembly. Their respective costs are indirectly evaluated by means of the manufacturability and assembly of disk cam mechanisms, and the quantitative correlation model between manufacturability versus tolerance and assembly versus tolerance must be established first.

Considering that there are  $n$  theoretical design parameters ( $r_1, r_2, \dots, r_n$ ) in a cam mechanism, for all the  $n$  dimensional tolerances ( $\Delta r_1, \Delta r_2, \dots, \Delta r_n$ ), they can be divided into two groups:  $h$  manufacturing tolerances ( $\Delta r_{M1}, \Delta r_{M2}, \dots, \Delta r_{Mh}$ ) and  $k$  assembly tolerances ( $\Delta r_{A1}, \Delta r_{A2}, \dots, \Delta r_{Ak}$ ) where  $n = h + k$ . Here, the manufacturing tolerances ( $\Delta r_{M1}, \Delta r_{M2}, \dots, \Delta r_{Mh}$ ) refer to the allowable deviations of the design parameters assigned for manufacturing inaccuracy, such as the radial-dimension tolerance of the cam profile. On the other hand, the assembly tolerances ( $\Delta r_{A1}, \Delta r_{A2}, \dots, \Delta r_{Ak}$ ) refer to the allowable deviations of the design parameters assigned for assembly misalignment, such as the tolerance amount for the

center distance between the cam and follower pivots or the tolerance amount for the follower offset. In other words, a manufacturing tolerance is assigned to the dimension of a design parameter that can quantitate the geometric characteristic of one rigid member, while an assembly tolerance is assigned to the dimension of a design parameter that can quantitate the geometric correlation between assembled rigid members. (It must be emphasized that fits for assembled members are not considered in the optimal procedure because they have already been standardized. In fact, the effects of fits for assembled members on influencing assembly tolerances can also be included if necessary.) Accordingly, a manufacturability index, MI, quantitatively modeling the level of difficulty of manufacturing members in a cam mechanism is defined as

$$MI \equiv \sum_{i=1}^h w_{Mi} |\Delta r_{Mi}| \text{ for } \sum_{i=1}^h w_{Mi} = 1 \text{ and } 0 < w_{Mi} < 1 \quad (4.1)$$

Additionally, an assembly index, AI, quantitatively modeling the level of difficulty of assembling members in a cam mechanism is defined as

$$AI \equiv \sum_{i=1}^k w_{Ai} |\Delta r_{Ai}| \text{ for } \sum_{i=1}^k w_{Ai} = 1 \text{ and } 0 < w_{Ai} < 1 \quad (4.2)$$

in which the coefficients ( $w_{M1}, w_{M2}, \dots, w_{Mh}$ ) and ( $w_{A1}, w_{A2}, \dots, w_{Ak}$ ) are the specified weighting factors that reveal the extents of manufacturability and assembly influenced by their respective tolerances. The indices MI and AI that can be respectively expressed in an exchanged consistent unit are employed here to quantitatively indicate the subtotal extent of the manufacturability and assembly when a disk cam mechanism is fabricated; the larger the specified tolerances, the more obtainable the manufacturability and assembly. Similarly, the magnitude of each weighting factor ( $w_{M1}, w_{M2}, \dots, w_{Mh}$ ) and ( $w_{A1}, w_{A2}, \dots, w_{Ak}$ ) quantitatively indicate that the larger the weighting factor specified to the tolerance amount of a design parameter, the more obtainable the manufacturability or assembly of this dimension. Hence, these weighting factors actually involve the information of manufacturing and assembly processes and their required effort and time. Thus, a larger weighting factor should be specified to the tolerance amount of a design

parameter that needs more complicated and expensive processes to achieve.

To simultaneously maximize the manufacturability (MI) and the assembly (AI) of a cam mechanism, a comprehensive index, CI, for quantitatively modeling the level of difficulty of manufacturing and assembling members in a cam mechanism, as the objective function of the optimization can be defined as

$$\begin{aligned} \text{CI} &= \text{CI}(\Delta r_1, \Delta r_2, \dots, \Delta r_n) \\ &\equiv w_{C,M} \text{MI} + w_{C,A} \text{AI} = \sum_{i=1}^h (w_{C,M} w_{Mi}) |\Delta r_{Mi}| + \sum_{i=1}^k (w_{C,A} w_{Ai}) |\Delta r_{Ai}| \end{aligned} \quad (4.3)$$

where

$$w_{C,M} + w_{C,A} = 1, \quad 0 < w_{C,M} < 1, \quad \text{and} \quad 0 < w_{C,A} < 1 \quad (4.4)$$

In these equations, the weighting factors  $w_{C,M}$  and  $w_{C,A}$  are respectively assigned to MI and AI to combine them into a single index for the multiobjective problem [107]. The comprehensive index, CI, can also be expressed in an exchanged consistent unit. The weighting factors  $w_{C,M}$  and  $w_{C,A}$  involve information on the relative complexity between the overall manufacturing and assembly processes, as well as their relative importance on influencing the expected overall production cost or time. The magnitude of these weighting factors can be assigned to MI and AI via the designers' judgements and experience. Practically, the factor  $w_{C,M}$  should be greater since the manufacturing processes may be more complicated than the assembly processes.

#### 4.2.2 The Optimization Model

As mentioned earlier, the optimal tolerance allocation for a cam mechanism is the maintenance of acceptable accuracy of its follower output motion with maximum manufacturability and assembly. In practice, considering the  $j$ -th maximum expected deviation function  $\Delta\psi_{j,\text{rss}}(\boldsymbol{\Theta})$  of the follower outputs shown in Eq. (3.8), its maximum value  $(\Delta\psi_{j,\text{rss}})_{\max}$  cannot exceed a specified upper bound,  $\Delta\psi_j^{(u)}$ . Also, the difference between the maximum and minimum values of  $\Delta\psi_{j,\text{rss}}(\boldsymbol{\Theta})$ ,  $(\Delta\psi_{j,\text{rss}})_{\max}$  and  $(\Delta\psi_{j,\text{rss}})_{\min}$ , must be smaller

than another specified upper bound,  $\delta_{\psi_j}^{(u)}$ , in order to maintain the relative accuracy of the expected positions of the follower, especially the relative accuracy of the positions between the low and high dwells. According to the comprehensive index, CI, defined in Eq. (4.3), the optimization model can be formulated as follows:

$$\text{find } \mathbf{X} = \begin{Bmatrix} \Delta r_1 \\ \Delta r_2 \\ \vdots \\ \Delta r_n \end{Bmatrix}$$

which maximize

$$f(\mathbf{X}) = \text{CI}(\Delta r_1, \Delta r_2, \dots, \Delta r_n) \quad (4.5)$$

subject to

$$(\Delta\psi_{j,\text{rss}})_{\max} \leq \Delta\psi_j^{(u)} \text{ for } j = 1, 2, \dots, m \quad (4.6)$$

$$\delta_{\psi_j} = (\Delta\psi_{j,\text{rss}})_{\max} - (\Delta\psi_{j,\text{rss}})_{\min} \leq \delta_{\psi_j}^{(u)} \text{ for } j = 1, 2, \dots, m \quad (4.7)$$

$$\Delta r_i^{(l)} \leq \Delta r_i \leq \Delta r_i^{(u)} \text{ for } i = 1, 2, \dots, n \quad (4.8)$$

in which,  $\Delta r_i^{(l)}$  and  $\Delta r_i^{(u)}$  respectively denote the lower and upper bounds on the  $i$ -th dimensional tolerance,  $\Delta r_i$ , in a cam mechanism. The evaluation of the extreme values  $(\Delta\psi_{j,\text{rss}})_{\max}$  and  $(\Delta\psi_{j,\text{rss}})_{\min}$  shown in Eqs. (4.6) and (4.7) is based on the sensitivity analysis method provided in Section 3.1, hence the sensitivity of each dimensional tolerance on influencing the output deviations of the cam mechanism can also be considered in the proposed optimization model. The optimization model shows a typical constrained optimization problem that must be solved numerically [107]. Existing package software, such as the MATLAB Optimization Toolbox [108], can be utilized to perform the computation.

## 4.3 A PRACTICAL CASE STUDY

The optimal procedure established in Section 4.2 is illustrated by a practical case study. The optimal tolerance allocation of the MEG X6061 planar cam-follower type pick-and-place device [106] (as shown in Figs. 3.29 and 3.30), whose mechanical error analysis has been undertaken in Section 3.7, is performed in this section.

### 4.3.1 Optimization Problem Description

According to the optimization model presented in Section 4.2, the 14 dimensional tolerances  $\Delta f_h$ ,  $\Delta f_v$ ,  $\Delta l_C$ ,  $\Delta l_D$ ,  $\Delta l_G$ ,  $\Delta l_H$ ,  $\Delta l_5$ ,  $\Delta l_6$ ,  $\Delta r_A$ ,  $\Delta r_B$ ,  $\Delta e$ ,  $\Delta \eta_A$ ,  $\Delta \eta_B$ , and  $\Delta \alpha_E$  of the MEG X6061 pick-and-place device desired to be optimized are divided into manufacturing and assembly tolerances. Their corresponding weighting factors and lower and upper bounds

**Table 4.1** Weighting factors and lower and upper bounds of tolerances.

Tolerance	Weighting factors		Lower bound	Upper bound
	$w_{Mi}$ or $w_{Ai}$	$(w_{C,M}w_{Mi})$ or $(w_{C,A}w_{Ai})$		
Assignment for manufacturing tolerances (with $w_{C,M} = 0.9$ )				
$\Delta l_C$	0.012	0.0108	0.002 mm	0.3 mm
$\Delta l_D$	0.012	0.0108	0.002 mm	0.3 mm
$\Delta l_G$	0.013	0.0117	0.0045 mm	0.46 mm
$\Delta l_H$	0.013	0.0117	0.0035 mm	0.4 mm
$\Delta l_5$	0.06	0.054	0.0045 mm	0.46 mm
$\Delta l_6$	0.06	0.054	0.0045 mm	0.46 mm
$\Delta r_A$	0.4	0.36	0.002 mm	0.3 mm
$\Delta r_B$	0.4	0.36	0.002 mm	0.3 mm
$\Delta \eta_A$	0.015	0.0135	0.002°	0.3°
$\Delta \eta_B$	0.015	0.0135	0.0012°	0.18°
Assignment for assembly tolerances (with $w_{C,A} = 0.1$ )				
$\Delta f_h$	0.3	0.03	0.002 mm	0.3 mm
$\Delta f_v$	0.3	0.03	0.002 mm	0.3 mm
$\Delta e$	0.1	0.01	0.0025 mm	0.35 mm
$\Delta \alpha_E$	0.3	0.03	0.0025°	0.35°

are given in Table 4.1. In this case, according to the cause of these tolerance amounts, the four tolerances  $\Delta f_h$ ,  $\Delta f_v$ ,  $\Delta e$ , and  $\Delta \alpha_E$  are allocated for assembly, while the other 10 tolerances are allocated for manufacturing. After roughly estimating the overall manufacturing and assembly processes and their required costs and times, the weighting factors  $w_{C,M}$  and  $w_{C,A}$  for this case are reasonably given as 0.9 and 0.1, respectively. The weighting factors of the radial cam profile tolerances are undoubtedly much greater than those of other tolerances since the cam profiles must be accurately machined and inspected with relatively complicated procedures. In fact, for different manufacturers, the weighting factors listed in Table 4.1 may be modified via their estimation. The lower and upper bounds on each tolerance are respectively based on the tolerance grades of IT1 and IT12 for their corresponding dimensions of design parameters. Note that the lower and upper bounds on the radial profile tolerances of cams A and B ( $\Delta r_A$  and  $\Delta r_B$ ) are based on the tolerances of their corresponding maximum radial dimensions.

Recall from Fig. 3.31(b) that the pick-and-place device is used to convey objects between the two working positions  $P_2$  and  $P_7$ ; thus, the relative accuracy between the two positions dominates the operating performance of this device. Hence, the relative variation of the horizontal output motion error  $\delta_{L_h} [= (\Delta L_{h,rss})_{\max} - (\Delta L_{h,rss})_{\min}]$  and that of the vertical output motion error  $\delta_{L_v} [= (\Delta L_{v,rss})_{\max} - (\Delta L_{v,rss})_{\min}]$  must be controlled in small amounts. Moreover, the maximum output errors  $(\Delta L_{h,rss})_{\max}$  and  $(\Delta L_{v,rss})_{\max}$  can be larger since they may be reduced by slightly adjusting the fixed location of the clamping device attached on the end-effector of the pick-and-place device. For this case, the upper bounds on the maximum output deviations are respectively given as follows:  $\Delta L_h^{(u)} = 0.22$  mm and  $\Delta L_v^{(u)} = 0.13$  mm, based on a large tolerance grade of IT11 for the corresponding horizontal and vertical strokes of point P, which are 100 and 30 mm, respectively. Also, for a tolerance grade of IT7 of the horizontal and vertical strokes, the upper bounds on the relative accuracy of the output motions are respectively given as  $\delta_{L_h}^{(u)} = 0.035$  mm and

$\delta_{L_v}^{(u)} = 0.021$  mm. Accordingly, the optimization model can be formulated as follows:

$$\text{find } \mathbf{X} = \{\Delta f_h, \Delta f_v, \Delta l_C, \Delta l_D, \Delta l_G, \Delta l_H, \Delta l_5, \Delta l_6, \Delta r_A, \Delta r_B, \Delta e, \Delta \eta_A, \Delta \eta_B, \Delta \alpha_E\}^T$$

which maximize

$$f(\mathbf{X}) = \text{CI}(\Delta f_h, \Delta f_v, \Delta l_C, \Delta l_D, \Delta l_G, \Delta l_H, \Delta l_5, \Delta l_6, \Delta r_A, \Delta r_B, \Delta e, \Delta \eta_A, \Delta \eta_B, \Delta \alpha_E) \quad (4.9)$$

subject to

$$(\Delta L_{h, \text{rss}})_{\max} \leq \Delta L_h^{(u)} \quad (4.10)$$

$$(\Delta L_{v, \text{rss}})_{\max} \leq \Delta L_v^{(u)} \quad (4.11)$$

$$\delta_{L_h} = (\Delta L_{h, \text{rss}})_{\max} - (\Delta L_{h, \text{rss}})_{\min} \leq \delta_{L_h}^{(u)} \quad (4.12)$$

$$\delta_{L_v} = (\Delta L_{v, \text{rss}})_{\max} - (\Delta L_{v, \text{rss}})_{\min} \leq \delta_{L_v}^{(u)} \quad (4.13)$$

$$\Delta f_h^{(l)} \leq \Delta f_h \leq \Delta f_h^{(u)} \quad (4.14)$$

$$\Delta f_v^{(l)} \leq \Delta f_v \leq \Delta f_v^{(u)} \quad (4.15)$$

$$\Delta l_C^{(l)} \leq \Delta l_C \leq \Delta l_C^{(u)} \quad (4.16)$$

$$\Delta l_D^{(l)} \leq \Delta l_D \leq \Delta l_D^{(u)} \quad (4.17)$$

$$\Delta l_G^{(l)} \leq \Delta l_G \leq \Delta l_G^{(u)} \quad (4.18)$$

$$\Delta l_H^{(l)} \leq \Delta l_H \leq \Delta l_H^{(u)} \quad (4.19)$$

$$\Delta l_5^{(l)} \leq \Delta l_5 \leq \Delta l_5^{(u)} \quad (4.20)$$

$$\Delta l_6^{(l)} \leq \Delta l_6 \leq \Delta l_6^{(u)} \quad (4.21)$$

$$\Delta r_A^{(l)} \leq \Delta r_A \leq \Delta r_A^{(u)} \quad (4.22)$$

$$\Delta r_B^{(l)} \leq \Delta r_B \leq \Delta r_B^{(u)} \quad (4.23)$$

$$\Delta e^{(l)} \leq \Delta e \leq \Delta e^{(u)} \quad (4.24)$$

$$\Delta\eta_A^{(l)} \leq \Delta\eta_A \leq \Delta\eta_A^{(u)} \quad (4.25)$$

$$\Delta\eta_B^{(l)} \leq \Delta\eta_B \leq \Delta\eta_B^{(u)} \quad (4.26)$$

$$\Delta\alpha_E^{(l)} \leq \Delta\alpha_E \leq \Delta\alpha_E^{(u)} \quad (4.27)$$

where the maximum expected deviations  $\Delta L_{h,\text{rss}}$  and  $\Delta L_{v,\text{rss}}$  shown in Eqs. (4.10)~(4.13) can be referred to in Eq. (3.163).

### 4.3.2 Optimization Process and Results

The MATLAB Optimization Toolbox [108] is utilized to solve the constrained optimization problem. The sequential quadratic programming (SQP) method on the basis of evaluating the Kuhn-Tucker (KT) conditions is used to search the optimal solution. Lagrange multipliers are computed directly by this method to balance the derivations in magnitude of the objective function and the constraint gradients since only active constraints should be included in the KT conditions. This method is characterized by closely imitating Newton's method for constrained optimization problems just as is done for unconstrained optimization problems. At each major iteration, the Hessian matrix of the Lagrange function is approximated by using a quasi-Newton updating procedure, in which the modified Broyden-Fletcher-Goldfarb-Shanno (BFGS) formula is employed to calculate the Hessian matrix. Then a quadratic programming (QP) subproblem is generated and solved. The solution of the QP subproblem is used to form a search direction for a line search procedure. Using the search direction, a step length which is sufficient to increase a merit function is determined. (The merit function must be increased if the objective function is expected to be maximized. On the contrary, the merit function must be decreased if the objective function is expected to be minimized.)

For the implementation of the SQP method, the convergence tolerances for the numerical evaluation of the design variables, the constraint violation and the objective function are given as  $1 \times 10^{-8}$ ,  $1 \times 10^{-8}$ , and  $1 \times 10^{-10}$ , respectively. The initial values of the 14 dimensional tolerances, namely the initial design variables, are listed in Table 4.2,

**Table 4.2** Initial design and computation results for the optimization.

Term	Initial value	Optimization result	Active constraint	Tolerance grade
$\Delta l_C$	0.019 mm	0.002 mm	Yes	IT1
$\Delta l_D$	0.019 mm	0.01179 mm	No	IT4~IT5
$\Delta l_G$	0.029 mm	0.19455 mm	No	IT10~IT11
$\Delta l_H$	0.025 mm	0.10422 mm	No	IT9~IT10
$\Delta l_5$	0.029 mm	0.17104 mm	No	IT9~IT10
$\Delta l_6$	0.029 mm	0.04519 mm	No	IT6~IT7
$\Delta r_A$	0.019 mm	0.02754 mm	No	IT6~IT7
$\Delta r_B$	0.019 mm	0.04511 mm	No	IT7~IT8
$\Delta \eta_A$	0.019°	0.00477°	No	IT2~IT3
$\Delta \eta_B$	0.011°	0.00162°	No	IT1~IT2
$\Delta f_h$	0.019 mm	0.00481 mm	No	IT2~IT3
$\Delta f_v$	0.019 mm	0.00208 mm	No	IT1~IT2
$\Delta e$	0.022 mm	0.35 mm	Yes	IT12
$\Delta \alpha_E$	0.022°	0.00534°	No	IT2~IT3
$(\Delta L_{h,\text{rss}})_{\max}$	0.16781 mm	0.22 mm	Yes	IT11
$(\Delta L_{v,\text{rss}})_{\max}$	0.09040 mm	0.13 mm	Yes	IT11
$\delta_{L_h}$	0.07075 mm	0.035 mm	Yes	IT7
$\delta_{L_v}$	0.02085 mm	0.00674 mm	No	IT4~IT5
CI	0.0202792	0.0454283	—	—
MI	0.0202880	0.0461793	—	—
AI	0.0202000	0.0386687	—	—
Improved rate of CI: 224.01%				
Improved rate of MI: 227.62%				
Improved rate of AI: 191.43%				

which are assigned based on a tolerance grade of IT6 for their corresponding dimensions of design parameters. The initial value of the objective function, CI, and those of the four extremes,  $(\Delta L_{h,\text{rss}})_{\max}$ ,  $(\Delta L_{v,\text{rss}})_{\max}$ ,  $\delta_{L_h}$ , and  $\delta_{L_v}$ , for evaluating the constraints are then calculated by adopting the initial design. It can be seen that the initial value of  $\delta_{L_h}$  is 0.07075 mm, which is more than twice its upper bound  $\delta_{L_h}^{(u)}$  ( $= 0.035$  mm). That is, the

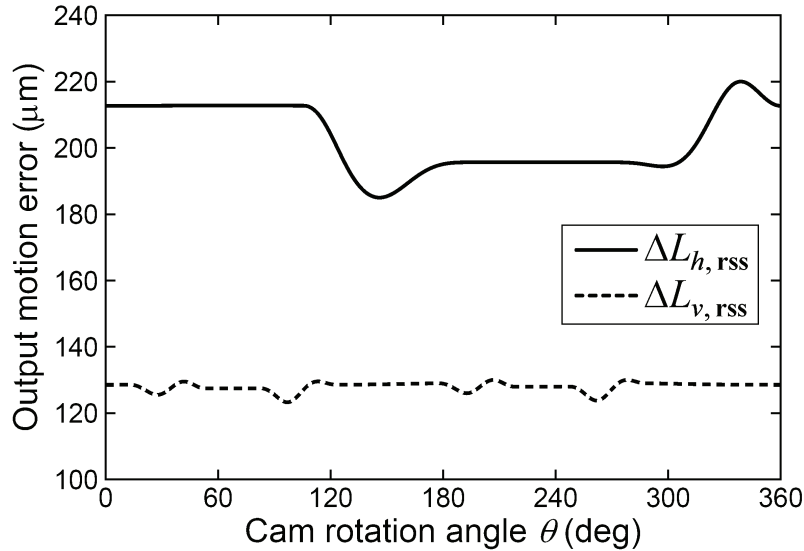


**Figure 4.1** Maximum expected deviations of a planar cam-follower type pick-and-place device caused by the optimized tolerances.

constraint of  $\delta_{L_h} \leq \delta_{L_h}^{(u)} = 0.035$  mm is violated, and the initial design is infeasible. After the iteration process, the optimization results are also listed in Table 4.2. The maximum expected deviations  $\Delta L_{h, rss}$  and  $\Delta L_{v, rss}$  caused by the optimal tolerances are computed and shown in Fig. 4.1.

As can be seen in Table 4.2, there are quite obvious differences between the initial values and the optimization results. The improved rates of CI, MI, and AI are 224.01%, 227.62%, and 191.43%, respectively. Both the manufacturability and assembly of the pick-and-place device can be increased twice with no constraint being violated if the optimized tolerances are adopted. That is, the SQP method is effective in searching the optimal design within the feasible region for the constrained optimization problem even the initial design is infeasible.

The optimal tolerances for  $l_C$ ,  $\eta_A$ ,  $\eta_B$ ,  $f_h$ ,  $f_v$ , and  $\alpha_E$  are referred to very small tolerance grades ranging from IT1 to IT3, especially  $\Delta l_C$  which is at its lower bound. In the contrast, the optimal tolerances for  $l_G$ ,  $l_H$ ,  $l_S$ , and  $e$  are referred to very large tolerance grades ranging from IT9 to IT12, especially  $\Delta e$  which is at its upper bound. The optimal tolerance grades for the radial dimensions of the cam profiles ( $r_A$  and  $r_B$ ) range from IT6 to IT8, which are larger than those for most of other parameters. This may be a benefit to help lower the

production costs of the cams. In particular, the optimal tolerance grades of parameters  $l_G$ ,  $l_H$ ,  $l_s$ , and  $e$  are larger than those of the cam profiles. It simply means that their deviations are more non-sensitive than the cam profile errors to contribute to the mechanical errors,  $\Delta L_{h,\text{rss}}$  and  $\Delta L_{v,\text{rss}}$ , or their relative variations,  $\delta_{L_h}$  and  $\delta_{L_v}$ . Hence, not every tolerance with a smaller weighting factor needs to have a smaller tolerance grade. The limitations of the kinematic accuracy of the functional output are all satisfied, especially  $\delta_{L_v}$  which is much smaller than its upper bound. As shown in Fig. 4.1, the relative deviations of the positions between the low and high dwells of  $L_h$  and  $L_v$  will not exceed 17.07 and 1.51  $\mu\text{m}$ , respectively. The operating performance of the pick-and-place device can thus be ensured when the obtained optimal tolerances are allocated.

In addition, although the manufacturability and the assembly have been maximized, the optimal tolerance grades for parameters  $l_C$ ,  $\eta_A$ ,  $\eta_B$ ,  $f_h$ ,  $f_v$ , and  $\alpha_E$ , ranging from IT1 to IT3, may be still too small for practical manufacture or assembly. This situation can be refined by reassessing the weighting factors of the tolerances or by magnifying the upper bounds on the kinematic deviations of the functional output to perform the re-optimization. The weighting factors of the tolerances involved in the actual manufacturing and assembly processes may not be easily readjusted. Hence, modifying the four upper bounds,  $\Delta L_h^{(u)}$ ,  $\Delta L_v^{(u)}$ ,  $\delta_{L_h}^{(u)}$ , and  $\delta_{L_v}^{(u)}$ , to slightly degrade the kinematic accuracy of the pick-and-place device would be a better solution. For this case, when the four upper bounds,  $\Delta L_h^{(u)}$ ,  $\Delta L_v^{(u)}$ ,  $\delta_{L_h}^{(u)}$ , and  $\delta_{L_v}^{(u)}$ , are respectively modified to 0.35, 0.21, 0.054, and 0.033 mm (based on a degraded tolerance grade of IT12 or IT8), the re-optimization results are as listed in Table 4.3. Also, the maximum expected deviations  $\Delta L_{h,\text{rss}}$  and  $\Delta L_{v,\text{rss}}$  caused by the re-optimized tolerances are computed and shown in Fig. 4.2. The improved rates of CI, MI, and AI are 347.95%, 364.07%, and 202.19%, respectively. It can be seen that the optimal tolerances of all parameters, except  $l_C$  and  $e$ , are increased to significantly magnify the optimized manufacturability index, MI, about 1.6 times more than the previous one listed

**Table 4.3** Initial design and computation results for the re-optimization.

Term	Initial value	Optimization result	Active constraint	Tolerance grade
$\Delta l_C$	0.019 mm	0.002 mm	Yes	IT1
$\Delta l_D$	0.019 mm	0.01908 mm	No	IT6~IT7
$\Delta l_G$	0.029 mm	0.30546 mm	No	IT11~IT12
$\Delta l_H$	0.025 mm	0.16840 mm	No	IT10~IT11
$\Delta l_5$	0.029 mm	0.27442 mm	No	IT10~IT11
$\Delta l_6$	0.029 mm	0.07291 mm	No	IT8~IT9
$\Delta r_A$	0.019 mm	0.04325 mm	No	IT7~IT8
$\Delta r_B$	0.019 mm	0.07288 mm	No	IT8~IT9
$\Delta \eta_A$	0.019°	0.00781°	No	IT3~IT4
$\Delta \eta_B$	0.011°	0.00258°	No	IT2~IT3
$\Delta f_h$	0.019 mm	0.00756 mm	No	IT3~IT4
$\Delta f_v$	0.019 mm	0.00330 mm	No	IT2~IT3
$\Delta e$	0.022 mm	0.35 mm	Yes	IT12
$\Delta \alpha_E$	0.022°	0.00861°	No	IT3~IT4
$(\Delta L_{h,\text{rss}})_{\max}$	0.16781 mm	0.35 mm	Yes	IT12
$(\Delta L_{v,\text{rss}})_{\max}$	0.09040 mm	0.21 mm	Yes	IT12
$\delta_{L_h}$	0.07111 mm	0.054 mm	Yes	IT8
$\delta_{L_v}$	0.02085 mm	0.01089 mm	No	IT5~IT6
CI	0.0202792	0.0705607	—	—
MI	0.0202880	0.0738626	—	—
AI	0.0202000	0.0408430	—	—
Improved rate of CI: 347.95%				
Improved rate of MI: 364.07%				
Improved rate of AI: 202.19%				

in Table 4.2, while the optimized assemblability index, AI, increases slightly. This may contribute to a lower production cost of the pick-and-place device with degraded accuracy. However, as shown in Fig. 4.2, the relative deviations of the positions between the low and high dwells of  $L_h$  and  $L_v$  will not exceed 26.34 and 2.44  $\mu\text{m}$ , respectively. Such slight kinematic inaccuracies can still be allowable for the operating performance of the pick-and-place device.

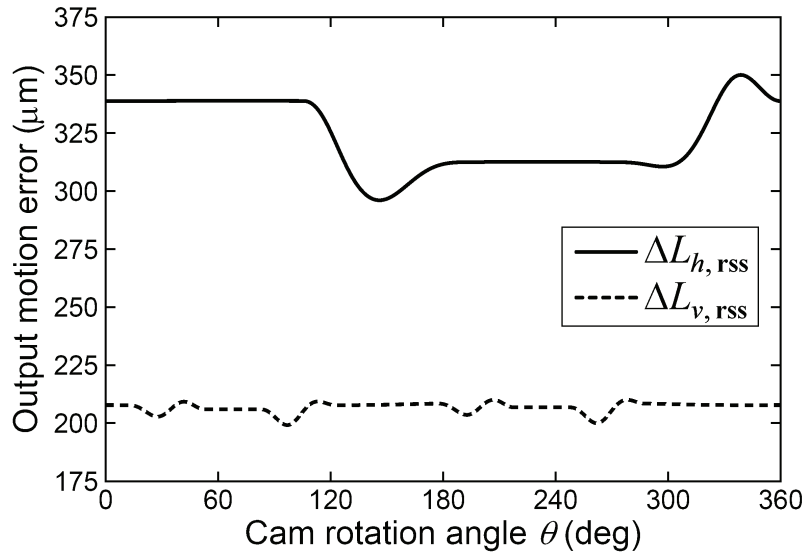


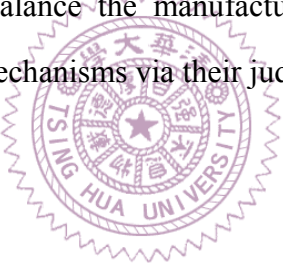
**Figure 4.2** Maximum expected deviations of a planar cam-follower type pick-and-place device caused by the re-optimized tolerances.

#### 4.4 CONCLUDING REMARKS

By employing the concept of DFMA, a systematic procedure of optimal tolerance allocation for disk cam mechanisms to maximize their manufacturability and assembly while maintaining acceptable kinematic accuracy is developed. The comprehensive index, CI, for quantitatively evaluating the level of difficulty of manufacturing and assembling disk cam mechanisms as the objective function is simply and reasonably defined as the summation of all manufacturing and assembly tolerances combining their corresponding weighting factors. The weighting factors for the tolerances actually involve the information of manufacturing and assembly processes and their required effort and time, and can be assigned to the tolerances via designers' judgements and experience. To evaluate the kinematic accuracy of the follower output as the design constraints, the equivalent linkage method should be employed to analytically perform the mechanical error analysis of disk cam mechanisms. The extreme values of the maximum expected deviations of the follower output and their relative differences should be simultaneously controlled in slight amounts to obtain reasonably acceptable performance of the cam mechanism.

The developed optimal tolerance allocation procedure is effectively applied to a

practical case study for tolerancing the MEG X6061 planar cam-follower type pick-and-place device. The SQP method is successfully applied to search the feasible tolerance combination for improving the manufacturability and assembly of the pick-and-place device, with the required kinematic accuracy of the device being satisfied. As compared to the initial design based on a tolerance grade of IT6, the optimization results can lead to an improved value of CI having a magnitude more than twice the initial one. The optimization results show that the optimal tolerance grades for the cam profiles, which are with the largest weighting factors, can be larger than those for most of other design parameters. This may be a significant benefit to help lower the production costs of the cams. Also, because the sensitivity of each tolerance on influencing the mechanical error is different, not every tolerance with a smaller weighting factor needs to have a smaller tolerance grade. By applying the presented optimization procedure, designers can systematically allocate the most appropriate tolerances to balance the manufacturability, the assembly, and the kinematic accuracy of disk cam mechanisms via their judgements and requirements.



# CHAPTER 5

## INSPECTING PROFILE ERRORS OF DISK CAMS WITH COORDINATE MEASUREMENT

### 5.1 INTRODUCTION

This chapter demonstrates an extended application of the shift angles of disk cams. As mentioned in Section 1.1, the machined cam profiles are usually inspected by using a coordinate measuring machine (CMM) [3, 6-8, 19-23] to check whether their dimensions meet the specified tolerances for quality control. But, the evaluation of the measured coordinate data is often a complicated task. Thus, in this chapter, a direct and simple method is proposed for inspecting the profile deviations of disk cams with coordinate measurement data. The method is based on applying the concept of the shift angle and the derived correlation between the radial-dimension errors and the normal-direction errors of disk cam profiles introduced in Sub-section 3.2.2. To verify the proposed method, an experiment of inspecting a pair of conjugate disk cam profiles, which was designed to drive an oscillating roller follower, was conducted. The experimental results obtained from the proposed method were compared with those of the Hermite interpolation method [91], a typical approach of computer aided geometric design with coordinate measurement data, to further demonstrate the accuracy and convenience of the proposed method.

### 5.2 COORDINATE MEASUREMENT AND PROFILE ERRORS INSPECTION OF DISK CAMS

As mentioned in Sub-section 3.2.2 that the accuracy of a machined cam is controlled through a properly specified tolerance of the radial dimension of the actual cam profile.

Thus, the radial dimensions of the actual cam profile with respect to corresponding cam angles must lie within a specified zone along the ideal profile. However, some difficulties may be encountered in using a CMM with a touch-trigger probe to measure the radial dimensions of a disk cam.

Figure 5.1 shows the diagram of measuring a disk cam profile with a touch-trigger probe through the direct computer control (DCC) measurement with the vector touch mode [109]. For clarity, the theoretical cam profile is shown in solid line, the actual cam profile in dashed line, and the profile deviation is exaggerated. The theoretical contact point (the target point) is designated by A, and its normal to the cam profile intersects the actual cam profile at point  $A_n$ ; line  $O_2A$  intersects the actual cam profile at point  $A_r$ . To measure the cam profile, the probe may move toward the normal vector  $A_nA$  to touch the cam surface at point  $A_n$ , and the coordinate of the stylus ball center of the probe,  $G_n$ , is recorded. Then the coordinate of point  $A_n$  is compensated by the stylus ball radius  $r_t$  along the normal direction. This operation can give reasonably acceptable normal-direction error  $\Delta n (= AA_n)$ , although

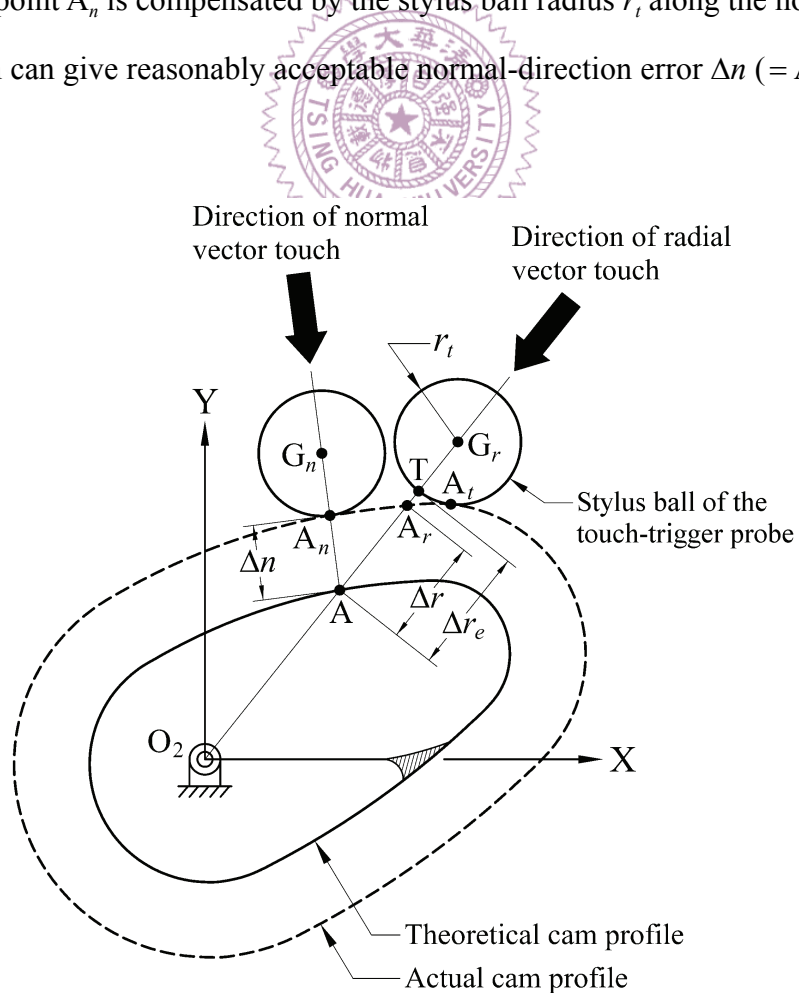


**Figure 5.1** Measuring a disk cam profile with a touch-trigger probe.

the normal vector to the actual cam profile may slightly deviate from the theoretical one. On the other hand, if the probe moves toward the radial vector  $\mathbf{A}_r\mathbf{A}$  to touch the cam surface at point  $A_r$ , some other point  $A_s$  rather than point  $A_r$  would be touched to sense the coordinate of the stylus ball center  $G_s$ . Thus, the coordinate of point T, instead of point  $A_r$ , would be obtained with probe compensation. Hence, the incorrect radial profile error  $\Delta r_e$  ( $= AT$ ) may be misjudged as the correct radial profile error  $\Delta r$  ( $= AA_r$ ). To avoid this measuring error, coordinates of the stylus ball centers of the probe,  $G_s$ , corresponding to specified cam angles are recorded to further model the pitch curve formed by these recorded points with using some interpolation algorithms. The actual cam contour can thus be approximated as the offset curve of the modeled pitch curve. (The modeled cam contour has a normal offset of  $r_t$  to the pitch curve.) Then the coordinate of point  $A_r$  can be estimated by finding the intersection of the modeled cam contour and the radial line passing through point A with numerical methods. Such approach is quite complicated. In order to effectively inspect whether the radial-dimension errors of the machined disk cam profiles can meet the specified tolerance, the correlation between the radial-dimension errors and the normal-direction errors of disk cam profiles is applied.

Recall from Figs. 3.2(a) and 3.2(b) and Eq. (3.9) that the correlation between the radial-dimension error,  $\Delta r$ , and the normal-direction error,  $\Delta n$ , of a disk cam profile can be approximated by

$$\Delta n \approx \Delta r \cos \lambda \quad (5.1)$$

where  $\lambda$  is the shift angle. If the normal-direction errors,  $\Delta n$ , of the cam profile have been measured by using a CMM, then the corresponding radial profile errors,  $\Delta r$ , of the cam can be reversely evaluated by

$$\Delta r \approx \Delta n \sec \lambda \quad (5.2)$$

Similarly, for the conjugate cam mechanism with an oscillating roller follower shown in Fig. 5.2 (referring to Fig. 2.8), applying the sine law to  $\triangle O_2AQ$  and  $\triangle O_2BQ$ , its shift

angles are

$$\lambda_A = \angle O_2 A Q = \sin^{-1} \left( \frac{q \sin \alpha_A}{\|O_2 A\|} \right) = \sin^{-1} \left\{ \frac{f v(\theta) \sin \alpha_A}{[1 - v(\theta)] \|R_A(\theta)\|} \right\} \quad (5.3)$$

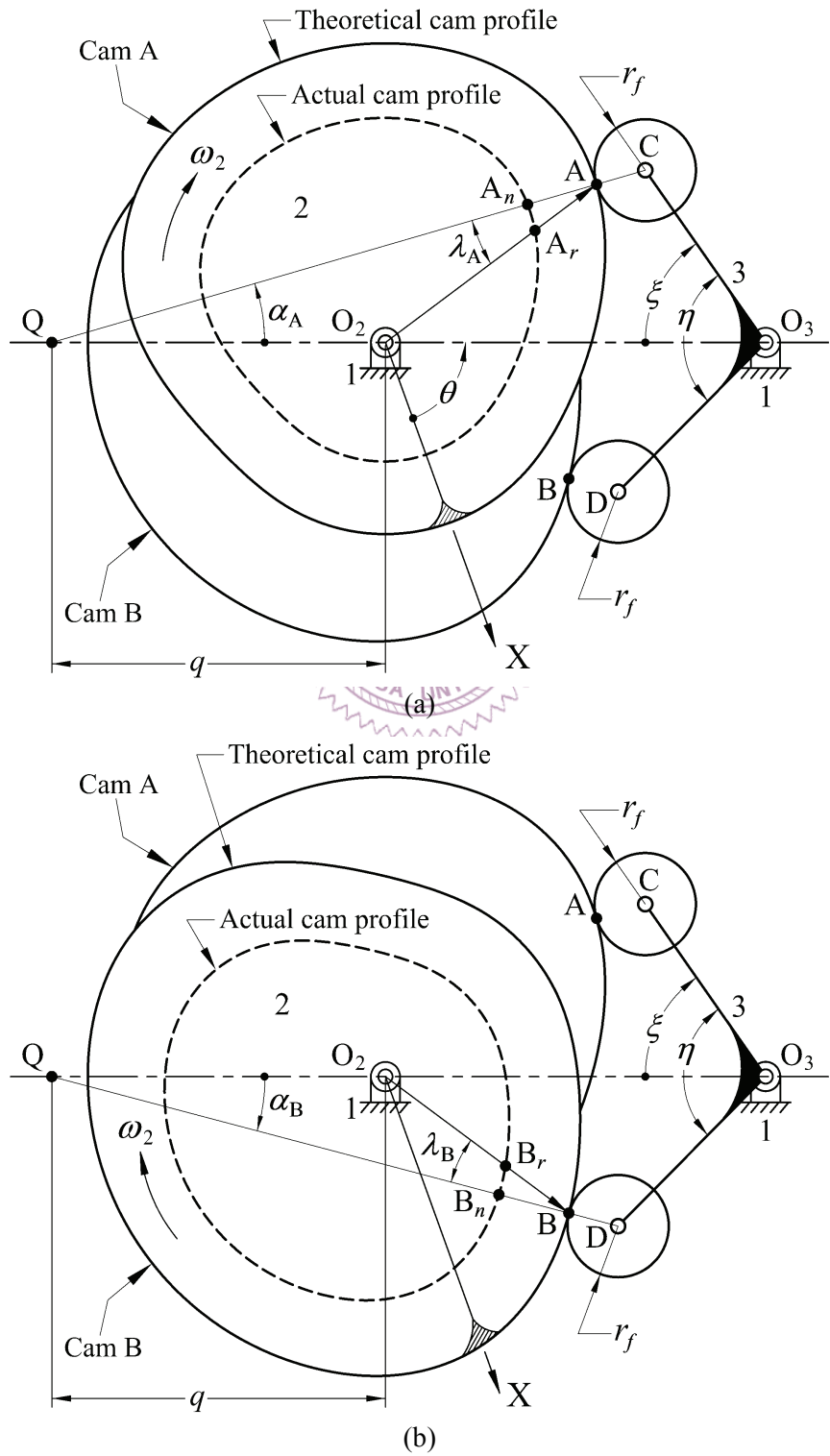


**Figure 5.2** Conjugate cam mechanism and its actual cam profiles.

$$\lambda_B = \angle O_2 BQ = \sin^{-1} \left( \frac{q \sin \alpha_B}{\|O_2 B\|} \right) = \sin^{-1} \left\{ \frac{fv(\theta) \sin \alpha_B}{[1 - v(\theta)] \|R_B(\theta)\|} \right\} \quad (5.4)$$

where  $\alpha_A$  and  $\alpha_B$  are defined in Eqs. (2.70) and (2.71), respectively. From Eqs. (5.2), (5.3), and (5.4), when the normal-direction errors of the conjugate cam profiles,  $\Delta n_A$  and  $\Delta n_B$ , have been measured, their corresponding radial-dimension errors,  $\Delta r_A$  and  $\Delta r_B$ , can be predicted respectively by

$$\Delta r_A \approx \Delta n_A \sec \lambda_A \quad (5.5)$$

$$\Delta r_B \approx \Delta n_B \sec \lambda_B \quad (5.6)$$

As shown, the magnitude of the radial profile errors is simultaneously influenced by the normal-direction errors and the shift angles in their secant forms.

Based upon the parametric vector equations derived in Section 2.7 and the analytical correlation between the radial-dimension errors and the normal-direction errors of conjugate cam profiles, the procedure of the proposed method for inspecting conjugate cam profile errors can be summarized as follows:

- Step 1. Apply Eqs. (2.77)~(2.80) to calculate the coordinates of the theoretical target points and their unit normal vectors with respect to their corresponding cam rotation angles.
- Step 2. Measure the coordinate data of machined cam profiles by a CMM through the DCC measurement with the normal vector touch mode [109].
- Step 3. Evaluate the normal-direction errors of the cam profiles by calculating the differences between the coordinate data of the measured points and their corresponding theoretical target points.
- Step 4. Apply Eqs. (5.3) and (5.4) to calculate the shift angles of the cam profiles with respect to their corresponding cam rotation angles.
- Step 5. Apply Eqs. (5.5) and (5.6) to evaluate the radial-dimension errors of the cam profiles with respect to their corresponding cam rotation angles and judge the satisfaction of the specified tolerance.

The five steps of inspecting profile errors of conjugate cams with a CMM are equally applicable to all types of disk cams.

### 5.3 EXPERIMENTAL DETAILS

To verify the feasibility and effectiveness of the proposed method, an experiment for inspecting conjugate cam profiles was performed. Referring to Fig. 2.8, a conjugate cam system was designed to drive the oscillating roller follower to oscillate  $30^\circ$  clockwise with cycloidal motion while the cam rotates clockwise from  $0^\circ$  to  $120^\circ$ , dwell for the next  $40^\circ$ , return with cycloidal motion for  $120^\circ$  cam rotation, and dwell for the remaining  $80^\circ$ . The distance between pivots,  $f$ , is 120 mm; the lengths of the follower arms,  $l_A$  and  $l_B$ , are both 66 mm. Both follower rollers have the same radius of  $r_f = 16$  mm. The base circle radius,  $r_b$ , of cam A is 60 mm, and the subtending angle of the follower arms,  $\eta$ , is  $100^\circ$ . In fact, the conjugate cam profiles satisfying the above requirements are shown in Fig. 2.8, in which, cams A and B have their maximum radial dimensions of 93.793 and 93.859 mm, respectively. In order to demonstrate the applicable extent of the proposed method, both cams were intentionally specified to have a radial profile tolerance of  $\pm 0.220$  mm, a considerably large tolerance grade of IT11.

The conjugate cams were made of stainless steel (JIS SUS304/AISI 304). Both cams had the same thickness of 12 mm and were manufactured with an electro-discharge wire-cutting machine. The cam profiles were measured by using a Giddings & Lewis Sheffield Measurement Cordax RS-25 CMM with a Renishaw touch-trigger probe (PH9 probe head and TP200 probe with a stylus for its ruby ball diameter of 2 mm) through the DCC measurement with the normal vector touch mode [109], as shown in Fig. 5.3. The CMM has a resolution of  $0.1 \mu\text{m}$  and an accuracy of  $\pm 3 \mu\text{m}$ . By setting up one end face of each cam as the axial datum ( $Z = 0$  mm), three data sets of 3600 points were measured in a full circle on each cam contour with an equal cam rotation angle interval of  $0.1^\circ$  under  $Z = 5$ , 6, and 7 mm, respectively. The coordinates of the target points and their corresponding

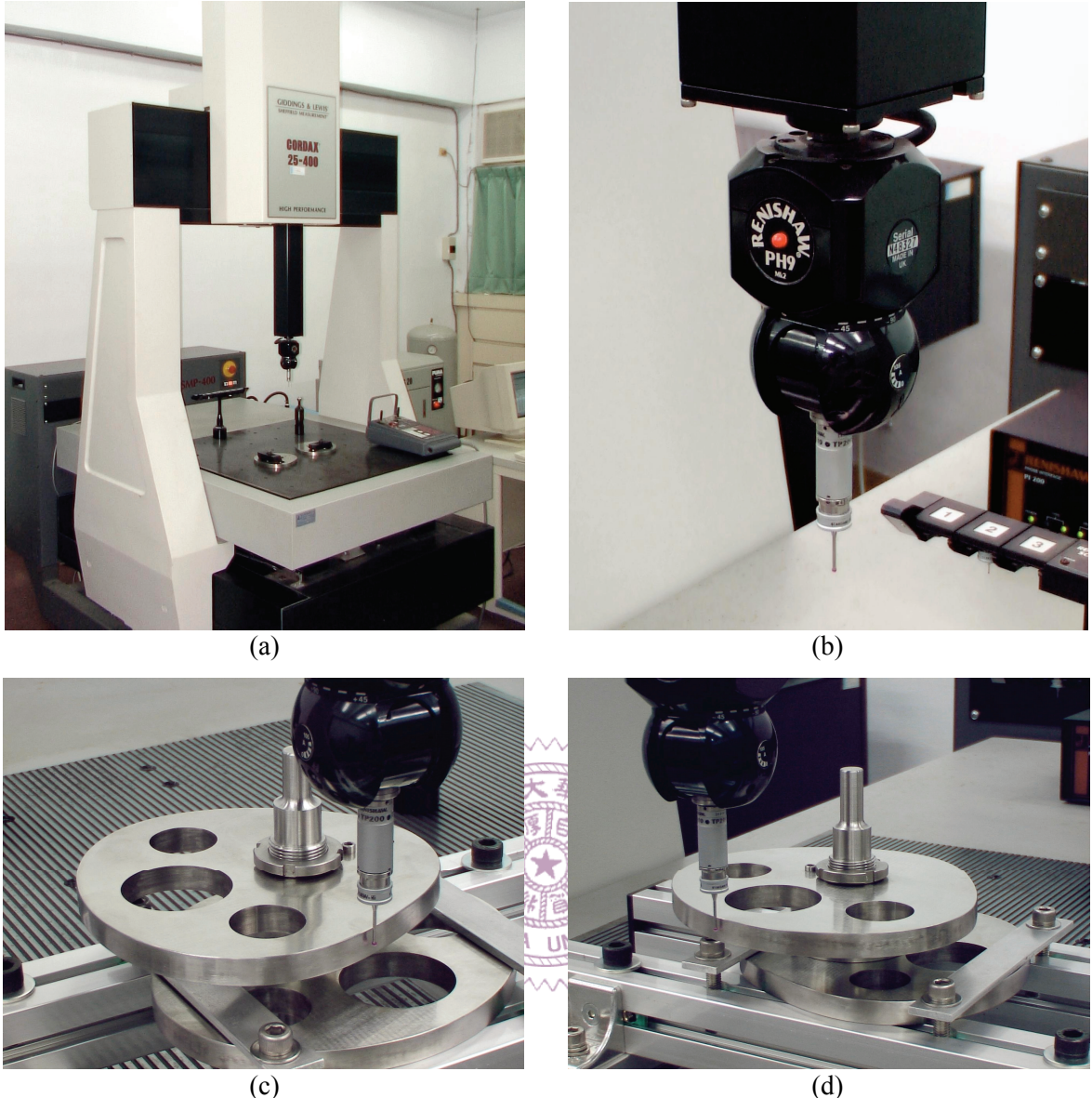


**Figure 5.3** Experiment for inspecting conjugate cam profiles by using a CMM:  
 (a) the CMM used in this experiment; (b) the touch-trigger probe used in this experiment; (c) the inspection of cam A; (d) the inspection of cam B.

normal vectors were calculated by using Eqs. (2.77)~(2.80). Then the average normal-direction errors of the conjugate cam profiles with corresponding cam rotation angles were evaluated. Furthermore, the average radial profile errors of the conjugate cams were predicted by using Eqs. (5.5) and (5.6).

In addition, a typical approach in handling the measured data points with the Hermite interpolation was given to compare with the proposed method. Two sets of 3600 segments of the fifth-degree Hermite interpolation curves [91] were generated to model the two cam

contours, respectively. Then the intersections of the interpolation curves and the radial lines with corresponding cam rotation angles were numerically calculated to evaluate the average radial profile errors of the conjugate cams. Appendix B shows the algorithm of generating the fifth-degree Hermite interpolation curves with measured coordinate data.

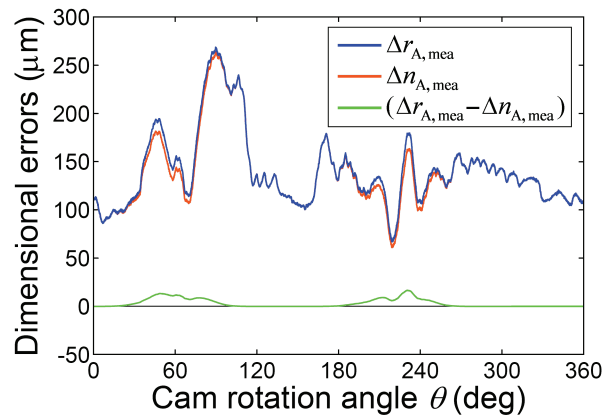
## 5.4 RESULTS AND DISCUSSION

The evaluated profile errors of cams A and B versus the cam rotation angle  $\theta$  are shown in Figs. 5.4 and 5.5, respectively, and the pressure angles and shift angles of the cam mechanism are shown in Fig. 5.6, while their extreme values are also listed in Table 5.1. Figure 5.4(a) shows the measured normal-direction error  $\Delta n_{A,\text{mea}}$  and the predicted radial profile error  $\Delta r_{A,\text{mea}}$  by Eq. (5.5); they had quite similar trends and had the same magnitude at the two dwell regions ( $\theta = 120^\circ \sim 160^\circ$  and  $\theta = 280^\circ \sim 360^\circ$ ) where the corresponding shift angle  $\lambda_A$  is zero. The magnitude of  $\Delta r_{A,\text{mea}}$  fell within the range of 66.95 and 268.89  $\mu\text{m}$  and had an average value of 140.81  $\mu\text{m}$ , while within the range of  $\theta = 80^\circ \sim 110^\circ$ , it exceeded the specified tolerance of  $\pm 220 \mu\text{m}$ . Figure 5.4(b) shows the measured normal-direction error  $\Delta n_{A,\text{mea}}$  and the predicted radial profile error  $\Delta r_{A,\text{int}}$  by the Hermite interpolation method. Since  $\Delta r_{A,\text{mea}}$  and  $\Delta r_{A,\text{int}}$  cannot be easily distinguished by inspection, their difference  $\delta_A$  and relative deviation  $\varepsilon_A$  are additionally shown in Figs. 5.4(c) and 5.4(d), respectively, where

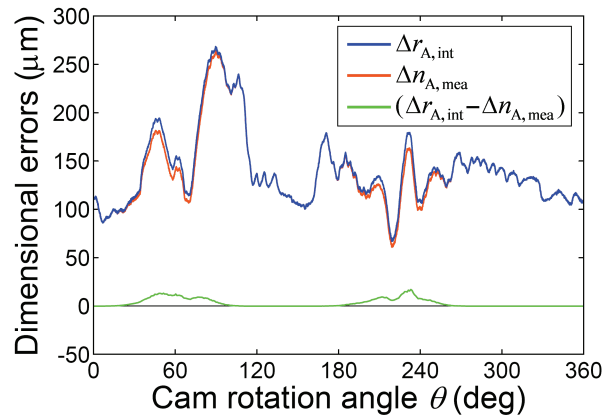
$$\delta_A = |\Delta r_{A,\text{mea}} - \Delta r_{A,\text{int}}| \quad (5.7)$$

$$\varepsilon_A = \left| \frac{\Delta r_{A,\text{mea}} - \Delta r_{A,\text{int}}}{\Delta r_{A,\text{int}}} \right| \times 100\% \quad (5.8)$$

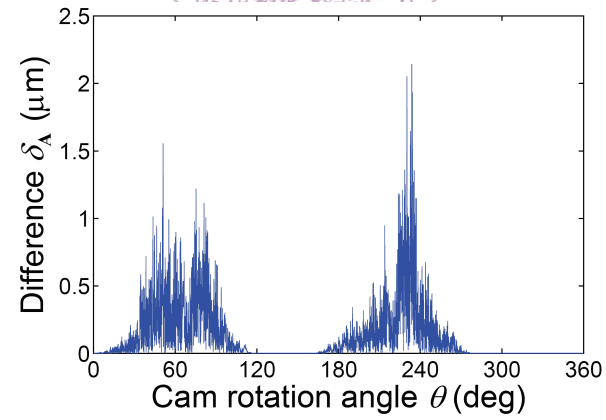
At  $\theta = 234^\circ$ ,  $\delta_A$  had an extreme magnitude of 2.144  $\mu\text{m}$ . The extreme value of  $\varepsilon_A$  also occurred at  $\theta = 234^\circ$  and had a magnitude of 1.3097%. Both extreme values were very close to  $\theta = 226.68^\circ$  where the extreme shift angle  $\lambda_A$  occurs.



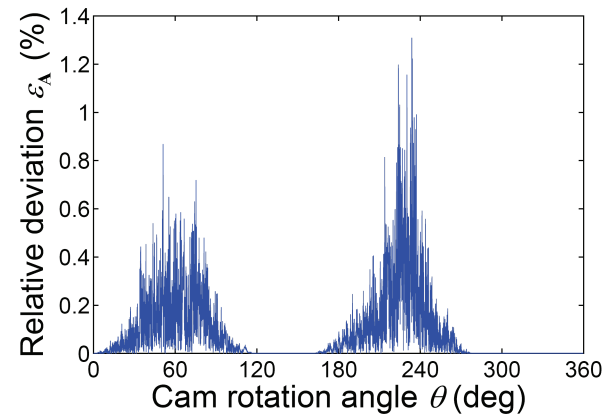
(a)



(b)

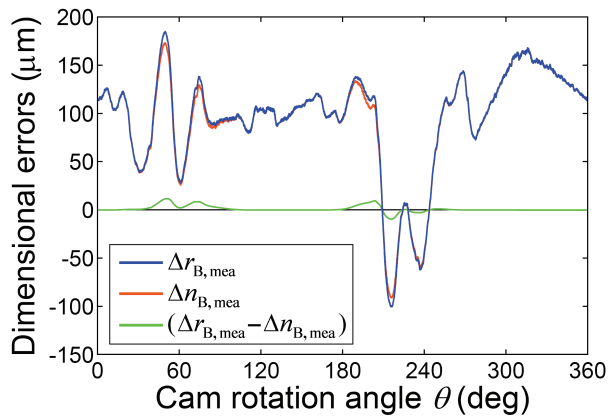


(c)

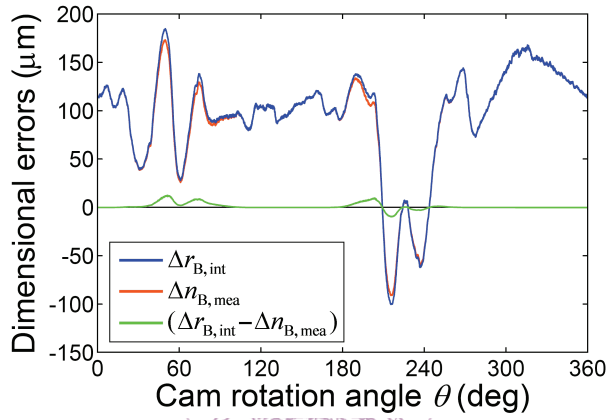


(d)

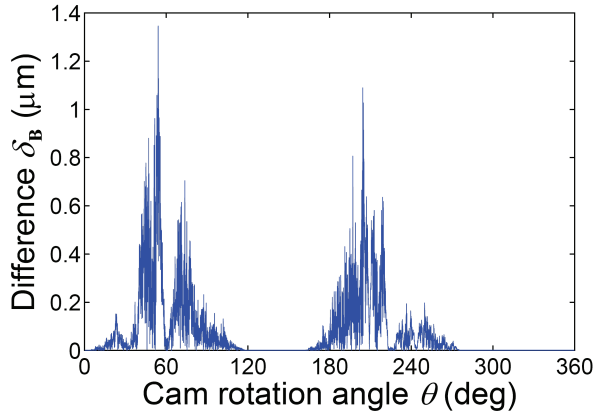
**Figure 5.4** Evaluated results of profile errors of cam A.



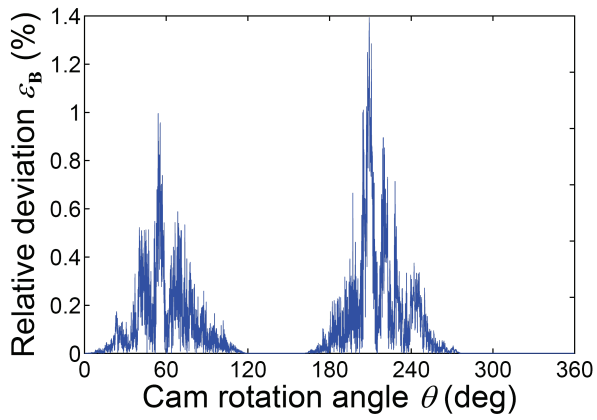
(a)



(b)



(c)



(d)

**Figure 5.5** Evaluated results of profile errors of cam B.

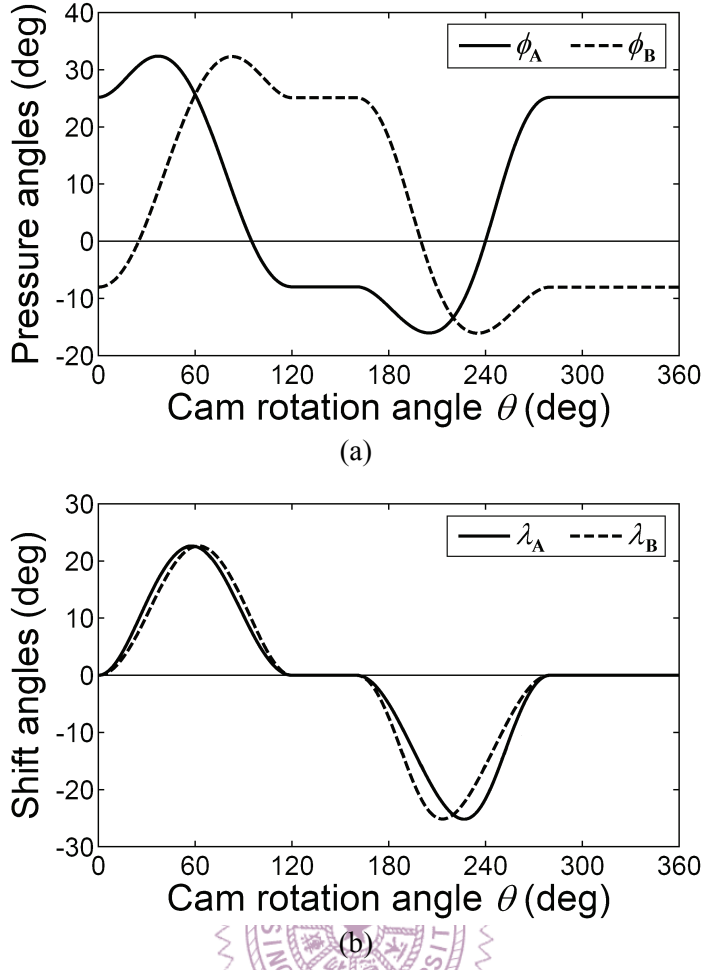


**Figure 5.6** Pressure angles and shift angles of the conjugate cam mechanism.

Similarly, Fig. 5.5(a) shows that the measured normal-direction error  $\Delta n_{B,\text{mea}}$  and the predicted radial profile error  $\Delta r_{B,\text{mea}}$  by Eq. (5.6) had quite similar trends and had the same magnitude at the two dwell regions where the corresponding shift angle  $\lambda_B$  is zero. The magnitude of  $\Delta r_{B,\text{mea}}$  fell within  $-100.46$  and  $185.12$   $\mu\text{m}$  and had an average value of  $94.83$   $\mu\text{m}$ ; it met the specified radial profile tolerance ( $\pm 220$   $\mu\text{m}$ ). Figure 5.5(b) shows the measured normal-direction error  $\Delta n_{B,\text{mea}}$  and the predicted radial profile error  $\Delta r_{B,\text{int}}$  by the Hermite interpolation method. Since  $\Delta r_{B,\text{mea}}$  and  $\Delta r_{B,\text{int}}$  cannot be easily distinguished by inspection, their difference  $\delta_B$  and relative deviation  $\varepsilon_B$  are additionally shown in Figs. 5.5(c) and 5.5(d), respectively, where

$$\delta_B = |\Delta r_{B,\text{mea}} - \Delta r_{B,\text{int}}| \quad (5.9)$$

**Table 5.1** Input angles and extreme values of the experiment of inspecting conjugate cam profiles by using a CMM and the profile errors evaluation.

Input angle	Extreme value
$\theta = 37.11^\circ$	$(\phi_A)_{\max} = 32.37^\circ$
$\theta = 49.7^\circ$	$(\Delta n_{B,\text{mea}})_{\max} = 173.5 \mu\text{m}$
$\theta = 49.7^\circ$	$(\Delta r_{B,\text{mea}})_{\max} = 185.12 \mu\text{m}$
$\theta = 49.7^\circ$	$(\Delta r_{B,\text{int}})_{\max} = 185.11 \mu\text{m}$
$\theta = 54^\circ$	$(\delta_B)_{\max} = 1.347 \mu\text{m}$
$\theta = 57.94^\circ$	$(\lambda_A)_{\max} = 22.60^\circ$
$\theta = 62.07^\circ$	$(\lambda_B)_{\max} = 22.60^\circ$
$\theta = 82.88^\circ$	$(\phi_B)_{\max} = 32.30^\circ$
$\theta = 89.6^\circ$	$(\Delta n_{A,\text{mea}})_{\max} = 264.24 \mu\text{m}$
$\theta = 89.6^\circ$	$(\Delta r_{A,\text{mea}})_{\max} = 268.89 \mu\text{m}$
$\theta = 89.6^\circ$	$(\Delta r_{A,\text{int}})_{\max} = 268.69 \mu\text{m}$
$\theta = 205^\circ$	$(\phi_A)_{\min} = -16.05^\circ$
$\theta = 209.1^\circ$	$(\varepsilon_B)_{\max} = 1.3991\%$
$\theta = 213.32^\circ$	$(\lambda_B)_{\min} = -25.14^\circ$
$\theta = 215.5^\circ$	$(\Delta n_{B,\text{mea}})_{\min} = -91.01 \mu\text{m}$
$\theta = 215.5^\circ$	$(\Delta r_{B,\text{mea}})_{\min} = -100.46 \mu\text{m}$
$\theta = 215.5^\circ$	$(\Delta r_{B,\text{int}})_{\min} = -100.31 \mu\text{m}$
$\theta = 219.3^\circ$	$(\Delta n_{A,\text{mea}})_{\min} = 61.05 \mu\text{m}$
$\theta = 219.3^\circ$	$(\Delta r_{A,\text{mea}})_{\min} = 66.95 \mu\text{m}$
$\theta = 219.3^\circ$	$(\Delta r_{A,\text{int}})_{\min} = 67.06 \mu\text{m}$
$\theta = 226.68^\circ$	$(\lambda_A)_{\min} = -25.17^\circ$
$\theta = 234^\circ$	$(\delta_A)_{\max} = 2.144 \mu\text{m}$
$\theta = 234^\circ$	$(\varepsilon_A)_{\max} = 1.3097\%$
$\theta = 235.01^\circ$	$(\phi_B)_{\min} = -16.09^\circ$

$$\varepsilon_B = \left| \frac{\Delta r_{B,\text{mea}} - \Delta r_{B,\text{int}}}{\Delta r_{B,\text{int}}} \right| \times 100\% \quad (5.10)$$

The extreme value of  $\delta_B$  occurred at  $\theta = 54^\circ$  and had a magnitude of  $1.347 \mu\text{m}$ , which occurred at the same cam rotation angle where  $\Delta n_{B,\text{mea}}$  and  $\Delta r_{B,\text{mea}}$  reached their extreme values. The extreme value of  $\varepsilon_B$  occurred at  $\theta = 209.1^\circ$  and had a magnitude of  $1.3991\%$ ;

it was very close to  $\theta = 213.32^\circ$  where the extreme shift angle  $\lambda_B$  occurs.

As observed, the differences,  $\delta_A$  and  $\delta_B$ , and the relative deviations,  $\varepsilon_A$  and  $\varepsilon_B$ , between the proposed method and the Hermite interpolation method were almost zero at the two dwell regions (the circular profile regions). Thus, both methods can have the same accuracy of predicting the profile errors of circular profiles. For the non-circular profile regions, the accuracy of the proposed method is mainly influenced by two factors, the degree of profile deviations and the variation of shift angles. The first factor dominates the magnitudes of the differences  $\delta_A$  and  $\delta_B$ , and apparently, a slighter profile deviation leads to a smaller difference. On the other hand, since a smaller shift angle will lead to a smaller relative deviation, the second factor, which appears in the secant form, affects the magnitudes of the relative deviations  $\varepsilon_A$  and  $\varepsilon_B$ . These arguments may be clarified by noticing that the profile errors of cam B fell within the range of  $\pm 22 \mu\text{m}$  (the radial profile tolerance of IT6) when  $\theta = 208.6^\circ \sim 209.9^\circ$ ,  $222^\circ \sim 229.9^\circ$ , and  $242^\circ \sim 245.2^\circ$ , where the magnitudes of  $\delta_B$  were significantly less than  $0.22 \mu\text{m}$  but those of  $\varepsilon_B$  were not strongly decreased. Because the accuracy of the used CMM is  $\pm 3 \mu\text{m}$ , such a fraction amount of  $0.22 \mu\text{m}$  can be ignored. That is, the differences,  $\delta_A$  and  $\delta_B$ , between the proposed method and the Hermite interpolation method are indeed smaller with slighter profile deviations (or with smaller tolerance grades). However, the relative deviations,  $\varepsilon_A$  and  $\varepsilon_B$ , between both methods are only slightly influenced by the degree of profile deviations. These properties cause the proposed method to have sufficient accuracy for inspecting disk cam profiles with smaller tolerance grades being specified. The experimental results showed that even though each cam was intentionally specified to have a large tolerance grade of IT11, the maximum difference and relative deviation between the proposed method and the Hermite interpolation method were considerably less than  $2.5 \mu\text{m}$  or  $1.4\%$ . In other words, the proposed method is verified to be a direct and effective means for inspecting disk cam profiles from an engineering viewpoint.

Alternatively, if the fifth-degree Hermite interpolation curves are adopted to model

the two cam contours, numerical differentiation must be employed to approximate the tangent and normal vectors at the measured points, and linear system solving methods must be then applied to estimate the coefficients of the fifth-degree polynomials. In addition, a time-consuming iterative process is unavoidably involved in calculating the intersections of the interpolation curves and the radial lines with corresponding cam rotation angles for evaluating the radial profile errors. Hence, a complicated programming and much central processing unit (CPU) time are required to perform the Hermite interpolation method. In contrast to the Hermite interpolation method that requires complicated computation to estimate cam profile errors, the proposed method has the advantage of analytically handling the measured data easily. To test the efficiency of the proposed method as compared with the Hermite interpolation method, the CPU time for computing the cam profile errors by using MATLAB was recorded and evaluated. The hardware environment of the computation was given as follows: an ASUS F3JC notebook computer with the Intel Core 2 Duo T5200 processor whose core speed is 1.6 GHz. The average CPU time for executing 60 times of the computation programs based on the two methods was: 0.484 seconds for the proposed method, and 30.254 seconds for the Hermite interpolation method, respectively. That is, the proposed method was 62.5 times faster than the conventional method in terms of the computational speed. As a result, the proposed method is simpler and more efficient than the Hermite interpolation method in the aspect of evaluating the profile deviations of disk cams with coordinate measurement data.

## 5.5 CONCLUDING REMARKS

With the aid of the correlation between the radial-dimension errors and the normal-direction errors of disk cam profiles and also their parametric expressions, the proposed method for inspecting the profile deviations of disk cams from the coordinate measurement data can be performed directly and efficiently. To examine its validity, the proposed method was applied to measure two machined conjugate disk cams, and the results were

compared with those obtained by using the Hermite interpolation method. Even though the two cams were intentionally specified to have a large tolerance grade of IT11 ( $\pm 220 \mu\text{m}$ ), the maximum difference and relative deviation between the proposed method and the Hermite interpolation method were less than  $2.5 \mu\text{m}$  or 1.4%. As compared to the Hermite interpolation method, the proposed method may analytically handle the measured data and eliminate the need for complex analysis procedures. Therefore, this chapter has provided an analytical method to deal with the coordinate measured data, contributing to the enhancement of efficiency in inspecting profile errors of disk cams by using a CMM.

In addition, this chapter has provided an experimental verification of the use of the shift angle to correlate the radial-dimension errors and the normal-direction errors of disk cam profiles. Through the presented experimental results, the use of the shift angle has been validated reasonable, feasible, and accurate from an engineering viewpoint.



# **CHAPTER 6**

## **SIMPLIFIED METHODS FOR EXAMINING PROFILE ERRORS OF CONJUGATE DISK CAMS — PART I: MEASURING FIXTURES AND CONJUGATE CONDITION ANALYSIS**

### **6.1 INTRODUCTION**

By employing the analytical approach with coordinate measurement data introduced in Chapter 5, the profile errors of disk cams can be efficiently and accurately evaluated after the cams are directly measured by using a coordinate measuring machine (CMM). However, the direct measurement itself is costly and time-consuming, especially for conjugate cams. As mentioned in Sub-section 1.2.2, the profile deviations of conjugate cams can be indirectly inspected by using a special measuring fixture [3] as shown in Fig. 1.6. As compared to the use of a CMM to inspect conjugate cams, such an indirect measurement method is convenient and inexpensive, and the only required measuring instrument is a dial indicator. Hence, it is especially suitable for quality control in mass production of conjugate cams. This simplified method is in essence to provide a quantitative evaluation of the conjugate condition of machined conjugate cams to indicate the profile deviations indirectly. Based on the simplified inspection concept, this chapter demonstrates how to measure the conjugate conditions of assembled conjugate cam mechanisms to reveal the cam profile errors and also develops analytical approaches for relating the variations of the conjugate conditions with the cam profile errors.

For a conjugate cam mechanism with an oscillating roller follower, two types of measuring fixtures for inspecting the cam profile errors are studied in this chapter. By applying the equivalent linkage method developed in Chapter 3, the analysis of conjugate

condition variations of assembled conjugate cam mechanisms can be performed analytically. Then conservative criteria for efficiently checking whether or not the profile deviations of inspected conjugate cams meet their specified tolerances by using the two types of measuring fixtures are defined with two examples illustrated.

## 6.2 FUNDAMENTALS OF THE CONJUGATE CAMS MEASURING FIXTURES

Measuring fixtures for a conjugate cam mechanism with an oscillating roller follower are introduced in this section. The principle of developing conjugate cams measuring fixtures is based on the following consideration.

A conjugate cam mechanism is a three-link direct-contact mechanism involving two cam-and-follower kinematic pairs. From Grubler's equation, it is an overconstrained mechanism with zero degree-of-freedom. But, the two cam profiles must conjugate each other to make the two normal lines through the points of contact and the line of centers always intersect at a common point, that is, the velocity instant center of the cam and the follower. This geometrical property makes the conjugate cam mechanism a paradoxical mechanism [110] with constrained motion. However, because the machined conjugate cams usually have slight profile errors, the geometrical property cannot be perfectly satisfied, and the mechanism will no longer be a paradoxical mechanism. Hence, if an additional one degree-of-freedom kinematic pair (a revolute joint or a prismatic joint) is added into the original conjugate cam mechanism to make a constant parameter  $r_i$  of the mechanism become a variable  $r_i^*$ , the new mechanism will then have constrained motion. When the cams rotate, in the perfect condition that the machined conjugate cams have no profile errors, because  $r_i^* = r_i$ , the added kinematic pair will be redundant. In practice, for the machined conjugate cams with profile errors, the variation of the parameter  $\Delta r_i (= r_i^* - r_i)$  can reflect the violation of the conjugate condition of each pair of conjugate cams

and may also indicate the variation of profile errors.

For the conjugate cam mechanism with an oscillating roller follower shown in Fig. 2.8, normally, the subtending angle of the follower arms,  $\eta$ , is a constant. If, as shown in Fig. 6.1, a revolute joint is intentionally added such that the subtending angle of the follower arms,  $\eta^*$ , is changed to be variable, the mechanism will no longer be overconstrained. In this case, the follower arms are two different links, links 3 and 4. When the cams rotate, in the ideal situation that the machined conjugate cams have no profile errors, the subtending angle of the follower arms  $\eta^*$  will always equal the constant  $\eta$ , and thus the added revolute joint will be redundant. In practice, for the machined conjugate cams with profile errors, the magnitude of angle  $\eta^*$  will vary with respect to the cam rotation angle  $\theta$ , and the variation of the subtending angle of the follower arms,  $\Delta\eta$  ( $=\eta^* - \eta$ ), may indicate the variation of profile errors. Then through actually measuring the magnitude of  $\Delta\eta$  with respect to  $\theta$ , the magnitude of the cam profile errors can be found. Thus, a measuring fixture consists of oscillating arms 3 and 4. The magnitude of the subtending angle variation between arms 3 and 4 can be measured by a dial indicator mounted to arm 3 with its contact tip touching the extended end of arm 4. This type of measuring fixture has been

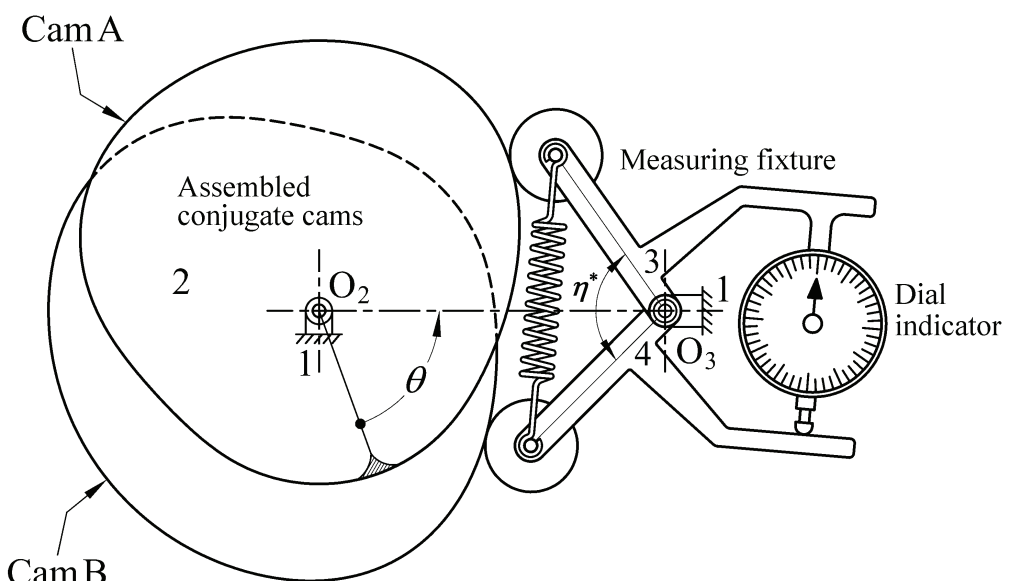


**Figure 6.1** Assembled conjugate cams with a measuring fixture consisting of two oscillating roller followers.

introduced by Koloc and Václavík [3] but without mathematical model to relate the subtending angle variation and the cam profile errors.

On the other hand, for the conjugate cam mechanism shown in Fig. 2.8, the distance from the cam center  $O_2$  to the follower pivot center  $O_3, f$ , is also a constant. If, as shown in Fig. 6.2, a slider (link 4) is intentionally added to connect the frame (link 1) and the follower (link 3) such that the center distance,  $f^*$ , is changed to be variable, the mechanism will no longer be overconstrained. In this case, the follower is pivoted to the slider as a floating link. When the cams rotate, in the extreme case that the machined conjugate cams have no profile errors, the center distance  $f^*$  will always equal the constant  $f$ , and thus the added slider will be redundant. Because the machined conjugate cams are unavoidably with profile errors, the magnitude of distance  $f^*$  will vary with respect to the cam rotation angle  $\theta$ , and the variation of the center distance,  $\Delta f$  ( $=f^* - f$ ), may indicate the variation of profile errors. Then through actually measuring the magnitude of  $\Delta f$  with respect to the cam rotation angle  $\theta$ , the magnitude of the cam profile errors can be found. Thus, a measuring fixture consists of floating link 3 pivoted to slider 4. The magnitude of the center distance variation can be measured by a dial indicator mounted to the frame with its

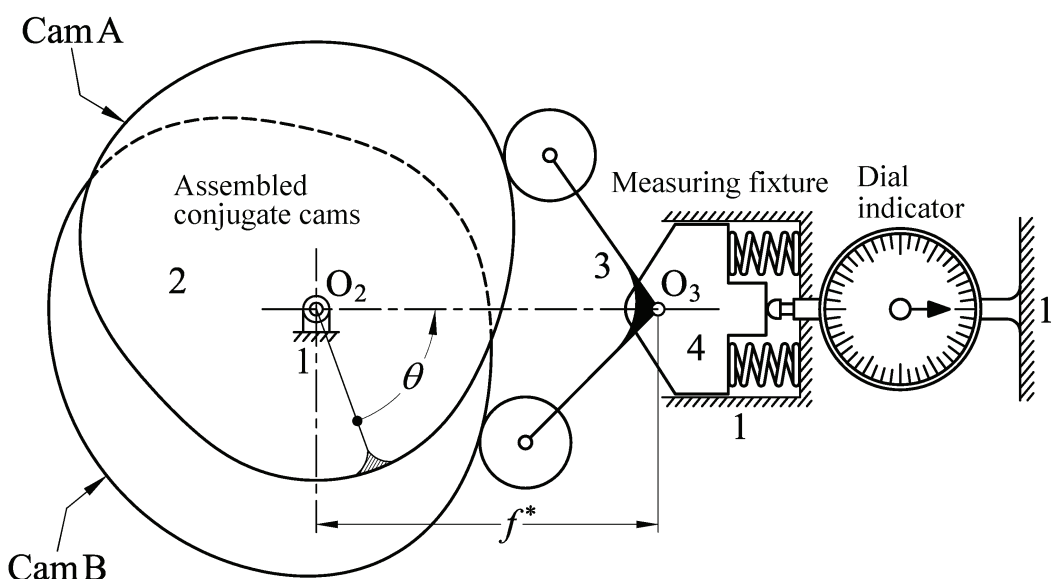


**Figure 6.2** Assembled conjugate cams with a measuring fixture consisting of a floating roller follower pivoted to a slider.

contact tip touching slider 4. The center distance variation,  $\Delta f$ , is a linear deviation amount and can be directly read from the dial indicator. But the subtending angle variation,  $\Delta\eta$ , is an angular deviation amount and must be transformed from the linear motion variation of the indicator reading. Therefore, in practice, the proposed mechanism shown in Fig. 6.2 should be more convenient than that shown in Fig. 6.1 for inspection tasks.

Both the concise measurement methods can be applied to quickly examine the conjugate conditions of assembled conjugate disk cams and are especially suitable for mass production. They must have mathematical models to relate the conjugate conditions (the subtending angle variation and the center distance variation) and the cam profile errors. Such models can be constructed by means of mechanical error analysis of disk cam mechanisms.

In addition, measuring fixtures for other types of conjugate cam mechanisms (conjugate cams with an offset translating roller follower, conjugate cams with an offset translating oblique flat-faced follower, and conjugate cams with an oscillating flat-faced follower) can also be developed. Based on the principle introduced in this section, some developed measuring fixtures for these cam mechanisms are given in Appendix C.

### 6.3 EQUIVALENT LINKAGE AND CONJUGATE CONDITION

#### ANALYSIS

The kinematic analysis of a conjugate cam mechanism can be simplified by replacing the mechanism by an equivalent linkage [10, 38, 100, 101]. In addition, such a replacement also provides a convenient means for determining the extent of the conjugate condition of the cam mechanism. That is, the equivalent linkage method developed in Chapter 3 can be applied to undertake the conjugate condition analysis of the two assembled conjugate cam mechanisms shown in Figs. 6.1 and 6.2. In the following analysis, only the tolerance on the dimension of the cam mechanism is considered to cause the conjugate condition variation. Other factors which may also affect the conjugate condition, such as the clearance in joints

and deflections of the links, can be dealt with by means of equivalent tolerance proposed by Garrett and Hall [103]. In practice, clearances in joints can be reduced by proper fit and applying preload [111].

### 6.3.1 Analysis of Subtending Angle Variation

For the assembled cam mechanism shown in Fig. 6.3(a), its two cams A and B are fixed on a common shaft, but its two followers are two different links, links 3 and 4. Let  $K_A$  and  $K_B$  be the respective centers of curvature of the cams in contact with the followers. Its equivalent linkage is the Watt II six-bar linkage shown in Fig. 6.3(b), in which the couplers (links 5 and 6) of the linkage connect the centers of curvature of the cams,  $K_A$  and  $K_B$ , and the roller centers, C and D, respectively. Then the instantaneous velocities and accelerations of the rockers (links 3 and 4) with respect to the crank (link 2) rotation shown in Fig. 6.3(b) are identical to those of the two respective followers with respect to the cam rotation shown in Fig. 6.3(a).

In practice, the profile of a machined cam may slightly deviate from the theoretical contour, and a deviation in the follower motion will be encountered. Since the instantaneous kinematic characteristics of a cam mechanism are identical to those of its equivalent linkage, the conjugate condition analysis of the assembled conjugate cam mechanism can be performed through the mechanical error analysis of its equivalent linkage. In other words, if the profile errors in the normal directions of the machined cams,  $\Delta n_A$  and  $\Delta n_B$ , equal the coupler-length errors of the equivalent linkage,  $\Delta r_5$  and  $\Delta r_6$ , respectively, their output links will also have the same respective angular motion deviations. Therefore, the conjugate condition analysis of the cam mechanism shown in Fig. 6.3(a) can be regarded as the mechanical error analysis of the linkage shown in Fig. 6.3(b). As a result, the equivalent linkage method proposed in Chapter 3 can be employed to calculate the subtending angle variation of the output links of the equivalent linkage.

For the two-loop linkage shown in Fig. 6.3(b), the two displacement equations, relating the parameters  $r_1$ ,  $r_{2A}$ ,  $r_{2B}$ ,  $r_3$ ,  $r_4$ ,  $r_5$ ,  $r_6$ ,  $\beta$  to the input and output variables  $\theta_2$ ,  $\theta_3$ ,

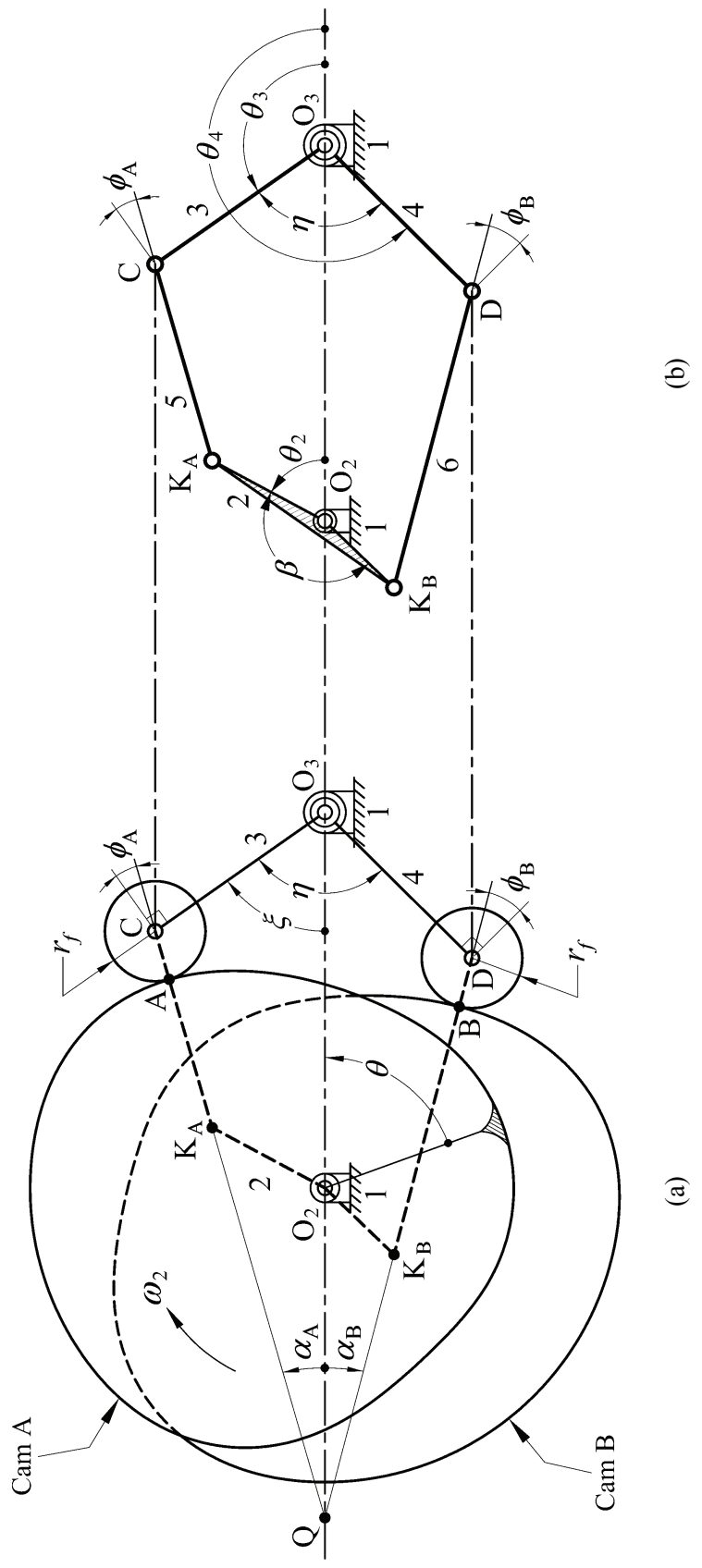


**Figure 6.3** Conjugate cam mechanism with two oscillating roller followers and its equivalent six-bar linkage.

and  $\theta_4$ , may be written as

$$\mathbf{F} = \begin{Bmatrix} F_A \\ F_B \end{Bmatrix} = \begin{Bmatrix} 0 \\ 0 \end{Bmatrix} \quad (6.1)$$

for

$$F_A = 2[r_1(r_3 \cos \theta_3 - r_{2A} \cos \theta_2) - r_{2A}r_3 \cos(\theta_2 - \theta_3)] + r_1^2 + r_{2A}^2 + r_3^2 - r_5^2 \quad (6.2)$$

$$F_B = 2\{r_1[r_4 \cos \theta_4 - r_{2B} \cos(\theta_2 + \beta)] + r_{2B}r_4 \cos(\theta_2 + \beta - \theta_4)\} + r_1^2 + r_{2B}^2 + r_4^2 - r_6^2 \quad (6.3)$$

where  $r_1 = O_2O_3 = f$ ,  $r_{2A} = O_2K_A$ ,  $r_{2B} = O_2K_B$ ,  $r_3 = O_3C = l_A$ ,  $r_4 = O_3D = l_B$ ,  $r_5 = K_AC$ ,  $r_6 = K_BD$ ,  $\beta = \angle K_AO_2K_B$ , and  $\theta_4 = \theta_3 + \eta$ . For small errors of all design parameters, the differentials of the functions  $F_A$  and  $F_B$  may be written in terms of their respective partial derivatives as

$$dF_A \approx \Delta F_A \\ = \frac{\partial F_A}{\partial r_1} \Delta r_1 + \frac{\partial F_A}{\partial r_{2A}} \Delta r_{2A} + \frac{\partial F_A}{\partial r_3} \Delta r_3 + \frac{\partial F_A}{\partial r_5} \Delta r_5 + \frac{\partial F_A}{\partial \theta_2} \Delta \theta_2 + \frac{\partial F_A}{\partial \theta_3} \Delta \theta_3 = 0 \quad (6.4)$$

$$dF_B \approx \Delta F_B \\ = \frac{\partial F_B}{\partial r_1} \Delta r_1 + \frac{\partial F_B}{\partial r_{2B}} \Delta r_{2B} + \frac{\partial F_B}{\partial r_4} \Delta r_4 + \frac{\partial F_B}{\partial r_6} \Delta r_6 + \frac{\partial F_B}{\partial \beta} \Delta \beta + \frac{\partial F_B}{\partial \theta_2} \Delta \theta_2 + \frac{\partial F_B}{\partial \theta_4} \Delta \theta_4 \\ = 0 \quad (6.5)$$

### **Variation caused by $\Delta r_5$ and $\Delta r_6$ :**

If only  $\Delta r_5$  is considered to induce the output error  $\Delta \theta_3$ , the output mechanical error of link 3 can be expressed as

$$\Delta \theta_3 = -\frac{\partial F_A / \partial r_5}{\partial F_A / \partial \theta_3} \Delta r_5 \quad (6.6)$$

The quantity  $\Delta r_5$  is the resultant deviation of the profile error of cam A,  $\Delta n_A$ , together with the radius error of roller C,  $\Delta r_{fC}$ . That is,  $\Delta r_5 = \Delta n_A + \Delta r_{fC}$  and  $\Delta r_{fC} = r_{fC} - r_f$  where  $r_{fC}$  and  $r_f$  denote the actual and theoretical radii of the follower roller C, respectively. Recall from Fig. 6.3 that  $\xi(\theta) = 180^\circ - \theta_3$ , and thus the motion error of follower 3 is  $\Delta S_A = \Delta \xi = -\Delta \theta_3$ .

After some manipulation and reduction, the mechanical errors  $\Delta S_{An}$  and  $\Delta S_{Arf}$  caused respectively by  $\Delta n_A$  and  $\Delta r_{fC}$  are

$$\begin{aligned}\Delta S_{An} &= -\Delta \theta_3 = \frac{r_5}{r_3[r_1 \sin \theta_3 + r_{2A} \sin(\theta_2 - \theta_3)]} (\Delta r_5 - \Delta r_{fC}) \\ &= \frac{\Delta r_5 - \Delta r_{fC}}{r_3 \cos \phi_A} = \frac{\Delta n_A}{l_A \cos \phi_A}\end{aligned}\quad (6.7)$$

$$\begin{aligned}\Delta S_{Arf} &= -\Delta \theta_3 = \frac{r_5}{r_3[r_1 \sin \theta_3 + r_{2A} \sin(\theta_2 - \theta_3)]} (\Delta r_5 - \Delta n_A) \\ &= \frac{\Delta r_5 - \Delta n_A}{r_3 \cos \phi_A} = \frac{\Delta r_{fC}}{l_A \cos \phi_A}\end{aligned}\quad (6.8)$$

Likewise, if only  $\Delta r_6$  is considered to induce the output error  $\Delta \theta_4$ , the output mechanical error of link 4 can be expressed as

$$\Delta \theta_4 = -\frac{\partial F_B / \partial r_6}{\partial F_B / \partial \theta_4} \Delta r_6 \quad (6.9)$$

Similarly, the quantity  $\Delta r_6$  is the resultant deviation of the profile error of cam B,  $\Delta n_B$ , together with the radius error of roller D,  $\Delta r_{fD}$ . That is,  $\Delta r_6 = \Delta n_B + \Delta r_{fD}$  and  $\Delta r_{fD} = r_{fD} - r_f$  where  $r_{fD}$  and  $r_f$  denote the actual and theoretical radii of the follower roller D, respectively. Recall from Fig. 6.3 that  $\xi(\theta) - \eta = 180^\circ - \theta_4$ , and thus the motion error of follower 4 is  $\Delta S_B = \Delta \xi = -\Delta \theta_4$ . After some manipulation and reduction, the mechanical errors  $\Delta S_{Bn}$  and  $\Delta S_{Brf}$  caused respectively by  $\Delta n_B$  and  $\Delta r_{fD}$  are

$$\begin{aligned}\Delta S_{Bn} &= -\Delta \theta_4 = \frac{r_6}{2r_4[r_1 \sin \theta_4 + r_{2B} \sin(\theta_2 + \beta - \theta_4)]} (\Delta r_6 - \Delta r_{fD}) \\ &= -\frac{\Delta r_6 - \Delta r_{fD}}{r_4 \cos \phi_B} = -\frac{\Delta n_B}{l_B \cos \phi_B}\end{aligned}\quad (6.10)$$

$$\begin{aligned}\Delta S_{Brf} &= -\Delta \theta_4 = \frac{r_6}{2r_4[r_1 \sin \theta_4 + r_{2B} \sin(\theta_2 + \beta - \theta_4)]} (\Delta r_6 - \Delta n_B) \\ &= -\frac{\Delta r_6 - \Delta n_B}{r_4 \cos \phi_B} = -\frac{\Delta r_{fD}}{l_B \cos \phi_B}\end{aligned}\quad (6.11)$$

Therefore, the variation of the subtending angle of the followers caused by the conjugate cam profile errors,  $\Delta\eta_n$ , is

$$\Delta\eta_n = \Delta S_{An} - \Delta S_{Bn} = \frac{\Delta n_A}{l_A \cos\phi_A} + \frac{\Delta n_B}{l_B \cos\phi_B} \quad (6.12)$$

Also, the variation of the subtending angle of the followers caused by the roller-radius errors,  $\Delta\eta_{rf}$ , is

$$\Delta\eta_{rf} = \Delta S_{A_{rf}} - \Delta S_{B_{rf}} = \frac{\Delta r_{fC}}{l_A \cos\phi_A} + \frac{\Delta r_{fD}}{l_B \cos\phi_B} \quad (6.13)$$

### ***Variation caused only by $\Delta r_i$ :***

If only  $\Delta r_1$  (or  $\Delta f$ ) is considered to induce the output error  $\Delta\theta_3$ , the output mechanical error of link 3 can be expressed as

$$\Delta\theta_3 = -\frac{\partial F_A / \partial r_1}{\partial F_A / \partial \theta_3} \Delta r_1 \quad (6.14)$$

After some manipulation and reduction, it follows that

$$\begin{aligned} \Delta S_{Af} = -\Delta\theta_3 &= -\frac{r_1 + r_3 \cos\theta_3 - r_{2A} \cos\theta_2}{r_3[r_1 \sin\theta_3 + r_{2A} \sin(\theta_2 - \theta_3)]} \Delta r_1 = -\frac{\Delta r_1 \sin(\theta_3 - \phi_A)}{r_3 \cos\phi_A} \\ &= -\frac{\Delta f \sin(\xi + \phi_A)}{l_A \cos\phi_A} = -\frac{\Delta f \cos\alpha_A}{l_A \cos\phi_A} \end{aligned} \quad (6.15)$$

Likewise, if only  $\Delta r_1$  (or  $\Delta f$ ) is considered to induce the output error  $\Delta\theta_4$ , the output mechanical error of link 4 can be expressed as

$$\Delta\theta_4 = -\frac{\partial F_B / \partial r_1}{\partial F_B / \partial \theta_4} \Delta r_1 \quad (6.16)$$

After some manipulation and reduction, it follows that

$$\begin{aligned} \Delta S_{Bf} = -\Delta\theta_4 &= -\frac{r_1 + r_4 \cos\theta_4 - r_{2B} \cos(\theta_2 + \beta)}{r_4[r_1 \sin\theta_4 + r_{2B} \sin(\theta_2 + \beta - \theta_4)]} \Delta r_1 = -\frac{\Delta r_1 \sin(\theta_4 + \phi_B)}{r_4 \cos\phi_B} \\ &= -\frac{\Delta f \sin(\xi - \eta - \phi_B)}{l_B \cos\phi_B} = \frac{\Delta f \cos\alpha_B}{l_B \cos\phi_B} \end{aligned} \quad (6.17)$$

Therefore, the variation of the subtending angle of the followers caused by the distance error between the cam and follower pivots,  $\Delta\eta_f$ , is

$$\Delta\eta_f = \Delta S_{Af} - \Delta S_{Bf} = -\Delta f \left( \frac{\cos\alpha_A}{l_A \cos\phi_A} + \frac{\cos\alpha_B}{l_B \cos\phi_B} \right) \quad (6.18)$$

### **Variation caused by $\Delta r_3$ and $\Delta r_4$ :**

If only  $\Delta r_3$  (or  $\Delta l_A$ ) is considered to induce the output error  $\Delta\theta_3$ , the output mechanical error of link 3 can be expressed as

$$\Delta\theta_3 = -\frac{\partial F_A / \partial r_3}{\partial F_A / \partial \theta_3} \Delta r_3 \quad (6.19)$$

After some manipulation and reduction, the final result is

$$\begin{aligned} \Delta S_{Al} = -\Delta\theta_3 &= -\frac{r_3 + r_1 \cos\theta_3 - r_{2A} \cos(\theta_2 - \theta_3)}{r_3[r_1 \sin\theta_3 + r_{2A} \sin(\theta_2 - \theta_3)]} \Delta r_3 \\ &= \frac{\Delta r_3 \tan\phi_A}{r_3} = \frac{\Delta l_A \tan\phi_A}{l_A} \end{aligned} \quad (6.20)$$

Likewise, if only  $\Delta r_4$  (or  $\Delta l_B$ ) is considered to induce the output error  $\Delta\theta_4$ , the output mechanical error of link 4 can be expressed as

$$\Delta\theta_4 = -\frac{\partial F_B / \partial r_4}{\partial F_B / \partial \theta_4} \Delta r_4 \quad (6.21)$$

After some manipulation and reduction, the final result is

$$\begin{aligned} \Delta S_{Bl} = -\Delta\theta_4 &= -\frac{r_4 + r_1 \cos\theta_4 + r_{2B} \cos(\theta_2 + \beta - \theta_4)}{r_4[r_1 \sin\theta_4 + r_{2B} \sin(\theta_2 + \beta - \theta_4)]} \Delta r_4 \\ &= -\frac{\Delta r_4 \tan\phi_B}{r_4} = -\frac{\Delta l_B \tan\phi_B}{l_B} \end{aligned} \quad (6.22)$$

Therefore, the variation of the subtending angle of the followers caused by the errors of the arm lengths,  $\Delta\eta_l$ , is

$$\Delta\eta_l = \Delta S_{Al} - \Delta S_{Bl} = \frac{\Delta l_A \tan\phi_A}{l_A} + \frac{\Delta l_B \tan\phi_B}{l_B} \quad (6.23)$$

Equations (6.12), (6.13), (6.18), and (6.23) indicate that the pressure angles have a significant effect on the resulting errors; it appears in the form of  $(1/\cos\phi_A)$  and  $(1/\cos\phi_B)$  to magnify them. In addition, it is interesting to note that in the final expressions of Eqs. (6.12), (6.13), (6.18), and (6.23), the parameters  $r_{2A}$ ,  $r_{2B}$ ,  $r_5$ ,  $r_6$ , and  $\beta$  are not actually involved. In other words, locating the curvature centers of the cam profiles in the analysis process is not really essential, and this fact makes the analysis easier to perform.

### **Variation caused by $\Delta r_A$ and $\Delta r_B$ :**

Recall from Fig. 5.2 and Eqs. (3.9), (5.3)~(5.6) that the correlation between the normal-direction errors and the radial-dimension errors of the conjugate cam profiles can be expressed as

$$\Delta n_A \approx \Delta r_A \cos \lambda_A \quad (6.24)$$

$$\Delta n_B \approx \Delta r_B \cos \lambda_B \quad (6.25)$$

Then from Eqs. (6.12), (6.24), and (6.25), the final result is

$$\Delta \eta_r = \Delta S_{Ar} - \Delta S_{Br} \approx \frac{\Delta r_A \cos \lambda_A}{l_A \cos \phi_A} + \frac{\Delta r_B \cos \lambda_B}{l_B \cos \phi_B} \quad (6.26)$$

This shows how the radial-dimension errors of the cam profiles affect the subtending angle variation of the oscillating followers. Note that the effect of the pressure angles on the resulting error is counteracted by the shift angles.

### **6.3.2 Analysis of Center Distance Variation**

For the conjugate cam mechanism shown in Fig. 6.4(a), its two cams A and B are fixed on a common shaft, while its roller follower, links 3, is pivoted on slider 4 instead of the frame (link 1). Let  $K_A$  and  $K_B$  be the centers of curvature of the cams in contact with the follower rollers. Its equivalent linkage is the Stephenson II six-bar linkage shown in Fig. 6.4(b), in which the couplers (links 5 and 6) of the linkage connect the centers of curvature of the cams,  $K_A$  and  $K_B$ , and the roller centers, C and D, respectively. The instantaneous

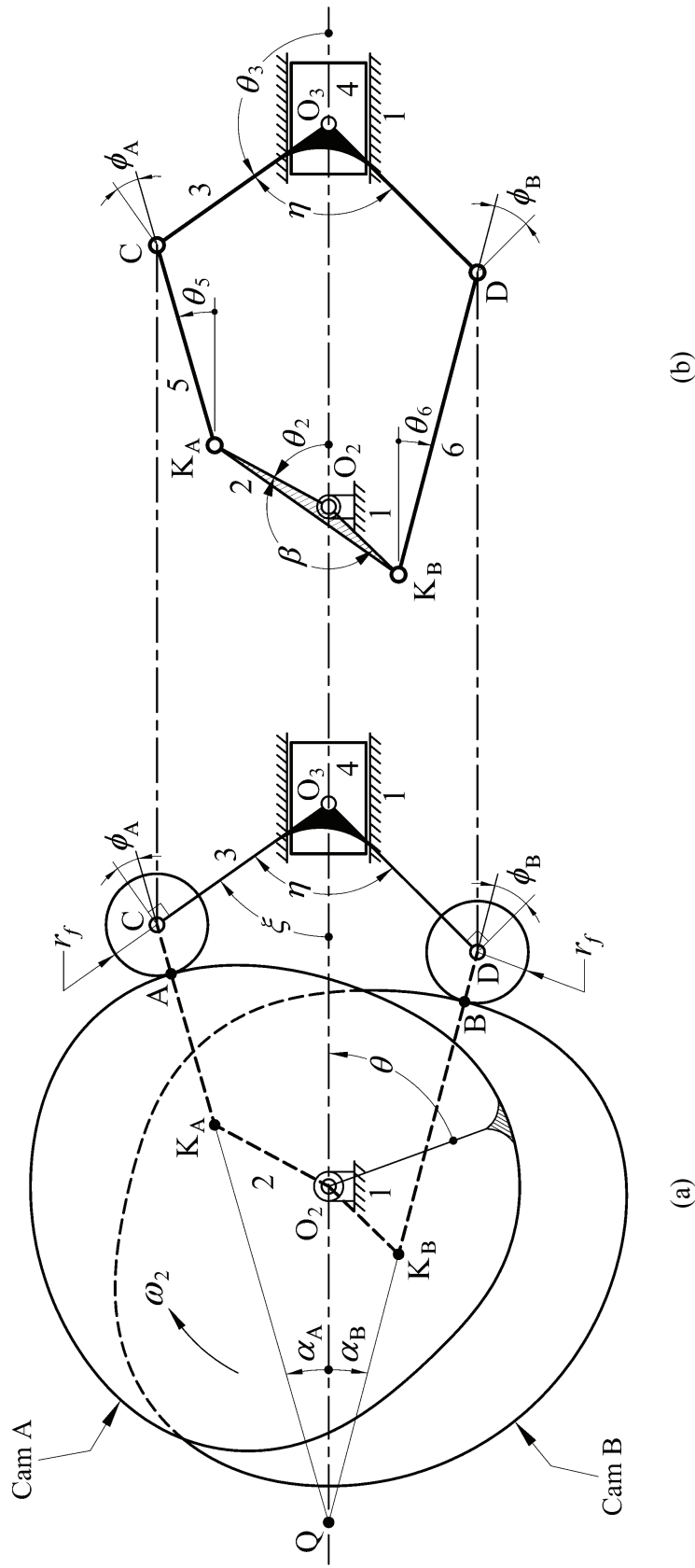


**Figure 6.4** Conjugate cam mechanism with a slider-pivoted floating roller follower and its equivalent six-bar linkage.

velocities and accelerations of the floating ternary link (link 3) and the frame-connected slider (link 4) with respect to the crank (link 2) rotation shown in Fig. 6.4(b) are identical to those of the respective follower and additional slider with respect to the cam rotation shown in Fig. 6.4(a). The conjugate condition analysis of the cam mechanism shown in Fig. 6.4(a) can be regarded as the mechanical error analysis of the equivalent linkage shown in Fig. 6.4(b). By employing the equivalent linkage method proposed in Chapter 3, the center distance variation of the output links of the equivalent linkage can be calculated.

For the two-loop linkage shown in Fig. 6.4(b), the two displacement equations, relating the parameters  $r_{2A}$ ,  $r_{2B}$ ,  $r_{3A}$ ,  $r_{3B}$ ,  $r_5$ ,  $r_6$ ,  $\beta$ ,  $\eta$  to the input and output variables  $\theta_2$ ,  $\theta_3$ , and  $r_1$ , may be written as

$$\mathbf{F} = \begin{Bmatrix} F_A \\ F_B \end{Bmatrix} = \begin{Bmatrix} 0 \\ 0 \end{Bmatrix} \quad (6.27)$$

for

$$F_A = 2[r_1(r_{3A} \cos \theta_3 - r_{2A} \cos \theta_2) - r_{2A}r_{3A} \cos(\theta_2 - \theta_3)] + r_1^2 + r_{2A}^2 + r_{3A}^2 - r_5^2 \quad (6.28)$$

$$F_B = 2\{r_1[r_{3B} \cos(\theta_3 + \eta) - r_{2B} \cos(\theta_2 + \beta)] - r_{2B}r_{3B} \cos(\theta_2 + \beta - \theta_3 - \eta)\} + r_1^2 + r_{2B}^2 + r_{3B}^2 - r_6^2 \quad (6.29)$$

where  $r_1 = O_2O_3 = f$ ,  $r_{2A} = O_2K_A$ ,  $r_{2B} = O_2K_B$ ,  $r_{3A} = O_3C = l_A$ ,  $r_{3B} = O_3D = l_B$ ,  $r_5 = K_AC$ ,  $r_6 = K_BD$ ,  $\beta = \angle K_AO_2K_B$ , and  $\eta = \angle CO_3D$ . For small values of the errors  $\Delta r_1$ ,  $\Delta r_{2A}$ ,  $\Delta r_{2B}$ ,  $\Delta r_{3A}$ ,  $\Delta r_{3B}$ ,  $\Delta r_5$ ,  $\Delta r_6$ ,  $\Delta \beta$ ,  $\Delta \eta$ ,  $\Delta \theta_2$ , and  $\Delta \theta_3$ , the differentials of the functions  $F_A$  and  $F_B$  may be written in terms of their partial derivatives as

$$dF_A \approx \Delta F_A = \frac{\partial F_A}{\partial r_1} \Delta r_1 + \frac{\partial F_A}{\partial r_{2A}} \Delta r_{2A} + \frac{\partial F_A}{\partial r_{3A}} \Delta r_{3A} + \frac{\partial F_A}{\partial r_5} \Delta r_5 + \frac{\partial F_A}{\partial \theta_2} \Delta \theta_2 + \frac{\partial F_A}{\partial \theta_3} \Delta \theta_3 = 0 \quad (6.30)$$

$$dF_B \approx \Delta F_B = \frac{\partial F_B}{\partial r_1} \Delta r_1 + \frac{\partial F_B}{\partial r_{2B}} \Delta r_{2B} + \frac{\partial F_B}{\partial r_{3B}} \Delta r_{3B} + \frac{\partial F_B}{\partial r_6} \Delta r_6 + \frac{\partial F_B}{\partial \beta} \Delta \beta + \frac{\partial F_B}{\partial \eta} \Delta \eta + \frac{\partial F_B}{\partial \theta_2} \Delta \theta_2 + \frac{\partial F_B}{\partial \theta_3} \Delta \theta_3 = 0 \quad (6.31)$$

### **Variation caused by $\Delta r_5$ and $\Delta r_6$ :**

If  $\Delta r_5$  and  $\Delta r_6$  are simultaneously considered to induce the output errors  $\Delta r_1$  and  $\Delta \theta_3$ , then from Eqs. (6.30) and (6.31), the mechanical error at the outputs (links 3 and 4) can be expressed as

$$\begin{Bmatrix} \Delta r_1 \\ \Delta \theta_3 \end{Bmatrix} = - \begin{bmatrix} \partial F_A / \partial r_1 & \partial F_A / \partial \theta_3 \\ \partial F_B / \partial r_1 & \partial F_B / \partial \theta_3 \end{bmatrix}^{-1} \begin{Bmatrix} (\partial F_A / \partial r_5) \Delta r_5 \\ (\partial F_B / \partial r_6) \Delta r_6 \end{Bmatrix} \quad (6.32)$$

The quantity  $\Delta r_5$  is the resultant deviation of the profile error of cam A,  $\Delta n_A$ , and the radius error of roller C,  $\Delta r_{fC}$ . That is,  $\Delta r_5 = \Delta n_A + \Delta r_{fC}$  and  $\Delta r_{fC} = r_{fC} - r_f$  where  $r_{fC}$  and  $r_f$  denote the actual and theoretical radii of the follower roller C, respectively. Also, the quantity  $\Delta r_6$  is the resultant deviation of the profile error of cam B,  $\Delta n_B$ , and the radius error of roller D,  $\Delta r_{fD}$ . That is,  $\Delta r_6 = \Delta n_B + \Delta r_{fD}$  and  $\Delta r_{fD} = r_{fD} - r_f$  where  $r_{fD}$  and  $r_f$  denote the actual and theoretical radii of the follower roller D, respectively. Recall from Fig. 6.4 that  $\Delta f = \Delta r_1$  and  $\Delta \xi = -\Delta \theta_3$ , after some manipulation and reduction, the mechanical errors  $\Delta f_n$  and  $\Delta \xi_n$  caused by  $\Delta n_A$  and  $\Delta n_B$  are

$$\begin{aligned} \Delta f_n = \Delta r_1 &= \frac{(\Delta r_5 - \Delta r_{fC})(r_{3B} \cos \phi_B) + (\Delta r_6 - \Delta r_{fD})(r_{3A} \cos \phi_A)}{r_{3A} \cos \phi_A \cos \theta_6 + r_{3B} \cos \phi_B \cos \theta_5} \\ &= \frac{\Delta n_A (l_B \cos \phi_B) + \Delta n_B (l_A \cos \phi_A)}{l_A \cos \phi_A \cos \alpha_B + l_B \cos \phi_B \cos \alpha_A} \end{aligned} \quad (6.33)$$

$$\begin{aligned} \Delta \xi_n = -\Delta \theta_3 &= \frac{(\Delta r_5 - \Delta r_{fC}) \cos \theta_6 - (\Delta r_6 - \Delta r_{fD}) \cos \theta_5}{r_{3A} \cos \phi_A \cos \theta_6 + r_{3B} \cos \phi_B \cos \theta_5} \\ &= \frac{\Delta n_A \cos \alpha_B - \Delta n_B \cos \alpha_A}{l_A \cos \phi_A \cos \alpha_B + l_B \cos \phi_B \cos \alpha_A} \end{aligned} \quad (6.34)$$

Likewise, the mechanical errors  $\Delta f_{rf}$  and  $\Delta \xi_{rf}$  caused by  $\Delta r_{fC}$  and  $\Delta r_{fD}$  are

$$\begin{aligned} \Delta f_{rf} = \Delta r_1 &= \frac{(\Delta r_5 - \Delta n_A)(r_{3B} \cos \phi_B) + (\Delta r_6 - \Delta n_B)(r_{3A} \cos \phi_A)}{r_{3A} \cos \phi_A \cos \theta_6 + r_{3B} \cos \phi_B \cos \theta_5} \\ &= \frac{\Delta r_{fC} (l_B \cos \phi_B) + \Delta r_{fD} (l_A \cos \phi_A)}{l_A \cos \phi_A \cos \alpha_B + l_B \cos \phi_B \cos \alpha_A} \end{aligned} \quad (6.35)$$

$$\begin{aligned}\Delta\xi_{rf} &= -\Delta\theta_3 = \frac{(\Delta r_5 - \Delta n_A) \cos\theta_6 - (\Delta r_6 - \Delta n_B) \cos\theta_5}{r_{3A} \cos\phi_A \cos\theta_6 + r_{3B} \cos\phi_B \cos\theta_5} \\ &= \frac{\Delta r_{fC} \cos\alpha_B - \Delta r_{fD} \cos\alpha_A}{l_A \cos\phi_A \cos\alpha_B + l_B \cos\phi_B \cos\alpha_A}\end{aligned}\quad (6.36)$$

### **Variation caused by $\Delta r_{3A}$ and $\Delta r_{3B}$ :**

If  $\Delta r_{3A}$  ( $= \Delta l_A$ ) and  $\Delta r_{3B}$  ( $= \Delta l_B$ ) are simultaneously considered to induce the output errors  $\Delta r_1$  and  $\Delta\theta_3$ , then from Eqs. (6.30) and (6.31), the mechanical error at the outputs (links 3 and 4) can be expressed as

$$\begin{Bmatrix} \Delta r_1 \\ \Delta\theta_3 \end{Bmatrix} = - \begin{bmatrix} \partial F_A / \partial r_1 & \partial F_A / \partial \theta_3 \\ \partial F_B / \partial r_1 & \partial F_B / \partial \theta_3 \end{bmatrix}^{-1} \begin{Bmatrix} (\partial F_A / \partial r_{3A}) \Delta r_{3A} \\ (\partial F_B / \partial r_{3B}) \Delta r_{3B} \end{Bmatrix} \quad (6.37)$$

After some manipulation and reduction, it follows that

$$\begin{aligned}\Delta f_l = \Delta r_1 &= \frac{\Delta r_{3A} (r_{3B} \cos\phi_B \sin\phi_A) + \Delta r_{3B} (r_{3A} \cos\phi_A \sin\phi_B)}{r_{3A} \cos\phi_A \cos\theta_6 + r_{3B} \cos\phi_B \cos\theta_5} \\ &= \frac{\Delta l_A (l_B \cos\phi_B \sin\phi_A) + \Delta l_B (l_A \cos\phi_A \sin\phi_B)}{l_A \cos\phi_A \cos\alpha_B + l_B \cos\phi_B \cos\alpha_A}\end{aligned}\quad (6.38)$$

$$\begin{aligned}\Delta\xi_l = -\Delta\theta_3 &= \frac{\Delta r_{3A} (\cos\theta_6 \sin\phi_A) - \Delta r_{3B} (\cos\theta_5 \sin\phi_B)}{r_{3A} \cos\phi_A \cos\theta_6 + r_{3B} \cos\phi_B \cos\theta_5} \\ &= \frac{\Delta l_A (\cos\alpha_B \sin\phi_A) - \Delta l_B (\cos\alpha_A \sin\phi_B)}{l_A \cos\phi_A \cos\alpha_B + l_B \cos\phi_B \cos\alpha_A}\end{aligned}\quad (6.39)$$

### **Variation caused only by $\Delta\eta$ :**

If only  $\Delta\eta$  is considered to induce the output errors  $\Delta r_1$  and  $\Delta\theta_3$ , then from Eqs. (6.30) and (6.31), the mechanical error at the outputs (links 3 and 4) can be expressed as

$$\begin{aligned}\begin{Bmatrix} \Delta r_1 \\ \Delta\theta_3 \end{Bmatrix} &= - \begin{bmatrix} \partial F_A / \partial r_1 & \partial F_A / \partial \theta_3 \\ \partial F_B / \partial r_1 & \partial F_B / \partial \theta_3 \end{bmatrix}^{-1} \begin{Bmatrix} (\partial F_A / \partial \eta) \Delta\eta \\ (\partial F_B / \partial \eta) \Delta\eta \end{Bmatrix} \\ &= - \begin{bmatrix} \partial F_A / \partial r_1 & \partial F_A / \partial \theta_3 \\ \partial F_B / \partial r_1 & \partial F_B / \partial \theta_3 \end{bmatrix}^{-1} \begin{Bmatrix} 0 \\ (\partial F_B / \partial \eta) \Delta\eta \end{Bmatrix}\end{aligned}\quad (6.40)$$

After some manipulation and reduction, the final results are

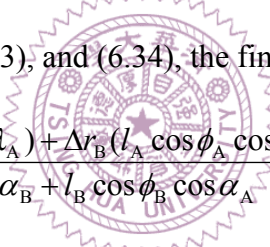
$$\begin{aligned}\Delta f_\eta = \Delta r_1 &= -\frac{\Delta\eta(r_{3A}r_{3B}\cos\phi_A\cos\phi_B)}{r_{3A}\cos\phi_A\cos\theta_6 + r_{3B}\cos\phi_B\cos\theta_5} \\ &= -\frac{\Delta\eta(l_A l_B \cos\phi_A \cos\phi_B)}{l_A \cos\phi_A \cos\alpha_B + l_B \cos\phi_B \cos\alpha_A}\end{aligned}\quad (6.41)$$

$$\begin{aligned}\Delta\xi_\eta = -\Delta\theta_3 &= -\frac{\Delta\eta(r_{3B}\cos\phi_B\cos\theta_5)}{r_{3A}\cos\phi_A\cos\theta_6 + r_{3B}\cos\phi_B\cos\theta_5} \\ &= -\frac{\Delta\eta(l_B \cos\phi_B \cos\alpha_A)}{l_A \cos\phi_A \cos\alpha_B + l_B \cos\phi_B \cos\alpha_A}\end{aligned}\quad (6.42)$$

It is interesting to note that in the final expressions of Eqs. (6.33)~(6.36), (6.38), (6.39), (6.41), and (6.42), the parameters  $r_{2A}$ ,  $r_{2B}$ ,  $r_5$ ,  $r_6$ , and  $\beta$  are not actually involved. In other words, locating the curvature centers of the cam profiles in the analysis process is not really essential, and this fact makes the analysis easier to perform.

#### **Variation caused by $\Delta r_A$ and $\Delta r_B$ :**

From Eqs. (6.24), (6.25), (6.33), and (6.34), the final results are



$$\Delta f_r = \Delta r_1 = \frac{\Delta r_A (l_B \cos\phi_B \cos\lambda_A) + \Delta r_B (l_A \cos\phi_A \cos\lambda_B)}{l_A \cos\phi_A \cos\alpha_B + l_B \cos\phi_B \cos\alpha_A} \quad (6.43)$$

$$\Delta\xi_r = -\Delta\theta_3 = \frac{\Delta r_A \cos\lambda_A \cos\alpha_B - \Delta r_B \cos\lambda_B \cos\alpha_A}{l_A \cos\phi_A \cos\alpha_B + l_B \cos\phi_B \cos\alpha_A} \quad (6.44)$$

This shows how the radial-dimension errors of the cam profiles affect the conjugate condition of the assembled cam mechanism.

## **6.4 EXAMPLES AND DISCUSSION**

The applications of the presented methods to a conjugate cam system will be illustrated by the following two examples. The illustrated conjugate cam system is the same of that designed for the experiment of Chapter 5. Referring to Fig. 2.8, the cam system requires the oscillating roller follower to oscillate  $30^\circ$  clockwise with cycloidal

motion while the cam rotates clockwise from  $0^\circ$  to  $120^\circ$ , dwell for the next  $40^\circ$ , return with cycloidal motion for  $120^\circ$  cam rotation, and dwell for the remaining  $80^\circ$ . The distance between pivots,  $f$ , is 120 mm, the lengths of the follower arms,  $l_A$  and  $l_B$ , are both equal to 66 mm, and both follower rollers have the same radius of 16 mm. The base circle radius of cam A,  $r_b$ , is 60 mm and the subtending angle of the follower arms,  $\eta$ , is  $100^\circ$ . The profiles of cams A and B, with respective maximum radial dimensions of 93.793 and 93.859 mm, are shown in Fig. 2.8.

#### 6.4.1 Application of Subtending Angle Variation

Considering the conjugate cam mechanism shown in Fig. 6.3(a), for a tolerance grade of IT6, the cam profiles may have deviations of  $\Delta r_A = \Delta r_B = 22 \mu\text{m}$ , the distance between pivots may have a deviation of  $\Delta f = 22 \mu\text{m}$ , and the follower arm lengths may have deviations of  $\Delta l_A = \Delta l_B = 19 \mu\text{m}$ . The radius errors of the rollers,  $\Delta r_{fC}$  and  $\Delta r_{fD}$ , may be ignored since they generally have a smaller tolerance grade and may have a magnitude of 3  $\mu\text{m}$  at most if precision rollers are used. Then the actual subtending angle of the follower arms will have deviations result from them, namely,  $\Delta\eta_r$  caused by  $\Delta r_A$  and  $\Delta r_B$ ,  $\Delta\eta_f$  caused by  $\Delta f$ , and  $\Delta\eta_l$  caused by  $\Delta l_A$  and  $\Delta l_B$ , respectively. The maximum limit variation of the subtending angle should be the sum of  $\Delta\eta_r$ ,  $\Delta\eta_f$ , and  $\Delta\eta_l$ . Note that this work is to provide a convenient and effective measurement method to inspect whether or not the cam profile deviations  $\Delta r_A$  and  $\Delta r_B$  lie within their specified tolerance zones along the ideal profiles. Therefore, for a measurement device constructed according to the presented approach, all design parameters other than the cam profiles should have been precisely measured and should be held constant. Accordingly, the three deviations of  $\Delta f$ ,  $\Delta l_A$  and  $\Delta l_B$  may be assumed to be known, and the magnitudes of subtending angle deviations  $\Delta\eta_f$  and  $\Delta\eta_l$  are to be evaluated.

In this example,  $\Delta f = 22 \mu\text{m}$  and  $\Delta l_A = \Delta l_B = 19 \mu\text{m}$  are assumed. The cam profile deviations may range from  $+\Delta r_A = +\Delta r_B = 22 \mu\text{m}$  to  $-\Delta r_A = -\Delta r_B = -22 \mu\text{m}$ , and the

upper and lower acceptable extreme deviations of the subtending angle will be

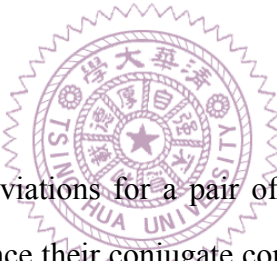
$$\Delta\eta^+ = \Delta\eta_r + \Delta\eta_f + \Delta\eta_l \quad (6.45)$$

and

$$\Delta\eta^- = -\Delta\eta_r + \Delta\eta_f + \Delta\eta_l \quad (6.46)$$

in which,  $\Delta\eta_r$  is caused by both  $+\Delta r_A$  and  $+\Delta r_B$ , and  $-\Delta\eta_r$  is caused by both  $-\Delta r_A$  and  $-\Delta r_B$ . A practical consequence of this argument is that, if the cam profile deviations fall within their specified tolerance zones, the measured value of the subtending angle variation  $\Delta\eta_{\text{mea}}$  will fall within the range of  $\Delta\eta^+ \sim \Delta\eta^-$ . In other words, if the measured value of  $\Delta\eta_{\text{mea}}$  falls outside the range of  $\Delta\eta^+ \sim \Delta\eta^-$ , then at least one cam profile deviation will fall outside its specified tolerance zones. That is, the necessary condition for a pair of qualified conjugate cam profiles is

$$\Delta\eta^- \leq \Delta\eta_{\text{mea}} \leq \Delta\eta^+ \quad (6.47)$$



On the other hand, the profile deviations for a pair of inspected cams may occasionally have compensating effect to enhance their conjugate condition. Therefore, even though the measured value of  $\Delta\eta_{\text{mea}}$  falls within the range of  $\Delta\eta^+ \sim \Delta\eta^-$ , this fact itself cannot ensure that both cam profiles are simultaneously qualified, but their conjugate condition may still be acceptable for the operating performance of the mechanism. Also note that the magnitude of the range  $\Delta\eta^+ \sim \Delta\eta^-$  varies at each position of the cam angle  $\theta$ . Thus, from the viewpoint of conjugate condition, a convenient but conservative criterion to qualify the cam profiles for a pair of inspected cams can be expressed as

$$(\Delta\eta_{\text{mea}})_{\text{max}} - (\Delta\eta_{\text{mea}})_{\text{min}} \leq (\Delta\eta^+ - \Delta\eta^-)_{\text{min}} = 2(\Delta\eta_r)_{\text{min}} \quad (6.48)$$

Since  $2(\Delta\eta_r)_{\text{min}}$  remains constant with  $\theta$ , this criterion will be easier to perform the inspection. Alternatively, another conservative criterion can be expressed as

$$(\Delta\eta_{\text{mea}})_{\text{max}} - (\Delta\eta_{\text{mea}})_{\text{min}} \leq \delta_\eta = \Delta\eta_{\text{min}}^+ - \Delta\eta_{\text{max}}^- \quad (6.49)$$

Also,  $(\Delta\eta_{\min}^+ - \Delta\eta_{\max}^-)$  is a constant. This criterion means that if the difference between the extremes of the measured subtending angle variation  $\Delta\eta_{\text{mea}}$  is less than  $\delta_\eta$ , the difference between the minimum value of  $\Delta\eta^+$  and the maximum value of  $\Delta\eta^-$ , the conjugate condition of the machined cam profiles are acceptable and are also on the conservative side.

The various resulting mechanical errors versus the cam rotation angle  $\theta$  of this conjugate cam mechanism are shown in Fig. 6.5, and the induced subtending angle variations are shown in Fig. 6.6, while their extreme values are also listed in Table 6.1. As can be seen from Figs. 6.5(a) and 6.5(b), a quite similarity between the pressure angle  $\phi_A$  and the shift angle  $\lambda_A$ , and also between the pressure angle  $\phi_B$  and the shift angle  $\lambda_B$  can be noted. Therefore, the variations of  $(1/\cos\phi_A)$  and  $(1/\cos\phi_B)$  are respectively flattened by  $\cos\lambda_A$  and  $\cos\lambda_B$ . As shown in Figs. 6.5(c) and 6.5(d), since  $0.9153 \leq (\cos\lambda_A / \cos\phi_A) \leq 1.1478$  and  $0.9156 \leq (\cos\lambda_B / \cos\phi_B) \leq 1.1468$ , the magnitudes of  $\Delta S_{A_r}$  and  $\Delta S_{B_r}$  have only slight variations. In Figs. 6.5(e) and 6.5(f), the variations of  $\Delta S_{A_r}$  and  $\Delta S_{B_r}$  are flatter than those of the other four error terms. As a result, the variation of  $\Delta\eta_r$  shown in Fig. 6.6(a) is also flatter than those of  $\Delta\eta_f$  and  $\Delta\eta_l$ . The minimum value of  $\Delta\eta_r$ , occurring at  $\theta = 220^\circ$ , has a magnitude of  $0.0358^\circ$ . In Fig. 6.6(b), the minimum value of  $\Delta\eta^+$ , occurring at  $\theta = 220.01^\circ$ , has a magnitude of  $0.0045^\circ$ , and the maximum value of  $\Delta\eta^-$ , occurring at  $\theta = 60.04^\circ$ , has a magnitude of  $-0.0643^\circ$ . As a result, the magnitude  $\delta_\eta$  (the difference between  $\Delta\eta_{\min}^+$  and  $\Delta\eta_{\max}^-$ ) is  $0.0688^\circ$ , which is very close to the magnitude of  $2(\Delta\eta_r)_{\min}$  ( $= 0.0716^\circ$ ). According to Eq. (6.49), if the difference between the extremes of the measured subtending angle variation  $\Delta\eta_{\text{mea}}$  is less than  $0.0688^\circ$ , the conjugate condition of a pair of assembled cam profiles is qualified to meet the level of the cam profile accuracy of tolerance grade IT6. Here, the region ranging between the two horizontal lines respectively passing through  $\Delta\eta_{\min}^+$  and  $\Delta\eta_{\max}^-$  is called the conservatively acceptable region for the cam profile inspection.

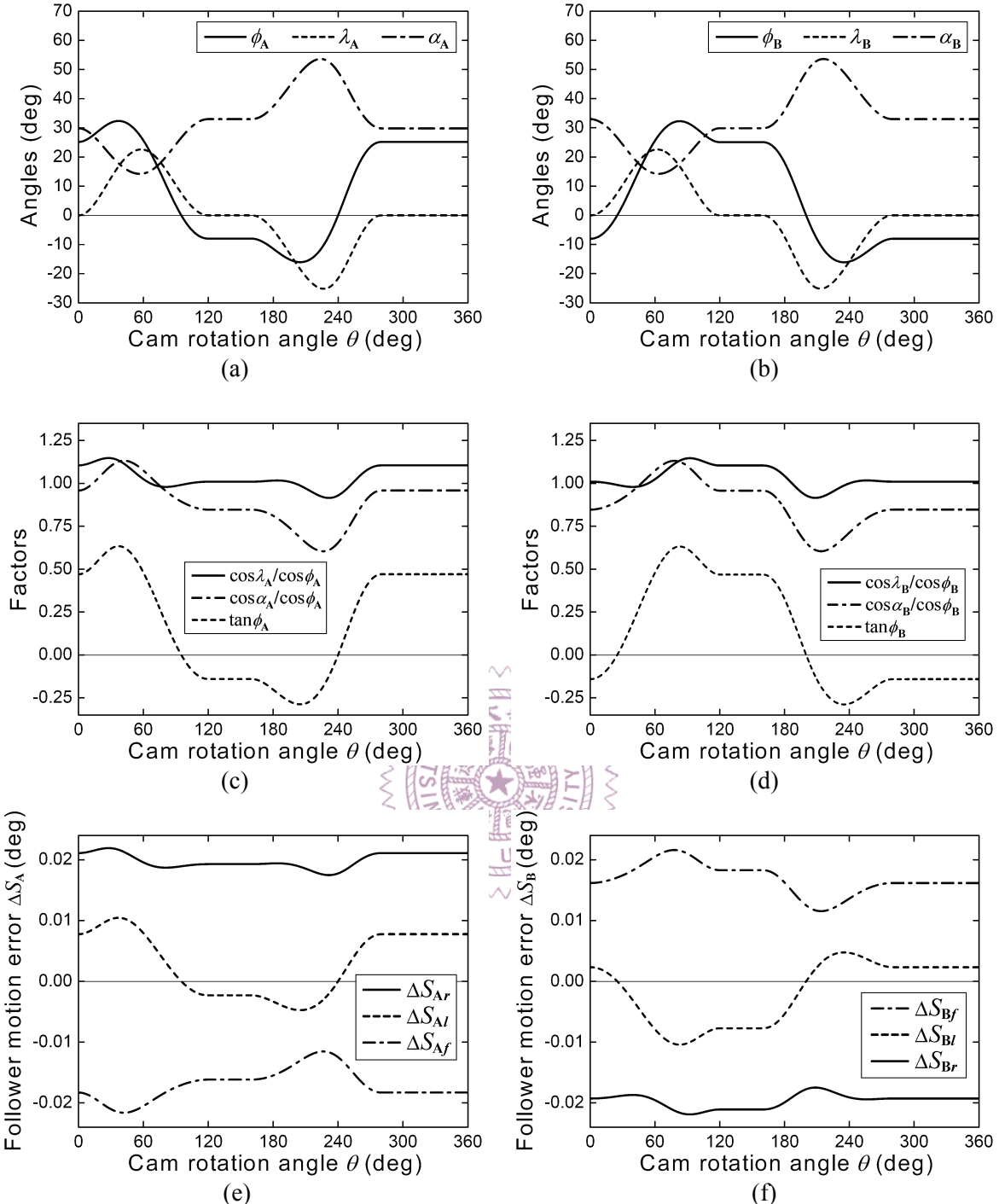


**Figure 6.5** Mechanical error analysis results of an assembled conjugate cam mechanism with two oscillating roller followers.

In practice, the magnitude of the subtending angle variation  $\Delta\eta_{\text{mea}}$  may be obtained by means of a dial indicator. As shown in Fig. 6.1, the perpendicular distance from the follower pivot center  $O_3$  to the measuring axis of the dial indicator is 76 mm. Then, a subtending angle variation  $\Delta\eta_{\text{mea}}$  of  $0.0688^\circ$  will be equivalent to a  $91.26 \mu\text{m}$  motion

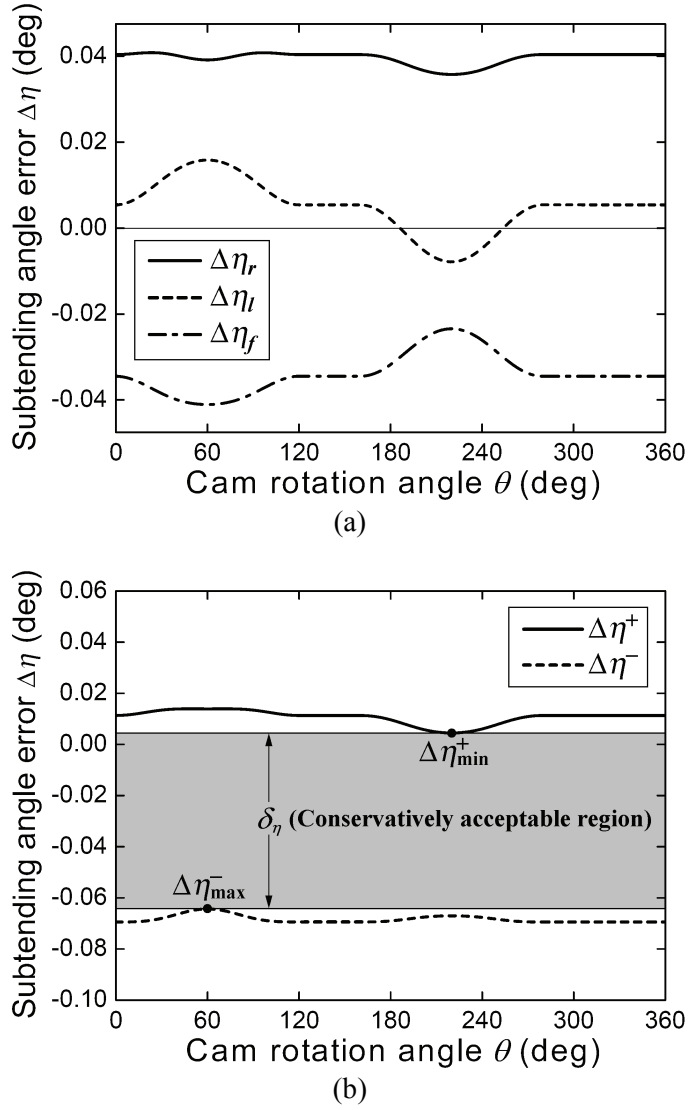


**Figure 6.6** Subtending angle variation of an assembled conjugate cam mechanism with two oscillating roller followers.

variation of the indicator reading, since  $76 \text{ mm} \times 0.0688^\circ \times \pi / 180^\circ = 91.26 \mu\text{m}$ . Therefore, in this case, in summary, the conjugate cam profiles are acceptable with sufficient accuracy if the motion variation of the indicator reading is less than  $91.26 \mu\text{m}$ , while the cam rotates  $360^\circ$  to complete one cycle.

If the tolerance grade of the cam profile errors is changed, the allowable variation of the subtending angle,  $\delta_\eta$ , will be correspondingly changed. Figure 6.7 shows the allowable variations of the subtending angle,  $\delta_\eta$ , with respect to various corresponding cam profile errors ( $\Delta r_A$  and  $\Delta r_B$ ) of some tolerance grades, while  $\Delta f = 22 \mu\text{m}$  and  $\Delta l_A = \Delta l_B = 19 \mu\text{m}$

**Table 6.1** Input angles and extreme values of an example for the application of subtending angle variation.

Input angle	Extreme value	Input angle	Extreme value
$\theta = 1.26^\circ$	$\Delta\eta_{\min}^- = -0.0694^\circ$	$\theta = 92.22^\circ$	$(\Delta S_{Br})_{\min} = -0.0219^\circ$
$\theta = 23.34^\circ$	$(\Delta\eta_r)_{\max} = 0.0408^\circ$	$\theta = 205^\circ$	$(\phi_A)_{\min} = -16.05^\circ$
$\theta = 27.79^\circ$	$(\cos\lambda_A / \cos\phi_A)_{\max} = 1.1478$	$\theta = 205^\circ$	$(\tan\phi_A)_{\min} = -0.2876$
$\theta = 27.79^\circ$	$(\Delta S_{Ar})_{\max} = 0.0219^\circ$	$\theta = 205^\circ$	$(\Delta S_{Al})_{\min} = -0.0047^\circ$
$\theta = 37.11^\circ$	$(\phi_A)_{\max} = 32.37^\circ$	$\theta = 208.43^\circ$	$(\cos\lambda_B / \cos\phi_B)_{\min} = 0.9156$
$\theta = 37.11^\circ$	$(\tan\phi_A)_{\max} = 0.6339$	$\theta = 208.43^\circ$	$(\Delta S_{Br})_{\max} = -0.0175^\circ$
$\theta = 37.11^\circ$	$(\Delta S_{Al})_{\max} = 0.0105^\circ$	$\theta = 213.32^\circ$	$(\lambda_B)_{\min} = -25.14^\circ$
$\theta = 42.05^\circ$	$(\cos\alpha_A / \cos\phi_A)_{\max} = 1.1325$	$\theta = 213.78^\circ$	$(\cos\alpha_B / \cos\phi_B)_{\min} = 0.6045$
$\theta = 42.05^\circ$	$(\Delta S_{Af})_{\min} = -0.0216^\circ$	$\theta = 213.78^\circ$	$(\Delta S_{Bf})_{\min} = 0.0115^\circ$
$\theta = 48.07^\circ$	$\Delta\eta_{\max}^+ = 0.014^\circ$	$\theta = 216.08^\circ$	$(\alpha_B)_{\max} = 53.62^\circ$
$\theta = 56.68^\circ$	$(\alpha_A)_{\min} = 14.23^\circ$	$\theta = 219.99^\circ$	$(\Delta\eta_f)_{\max} = -0.0234^\circ$
$\theta = 57.94^\circ$	$(\lambda_A)_{\max} = 22.60^\circ$	$\theta = 220^\circ$	$(\Delta\eta_r)_{\min} = 0.0358^\circ$
$\theta = 59.92^\circ$	$(\Delta\eta_f)_{\min} = -0.041^\circ$	$\theta = 220^\circ$	$(\Delta\eta_l)_{\min} = -0.0078^\circ$
$\theta = 59.97^\circ$	$(\Delta\eta_l)_{\max} = 0.0158^\circ$	$\theta = 220.01^\circ$	$\Delta\eta_{\min}^+ = 0.0045^\circ$
$\theta = 60.04^\circ$	$\Delta\eta_{\max}^- = -0.0643^\circ$	$\theta = 226.19^\circ$	$(\cos\alpha_A / \cos\phi_A)_{\min} = 0.6042$
$\theta = 62.07^\circ$	$(\lambda_B)_{\max} = 22.60^\circ$	$\theta = 226.19^\circ$	$(\Delta S_{Af})_{\max} = -0.0115^\circ$
$\theta = 63.31^\circ$	$(\alpha_B)_{\min} = 14.24^\circ$	$\theta = 226.68^\circ$	$(\lambda_A)_{\min} = -25.17^\circ$
$\theta = 77.92^\circ$	$(\cos\alpha_B / \cos\phi_B)_{\max} = 1.1315$	$\theta = 231.53^\circ$	$(\cos\lambda_A / \cos\phi_A)_{\min} = 0.9153$
$\theta = 77.92^\circ$	$(\Delta S_{Bf})_{\max} = 0.0216^\circ$	$\theta = 231.53^\circ$	$(\Delta S_{Ar})_{\min} = 0.0175^\circ$
$\theta = 82.88^\circ$	$(\phi_B)_{\max} = 32.30^\circ$	$\theta = 235.01^\circ$	$(\phi_B)_{\min} = -16.09^\circ$
$\theta = 82.88^\circ$	$(\tan\phi_B)_{\max} = 0.6321$	$\theta = 235.01^\circ$	$(\tan\phi_B)_{\min} = -0.2885$
$\theta = 82.88^\circ$	$(\Delta S_{Bl})_{\min} = -0.0104^\circ$	$\theta = 235.01^\circ$	$(\Delta S_{Bl})_{\max} = 0.0048^\circ$
$\theta = 92.22^\circ$	$(\cos\lambda_B / \cos\phi_B)_{\max} = 1.1468$	$\theta = 239.91^\circ$	$(\alpha_A)_{\max} = 53.63^\circ$

remain unchanged. It is interesting to note that  $\delta_\eta$  is approximately proportional to the radial profile errors; their correlation may be approximated by a straight line. In fact, the five points in the figure represent the calculated results according to the tolerance grades of IT5 to IT9, while the corresponding values of these five points are also listed in Table 6.2. Through the aid of this approximately linear correlation, the profile errors of a pair of conjugate cams can be easily evaluated by means of the corresponding motion variation of the indicator reading.

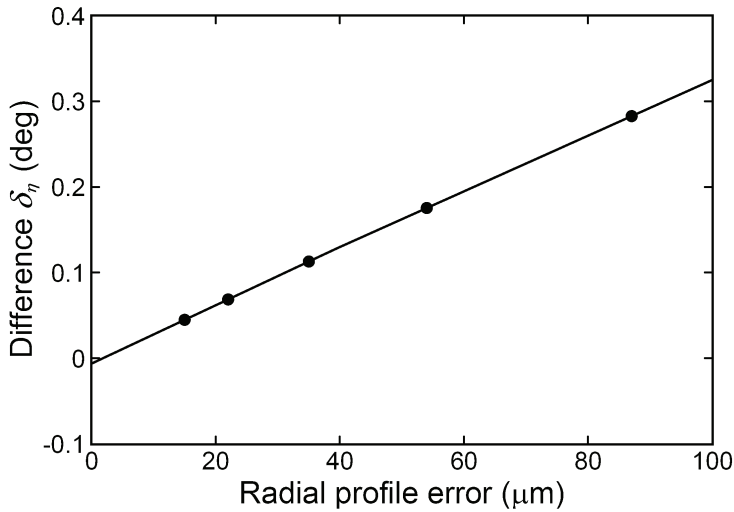


**Figure 6.7** Relative variations of the subtending angle with respect to the radial profile errors.

**Table 6.2** Tolerance grades and relative variations of the subtending angle.

Tolerance grade	$\Delta r_A$ and $\Delta r_B$	$\delta_\eta$
IT5	15 $\mu\text{m}$	0.0450°
IT6	22 $\mu\text{m}$	0.0688°
IT7	35 $\mu\text{m}$	0.1131°
IT8	54 $\mu\text{m}$	0.1756°
IT9	87 $\mu\text{m}$	0.2829°

#### 6.4.2 Application of Center Distance Variation

Considering the conjugate cam mechanism shown in Fig. 6.4(a), for a tolerance grade of IT6, the cam profiles may have deviations of  $\Delta r_A = \Delta r_B = 22 \mu\text{m}$ , the follower arm lengths may have deviations of  $\Delta l_A = \Delta l_B = 19 \mu\text{m}$  and the subtending angle of the follower arms may have a deviation of  $\Delta\eta = 0.022^\circ = 3.84 \times 10^{-4} \text{ rad}$ . The radius errors of the rollers,  $\Delta r_{fC}$  and  $\Delta r_{fD}$ , may be ignored since they generally have a smaller tolerance grade and may have a magnitude of 3  $\mu\text{m}$  at most if precision rollers are used. Then the actual center distance between the cam and follower pivots as well as the actual angular displacement of the follower will have deviations induced by them,  $\Delta f_r$  and  $\Delta\xi_r$ , caused by  $\Delta r_A$  and  $\Delta r_B$ ,  $\Delta f_l$

and  $\Delta\xi_l$  caused by  $l_A$  and  $\Delta l_B$ , and  $\Delta f_\eta$  and  $\Delta\xi_\eta$  caused by  $\Delta\eta$ , respectively. Note that this work is to provide a convenient and effective measurement method to inspect whether or not the cam profile deviations  $\Delta r_A$  and  $\Delta r_B$  lie within their specified tolerance zones along the ideal profiles. Therefore, for a measurement device constructed according to the presented approach, all design parameters other than the cam profiles should have been precisely measured and should be held constant. Accordingly, the three deviations of  $\Delta l_A$ ,  $\Delta l_B$ , and  $\Delta\eta$  may be assumed to be known, and the magnitudes of center distance deviations  $\Delta f_l$  and  $\Delta f_\eta$  are to be evaluated.

In this example,  $\Delta l_A = \Delta l_B = 19 \mu\text{m}$  and  $\Delta\eta = 0.022^\circ$  are assumed. The cam profile deviations may respectively range from  $+\Delta r_A = +\Delta r_B = 22 \mu\text{m}$  to  $-\Delta r_A = -\Delta r_B = -22 \mu\text{m}$ , and the upper and lower extreme deviations of the center distance will be

$$\Delta f^+ = \Delta f_r + \Delta f_l + \Delta f_\eta \quad (6.50)$$

and

$$\Delta f^- = -\Delta f_r + \Delta f_l + \Delta f_\eta \quad (6.51)$$



in which,  $\Delta f_r$  is caused by both  $+\Delta r_A$  and  $+\Delta r_B$ , and  $-\Delta f_r$  is caused by both  $-\Delta r_A$  and  $-\Delta r_B$ . A practical consequence of this argument is that, if the cam profile deviations fall within their specified tolerance zones, the measured value of the center distance variation  $\Delta f_{\text{mea}}$  will fall within the range of  $\Delta f^+ \sim \Delta f^-$ . In other words, if the measured value of  $\Delta f_{\text{mea}}$  falls outside the range of  $\Delta f^+ \sim \Delta f^-$ , then at least one cam profile deviation will fall outside its specified tolerance zones. That is, the necessary condition for a pair of qualified conjugate cam profiles is

$$\Delta f^- \leq \Delta f_{\text{mea}} \leq \Delta f^+ \quad (6.52)$$

On the other hand, the profile deviations for a pair of inspected cams may occasionally have compensating effect to enhance their conjugate condition. Therefore, even though the measured value of  $\Delta f_{\text{mea}}$  falls within the range of  $\Delta f^+ \sim \Delta f^-$ , this fact itself cannot ensure

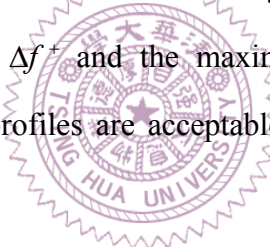
that both cam profiles are simultaneously qualified, but their conjugate condition may still be acceptable for the operating performance of the mechanism. Also note that, depending on the value of cam angle  $\theta$ , the magnitude of the range  $\Delta f^+ \sim \Delta f^-$  varies. Thus, from the viewpoint of conjugate condition, a convenient but conservative criterion to qualify the cam profiles for a pair of inspected cams can be expressed as

$$(\Delta f_{\text{mea}})_{\max} - (\Delta f_{\text{mea}})_{\min} \leq (\Delta f^+ - \Delta f^-)_{\min} = 2(\Delta f_r)_{\min} \quad (6.53)$$

Since  $2(\Delta f_r)_{\min}$  remains constant with  $\theta$ , this criterion will be easier to perform the inspection. Alternatively, another conservative criterion can be expressed as

$$(\Delta f_{\text{mea}})_{\max} - (\Delta f_{\text{mea}})_{\min} \leq \delta_f = \Delta f_{\min}^+ - \Delta f_{\max}^- \quad (6.54)$$

Also,  $(\Delta f_{\min}^+ - \Delta f_{\max}^-)$  is a constant. This criterion means that if the difference between the extremes of the measured center distance variation  $\Delta f_{\text{mea}}$  is less than  $\delta_f$ , the difference between the minimum value of  $\Delta f^+$  and the maximum value of  $\Delta f^-$ , the conjugate condition of the machined cam profiles are acceptable and are also on the conservative side.



The various resulting mechanical errors versus the cam rotation angle  $\theta$  of this conjugate cam mechanism are shown in Fig. 6.8, and the extreme deviations of the center distance is shown in Fig. 6.9, while their extreme values are also listed in Table 6.3. Figures 6.8(a) and 6.8(b) show that the extreme values of  $\phi_A$  are pretty close to those of  $\phi_B$ , and similar situations can be found between extreme values of  $\lambda_A$  and  $\lambda_B$  or between those of  $\alpha_A$  and  $\alpha_B$ . In Fig 6.8(c), if the signs of  $\Delta f_r$  and  $\Delta f_\eta$  are ignored, they will have the same trends. That is, the center distance variation caused by the positive cam profile deviations ( $\Delta r_A > 0$  and  $\Delta r_B > 0$ ) will be reduced by that caused by the negative subtending angle deviation ( $\Delta \eta < 0$ ), and vice versa. The extreme values of  $\Delta f_r$ ,  $\Delta f_l$ , and  $\Delta f_\eta$  occur at almost the same positions (about  $\theta = 60^\circ$  and  $\theta = 220^\circ$ ). Besides, Fig. 6.8(d) shows that the magnitude of  $\Delta \xi_r$  is much slighter than those of  $\Delta \xi_l$  and  $\Delta \xi_\eta$  and may be ignored since

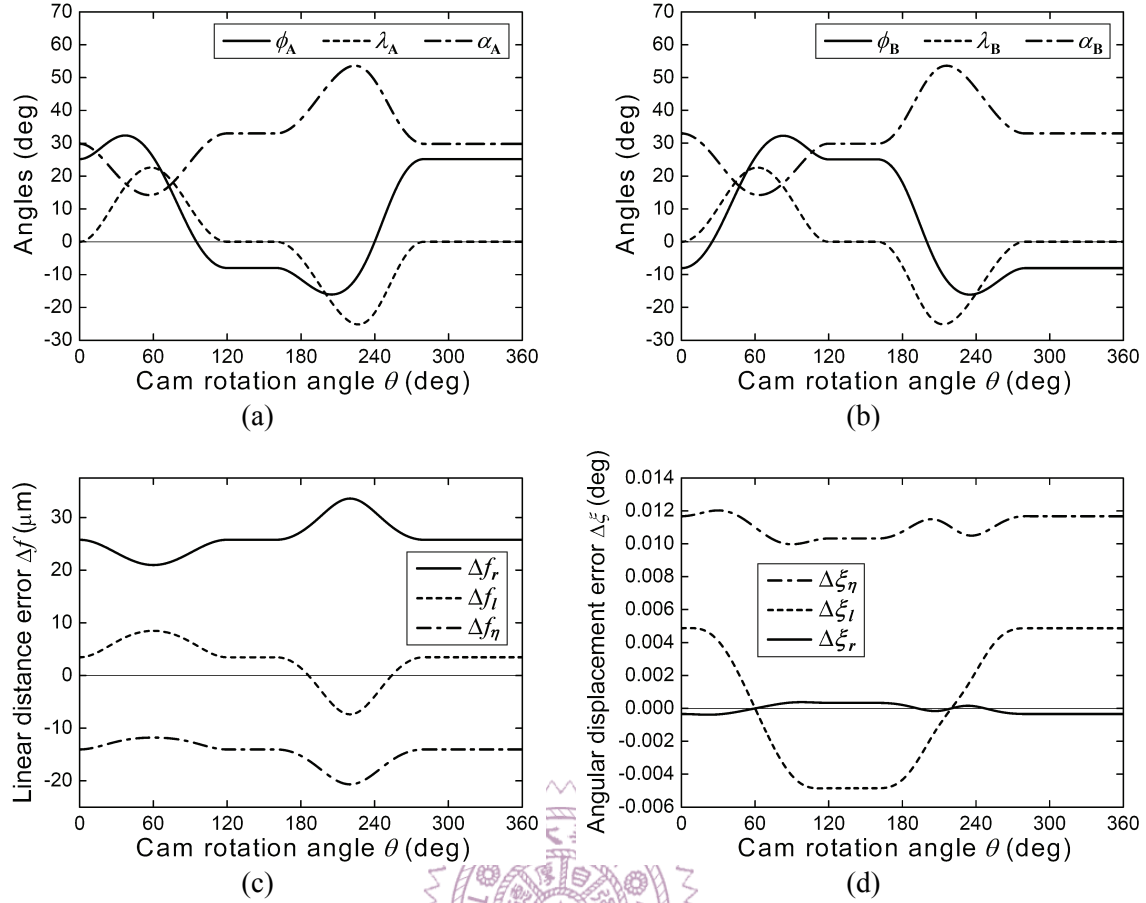


**Figure 6.8** Mechanical error analysis results of an assembled conjugate cam mechanism with a slider-pivoted floating roller follower.

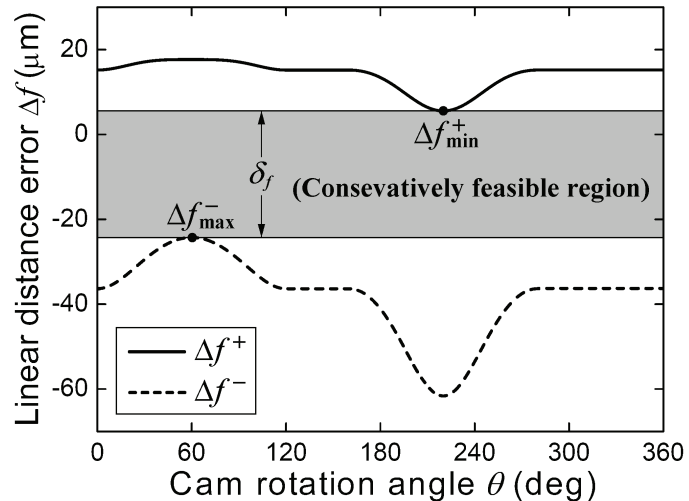


**Figure 6.9** Upper and lower limits of the center distance variation.

$-0.0004^\circ < \Delta\xi_r < 0.0004^\circ$ . It can be seen that the angular displacement error arising from the cam profile deviations may be slight if the amounts of  $\Delta r_A$  and  $\Delta r_B$  are close to each

**Table 6.3** Input angles and extreme values of an example for the application of center distance variation.

Input angle	Extreme value	Input angle	Extreme value
$\theta = 7.29^\circ$	$(\Delta\xi_l)_{\max} = 0.0049^\circ$	$\theta = 90.06^\circ$	$(\Delta\xi_\eta)_{\min} = 0.01^\circ$
$\theta = 22^\circ$	$(\Delta\xi_r)_{\min} = -0.0004^\circ$	$\theta = 98^\circ$	$(\Delta\xi_r)_{\max} = 0.0004^\circ$
$\theta = 29.97^\circ$	$(\Delta\xi_\eta)_{\max} = 0.012^\circ$	$\theta = 112.72^\circ$	$(\Delta\xi_l)_{\min} = -0.0049^\circ$
$\theta = 37.11^\circ$	$(\phi_A)_{\max} = 32.37^\circ$	$\theta = 205^\circ$	$(\phi_A)_{\min} = -16.05^\circ$
$\theta = 56.68^\circ$	$(\alpha_A)_{\min} = 14.23^\circ$	$\theta = 213.32^\circ$	$(\lambda_B)_{\min} = -25.14^\circ$
$\theta = 57.94^\circ$	$(\lambda_A)_{\max} = 22.60^\circ$	$\theta = 216.08^\circ$	$(\alpha_B)_{\max} = 53.62^\circ$
$\theta = 58.77^\circ$	$\Delta f_r^+ = 17.67 \mu\text{m}$	$\theta = 219.99^\circ$	$(\Delta f_r)_{\max} = 33.59 \mu\text{m}$
$\theta = 59.92^\circ$	$(\Delta f_\eta)_{\max} = -11.79 \mu\text{m}$	$\theta = 219.99^\circ$	$(\Delta f_\eta)_{\min} = -20.67 \mu\text{m}$
$\theta = 59.99^\circ$	$(\Delta f_l)_{\max} = 8.49 \mu\text{m}$	$\theta = 219.99^\circ$	$\Delta f_r^- = -61.63 \mu\text{m}$
$\theta = 59.99^\circ$	$\Delta f_r^- = -24.28 \mu\text{m}$	$\theta = 220^\circ$	$(\Delta f_l)_{\min} = -7.37 \mu\text{m}$
$\theta = 60^\circ$	$(\Delta f_r)_{\min} = 20.97 \mu\text{m}$	$\theta = 220^\circ$	$\Delta f_r^+ = 5.56 \mu\text{m}$
$\theta = 62.07^\circ$	$(\lambda_B)_{\max} = 22.60^\circ$	$\theta = 226.68^\circ$	$(\lambda_A)_{\min} = -25.17^\circ$
$\theta = 63.31^\circ$	$(\alpha_B)_{\min} = 14.24^\circ$	$\theta = 235.01^\circ$	$(\phi_B)_{\min} = -16.09^\circ$
$\theta = 82.88^\circ$	$(\phi_B)_{\max} = 32.30^\circ$	$\theta = 239.91^\circ$	$(\alpha_A)_{\max} = 53.63^\circ$

other. In Fig. 6.9,  $\Delta f_r^-$  and  $\Delta f_{\min}^+$  also occur at about  $\theta = 60^\circ$  or  $\theta = 220^\circ$  and have magnitudes of  $-24.28$  and  $5.56 \mu\text{m}$ , respectively. Hence, the magnitude of  $\delta_f$  (the difference between  $\Delta f_{\min}^+$  and  $\Delta f_{\max}^-$ ) is evaluated as  $29.83 \mu\text{m}$ , which is about 70 percent of the magnitude of  $2(\Delta f_r)_{\min}$  ( $= 41.94 \mu\text{m}$ ). According to Eq. (6.54), if the difference between the extremes of the measured center distance variation  $\Delta f_{\text{mea}}$  is less than  $29.83 \mu\text{m}$ , the conjugate condition of a pair of assembled cam profiles is qualified to meet the level of cam profile accuracy of tolerance grade IT6. In other words, the relative motion variation of the dial indicator cannot exceed  $29.83 \mu\text{m}$  to ensure the cam profile accuracy. Here, the region ranging between the two horizontal lines respectively passing through  $\Delta f_{\min}^+$  and  $\Delta f_{\max}^-$  is called the conservatively acceptable region for the cam profile inspection.

If the tolerance grade of the cam profile errors is changed, the allowable variation of the center distance,  $\delta_f$ , will be correspondingly changed. Figure 6.10 shows the allowable

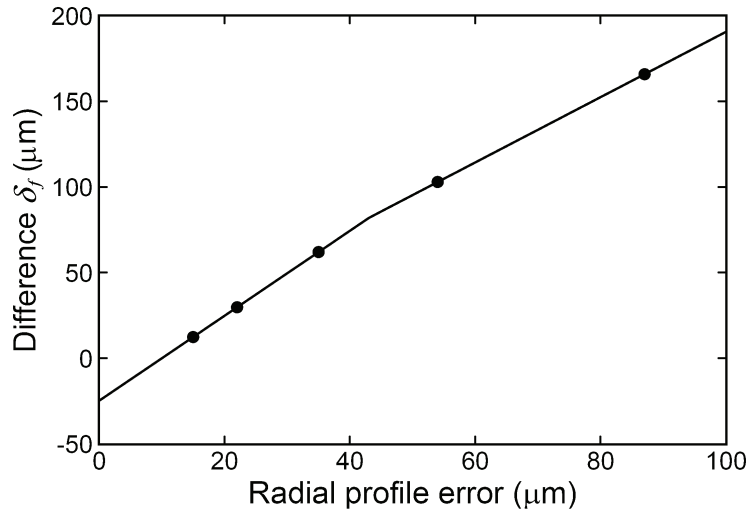


**Figure 6.10** Relative variations of the center distance with respect to the radial profile errors.

**Table 6.4** Tolerance grades and relative variations of the center distance.

Tolerance grade	$\Delta r_A$ and $\Delta r_B$	$\delta_f$
IT5	15 μm	12.47 μm
IT6	22 μm	29.83 μm
IT7	35 μm	62.08 μm
IT8	54 μm	102.97 μm
IT9	87 μm	165.89 μm

varyations of the center distance,  $\delta_f$ , with respect to various corresponding cam profile errors ( $\Delta r_A$  and  $\Delta r_B$ ) of some tolerance grades, while  $\Delta l_A = \Delta l_B = 19$  μm and  $\Delta\eta = 0.022^\circ$  remain unchanged. It is interesting to note that  $\delta_f$  is linearly proportional to the radial profile errors but with two slopes for the profile errors increasing from 0 to 43.12 μm and from 43.12 to 100 μm, respectively. The discontinuousness of  $\delta_f$  occurring at  $\Delta r_A = \Delta r_B = 43.12$  μm simply induced by the suddenly positional change of  $\Delta f_{\min}^+$  from  $\theta = 220^\circ$  to  $\theta = 60^\circ$  with increased radial profile errors. When  $\Delta r_A$  and  $\Delta r_B$  are both greater than 43.12 μm, the two extreme values  $\Delta f_{\min}^+$  and  $\Delta f_{\max}^-$  both occur at about  $\theta = 60^\circ$ , and thus the correlation of  $\delta_f = 2(\Delta f_r)_{\min}$  may exist in this case. In fact, the five points in the figure represent the calculated results according to the tolerance grades of IT5 to IT9, while the

corresponding values of these five points are also listed in Table 6.4. Through the aid of this approximately linear correlation, the profile errors of a pair of conjugate cams can be easily evaluated by means of the corresponding motion variation of the indicator reading.

## 6.5 CONCLUDING REMARKS

Two types of conjugate cams measuring fixtures, modified from adding a one degree-of-freedom kinematic pair into a conjugate cam mechanism with an oscillating roller follower, are studied in this chapter. By applying the assembled conjugate cam mechanism consisted of a pair of assembled conjugate cams and the measuring fixture, the profile errors of the conjugate disk cams can be conveniently examined. The conjugate condition of assembled conjugate cams can be quantitatively measured by the variation of the subtending angle of the follower arms or by the variation of the distance from the cam pivot center to the follower pivot center. The magnitudes of the subtending angle variation and the center distance variation can further be obtained by means of the corresponding motion variation of the indicator reading. Both indirect measurement methods are based on the conjugate condition analysis of the assembled conjugate cam mechanisms, which is in essence an extended application of the mechanical error analysis of disk cam mechanisms, and the only required measuring instrument is a dial indicator. These indirect methods can provide inexpensive and efficient ways of measuring the conjugate condition of conjugate disk cams for further inspecting the conjugate cam profile deviations, and are practically useful for the quality control of conjugate cam mechanisms. Two illustrated examples demonstrate the procedures of defining the conservatively acceptable regions of conjugate condition variations for the extreme cam profile deviations with respect to their specified tolerances. With the aid of the proposed conservative criteria, the cam profile inspection with the indirect methods can be quick and easy tasks.

# **CHAPTER 7**

## **SIMPLIFIED METHODS FOR EXAMINING PROFILE ERRORS OF CONJUGATE DISK CAMS — PART II: PROFILE ERRORS ESTIMATION AND EXPERIMENTAL VERIFICATION**

### **7.1 INTRODUCTION**

In Chapter 6, the principle of developing measuring fixtures for indirectly examining profile deviations of assembled conjugate disk cams has been demonstrated. The conjugate condition variations of assembled conjugate cam mechanisms can be measured by using a dial indicator to further judge whether the machined cam profiles meet required accuracy. A critical concern of the practical implementation of the simplified methods is if the measuring fixtures can be applied to directly obtain each individual profile error of the conjugate disk cams. If so, then the measuring fixtures may replace coordinate measuring machines (CMMs) to measure conjugate disk cams, and their potential development and added value will be considerable. To this end, this chapter extends the indirect measurement methods introduced in Chapter 6 to present a simple means of estimating cam profile errors from the indicator reading. To verify the presented method, experiments of examining a pair of conjugate disk cams by using a built integrated-type measuring fixture to measure the conjugate condition variations and to estimate the cam profile errors were conducted. The experimental results obtained from the presented method were compared with those obtained from the experiment of Chapter 5 by using a CMM, in order to test the accuracy of the use of the developed indirect measurement methods.

## 7.2 CONJUGATE CONDITIONS AND THE PROFILE ERRORS ESTIMATION

The measurement of the conjugate conditions of the assembled conjugate cam mechanisms can indirectly reveal the cam profile errors. By applying the analytical approach of the conjugate condition analysis introduced in Section 6.3, an extended means of estimating the profile errors of conjugate disk cams can be developed.

### 7.2.1 Application of Subtending Angle Variation

As shown in Figs. 2.8 and 6.1, the difference between the variable subtending angle  $\eta^*$  of the assembled follower arms and its ideally constant angle  $\eta$  may be induced by the radial-dimension errors of cams A and B,  $\Delta r_A$  and  $\Delta r_B$ , the roller-radius errors of rollers C and D,  $\Delta r_{fC}$  and  $\Delta r_{fD}$ , the distance error between the cam and follower pivots,  $\Delta f$ , and the errors of the arm lengths,  $\Delta l_A$  and  $\Delta l_B$ . In Sub-section 6.3.1, the theoretical modeling of the subtending angle variations,  $\Delta\eta_r$  caused by  $\Delta r_A$  and  $\Delta r_B$ ,  $\Delta\eta_{rf}$  caused by  $\Delta r_{fC}$  and  $\Delta r_{fD}$ ,  $\Delta\eta_f$  caused by  $\Delta f$ , and  $\Delta\eta_l$  caused by  $\Delta l_A$  and  $\Delta l_B$ , have been respectively derived as follows:

$$\Delta\eta_r \approx \frac{\Delta r_A \cos \lambda_A}{l_A \cos \phi_A} + \frac{\Delta r_B \cos \lambda_B}{l_B \cos \phi_B} \quad (7.1)$$

$$\Delta\eta_{rf} = \frac{\Delta r_{fC}}{l_A \cos \phi_A} + \frac{\Delta r_{fD}}{l_B \cos \phi_B} \quad (7.2)$$

$$\Delta\eta_f = -\Delta f \left( \frac{\cos \alpha_A}{l_A \cos \phi_A} + \frac{\cos \alpha_B}{l_B \cos \phi_B} \right) \quad (7.3)$$

$$\Delta\eta_l = \frac{\Delta l_A \tan \phi_A}{l_A} + \frac{\Delta l_B \tan \phi_B}{l_B} \quad (7.4)$$

where  $l_A$  and  $l_B$  are the follower arm lengths,  $\phi_A$  and  $\phi_B$  are the pressure angles,  $\lambda_A$  and  $\lambda_B$  are the shift angles, and  $\alpha_A$  and  $\alpha_B$  are the subtending angles between the contact normals and the line passing through the cam center and the follower pivot. Note that in practice,

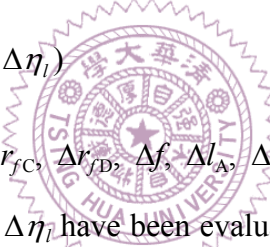
depending on the value of cam rotation angle  $\theta$ , the magnitudes of cam profile errors  $\Delta r_A$  and  $\Delta r_B$  may vary, while  $\Delta r_{fC}$ ,  $\Delta r_{fD}$ ,  $\Delta f$ ,  $\Delta l_A$ , and  $\Delta l_B$  remain constant. That is,  $\Delta r_A = \Delta r_A(\theta)$  and  $\Delta r_B = \Delta r_B(\theta)$ . Assuming that the small manufacturing or assembly errors  $\Delta r_A(\theta)$ ,  $\Delta r_B(\theta)$ ,  $\Delta r_{fC}$ ,  $\Delta r_{fD}$ ,  $\Delta f$ ,  $\Delta l_A$ , and  $\Delta l_B$  in the assembled conjugate cam mechanism have been precisely measured, the overall subtending angle variation can be estimated by

$$\Delta\eta_{\text{est}} = \Delta\eta_r + \Delta\eta_{rf} + \Delta\eta_f + \Delta\eta_l \quad (7.5)$$

Ideally, the predicted variation  $\Delta\eta_{\text{est}}$  will almost be equal to the measured value  $\Delta\eta_{\text{mea}}$  obtained by means of a dial indicator as shown in Fig. 6.1.

The measurement of the subtending angle variation can be extended to develop a simple means of estimating conjugate cam profile errors. Considering that the correlation of  $\Delta\eta_{\text{mea}} \approx \Delta\eta_{\text{est}}$  exists, it follows that

$$\Delta\eta_r \approx \Delta\eta_{\text{mea}} - (\Delta\eta_{rf} + \Delta\eta_f + \Delta\eta_l) \quad (7.6)$$



Assuming that the error terms  $\Delta r_{fC}$ ,  $\Delta r_{fD}$ ,  $\Delta f$ ,  $\Delta l_A$ ,  $\Delta l_B$ , and  $\Delta\eta_{\text{mea}}$  have been precisely measured and then  $\Delta\eta_{rf}$ ,  $\Delta\eta_f$ , and  $\Delta\eta_l$  have been evaluated, Eq. (7.6) gives a prediction of the subtending angle variation  $\Delta\eta_r$ , while its corresponding cam profile errors  $\Delta r_A$  and  $\Delta r_B$  are unknown. However, to estimate the cam profile error  $\Delta r_A$ , the radial profile error of cam B must be measured in advance. If so, then from Eqs. (7.1) and (7.6), the estimated radial profile error of cam A will be

$$\Delta r_{A,\text{est}} \approx \left[ \Delta\eta_{\text{mea}} - (\Delta\eta_{rf} + \Delta\eta_f + \Delta\eta_l) - \frac{\Delta r_{B,\text{mea}} \cos \lambda_B}{l_B \cos \phi_B} \right] \frac{l_A \cos \phi_A}{\cos \lambda_A} \quad (7.7)$$

where  $\Delta r_{B,\text{mea}}$  is the measured radial profile error of cam B. Similarly, if the radial profile error of cam A has been measured, the cam profile error  $\Delta r_B$  can be estimated by

$$\Delta r_{B,\text{est}} \approx \left[ \Delta\eta_{\text{mea}} - (\Delta\eta_{rf} + \Delta\eta_f + \Delta\eta_l) - \frac{\Delta r_{A,\text{mea}} \cos \lambda_A}{l_A \cos \phi_A} \right] \frac{l_B \cos \phi_B}{\cos \lambda_B} \quad (7.8)$$

where  $\Delta r_{A,\text{mea}}$  is the measured radial profile error of cam A. In the ideal situation,  $\Delta r_{A,\text{est}} \approx \Delta r_{A,\text{mea}}$  and  $\Delta r_{B,\text{est}} \approx \Delta r_{B,\text{mea}}$ . Based on this consideration, an alternative means of measuring the conjugate cam profile errors is suggested below.

A pair of conjugate cams  $\hat{A}$  and  $\hat{B}$  are accurately machined and then are precisely measured to obtain their profile errors. Also, two follower subassemblies (the measuring fixtures) with identical specifications featuring a variable subtending angle of the follower arms are built. The two cams  $\hat{A}$  and  $\hat{B}$  are treated as the master conjugate cams. They are separately assembled with two measuring fixtures to inspect other machined cams, A and B, which are respectively assembled and conjugated with them. In other words, if a pair of master conjugate cams with known profile errors is additionally available, through the measured conjugate condition variations of a pair of assembled conjugate cams consisting of one master cam and the other being an inspected cam, then the profile errors of each individual inspected cam can be estimated. Although two sets of measuring fixtures and a pair of master conjugate cams are required, this indirect measurement method is still suitable for quality control in mass production of conjugate cams.

### 7.2.2 Application of Center Distance Variation

As shown in Figs. 2.8 and 6.2, the difference between the variable center distance  $f^*$  of the cam and follower pivots and its ideally constant distance  $f$  may be induced by the radial-dimension errors of cams A and B,  $\Delta r_A$  and  $\Delta r_B$ , the roller-radius errors of rollers C and D,  $\Delta r_{fC}$  and  $\Delta r_{fD}$ , the errors of the arm lengths,  $\Delta l_A$  and  $\Delta l_B$ , and the subtending angle error of the follower arms,  $\Delta\eta$ . In Sub-section 6.3.2, the theoretical modeling of the center distance variations,  $\Delta f_r$  caused by  $\Delta r_A$  and  $\Delta r_B$ ,  $\Delta f_{rf}$  caused by  $\Delta r_{fC}$  and  $\Delta r_{fD}$ ,  $\Delta f_l$  caused by  $\Delta l_A$  and  $\Delta l_B$ , and  $\Delta f_\eta$  caused by  $\Delta\eta$ , have been respectively derived as follows:

$$\Delta f_r \approx \frac{\Delta r_A (l_B \cos \phi_B \cos \lambda_A) + \Delta r_B (l_A \cos \phi_A \cos \lambda_B)}{l_A \cos \phi_A \cos \alpha_B + l_B \cos \phi_B \cos \alpha_A} \quad (7.9)$$

$$\Delta f_{rf} = \frac{\Delta r_{fC}(l_B \cos \phi_B) + \Delta r_{fD}(l_A \cos \phi_A)}{l_A \cos \phi_A \cos \alpha_B + l_B \cos \phi_B \cos \alpha_A} \quad (7.10)$$

$$\Delta f_l = \frac{\Delta l_A(l_B \cos \phi_B \sin \phi_A) + \Delta l_B(l_A \cos \phi_A \sin \phi_B)}{l_A \cos \phi_A \cos \alpha_B + l_B \cos \phi_B \cos \alpha_A} \quad (7.11)$$

$$\Delta f_\eta = -\frac{\Delta \eta(l_A l_B \cos \phi_A \cos \phi_B)}{l_A \cos \phi_A \cos \alpha_B + l_B \cos \phi_B \cos \alpha_A} \quad (7.12)$$

Note that in practice, depending on the value of cam rotation angle  $\theta$ , the magnitudes of the cam profile errors  $\Delta r_A$  and  $\Delta r_B$  may vary, while  $\Delta r_{fC}$ ,  $\Delta r_{fD}$ ,  $\Delta l_A$ ,  $\Delta l_B$ , and  $\Delta \eta$  remain constant. In other words,  $\Delta r_A = \Delta r_A(\theta)$  and  $\Delta r_B = \Delta r_B(\theta)$ . Assuming that the small manufacturing or assembly errors  $\Delta r_A(\theta)$ ,  $\Delta r_B(\theta)$ ,  $\Delta r_{fC}$ ,  $\Delta r_{fD}$ ,  $\Delta l_A$ ,  $\Delta l_B$ , and  $\Delta \eta$  in the assembled conjugate cam mechanism have been precisely measured, the overall center distance variation can be estimated by

$$\Delta f_{\text{est}} = \Delta f_r + \Delta f_{rf} + \Delta f_l + \Delta f_\eta \quad (7.13)$$

Ideally, the predicted variation  $\Delta f_{\text{est}}$  will almost be equal to the measured value  $\Delta f_{\text{mea}}$  obtained by means of a dial indicator as shown in Fig. 6.2.

The measurement of the center distance variation can be extended to develop a simple means of estimating conjugate cam profile errors. Considering that the correlation of  $\Delta f_{\text{mea}} \approx \Delta f_{\text{est}}$  exists, it follows that

$$\Delta f_r \approx \Delta f_{\text{mea}} - (\Delta f_{rf} + \Delta f_l + \Delta f_\eta) \quad (7.14)$$

Assuming that the error terms  $\Delta r_{fC}$ ,  $\Delta r_{fD}$ ,  $\Delta l_A$ ,  $\Delta l_B$ ,  $\Delta \eta$ , and  $\Delta f_{\text{mea}}$  have been precisely measured and then  $\Delta f_{rf}$ ,  $\Delta f_l$ , and  $\Delta f_\eta$  have been evaluated, Eq. (7.14) gives a prediction of the center distance variation  $\Delta f_r$  while its corresponding cam profile errors  $\Delta r_A$  and  $\Delta r_B$  are unknown. However, to estimate the cam profile error  $\Delta r_A$ , the radial profile error of cam B must be measured in advance. If so, then from Eqs. (7.9) and (7.14), the estimated radial profile error of cam A will be

$$\Delta r_{A,\text{est}} \approx \frac{1}{l_B \cos \phi_B \cos \lambda_A} \left\{ (l_A \cos \phi_A \cos \alpha_B + l_B \cos \phi_B \cos \alpha_A) [\Delta f_{\text{mea}} - (\Delta f_{rf} + \Delta f_l + \Delta f_\eta)] - \Delta r_{B,\text{mea}} (l_A \cos \phi_A \cos \lambda_B) \right\} \quad (7.15)$$

where  $\Delta r_{B,\text{mea}}$  is the measured radial profile error of cam B. Likewise, if the radial profile error of cam A has been measured, then the cam profile error  $\Delta r_B$  can be estimated by

$$\Delta r_{B,\text{est}} \approx \frac{1}{l_A \cos \phi_A \cos \lambda_B} \left\{ (l_A \cos \phi_A \cos \alpha_B + l_B \cos \phi_B \cos \alpha_A) [\Delta f_{\text{mea}} - (\Delta f_{rf} + \Delta f_l + \Delta f_\eta)] - \Delta r_{A,\text{mea}} (l_B \cos \phi_B \cos \lambda_A) \right\} \quad (7.16)$$

where  $\Delta r_{A,\text{mea}}$  is the measured radial profile error of cam A. In the ideal situation,  $\Delta r_{A,\text{est}} \approx \Delta r_{A,\text{mea}}$  and  $\Delta r_{B,\text{est}} \approx \Delta r_{B,\text{mea}}$ . Based on this consideration, an alternative method for measuring the conjugate cam profile errors, which is similar to the concept proposed in Sub-section 7.2.1, is suggested. If a pair of master conjugate cams with known profile errors is additionally available, through the measured conjugate condition variations of a pair of assembled conjugate cams consisting of one master cam and the other being an inspected cam, then the profile errors of each individual inspected cam can be estimated. A pair of master conjugate cams and two sets of measuring fixtures should be built for the cam profile measurement and error estimation tasks.

### 7.3 EXPERIMENTAL APPARATUS

An assembled conjugate cam mechanism with an integrated-type measuring fixture, whose subtending angle of the follower arms or center distance between the cam and follower pivots is variable, was designed and built for the experiments. The three-dimensional CAD model of the conjugate disk cams with the integrated-type measuring fixture, and its exploded assemblies are shown in Figs. 7.1(a) and 7.1(b), respectively. The cam mechanism mainly consisted of a base plate, a conjugate cam subassembly, a follower subassembly, and a driving subassembly. The base plate was considered a stationary frame.

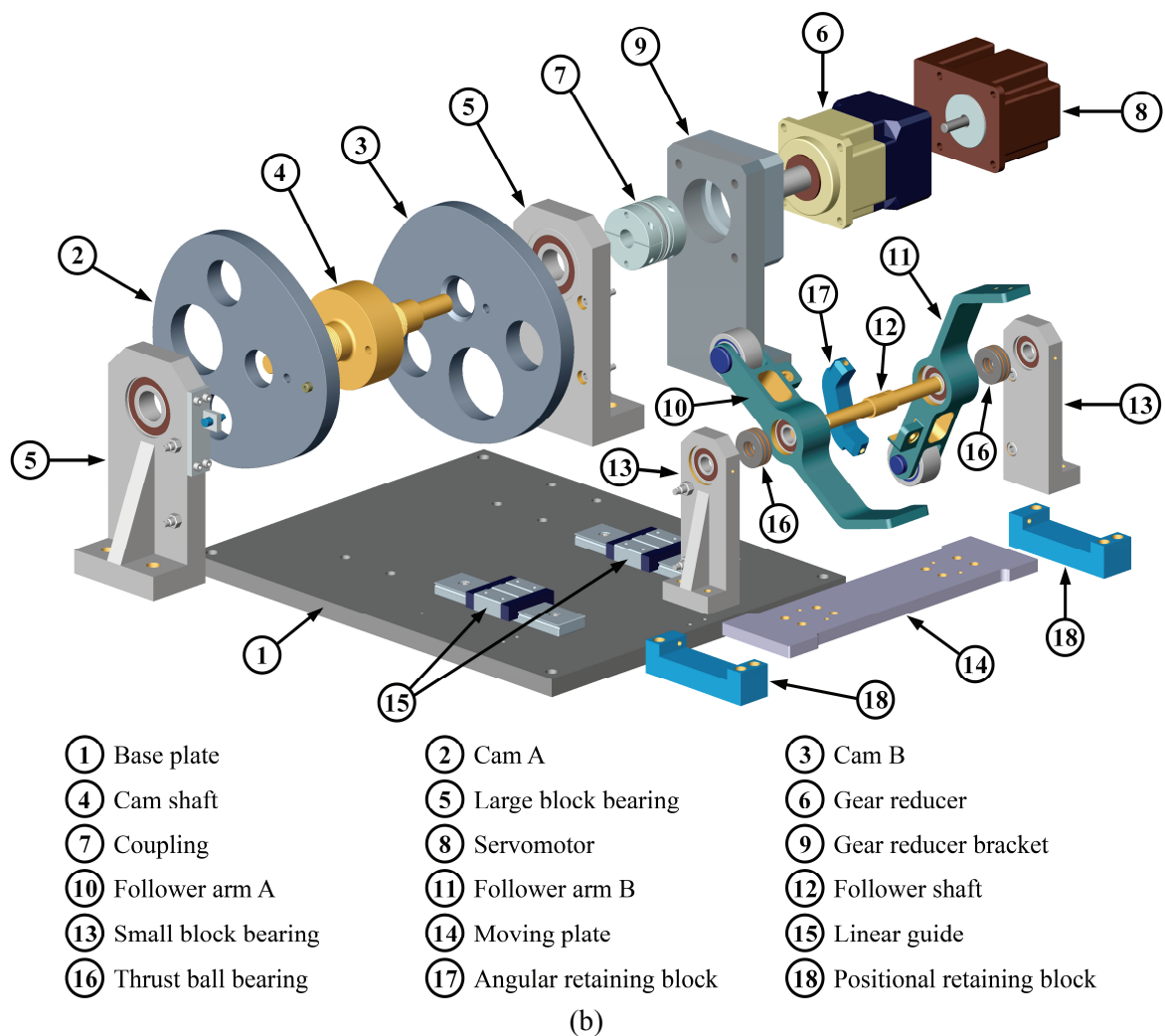
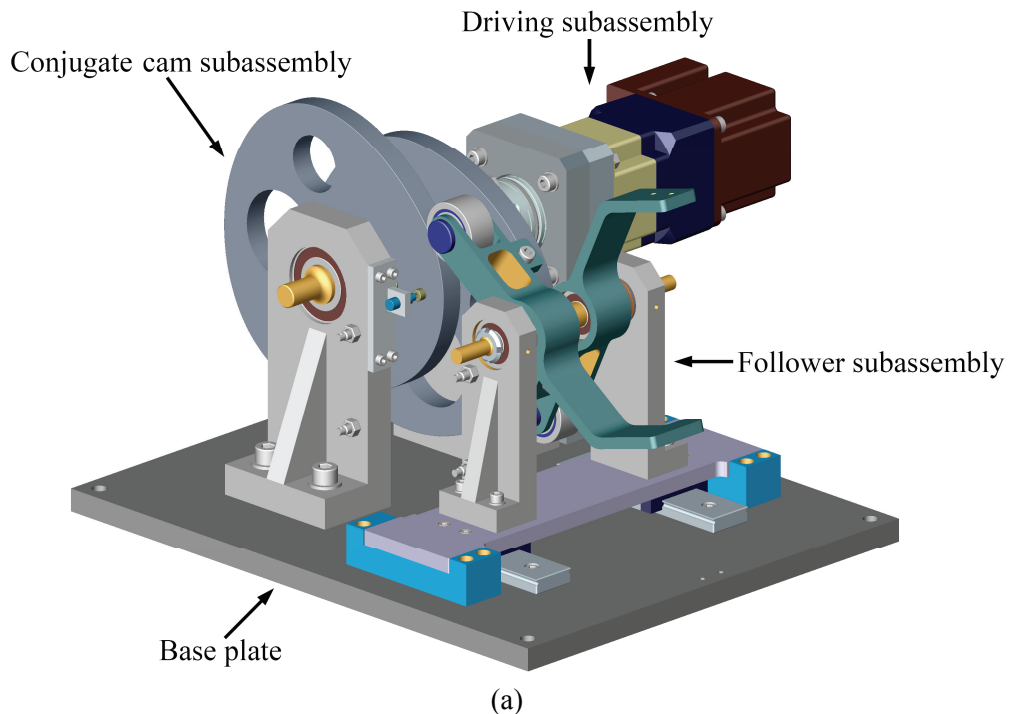


**Figure 7.1** Solid CAD model of an assembled conjugate cam mechanism with an integrated-type measuring fixture and its exploded assemblies.

The conjugate cam subassembly, consisting of a pair of cams A and B simultaneously fixed to a cam shaft, was supported by two large block bearings whose blocks were mounted to the base plate. A pair of angular contact ball bearings was respectively inserted in the two large bearing blocks as support for the cam shaft, as shown in Fig. 7.2. The two bearings were preloaded by their outer races being thrust in opposite directions when the two large bearing blocks were axially pressed close to each other before being fastened to the base plate. The cam shaft connected the output shaft of a gear reducer by using a disk-clamping type coupling and was driven by a servomotor with a torque multiplied by the gear reducer. The servomotor and the gear reducer joining together constituted the driving subassembly, which was also mounted to the base plate by intermediately arranging a gear reducer bracket. The follower subassembly, mainly consisting of two independently rotatable follower arms A and B both pivoting on a follower shaft, was supported by two small block bearings whose blocks were mounted to a moving plate, instead of the base plate. Two linear guides paralleling each other were mounted between the moving plate and the base plate to make them have relative translation. A pair of angular contact ball bearings in tandem arrangement [111] was mounted between the follower shaft and each follower arm, as shown in Fig. 7.3, while a thrust ball bearing was mounted between each follower arm and its adjacent bearing block. A pair of angular contact ball bearings respectively inserted in the two small bearing blocks was preloaded in opposite directions by using two locknuts separately thrusting their inner races. The thrust forces transmitted along the follower shaft also provide a preload for the other bearings used in the follower subassembly. The two rollers mounted to the follower arms were crowned rollers [6, 7], which were chosen instead of cylindrical rollers to avoid the edge contact phenomenon [7, 53] as well as to reduce the contact stress concentration between the cam and roller surfaces. To keep the subtending angle of the two follower arms invariant, an angular retaining block was screwed to both follower arms. Also, two positional retaining blocks respectively screwed to both the moving plate and the base plate constrained the motion of the moving plate so as to fix the center distance between the cam and follower shafts. The three-dimensional

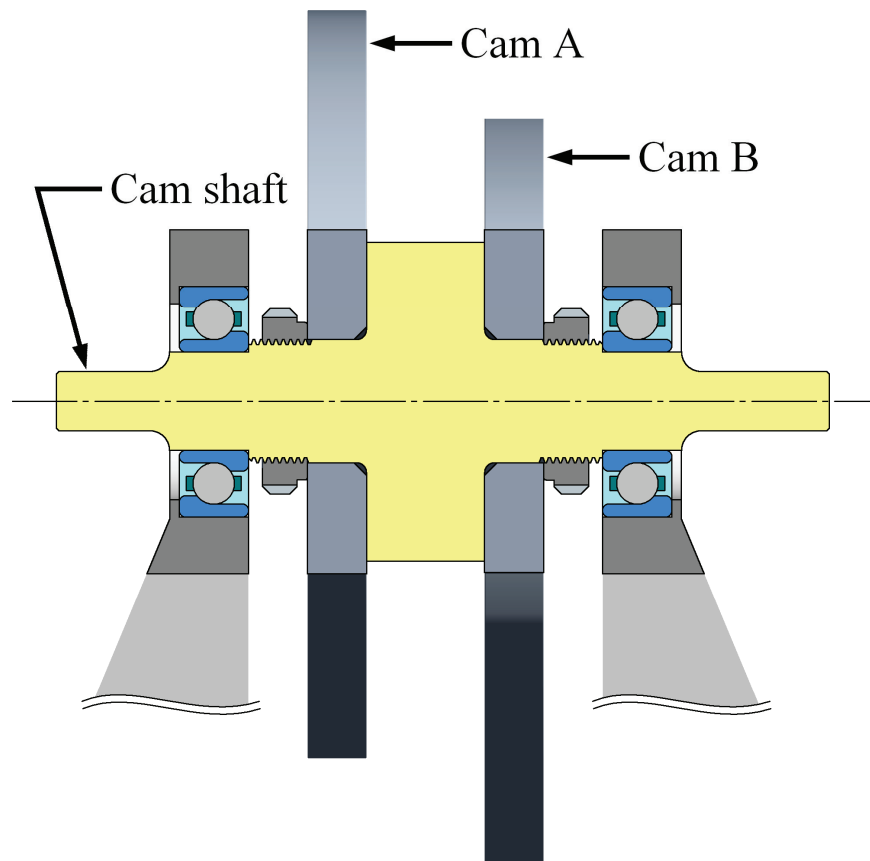


**Figure 7.2** Partially sectional drawing of the conjugate cam subassembly.

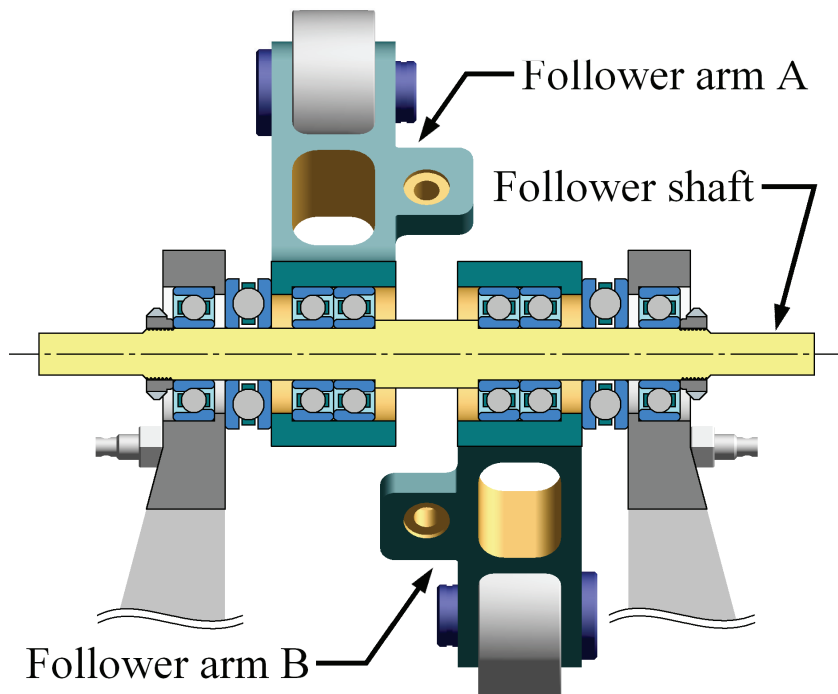


**Figure 7.3** Partially sectional drawing of the follower subassembly.

CAD model of the follower subassembly is individually shown in Fig. 7.4. It clearly shows that the angular retaining block and the two positional retaining blocks simultaneously work to make the follower subassembly a common oscillating roller follower used in conjugate cam mechanisms.

When applying the integrated-type measuring fixture for the measurement of the subtending angle variation, the angular retaining block shown in Fig. 7.4 was disassembled. As shown in Fig. 7.5(a), the angular retaining block was replaced by a tension spring pulling the follower arms in opposite directions to keep the follower rollers in contact with the cam surfaces. Then a digimatic indicator was mounted to the follower arm B with its contact tip touching the extended end of the follower arm A to measure the subtending angle variation, as shown in Fig. 7.5(b). On the other hand, when applying the integrated-type measuring fixture for the measurement of the center distance variation, the two positional retaining blocks shown in Fig. 7.4 were disassembled. Four tension springs were thus employed to pull the follower subassembly towards the cam center for keeping the contact between the cam and roller surfaces, as shown in Figs. 7.6(a) and 7.6(b). A digimatic indicator was mounted to the base plate for measuring the center distance variation, as shown in Fig. 7.6(b), while the contact tip of the indicator touched a thin plate screwed to both the two smaller bearing blocks. The measuring axis of the indicator must

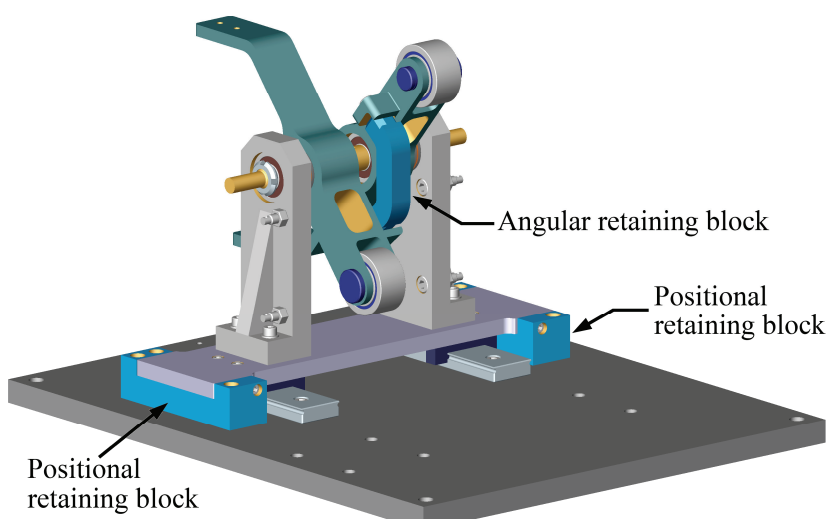


**Figure 7.4** Solid CAD model of the follower subassembly.

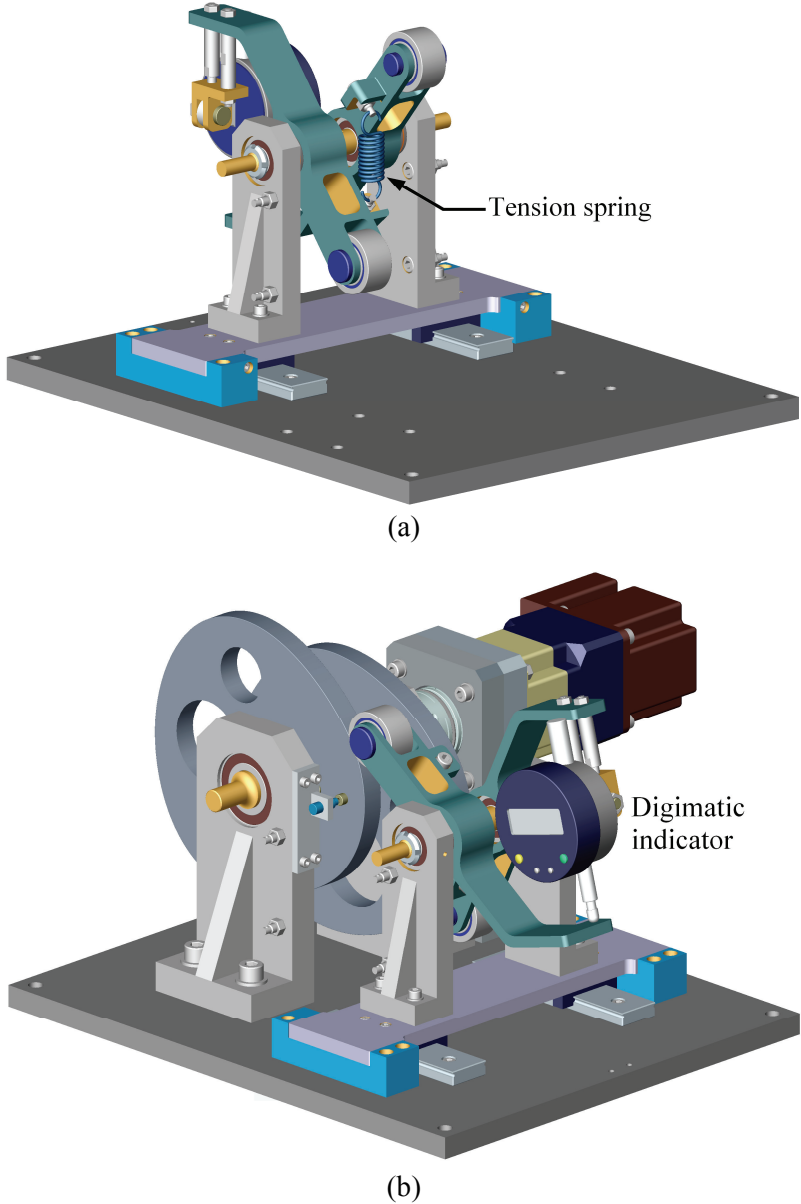


**Figure 7.5** Setup of the follower subassembly for measuring the subtending angle variation.

be placed perpendicular and coplanar to the axes of the cam and follower shafts as far as possible to reduce the effect of the Abbe error [112, 113].

The built conjugate cam mechanism, that is, the assembled conjugate cams with the integrated-type measuring fixture, is shown in Fig. 7.7. The specified design parameters of this built mechanism are identical to those of the cam system illustrated in Section 6.4 (and also the same of those designed for the experiment of Chapter 5). It requires the oscillating roller follower to oscillate  $30^\circ$  clockwise with cycloidal motion while the cam rotates clockwise from  $0^\circ$  to  $120^\circ$ , dwell for the next  $40^\circ$ , return with cycloidal motion for  $120^\circ$

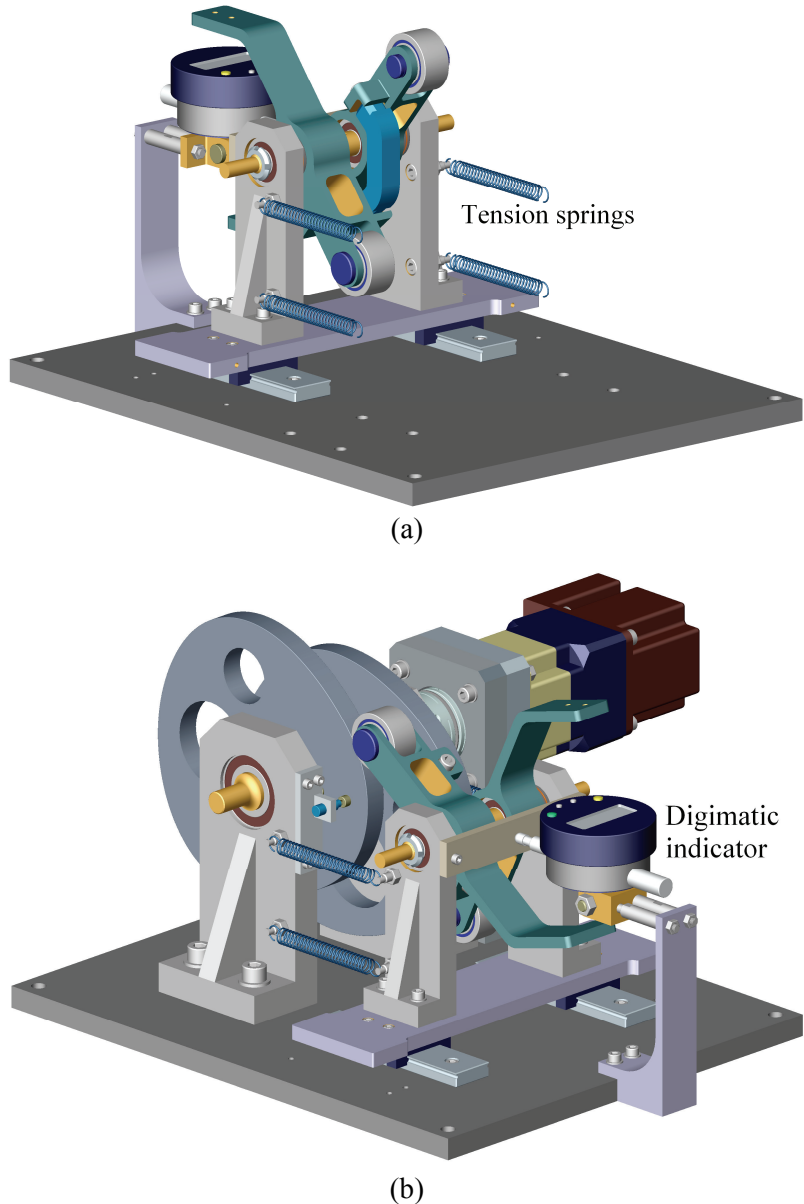


**Figure 7.6** Setup of the follower subassembly for measuring the center distance variation.

cam rotation, and dwell for the remaining  $80^\circ$ . The theoretical distance between pivots,  $f$ , is 120 mm. The lengths of the follower arms,  $l_A$  and  $l_B$ , are both equal to 66 mm, and both follower rollers have the same radius of 16 mm. The theoretical subtending angle of the follower arms,  $\eta$ , is  $100^\circ$ . The conjugate cams, the follower arms, the cam and follower shafts, the follower roller pins, and the angular retaining block were made of stainless steel (JIS SUS304/AISI 304). The base plate, the moving plate, the bearing blocks, the gear reducer bracket, and the positional retaining blocks were made of aluminum alloy (A6061). Both cams had the same thickness of 12 mm and were manufactured with an electro-

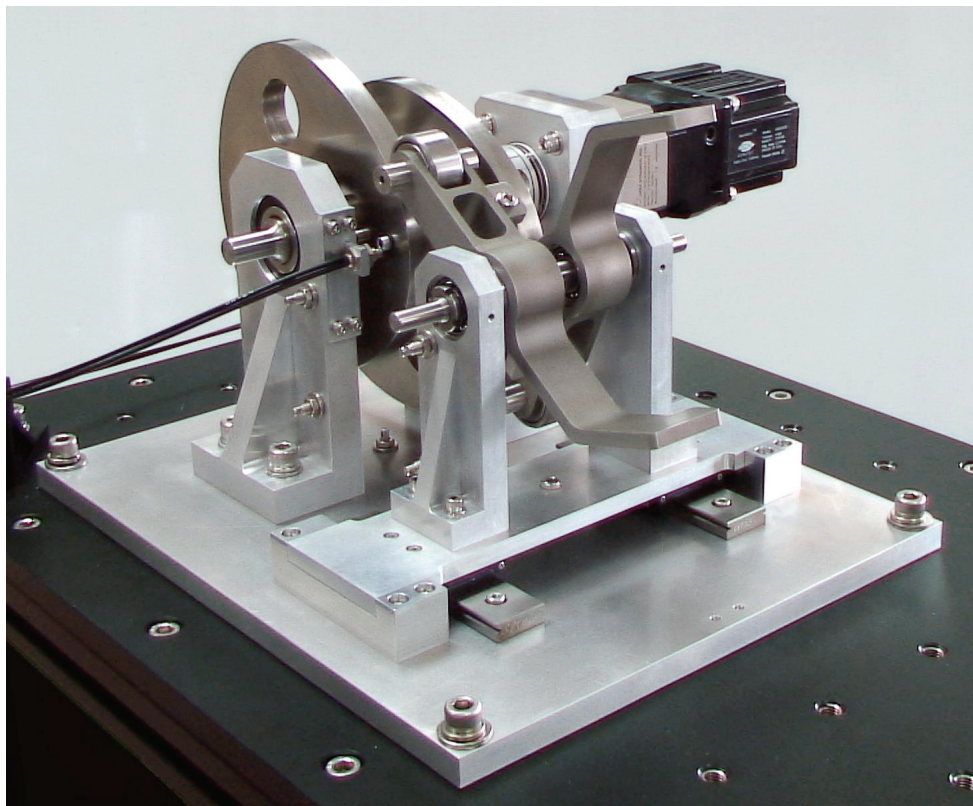


**Figure 7.7** Built assembled conjugate cams with integrated-type measuring fixture.

discharge wire-cutting machine. In order to make the conjugate condition variations larger so that the induced motion variations of the digimatic indicator could be easily sensed and read in the experiments, both cams were intentionally specified to have a radial profile tolerance of  $\pm 220 \mu\text{m}$ , a considerably large tolerance grade of IT11. (The two cams were identical to those measured by using a CMM in the experiment of Chapter 5.) The MISUMI NASTZ12 crowned rollers with a diameter of 32 mm and a thickness of 16 mm, the MISUMI SSEBWV14-110 miniature linear guides, and the Koyo 51100 thrust ball bearings were adopted for the follower subassembly. The angular contact ball bearings chosen for the built mechanism were the NTN precision bearings. The driving subassembly consisted of an Animatics SM2315D 0.13 kW direct current (DC) servomotor and an Apex Dynamics AB060-S1-P1 gear reducer with a reduction ratio of 9:1. The Animatics SM2315D servomotor is a single component combining the motor, the angular encoder, the motion controller, and the servo amplifier together. A MISUMI CPDT40-12-16 disk-clamping type coupling was used to connect the output shaft of the gear reducer and the

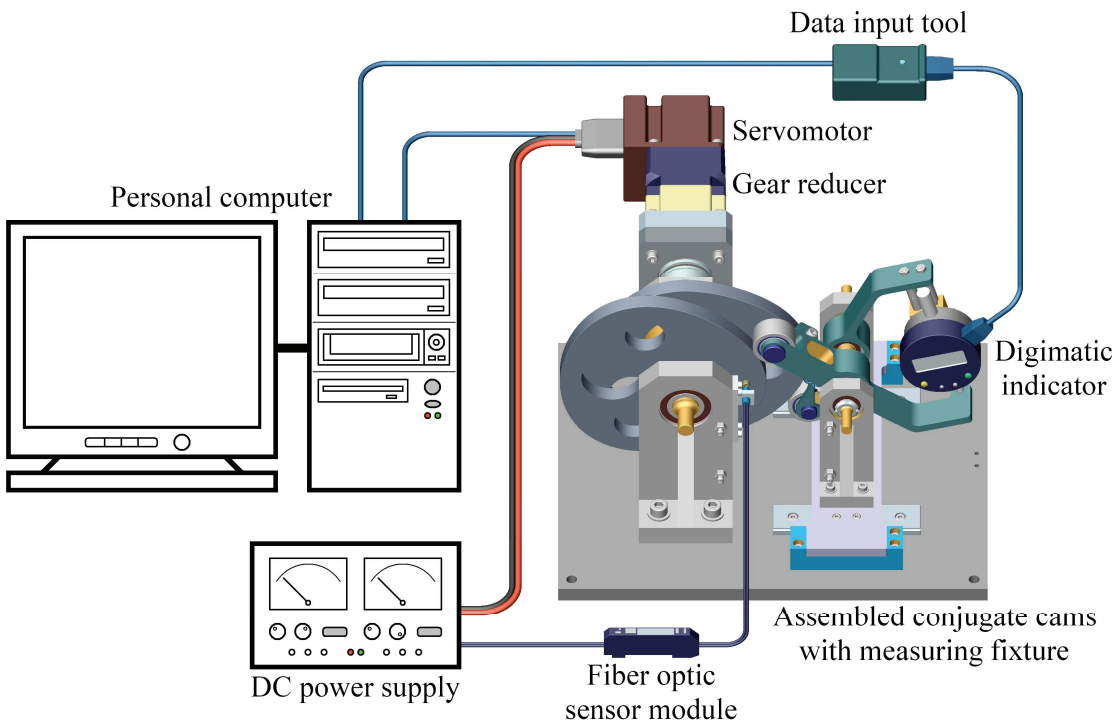


**Figure 7.8** Schematic of the experimental apparatus and instrumentation.

cam shaft for transmitting power.

The experimental apparatus and instrumentation are schematically shown in Fig. 7.8. A personal computer was prepared to control and monitor the servomotor through a communication cable (Animatics CBLSM1) connecting the servomotor and the RS-232 port of the computer. The servomotor was powered by a DC power supply. A Mitutoyo ID-C112M 543-251 digimatic indicator, whose resolution and accuracy are 0.001 mm and  $\pm 3 \mu\text{m}$ , respectively, was employed to measure the conjugate condition variations of the built conjugate cam mechanism. The digital measuring data read from the digimatic indicator were inputted to the same personal computer by using a Mitutoyo IT-012U data input tool connecting the digimatic indicator and a universal serial bus (USB) port of the computer. To identify the initial angular position for the cam rotation, and also to ensure that the conjugate cams can actually return to the initial angular position in each rotation cycle, a Keyence FU-25/FS-V31 fiber optic sensor module was applied. The fiber optic sensor module was powered by the same DC power supply. As shown in Fig. 7.9, the Keyence FU-25 fiber optic head unit, beaming one end face of cam A, was mounted to one

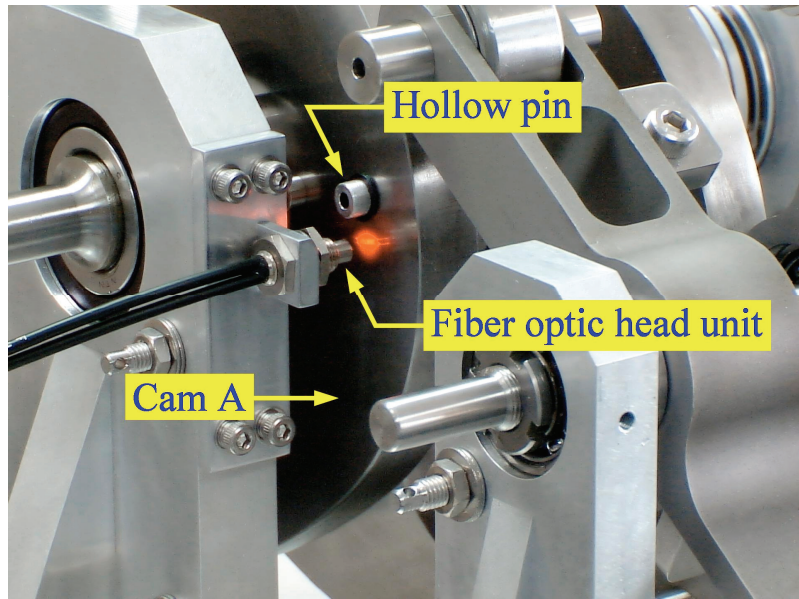


**Figure 7.9** Identifying the initial angular position for the cam rotation by using a fiber optic sensor.

of the large bearing blocks. A hollow pin with a small hole of diameter 2.5 mm was mounted to cam A as the angular positioning reference. When the small hole of the hollow pin approached the beam of the fiber optic head unit, the digital signal read from the Keyence FS-V31 digital display amplifier varied sensitively, and the initial angular position of the conjugate cams could be sensed and calibrated.

## 7.4 EXPERIMENTAL PROCEDURE

Before the measurement of the conjugate conditions was conducted, the conjugate cam profiles were measured by using a Giddings & Lewis Sheffield Measurement Cordax RS-25 CMM with a Renishaw touch-trigger probe (PH9 probe head and TP200 probe with a stylus for its ruby ball diameter of 2 mm) in the experiment of Chapter 5, as shown in Fig. 5.3. The radial profile errors of the cams were then evaluated from the coordinate measurement data by employing the analytical approach proposed in Section 5.2. The dimensions of the follower arms and the rollers were also measured by using the CMM before they were assembled. Thus, the measured radial-dimension errors of cams A and B,

$\Delta r_{A,\text{mea}}(\theta)$  and  $\Delta r_{B,\text{mea}}(\theta)$ , the roller-radius errors of rollers C and D,  $\Delta r_{fC}$  and  $\Delta r_{fD}$ , and the errors of the arm lengths,  $\Delta l_A$  and  $\Delta l_B$ , were obtained.

After the built follower subassembly was set for the measurement of the subtending angle variation, as shown in Fig. 7.10, the fixed distance between the cam and follower shafts was also measured by using the CMM. The constant center distance deviation,  $\Delta f$ , was thus obtained. Then the conjugate cams rotated slowly and intermittently with an equal cam rotation angle interval of  $0.1^\circ$  for six revolutions. Six data sets of 3600 values of the motion variations of the digimatic indicator for each cam revolution were recorded and converted to their corresponding subtending angle variations. [As shown in Fig. 6.1, assuming the perpendicular distance from the follower pivot center  $O_3$  to the measuring axis of the dial indicator is  $D$ . The subtending angle variation,  $\Delta\eta$ , is evaluated from the motion variation of the indicator reading,  $\delta$ , by  $\Delta\eta \approx \tan^{-1}(\delta/D) \approx \delta/D$  (in radians). In the experiment, the distance  $D$  was 76.124 mm.] The averages of the evaluated subtending angle variations with corresponding cam rotation angles were then calculated. They were

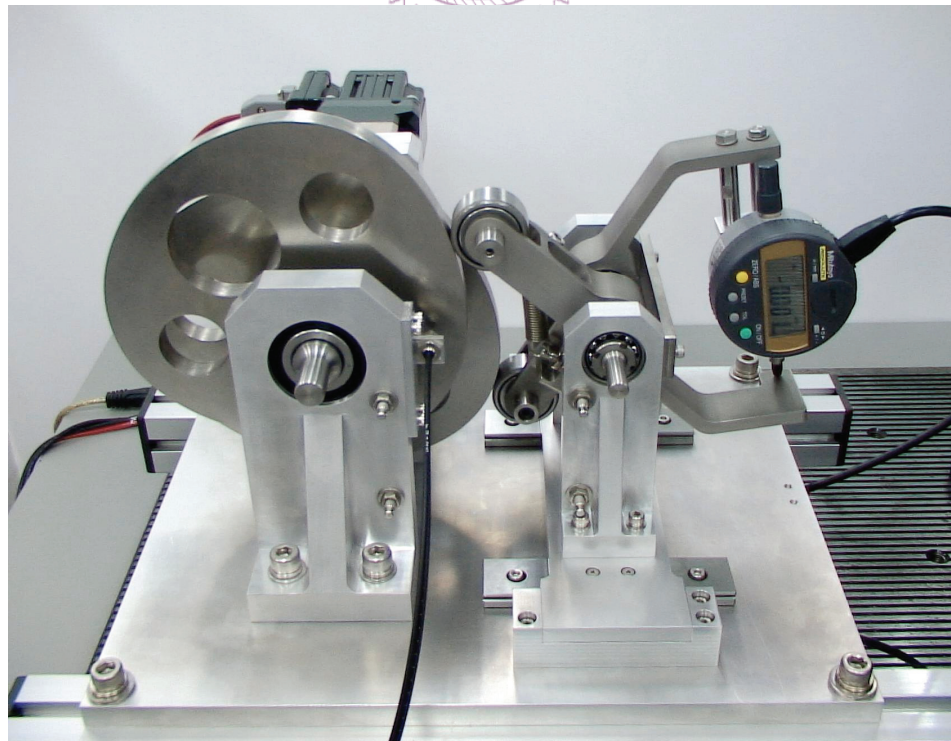


**Figure 7.10** Experiment for measuring the subtending angle variation by using a digimatic indicator.

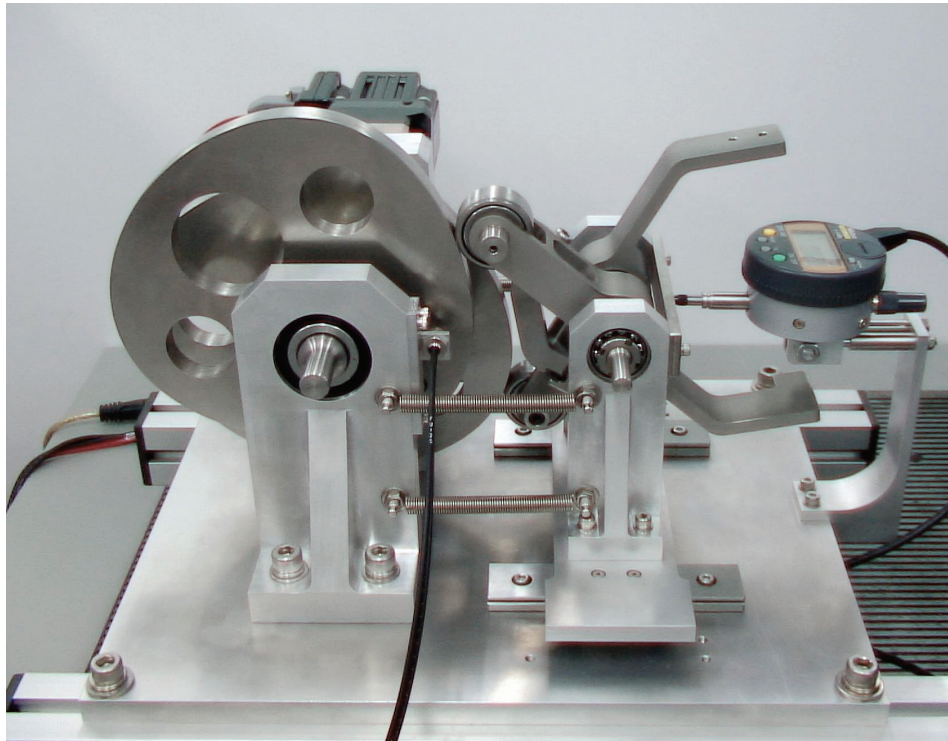


**Figure 7.11** Experiment for measuring the center distance variation by using a digimatic indicator.

considered as representatives of the experimental data function of angle  $\theta$ , that is,  $\Delta\eta_{\text{mea}}(\theta)$ , for comparing with the predicted subtending angle variations obtained by using Eq. (7.5).

Similarly, after the built follower subassembly was set for the measurement of the center distance variation, as shown in Fig. 7.11, the fixed subtending angle of the follower arms was also measured by using the CMM. The constant subtending angle deviation,  $\Delta\eta$ , was thus obtained. Then the conjugate cams rotated slowly and intermittently with an equal cam rotation angle interval of  $0.1^\circ$  for six revolutions. Six data sets of 3600 values of the motion variations of the digimatic indicator for each cam revolution, namely, the center distance variations, were recorded. The averages of the measured center distance variations with corresponding cam rotation angles were then calculated. They were considered as representatives of the experimental data function of angle  $\theta$ , namely,  $\Delta f_{\text{mea}}(\theta)$ , for comparing with the predicted center distance variations obtained by using Eq. (7.13).

The experimental data of  $\Delta\eta_{\text{mea}}(\theta)$ ,  $\Delta f_{\text{mea}}(\theta)$ ,  $\Delta r_{A,\text{mea}}(\theta)$ , and  $\Delta r_{B,\text{mea}}(\theta)$  were then adopted for the estimation of the radial profile errors of cams A and B using Eqs. (7.7) and

(7.8) or Eqs. (7.15) and (7.16), respectively. The data of the estimated cam profile errors,  $\Delta r_{A,\text{est}}(\theta)$  and  $\Delta r_{B,\text{est}}(\theta)$ , were thus calculated.

## 7.5 RESULTS AND DISCUSSION

The actual dimensions of the constant parameters,  $f$ ,  $l_A$ ,  $l_B$ ,  $r_{fC}$ ,  $r_{fD}$ , and  $\eta$ , and their corresponding errors in the built conjugate cam mechanism are listed in Table 7.1. These data were adopted for predicting the conjugate condition variations. Note that the errors of parameters  $f$  and  $\eta$  (i.e.,  $\Delta f$  and  $\Delta \eta$ ) did not exist simultaneously in the experiments.

The experimental and predicted results of the measurement of the subtending angle variation are shown in Fig. 7.12, and the measured and estimated cam profile errors are shown in Fig. 7.13, while their extreme values are also listed in Table 7.2. Figure 7.12(a) shows the predicted subtending angle variations respectively caused by the cam profile errors  $\Delta r_{A,\text{mea}}$  and  $\Delta r_{B,\text{mea}}$ , the roller-radius errors  $\Delta r_{fC}$  and  $\Delta r_{fD}$ , the arm length errors  $\Delta l_A$  and  $\Delta l_B$ , and the center distance error  $\Delta f$ . It can be seen that the magnitudes of  $\Delta \eta_r$  and  $\Delta \eta_f$  were much greater than those of  $\Delta \eta_{rf}$  and  $\Delta \eta_l$ . As compared with the other three error terms,  $\Delta \eta_{rf}$  was almost a horizontal line since  $-0.0202^\circ \leq \Delta \eta_{rf} \leq -0.0186^\circ$ . Thus,  $\Delta \eta_{rf}$  and  $\Delta \eta_l$  had only slight influences on the magnitude and trend of the overall subtending angle variation,  $\Delta \eta_{\text{est}}$ , as shown in Fig. 7.12(b). The cam profile errors,  $\Delta r_{A,\text{mea}}$  and  $\Delta r_{B,\text{mea}}$ , shown

**Table 7.1** Nominal and actual values of the constant parameters.

Parameter	Nominal value	Actual value (in average)	Error (in average)
$f$	120 mm	120.072 mm	72 $\mu\text{m}$
$l_A$	66 mm	65.984 mm	-16 $\mu\text{m}$
$l_B$	66 mm	65.932 mm	-68 $\mu\text{m}$
$r_{fC}$	16 mm	15.989 mm	-11 $\mu\text{m}$
$r_{fD}$	16 mm	15.990 mm	-10 $\mu\text{m}$
$\eta$	100°	100.287°	0.287° ( $\approx 5 \times 10^{-3}$ rad)

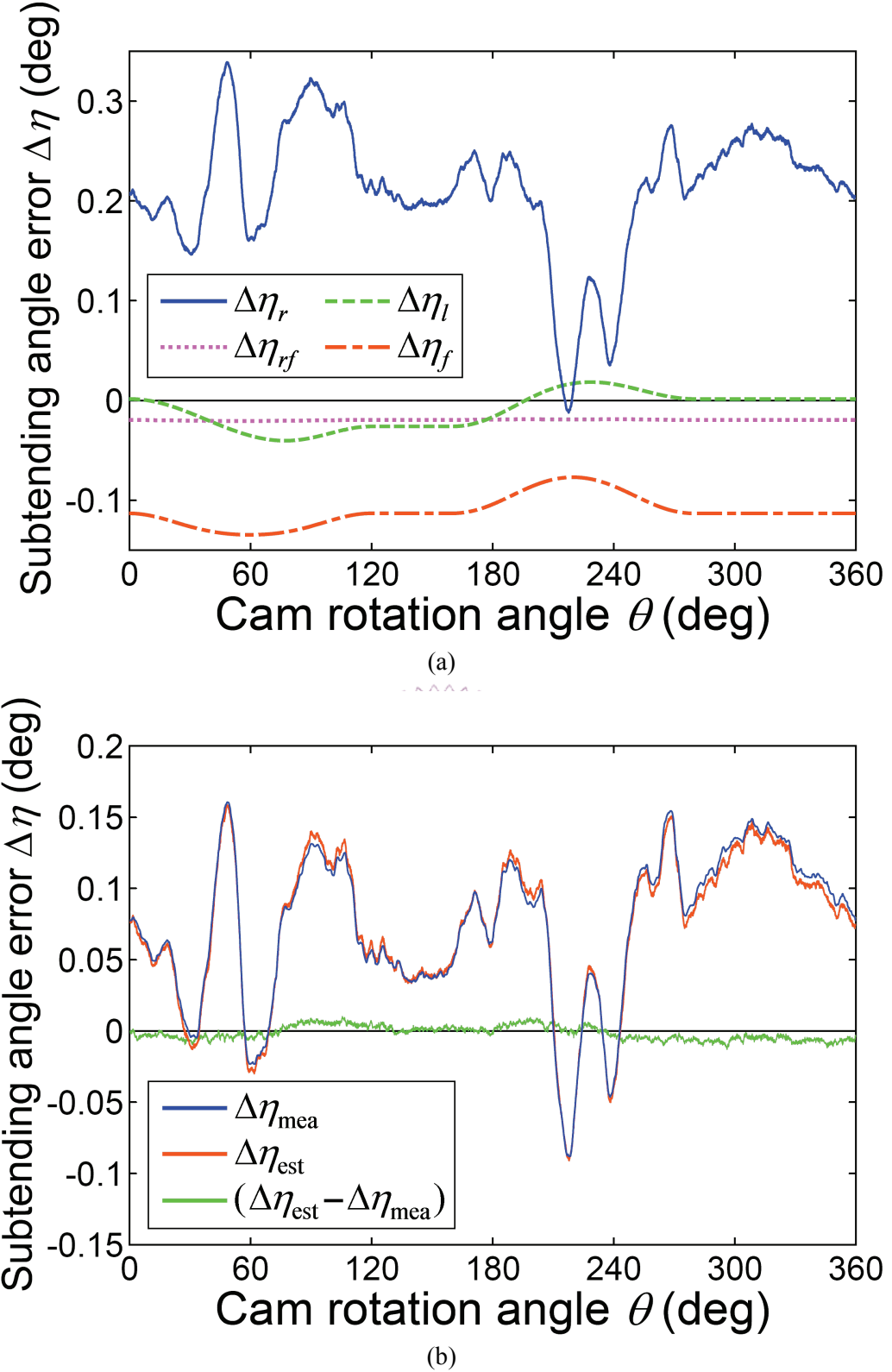
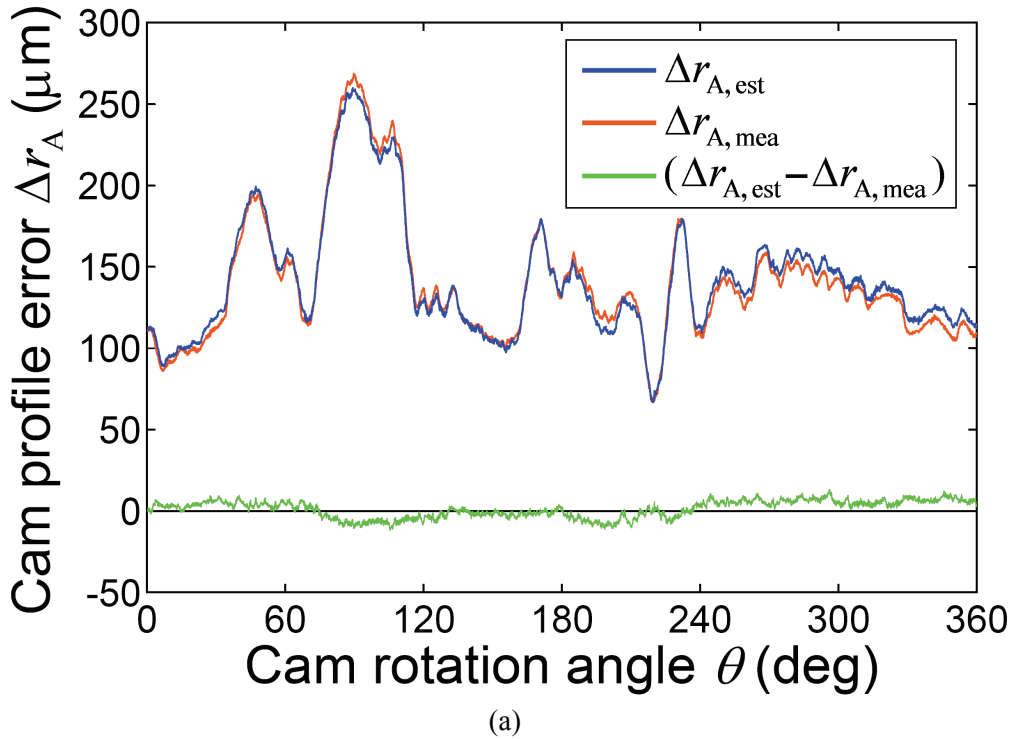
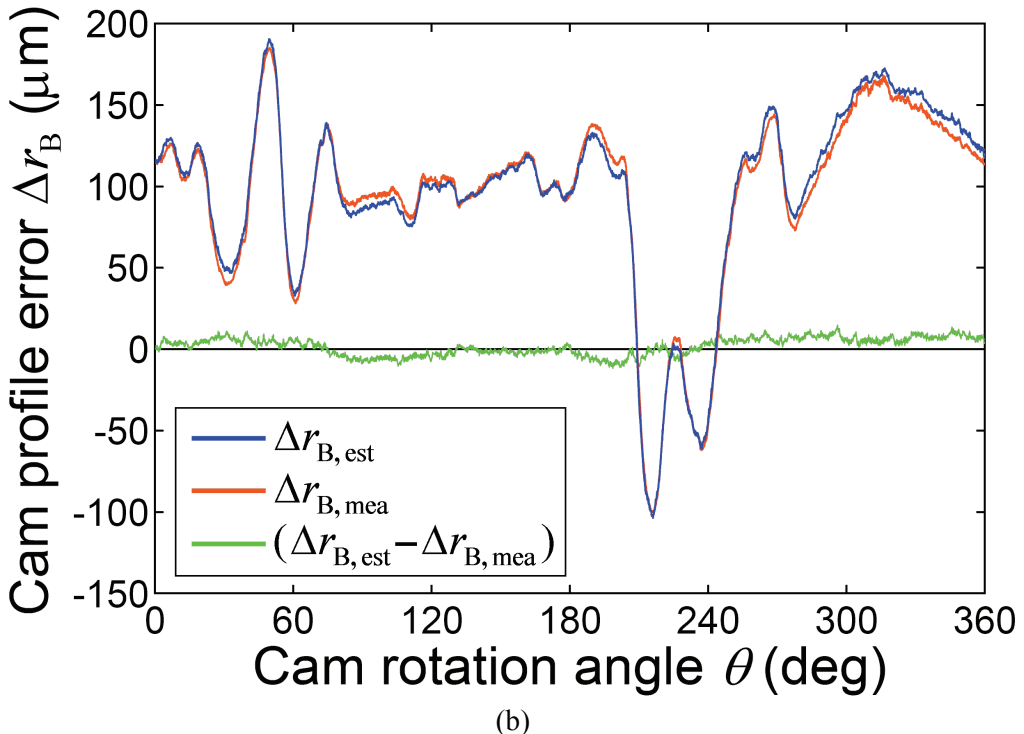


**Figure 7.12** Measured and predicted results of the subtending angle variation.

in Fig. 7.13 mainly dominated the trend of  $\Delta\eta_{est}$ . The measured subtending angle variation,  $\Delta\eta_{mea}$ , and the difference between  $\Delta\eta_{mea}$  and  $\Delta\eta_{est}$  are also shown in Fig. 7.12(b). As



(a)



(b)

**Figure 7.13** Measured and predicted results of the cam profile errors (based on the experiment for measuring the subtending angle variation).

expected,  $\Delta\eta_{\text{mea}}$  and  $\Delta\eta_{\text{est}}$  are very close to each other, while their difference, having values between  $-0.0129^\circ$  and  $0.0103^\circ$ , is once again shown in Fig. 7.14(a) for clarity of illustration. The root-mean-square value of the difference  $(\Delta\eta_{\text{est}} - \Delta\eta_{\text{mea}})$  in a complete

**Table 7.2** Input angles and extreme values of the experiment for measuring the subtending angle variation and the profile errors estimation.

Input angle	Extreme value
$\theta = 48.4^\circ$	$(\Delta\eta_r)_{\max} = 0.3392^\circ$
$\theta = 48.4^\circ$	$(\Delta\eta_{\text{mea}})_{\max} = 0.1607^\circ$
$\theta = 48.4^\circ$	$(\Delta\eta_{\text{est}})_{\max} = 0.1586^\circ$
$\theta = 49.4^\circ$	$(\Delta r_{B,\text{est}})_{\max} = 190.61 \mu\text{m}$
$\theta = 49.7^\circ$	$(\Delta r_{B,\text{mea}})_{\max} = 185.12 \mu\text{m}$
$\theta = 53.7^\circ$	$(\Delta\eta_{rf})_{\min} = -0.0202^\circ$
$\theta = 59.9^\circ$	$(\Delta\eta_f)_{\min} = -0.1343^\circ$
$\theta = 77.3^\circ$	$(\Delta\eta_l)_{\min} = -0.04^\circ$
$\theta = 89.2^\circ$	$(\Delta r_{A,\text{est}})_{\max} = 260.16 \mu\text{m}$
$\theta = 89.6^\circ$	$(\Delta r_{A,\text{mea}})_{\max} = 268.89 \mu\text{m}$
$\theta = 105.4^\circ$	$(\Delta\eta_{\text{est}} - \Delta\eta_{\text{mea}})_{\max} = 0.0103^\circ$
$\theta = 105.4^\circ$	$(\Delta r_{A,\text{est}} - \Delta r_{A,\text{mea}})_{\min} = -11.78 \mu\text{m}$
$\theta = 198.6^\circ$	$(\Delta r_{B,\text{est}} - \Delta r_{B,\text{mea}})_{\min} = -11.84 \mu\text{m}$
$\theta = 215.5^\circ$	$(\Delta r_{B,\text{mea}})_{\min} = -100.46 \mu\text{m}$
$\theta = 216^\circ$	$(\Delta r_{B,\text{est}})_{\min} = -103.74 \mu\text{m}$
$\theta = 217.8^\circ$	$(\Delta\eta_r)_{\min} = -0.012^\circ$
$\theta = 217.8^\circ$	$(\Delta\eta_{\text{est}})_{\min} = -0.0919^\circ$
$\theta = 218^\circ$	$(\Delta\eta_{\text{mea}})_{\min} = -0.088^\circ$
$\theta = 219.3^\circ$	$(\Delta r_{A,\text{mea}})_{\min} = 66.95 \mu\text{m}$
$\theta = 219.5^\circ$	$(\Delta r_{A,\text{est}})_{\min} = 66.99 \mu\text{m}$
$\theta = 220^\circ$	$(\Delta\eta_f)_{\max} = -0.0766^\circ$
$\theta = 228.7^\circ$	$(\Delta\eta_l)_{\max} = 0.0187^\circ$
$\theta = 242.2^\circ$	$(\Delta\eta_{rf})_{\max} = -0.0186^\circ$
$\theta = 296.1^\circ$	$(\Delta\eta_{\text{est}} - \Delta\eta_{\text{mea}})_{\min} = -0.0129^\circ$
$\theta = 296.1^\circ$	$(\Delta r_{A,\text{est}} - \Delta r_{A,\text{mea}})_{\max} = 13.49 \mu\text{m}$
$\theta = 296.1^\circ$	$(\Delta r_{B,\text{est}} - \Delta r_{B,\text{mea}})_{\max} = 14.76 \mu\text{m}$

cam revolution was  $0.00497^\circ$ , and the root-mean-square values of  $\Delta\eta_{\text{mea}}$  and  $\Delta\eta_{\text{est}}$  in a complete cam revolution were  $0.09054^\circ$  and  $0.08923^\circ$ , respectively. From a statistical viewpoint, the relative deviation between  $\Delta\eta_{\text{mea}}$  and  $\Delta\eta_{\text{est}}$  in a root-mean-square form was 5.49% [ $= (0.00497^\circ / 0.09054^\circ) \times 100\%$ ]. Also, considering that  $\Delta\eta_{\text{mea}}$  ranged between

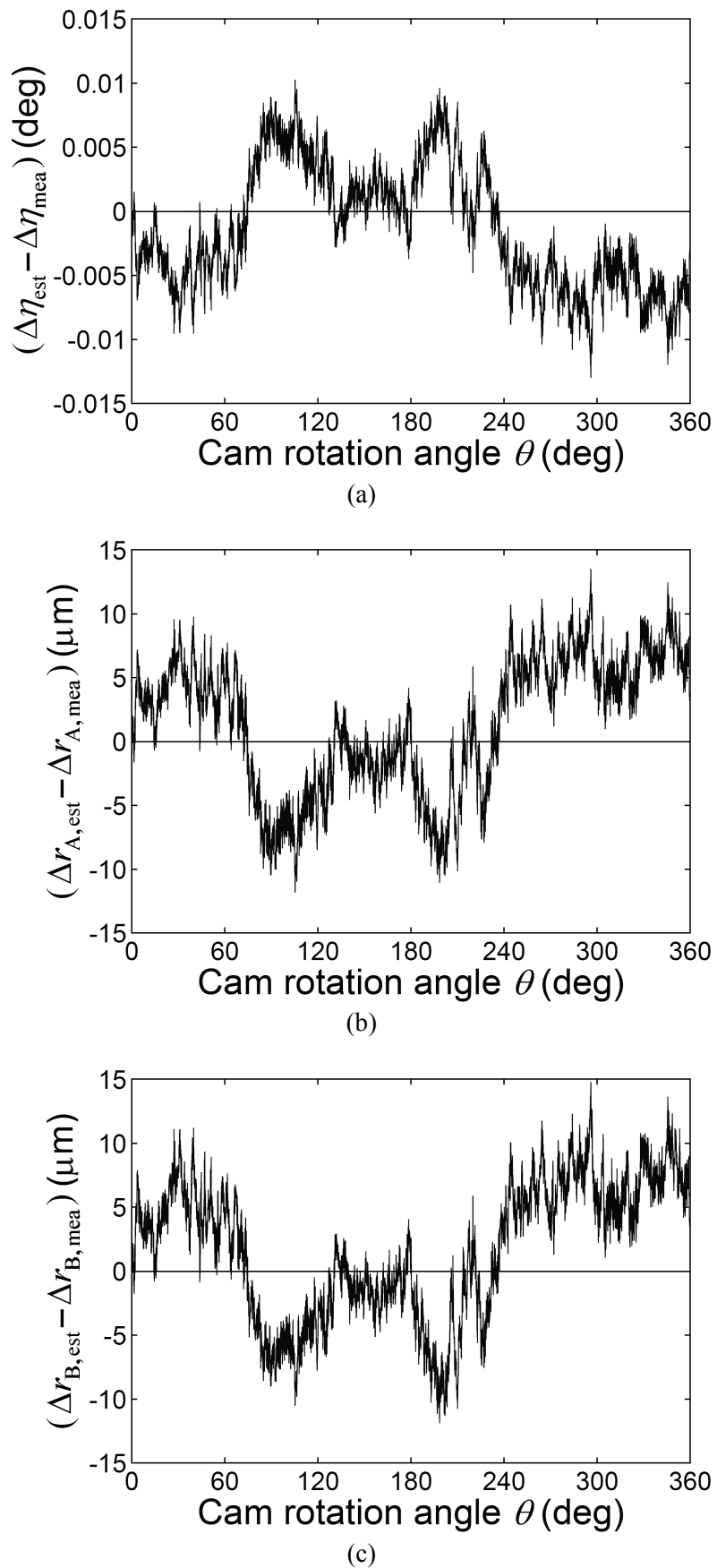
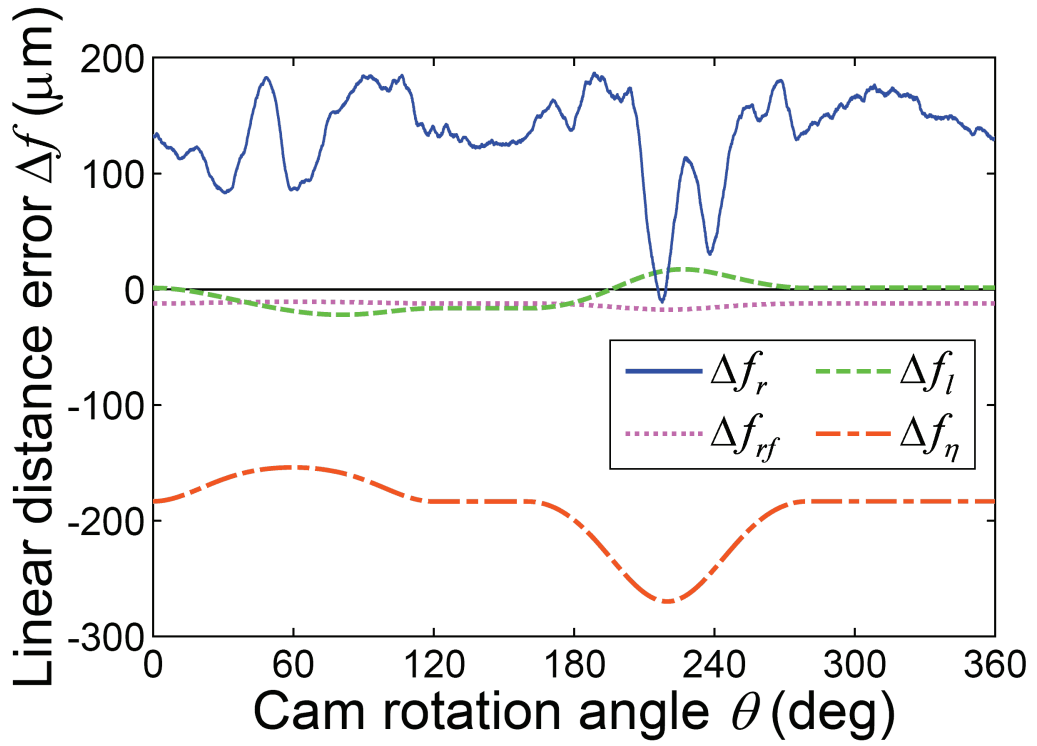


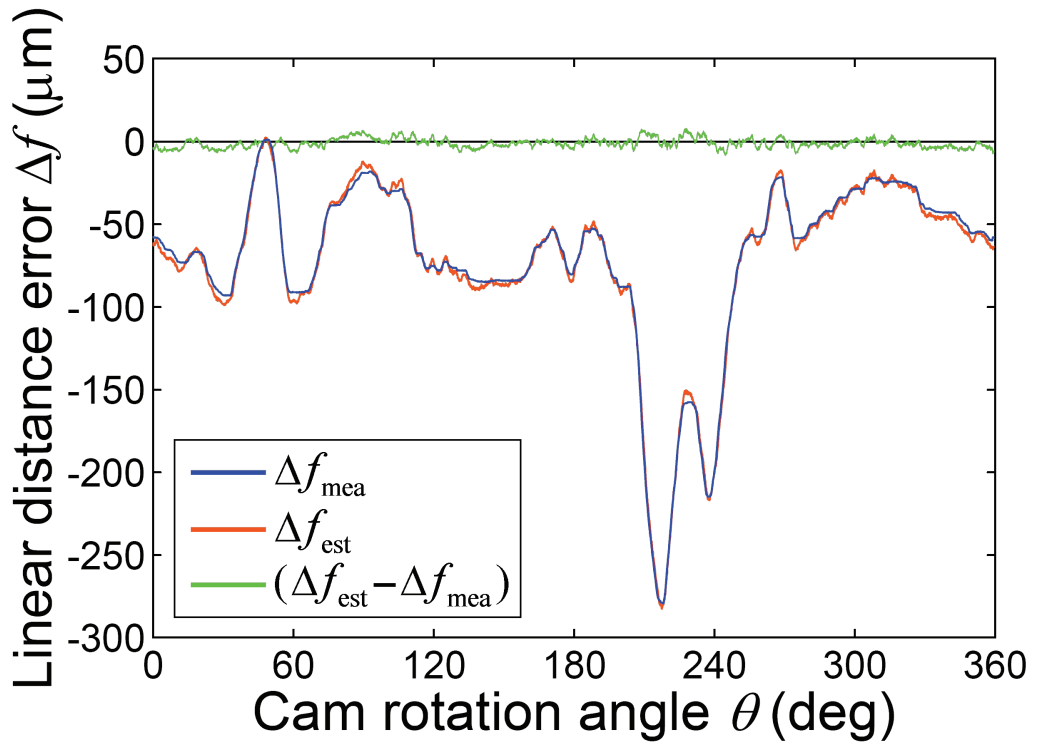
**Figure 7.14** Differences between the measured and predicted results (based on the experiment for measuring the subtending angle variation).

$-0.088^\circ$  and  $0.1607^\circ$  and averaged  $0.0742^\circ$ , such a root-mean-square value of the difference ( $\Delta\eta_{\text{est}} - \Delta\eta_{\text{mea}}$ ), less than  $0.005^\circ$ , implies a good agreement between the measurement and prediction results of the subtending angle variation.

By applying the data of the measured subtending angle variation,  $\Delta\eta_{\text{mea}}$ , the estimated radial profile errors of cams A and B are shown in Figs. 7.13(a) and 7.13(b), respectively, in which  $\Delta r_{A,\text{est}}$  was calculated by substituting the experimental data of  $\Delta\eta_{\text{mea}}$  and  $\Delta r_{B,\text{mea}}$  into Eq. (7.7). Also,  $\Delta r_{B,\text{est}}$  was calculated by substituting the experimental data of  $\Delta\eta_{\text{mea}}$  and  $\Delta r_{A,\text{mea}}$  into Eq. (7.8). As can be seen, the trends and magnitudes of the estimated profile errors are consistent with those of the measured ones. The minor deviations between the estimated and measured profile errors, once again shown in Figs. 7.14(b) and 7.14(c) for clarity of illustration, were in the range of about  $-12 \sim 15 \mu\text{m}$ . The root-mean-square values of the differences ( $\Delta r_{A,\text{est}} - \Delta r_{A,\text{mea}}$ ) and ( $\Delta r_{B,\text{est}} - \Delta r_{B,\text{mea}}$ ) in a complete cam revolution were  $5.42$  and  $5.62 \mu\text{m}$ , respectively. The root-mean-square values of  $\Delta r_{A,\text{mea}}$  and  $\Delta r_{B,\text{mea}}$  in a complete cam revolution were  $146.13$  and  $109.50 \mu\text{m}$ , respectively. Also, the root-mean-square values of  $\Delta r_{A,\text{est}}$  and  $\Delta r_{B,\text{est}}$  in a complete cam revolution were  $146.95$  and  $111.57 \mu\text{m}$ , respectively. From a statistical viewpoint, the relative deviation between  $\Delta r_{A,\text{mea}}$  and  $\Delta r_{A,\text{est}}$  in a root-mean-square form was  $3.71\% [= (5.42/146.13) \times 100\%]$ , and the relative deviation between  $\Delta r_{B,\text{mea}}$  and  $\Delta r_{B,\text{est}}$  in a root-mean-square form was  $5.13\% [= (5.62/109.50) \times 100\%]$ . As compared with  $\Delta r_{A,\text{mea}}$  ranging between  $66.95$  and  $268.89 \mu\text{m}$  and averaging  $140.81 \mu\text{m}$  or  $\Delta r_{B,\text{mea}}$  ranging between  $-100.46$  and  $185.12 \mu\text{m}$  and averaging  $94.83 \mu\text{m}$ , the slight root-mean-square values of the deviations between the estimated and measured profile errors, less than  $6 \mu\text{m}$ , show the effectiveness of the profile errors estimation. That is, Eqs. (7.7) and (7.8) are validated as applicable for estimating conjugate cam profile errors with the data of the measured subtending angle variations.



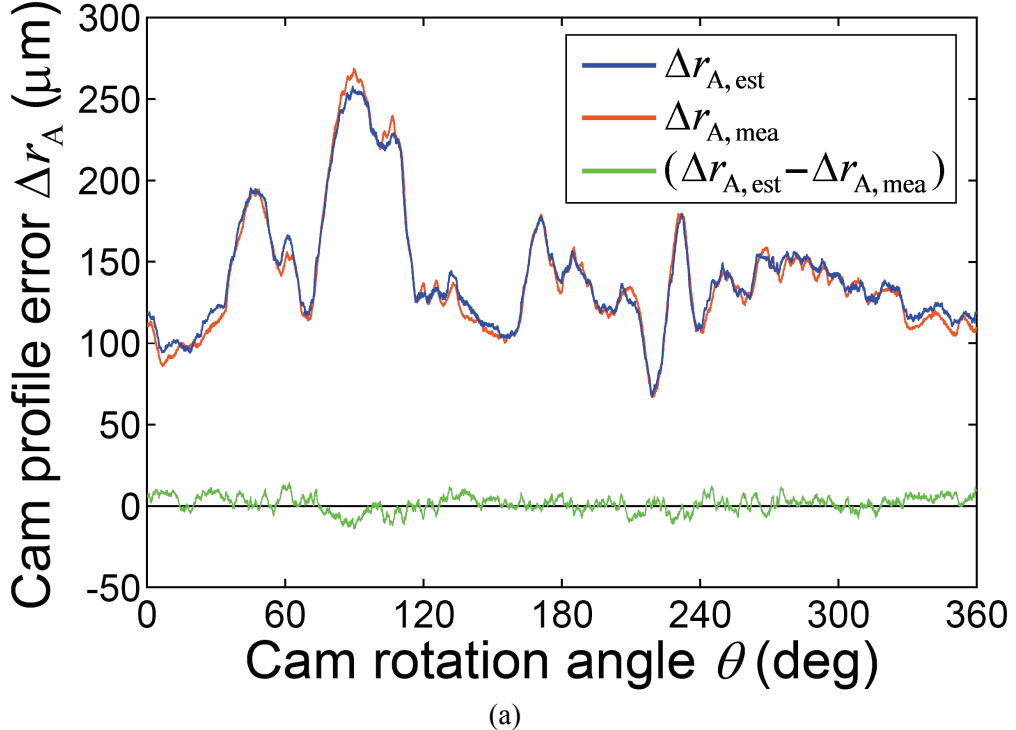
(a)



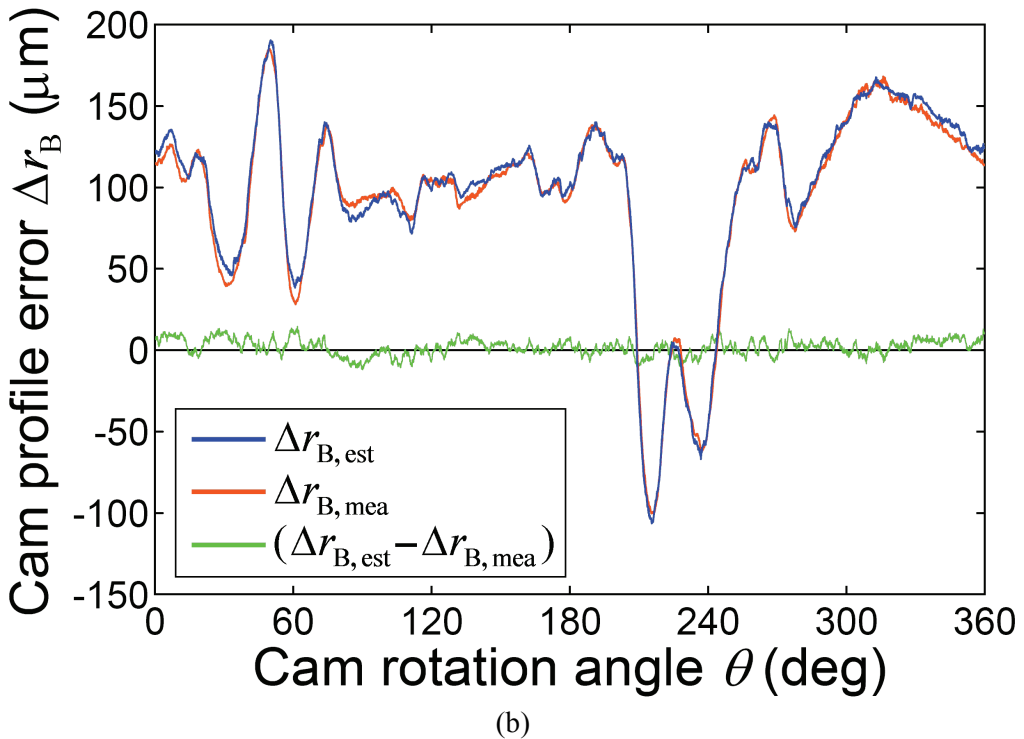
(b)

**Figure 7.15** Measured and predicted results of the center distance variation.

The experimental and predicted results of the measurement of the center distance variation are shown in Fig. 7.15, and the measured and estimated cam profile errors are



(a)



(b)

**Figure 7.16** Measured and predicted results of the cam profile errors (based on the experiment for measuring the center distance variation).

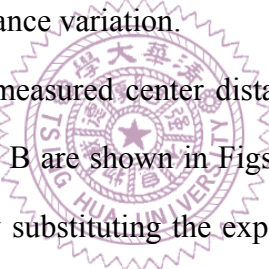
shown in Fig. 7.16, while their extreme values are also listed in Table 7.3. Figure 7.15(a) shows the predicted center distance variations respectively caused by the cam profile errors  $\Delta r_{A, \text{mea}}$  and  $\Delta r_{B, \text{mea}}$ , the roller-radius errors  $\Delta r_{fC}$  and  $\Delta r_{fD}$ , the arm length errors  $\Delta l_A$  and  $\Delta l_B$ ,

**Table 7.3** Input angles and extreme values of the experiment for measuring the center distance variation and the profile errors estimation.

Input angle	Extreme value
$\theta = 48.4^\circ$	$(\Delta f_{\text{est}})_{\text{max}} = 2.57 \mu\text{m}$
$\theta = 48.8^\circ$	$(\Delta f_{\text{mea}})_{\text{max}} = 1.32 \mu\text{m}$
$\theta = 49.7^\circ$	$(\Delta r_{B, \text{mea}})_{\text{max}} = 185.12 \mu\text{m}$
$\theta = 50.1^\circ$	$(\Delta r_{B, \text{est}})_{\text{max}} = 190.45 \mu\text{m}$
$\theta = 59.9^\circ$	$(\Delta f_\eta)_{\text{max}} = -153.82 \mu\text{m}$
$\theta = 61.7^\circ$	$(\Delta r_{A, \text{est}} - \Delta r_{A, \text{mea}})_{\text{max}} = 14.81 \mu\text{m}$
$\theta = 61.7^\circ$	$(\Delta r_{B, \text{est}} - \Delta r_{B, \text{mea}})_{\text{max}} = 14.6 \mu\text{m}$
$\theta = 62.4^\circ$	$(\Delta f_{rf})_{\text{max}} = -10.84 \mu\text{m}$
$\theta = 80.7^\circ$	$(\Delta f_l)_{\text{min}} = -22 \mu\text{m}$
$\theta = 89.2^\circ$	$(\Delta r_{A, \text{est}})_{\text{max}} = 257.93 \mu\text{m}$
$\theta = 89.6^\circ$	$(\Delta r_{A, \text{mea}})_{\text{max}} = 268.89 \mu\text{m}$
$\theta = 90^\circ$	$(\Delta r_{A, \text{est}} - \Delta r_{A, \text{mea}})_{\text{min}} = -13.98 \mu\text{m}$
$\theta = 90^\circ$	$(\Delta r_{B, \text{est}} - \Delta r_{B, \text{mea}})_{\text{min}} = -12.02 \mu\text{m}$
$\theta = 188.6^\circ$	$(\Delta f_r)_{\text{max}} = 187.17 \mu\text{m}$
$\theta = 215.5^\circ$	$(\Delta r_{B, \text{mea}})_{\text{min}} = -100.46 \mu\text{m}$
$\theta = 215.5^\circ$	$(\Delta r_{B, \text{est}})_{\text{min}} = -106.43 \mu\text{m}$
$\theta = 217.8^\circ$	$(\Delta f_r)_{\text{min}} = -11.25 \mu\text{m}$
$\theta = 217.8^\circ$	$(\Delta f_{\text{est}})_{\text{min}} = -282.47 \mu\text{m}$
$\theta = 218^\circ$	$(\Delta f_{\text{mea}})_{\text{min}} = -279.04 \mu\text{m}$
$\theta = 219.1^\circ$	$(\Delta r_{A, \text{est}})_{\text{min}} = 67.63 \mu\text{m}$
$\theta = 219.3^\circ$	$(\Delta r_{A, \text{mea}})_{\text{min}} = 66.95 \mu\text{m}$
$\theta = 219.9^\circ$	$(\Delta f_{rf})_{\text{min}} = -17.6 \mu\text{m}$
$\theta = 220^\circ$	$(\Delta f_\eta)_{\text{min}} = -269.59 \mu\text{m}$
$\theta = 226.6^\circ$	$(\Delta f_l)_{\text{max}} = 17.28 \mu\text{m}$
$\theta = 228.1^\circ$	$(\Delta f_{\text{est}} - \Delta f_{\text{mea}})_{\text{max}} = 8.01 \mu\text{m}$
$\theta = 245^\circ$	$(\Delta f_{\text{est}} - \Delta f_{\text{mea}})_{\text{min}} = -8.21 \mu\text{m}$

and the subtending angle error  $\Delta\eta$ . As observed, the magnitudes of  $\Delta f_r$  and  $\Delta f_\eta$  were much greater than those of  $\Delta f_{rf}$  and  $\Delta f_l$ . Thus,  $\Delta f_{rf}$  and  $\Delta f_l$  were less important in influencing the magnitude and trend of the overall center distance variation,  $\Delta f_{\text{est}}$ , as shown in Fig. 7.15(b). The cam profile errors,  $\Delta r_{A, \text{mea}}$  and  $\Delta r_{B, \text{mea}}$ , shown in Fig. 7.16, and the subtending angle

error,  $\Delta\eta$ , mainly dominated the variation of  $\Delta f_{\text{est}}$ . The measured center distance variation,  $\Delta f_{\text{mea}}$ , and the difference between  $\Delta f_{\text{mea}}$  and  $\Delta f_{\text{est}}$  are also shown in Fig. 7.15(b). As expected,  $\Delta f_{\text{mea}}$  and  $\Delta f_{\text{est}}$  are very close to each other and have almost the same trend, while their difference, having values between  $-8.21$  and  $8.01$   $\mu\text{m}$ , is once again shown in Fig. 7.17(a) for clarity of illustration. The root-mean-square value of the difference ( $\Delta f_{\text{est}} - \Delta f_{\text{mea}}$ ) in a complete cam revolution was  $3.02$   $\mu\text{m}$ , and the root-mean-square values of  $\Delta f_{\text{mea}}$  and  $\Delta f_{\text{est}}$  in a complete cam revolution were  $87.99$  and  $88.67$   $\mu\text{m}$ , respectively. From a statistical viewpoint, the relative deviation between  $\Delta f_{\text{mea}}$  and  $\Delta f_{\text{est}}$  in a root-mean-square form was  $3.43\% [= (3.02 / 87.99) \times 100\%]$ . Also, considering that  $\Delta f_{\text{mea}}$  ranged between  $-279.04$  and  $1.32$   $\mu\text{m}$  and averaged  $-71.13$   $\mu\text{m}$ , such a root-mean-square value of the difference ( $\Delta f_{\text{est}} - \Delta f_{\text{mea}}$ ), about  $3$   $\mu\text{m}$ , implies a good agreement between the measurement and prediction results of the center distance variation.



By applying the data of the measured center distance variation,  $\Delta f_{\text{mea}}$ , the estimated radial profile errors of cams A and B are shown in Figs. 7.16(a) and 7.16(b), respectively, in which,  $\Delta r_{A,\text{est}}$  was calculated by substituting the experimental data of  $\Delta f_{\text{mea}}$  and  $\Delta r_{B,\text{mea}}$  into Eq. (7.15). Also,  $\Delta r_{B,\text{est}}$  was calculated by substituting the experimental data of  $\Delta f_{\text{mea}}$  and  $\Delta r_{A,\text{mea}}$  into Eq. (7.16). It shows that the estimated and measured profile errors are very close to each other. The minor deviations between the estimated and measured profile errors, once again shown in Figs. 7.17(b) and 7.17(c) for clarity of illustration, were in the range of about  $\pm 15$   $\mu\text{m}$ . The root-mean-square values of the differences ( $\Delta r_{A,\text{est}} - \Delta r_{A,\text{mea}}$ ) and ( $\Delta r_{B,\text{est}} - \Delta r_{B,\text{mea}}$ ) in a complete cam revolution were  $5.14$  and  $5.22$   $\mu\text{m}$ , respectively. The root-mean-square values of  $\Delta r_{A,\text{mea}}$  and  $\Delta r_{B,\text{mea}}$  in a complete cam revolution were  $146.13$  and  $109.50$   $\mu\text{m}$ , respectively. Also, the root-mean-square values of  $\Delta r_{A,\text{est}}$  and  $\Delta r_{B,\text{est}}$  in a complete cam revolution were  $147.01$  and  $111.45$   $\mu\text{m}$ , respectively. From a statistical viewpoint, the relative deviation between  $\Delta r_{A,\text{mea}}$  and  $\Delta r_{A,\text{est}}$  in a root-mean-

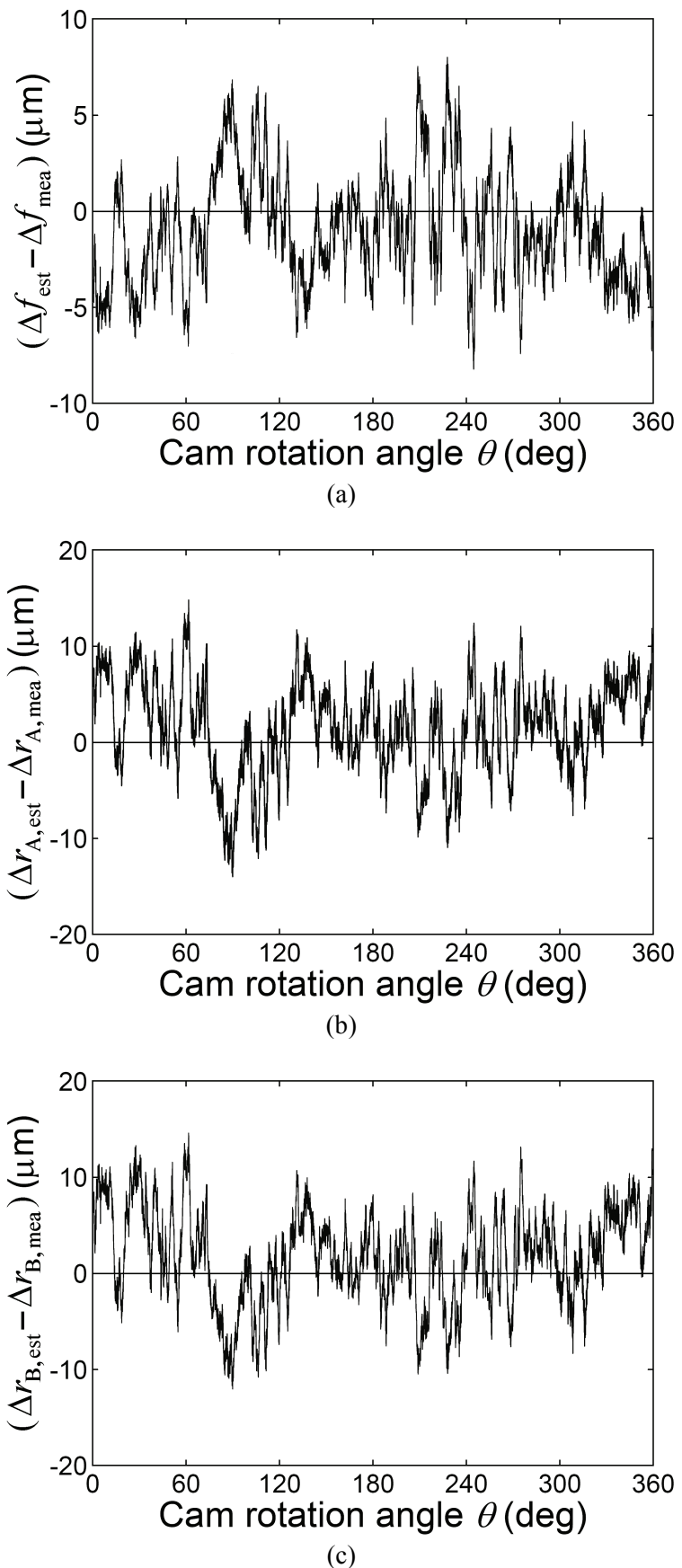


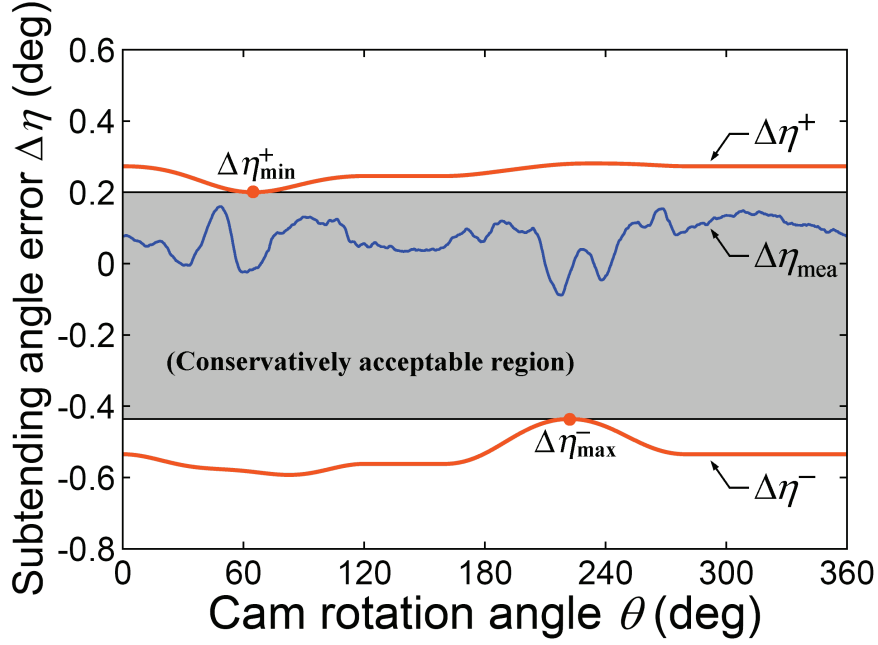
Figure 7.17 Differences between the measured and predicted results (based on the experiment for measuring the center distance variation).

square form was 3.52% [ $=(5.14/146.13) \times 100\%$ ], and the relative deviation between  $\Delta r_{B,\text{mea}}$  and  $\Delta r_{B,\text{est}}$  in a root-mean-square form was 4.76% [ $=(5.22/109.50) \times 100\%$ ]. As compared with  $\Delta r_{A,\text{mea}}$  ranging between 66.95 and 268.89  $\mu\text{m}$  and averaging 140.81  $\mu\text{m}$  or  $\Delta r_{B,\text{mea}}$  ranging between -100.46 and 185.12  $\mu\text{m}$  and averaging 94.83  $\mu\text{m}$ , the slight root-mean-square values of the deviations between the estimated and measured profile errors, which were about 5  $\mu\text{m}$ , show the effectiveness of the profile errors estimation. Hence, Eqs. (7.15) and (7.16) are validated as applicable for estimating conjugate cam profile errors with the data of measured center distance variations.

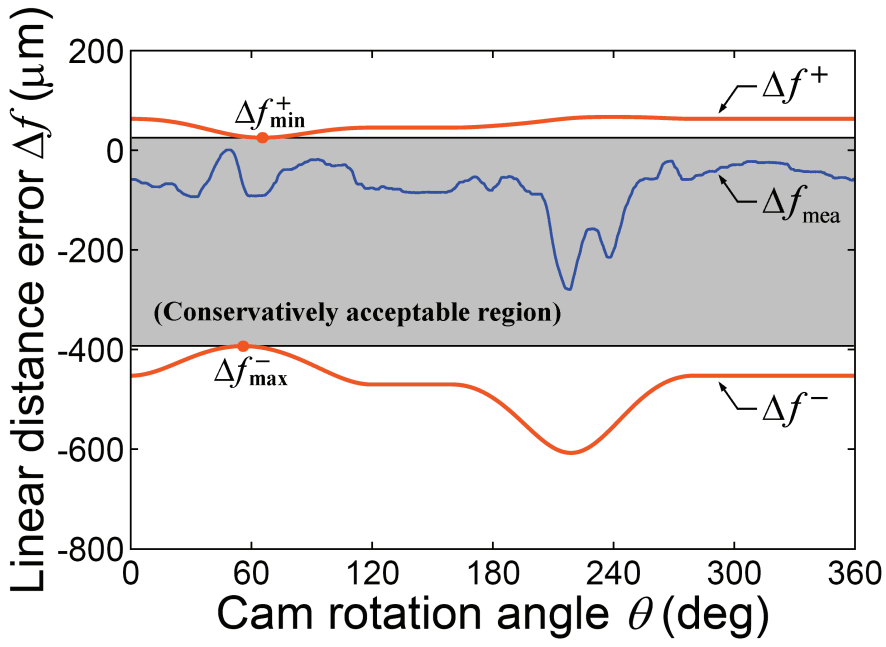
In Figs. 7.14 and 7.17, it is interesting to note that without considering the scale or unit, the waves of differences  $(\Delta\eta_{\text{est}} - \Delta\eta_{\text{mea}})$  and  $(\Delta f_{\text{est}} - \Delta f_{\text{mea}})$  were both upside down to the waves of their corresponding differences  $(\Delta r_{A,\text{est}} - \Delta r_{A,\text{mea}})$  and  $(\Delta r_{B,\text{est}} - \Delta r_{B,\text{mea}})$ . That is, the deviations between the measured and predicted conjugate condition variations should proportionally influence the accuracy of the profile errors estimation.

In addition, recall from Section 7.3 that the conjugate cams were specified to have the radial profile tolerance of  $\pm 220 \mu\text{m}$ , a tolerance grade of IT11. By applying the conservative criteria defined in Section 6.4, the allowable upper and lower limits of the conjugate condition variations are shown in Fig. 7.18. As shown, the measured values of  $\Delta\eta_{\text{mea}}$  and  $\Delta f_{\text{mea}}$  fell within the range of  $\Delta\eta^+ \sim \Delta\eta^-$  and  $\Delta f^+ \sim \Delta f^-$ , respectively, and also fall within their conservatively acceptable regions. It simply means that the conjugate condition of the two inspected cams, for a tolerance grade of IT11, was qualified. However, in Figs. 7.13 and 7.16, it can be seen that the magnitude of  $\Delta r_{A,\text{mea}}$  exceeded the specified tolerance of  $\pm 220 \mu\text{m}$  at about  $\theta = 80^\circ \sim 110^\circ$ , where the magnitude of  $\Delta r_{B,\text{mea}}$  was much smaller than the specified tolerance. Therefore, it can be concluded that even though the profile errors for a pair of inspected cams exceed the specified tolerance, the conjugate condition of the two cams may still be qualified or acceptable, provided that the profile errors of the two cams have compensating effect to enhance their conjugate condition.

The experimental results of measuring the conjugate condition variations are highly



(a)



(b)

Figure 7.18 Allowable upper and lower limits of the conjugate condition variations.

consistent with their mathematical models. The two different types of measured variations,  $\Delta\eta_{\text{mea}}$  and  $\Delta f_{\text{mea}}$ , were independently and successfully applied to estimate the conjugate cam profile errors. However, one may suspect why the experimental data of  $\Delta\eta_{\text{mea}}$  and  $\Delta f_{\text{mea}}$  were not simultaneously considered for the profile errors estimation. This question can be answered by the following derivation. From Eqs. (7.1), (7.6), (7.9), and (7.14), the

correlation between the two measured variations,  $\Delta\eta_{\text{mea}}$  and  $\Delta f_{\text{mea}}$ , and the two unknown profile errors,  $\Delta r_A$  and  $\Delta r_B$ , can be expressed as

$$\mathbf{M} \begin{Bmatrix} \Delta r_A \\ \Delta r_B \end{Bmatrix} = \begin{Bmatrix} \Delta\eta_r \\ \Delta f_r \end{Bmatrix} \approx \begin{Bmatrix} \Delta\eta_{\text{mea}} - (\Delta\eta_{rf} + \Delta\eta_f + \Delta\eta_l) \\ \Delta f_{\text{mea}} - (\Delta f_{rf} + \Delta f_l + \Delta f_\eta) \end{Bmatrix} \quad (7.17)$$

for

$$\mathbf{M} = \begin{bmatrix} \cos\lambda_A/(l_A \cos\phi_A) & \cos\lambda_B/(l_B \cos\phi_B) \\ \frac{l_B \cos\phi_B \cos\lambda_A}{l_A \cos\phi_A \cos\alpha_B + l_B \cos\phi_B \cos\alpha_A} & \frac{l_A \cos\phi_A \cos\lambda_B}{l_A \cos\phi_A \cos\alpha_B + l_B \cos\phi_B \cos\alpha_A} \end{bmatrix} \quad (7.18)$$

Equations (7.17) and (7.18) show a linear system. However, coincidentally,

$$\det(\mathbf{M}) = \frac{\cos\lambda_A \cos\lambda_B - \cos\lambda_A \cos\lambda_B}{l_A \cos\phi_A \cos\alpha_B + l_B \cos\phi_B \cos\alpha_A} = 0 \quad (7.19)$$

Because the determinant of the coefficient matrix  $\mathbf{M}$  is zero, the two unknowns,  $\Delta r_A$  and  $\Delta r_B$ , cannot be simultaneously solved in such a linear dependent system. Therefore, the experimental data of  $\Delta\eta_{\text{mea}}$  and  $\Delta f_{\text{mea}}$  cannot be simultaneously considered for the profile errors estimation.

## 7.6 CONCLUDING REMARKS

Based on the indirect measurement methods of examining conjugate cam profiles introduced in Chapter 6, an extended simple means of estimating cam profile errors from the indicator reading is presented. The magnitudes of profile errors of conjugate cams can be estimated from the indicator reading with employing a pair of master conjugate cams and two sets of identical measuring fixture. If a pair of master conjugate cams with known profile errors is additionally available, through the measured conjugate condition variations of a pair of assembled conjugate cams consisting of one master cam and the other being an inspected cam, then the profile errors of each individual inspected cam can be estimated.

Although a pair of master conjugate cams and two sets of measuring fixtures are required, this inexpensive and efficient means is still suitable for quality control in mass production of conjugate cams as compared to the use of CMMs.

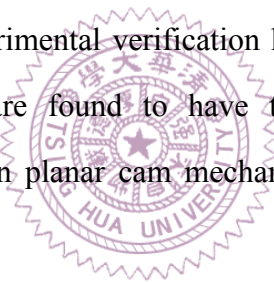
Experiments for examining the profile deviations of a pair of conjugate disk cams with a built integrated-type measuring fixture were performed. The measured conjugate condition variations by using a digimatic indicator were compared with the predicted ones from the derived mathematical models, and a good agreement between the measurement and prediction results was indicated. From a statistical viewpoint, the relative deviation between the predicted and measured conjugate condition variations in a root-mean-square form was less than 5.5%. The estimated profile errors were then compared with those measured by using a CMM (i.e., the experimental results of Chapter 5). Even the two cams were intentionally specified to have a large tolerance grade of IT11 ( $\pm 220 \mu\text{m}$ ), the root-mean-square values of the differences between the estimated and measured profile errors were significantly less than  $6 \mu\text{m}$ . From a statistical viewpoint, the relative deviation between the estimated and measured profile errors in a root-mean-square form was less than 5.2%. Also, it is found that even though the profile errors for a pair of inspected cams exceed the specified tolerance, the conjugate condition of the two cams may still be qualified or acceptable, provided that the profile errors of the two cams have compensating effect to enhance their conjugate condition. According to the experimental results, not only the derived mathematical models for the conjugate condition analysis but also their extended profile error estimation methods are validated to be practically applicable. Therefore, the developed measuring fixtures may replace CMMs for examining conjugate disk cams. More importantly, the fundamental of the conjugate condition analysis, the equivalent linkage method, has also been experimentally validated to be a correct and accurate means for analyzing mechanical errors of disk cam mechanisms.

# CHAPTER 8

## CONCLUSIONS AND RECOMMENDATIONS

### 8.1 CONCLUSIONS

This dissertation has presented the improvement of methodologies for analyzing and synthesizing the tolerances in planar cam mechanisms and for inspecting the tolerances of planar cams. A simple and systematic analytical method, called the equivalent linkage method, for analyzing the mechanical errors of planar cam mechanisms has been developed. This developed tolerance analysis method has been successfully applied to undertake the optimal tolerance allocation and profile error inspection tasks. Both theoretical investigation and experimental verification have been performed in this work, and the presented approaches are found to have the potential for simplifying the complexity of producing precision planar cam mechanisms. Several conclusions can be drawn from these results:



#### ***Mechanical error analysis:***

By employing the concept of equivalent linkage and the derived correlation between the radial-dimension errors and the normal-direction errors of the cam profile, the mechanical errors of disk cam mechanisms can be determined systematically; the same approach is equally applicable to planar mechanisms incorporating linkages and cams. The displacement, velocity, and acceleration error equations of the follower motion arising from the variation in each design parameter can be derived analytically. The resulting error equations do not really involve the location of the curvature center of the cam profile, and thus locating the curvature center of the cam profile is not essential while the analysis is undertaken. The method has been validated through analyzing an eccentric circular cam mechanism whose exact solution is available. As compared with the exact solutions, the results predicted by the presented method can have a relative deviation less than 0.01%

when the cam profile is specified to have a tolerance grade of IT6. Even the cam profile is specified to have a considerably large tolerance grade of IT13, the method can still provide a relative deviation less than 1%, sufficiently accurate from an engineering viewpoint. Also, for an exaggerated case whose relatively large profile error is assumed to be caused by adopting an incorrect follower motion program, the cam profile errors evaluated by using the shift angle is found to have a relative deviation less than 7% when compared with their exact values. Although the extreme cam profile errors in this exaggerated case have a quite large tolerance grade ranging from IT16 to IT17, the use of the shift angle to correlate the radial-dimension errors and the normal-direction errors of the cam profile can still provide acceptable accuracy from an engineering viewpoint.

The equivalent linkage method has been illustrated through analyzing the mechanical errors of all four types of disk cam mechanisms and analyzing the mechanical errors of the MEG X6061 planar cam-follower type pick-and-place device. It is found that the pressure angle has the most dominating effect on the resulting error, and the larger pressure angle will result in the larger mechanical error. The design parameter that may result in a larger resulting error should have a smaller tolerance. In the worst case, owing to the joined effects of various design parameters, the accuracy of the follower motion may degrade considerably. For most cases, the extreme value of the worst-case deviation occurs very close to where the extreme pressure angle occurs. For the roller follower and the oscillating flat-faced follower cases, the acceleration error functions have a sudden change at each beginning and end of the motion even though the theoretical follower displacement is cycloidal motion. However, for the translating flat-faced follower case, neither the error of the cam profile nor the variation of offset amount will cause the sudden change of the acceleration error function. This implies that a translating flat-faced follower is a potentially superior choice over other types of followers for generating smoother motions.

### ***Optimal tolerance allocation:***

By incorporating the equivalent linkage method and the concept of design for manufacture and assembly (DFMA), this study has developed a procedure of optimal

tolerance allocation for planar cam mechanisms. The optimized tolerance combination will result in the maximized manufacturability and assembly of the cam mechanism while maintaining acceptable kinematic accuracy of the follower motion. A comprehensive index, CI, has been proposed for quantitatively evaluating the correlation between the extent of difficulty of manufacturing and assembling the cam mechanism and the tolerances in its theoretical design parameters. This comprehensive index, which is defined as the weighted sum of all manufacturing and assembly tolerances quantitatively expressed in an exchanged consistent unit, is used as the objective function for the optimal design problem. The selection of the weighting factor of each tolerance actually involves the information of manufacturing and assembly processes and their respectively required cost and time. To obtain a reasonably acceptable optimal solution, the extreme values of the maximum expected deviations of the follower output and their relative differences should be simultaneously controlled precisely.

This optimal procedure has been illustrated by allocating the tolerances in the MEG X6061 planar cam-follower type pick-and-place device. As compared to the initial design based on a tolerance grade of IT6, the optimization results can lead to an improved value of CI having a magnitude more than twice the initial one. It is found that the optimal tolerance grades for the cam profiles, which have the largest weighting factors, can be larger than other design parameters. Also, because the sensitivity of each tolerance on influencing the mechanical error is quite different, not every tolerance with a smaller weighting factor always needs to have a smaller tolerance grade.

#### ***Profile error inspection:***

In order to inspect the profile deviations of disk cams, a direct and concise analytical method for dealing with the coordinate measurement data obtained from a coordinate measuring machine (CMM) has been proposed. This method is based on the derived correlation between the radial-dimension errors and the normal-direction errors of the cam profile. To verify this method, an experiment of inspecting a pair of conjugate disk cams was conducted. The experimental results obtained from the proposed method were

compared with those obtained by using the Hermite interpolation method. Even the two cams were intentionally specified to have a large tolerance grade of IT11 ( $\pm 220 \mu\text{m}$ ), either the maximum difference or relative deviation between the proposed method and the Hermite interpolation method were less than  $2.2 \mu\text{m}$  or 1.4%. As compared with the Hermite interpolation method, the proposed method may analytically handle the measured data and may eliminate the need for complex analysis procedures. Therefore, it is an efficient means for dealing with the coordinate measurement data to inspect the profile errors of disk cams.

This study has also demonstrated how to use a special measuring fixture to measure the conjugate condition of an assembled conjugate cam mechanism so as to indirectly evaluate the deviations of conjugate cam profiles; for such an indirect measurement method, the only required measuring instrument is a dial indicator. For a conjugate cam mechanism being examined, by employing the equivalent linkage method, the correlation between the conjugate condition variations and the cam profile errors can be derived analytically. Based on the correlation, conservative criteria for qualify control of assembled conjugate cams have been proposed. This indirect measurement method is particularly suitable for the quality control in mass production of conjugate cams. Furthermore, if a pair of master conjugate cams with known profile errors is additionally available, through the measured conjugate condition variations of a pair of assembled conjugate cams consisting of one master cam and the other being an inspected cam, then the profile errors of each individual inspected cam can be estimated. The indirect measurement method has been illustrated through examining a conjugate cam mechanism with an oscillating roller follower; either the variation of the subtending angle of the follower arms or the variation of the distance from the cam center to the follower pivot center can reveal the cam profile errors. Two examples of the indirect measurement method have been illustrated. Also, a pair of conjugate cams were examined by the method and also measured using a CMM to test the accuracy of the method. The measured conjugate condition variations by using a digimatic indicator were compared with the predicted ones, and a good agreement between

the measurement and prediction results was verified. From a statistical viewpoint, the relative deviation between the predicted and measured conjugate condition variations in a root-mean-square form was less than 5.5%. The estimated profile errors by the measured data of the conjugate condition variations were then compared with those directly measured by using a CMM. Even the two cams were intentionally specified to have a large tolerance grade of IT11 ( $\pm 220 \mu\text{m}$ ), the root-mean-square values of the deviations between the estimated and measured profile errors were less than  $6 \mu\text{m}$ . From a statistical viewpoint, the relative deviation between the estimated and measured profile errors in a root-mean-square form was less than 5.2%. Also, it is found that even though a pair of conjugate cam profiles exceeds their specified tolerances, the conjugate condition of the dual disk cams may still be qualified or acceptable if the profile errors of the two cams have compensating effect to enhance their conjugate condition. According to the experimental results, the indirect measurement method has been validated to be practically applicable. Therefore, this method may have potential superiority of replacing CMMs for examining conjugate disk cams. More importantly, the equivalent linkage method has also been experimentally verified to be a correct and accurate means for analyzing mechanical errors of planar cam mechanisms.

## 8.2 RECOMMENDATIONS

The following subjects may be further explored in the future research.

1. Since the equivalent linkage method is suitable for dealing with dimensional tolerances in planar cam mechanisms, the same analysis techniques can be modified and further extended to deal with a three-dimensional aspect, such as to evaluate the mechanical errors of cam mechanisms caused by geometrical tolerances as well as parallelism errors between axes.
2. The effects of deformation of links, clearances in joints, and thermal expansion caused by temperature variation on the mechanical errors of cam mechanisms may also be

investigated.

3. The concept of indirectly measuring conjugate cam profiles with a measuring fixture could be integrated with machine system design to develop a commercial measuring system to replace the use of expensive CMMs in some aspects.



# APPENDIX A

## VELOCITY AND ACCELERATION ERROR FUNCTIONS FOR DISK CAM MECHANISMS

### A.1 DISK CAM WITH AN OFFSET TRANSLATING ROLLER FOLLOWER

The velocity and acceleration error functions for disk cams with an offset translating roller follower are presented below.

*Velocity and acceleration errors caused only by  $\Delta e$ :*

The velocity and acceleration error functions caused by  $\Delta e$  are respectively the first and second derivatives of displacement error function  $\Delta S_e$  with respect to time. Therefore, differentiation of Eq. (3.23) once and twice, respectively, gives

$$\Delta V_e = \frac{d(\Delta S_e)}{dt} = \frac{d(\Delta S_e)}{d\theta} \frac{d\theta}{dt} = \frac{d(\Delta S_e)}{d\theta} \omega_2 \quad (\text{A.1})$$

$$\Delta A_e = \frac{d^2(\Delta S_e)}{dt^2} = \frac{d^2(\Delta S_e)}{d\theta^2} \omega_2^2 + \frac{d(\Delta S_e)}{d\theta} \alpha_2 \quad (\text{A.2})$$

and

$$\frac{d(\Delta S_e)}{d\theta} = \Delta e(1 + \tan^2 \phi) \frac{d\phi}{d\theta} \quad (\text{A.3})$$

$$\frac{d^2(\Delta S_e)}{d\theta^2} = \Delta e(1 + \tan^2 \phi) \left[ 2 \left( \frac{d\phi}{d\theta} \right)^2 \tan \phi + \frac{d^2\phi}{d\theta^2} \right] \quad (\text{A.4})$$

in which, from Eq. (2.17), the first and second derivatives of the pressure angle  $\phi$  with respect to the cam rotation angle  $\theta$  are

$$\frac{d\phi}{d\theta} = \frac{aL - v(v-e)}{L^2 + (v-e)^2} \quad (\text{A.5})$$

$$\frac{d^2\phi}{d\theta^2} = \frac{L^2[jL + a(e-3v)] + (v-e)^2[jL + a(v+e)] + 2L(v-e)(v^2-a^2)}{[L^2 + (v-e)^2]^2} \quad (\text{A.6})$$

where  $L$ ,  $v$ ,  $a$ , and  $j$  are the linear displacement, velocity, acceleration, and jerk functions of the follower, respectively.

#### ***Velocity and acceleration errors caused only by $\Delta r_f$ :***

The velocity and acceleration error functions caused by  $\Delta r_f$  are respectively the first and second derivatives of displacement error function  $\Delta S_{rf}$  with respect to time. Therefore, differentiation of Eq. (3.19) once and twice, respectively, gives

$$\Delta V_{rf} = \frac{d(\Delta S_{rf})}{dt} = \frac{d(\Delta S_{rf})}{d\theta} \frac{d\theta}{dt} = \frac{d(\Delta S_{rf})}{d\theta} \omega_2 \quad (\text{A.7})$$

$$\Delta A_{rf} = \frac{d^2(\Delta S_{rf})}{dt^2} = \frac{d^2(\Delta S_{rf})}{d\theta^2} \omega_2^2 + \frac{d(\Delta S_{rf})}{d\theta} \alpha_2 \quad (\text{A.8})$$

and

$$\frac{d(\Delta S_{rf})}{d\theta} = \Delta r_f \frac{d\phi}{d\theta} \tan \phi \sec \phi \quad (\text{A.9})$$

$$\frac{d^2(\Delta S_{rf})}{d\theta^2} = \Delta r_f \left[ \frac{d^2\phi}{d\theta^2} \tan \phi + \left( \frac{d\phi}{d\theta} \right)^2 (1 + 2 \tan^2 \phi) \right] \sec \phi \quad (\text{A.10})$$

in which, the first and second derivatives of the pressure angle  $\phi$  with respect to the cam rotation angle  $\theta$  are shown in Eqs. (A.5) and (A.6).

#### ***Velocity and acceleration errors caused only by $\Delta r$ :***

The velocity and acceleration error functions caused by  $\Delta r$  are respectively the first and second derivatives of displacement error function  $\Delta S_r$  with respect to time. Therefore, differentiation of Eq. (3.26) once and twice, respectively, gives

$$\Delta V_r = \frac{d(\Delta S_r)}{dt} = \frac{d(\Delta S_r)}{d\theta} \omega_2 \quad (\text{A.11})$$

$$\Delta A_r = \frac{d^2(\Delta S_r)}{dt^2} = \frac{d^2(\Delta S_r)}{d\theta^2} \omega_2^2 + \frac{d(\Delta S_r)}{d\theta} \alpha_2 \quad (\text{A.12})$$

where

$$\frac{d(\Delta S_r)}{d\theta} = \Delta r \left( \frac{d\phi}{d\theta} \tan \phi \cos \lambda - \frac{d\lambda}{d\theta} \sin \lambda \right) \sec \phi \quad (\text{A.13})$$

$$\begin{aligned} \frac{d^2(\Delta S_r)}{d\theta^2} = & \Delta r \left\{ \left[ (1 + 2 \tan^2 \phi) \left( \frac{d\phi}{d\theta} \right)^2 + \frac{d^2 \phi}{d\theta^2} \tan \phi - \left( \frac{d\lambda}{d\theta} \right)^2 \right] \cos \lambda \right. \\ & \left. - \left( 2 \frac{d\lambda}{d\theta} \frac{d\phi}{d\theta} \tan \phi + \frac{d^2 \lambda}{d\theta^2} \right) \sin \lambda \right\} \sec \phi \end{aligned} \quad (\text{A.14})$$

in which, from Eq. (3.25), the first and second derivatives of the shift angle  $\lambda$  with respect to the cam rotation angle  $\theta$  are

$$\frac{d\lambda}{d\theta} = \frac{W_{a1}}{\|\mathbf{R}\| \cos \lambda} \quad (\text{A.15})$$

$$\frac{d^2 \lambda}{d\theta^2} = \frac{W_{a1} \left( \|\mathbf{R}\| \frac{d\lambda}{d\theta} \sin \lambda - \frac{\mathbf{R} \bullet \mathbf{R}'}{\|\mathbf{R}\|} \cos \lambda \right) + (W_{a2} \cos \phi + W_{a3} \sin \phi) \|\mathbf{R}\| \cos \lambda}{\|\mathbf{R}\|^2 \cos^2 \lambda} \quad (\text{A.16})$$

where

$$W_{a1} = \left( a - v \frac{\mathbf{R} \bullet \mathbf{R}'}{\|\mathbf{R}\|^2} \right) \cos \phi - v \frac{d\phi}{d\theta} \sin \phi \quad (\text{A.17})$$

$$W_{a2} = j - a \frac{\mathbf{R} \bullet \mathbf{R}'}{\|\mathbf{R}\|^2} - v \left[ \left( \frac{d\phi}{d\theta} \right)^2 + \frac{(\mathbf{R}' \bullet \mathbf{R}' + \mathbf{R} \bullet \mathbf{R}'') \|\mathbf{R}\|^2 - 2(\mathbf{R} \bullet \mathbf{R}')^2}{\|\mathbf{R}\|^4} \right] \quad (\text{A.18})$$

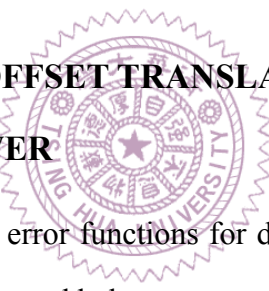
$$W_{a3} = \left( v \frac{\mathbf{R} \bullet \mathbf{R}'}{\|\mathbf{R}\|^2} - 2a \right) \frac{d\phi}{d\theta} - v \frac{d^2 \phi}{d\theta^2} \quad (\text{A.19})$$

$$\mathbf{R}' = \frac{d\mathbf{R}}{d\theta} = \begin{cases} (v - e) \cos \theta - L \sin \theta + r_f \left( 1 - \frac{d\phi}{d\theta} \right) \sin(\theta - \phi) \\ (v - e) \sin \theta + L \cos \theta - r_f \left( 1 - \frac{d\phi}{d\theta} \right) \cos(\theta - \phi) \end{cases} \quad (\text{A.20})$$

$$\begin{aligned} \mathbf{R}'' &= \frac{d^2\mathbf{R}}{d\theta^2} \\ &= \begin{cases} (a - L) \cos \theta - (2v - e) \sin \theta + r_f \left[ \left( 1 - \frac{d\phi}{d\theta} \right)^2 \cos(\theta - \phi) - \frac{d^2\phi}{d\theta^2} \sin(\theta - \phi) \right] \\ (a - L) \sin \theta + (2v - e) \cos \theta + r_f \left[ \left( 1 - \frac{d\phi}{d\theta} \right)^2 \sin(\theta - \phi) + \frac{d^2\phi}{d\theta^2} \cos(\theta - \phi) \right] \end{cases} \quad (\text{A.21}) \end{aligned}$$

in which, the parametric vector equations of the theoretical cam profile coordinates,  $\mathbf{R}$ , are shown in Eq. (2.22).

## A.2 DISK CAM WITH AN OFFSET TRANSLATING OBLIQUE FLAT-FACED FOLLOWER



The velocity and acceleration error functions for disk cams with an offset translating oblique flat-faced follower are presented below.

**Velocity and acceleration errors caused only by  $\Delta\phi$ :**

The velocity and acceleration error functions caused by  $\Delta\phi$  are respectively the first and second derivatives of displacement error function  $\Delta S_\phi$  with respect to time. Therefore, differentiation of Eq. (3.37) once and twice, respectively, gives

$$\Delta V_\phi = \frac{d(\Delta S_\phi)}{dt} = \frac{d(\Delta S_\phi)}{d\theta} \frac{d\theta}{dt} = \frac{d(\Delta S_\phi)}{d\theta} \omega_2 \quad (\text{A.22})$$

$$\Delta A_\phi = \frac{d^2(\Delta S_\phi)}{dt^2} = \frac{d^2(\Delta S_\phi)}{d\theta^2} \omega_2^2 + \frac{d(\Delta S_\phi)}{d\theta} \alpha_2 \quad (\text{A.23})$$

where

$$\frac{d(\Delta S_\phi)}{d\theta} = \Delta\phi(v \tan \phi + a) \quad (\text{A.24})$$

$$\frac{d^2(\Delta S_\phi)}{d\theta^2} = \Delta\phi(a \tan \phi + j) \quad (\text{A.25})$$

in which,  $L$ ,  $v$ ,  $a$ , and  $j$  are the linear displacement, velocity, acceleration, and jerk functions of the follower, respectively.

#### **Velocity and acceleration errors caused only by $\Delta e$ :**

The velocity and acceleration error functions caused by  $\Delta e$  are respectively the first and second derivatives of displacement error function  $\Delta S_e$  with respect to time. Therefore, differentiation of Eq. (3.42) once and twice, respectively, gives

$$\Delta V_e = \frac{d(\Delta S_e)}{dt} = \frac{d(\Delta S_e)}{d\theta} \frac{d\theta}{dt} = \frac{d(\Delta S_e)}{d\theta} \omega_2 \quad (\text{A.26})$$

$$\Delta A_e = \frac{d^2(\Delta S_e)}{dt^2} = \frac{d^2(\Delta S_e)}{d\theta^2} \omega_2^2 + \frac{d(\Delta S_e)}{d\theta} \alpha_2 \quad (\text{A.27})$$

where

$$\frac{d(\Delta S_e)}{d\theta} = 0 \quad (\text{A.28})$$

$$\frac{d^2(\Delta S_e)}{d\theta^2} = 0 \quad (\text{A.29})$$

That is,  $\Delta V_e$  and  $\Delta A_e$  are both zero since  $\Delta S_e$  is a constant.

#### **Velocity and acceleration errors caused only by $\Delta r$ :**

The velocity and acceleration error functions caused by  $\Delta r$  are respectively the first and second derivatives of displacement error function  $\Delta S_r$  with respect to time. Therefore, differentiation of Eq. (3.47) once and twice, respectively, gives

$$\Delta V_r = \frac{d(\Delta S_r)}{dt} = \frac{d(\Delta S_r)}{d\theta} \omega_2 \quad (\text{A.30})$$

$$\Delta A_r = \frac{d^2(\Delta S_r)}{dt^2} = \frac{d^2(\Delta S_r)}{d\theta^2} \omega_2^2 + \frac{d(\Delta S_r)}{d\theta} \alpha_2 \quad (\text{A.31})$$

where

$$\frac{d(\Delta S_r)}{d\theta} = -\Delta r \frac{d\lambda}{d\theta} \sin \lambda \sec \phi \quad (\text{A.32})$$

$$\frac{d^2(\Delta S_r)}{d\theta^2} = -\Delta r \left[ \left( \frac{d\lambda}{d\theta} \right)^2 \cos \lambda + \frac{d^2 \lambda}{d\theta^2} \sin \lambda \right] \sec \phi \quad (\text{A.33})$$

in which, from Eq. (3.46), the first and second derivatives of the shift angle  $\lambda$  with respect to the cam rotation angle  $\theta$  are

$$\frac{d\lambda}{d\theta} = \frac{W_{b1}}{\|\mathbf{R}\| \cos \lambda} \quad (\text{A.34})$$

$$\frac{d^2 \lambda}{d\theta^2} = \frac{W_{b1} \left( \|\mathbf{R}\| \frac{d\lambda}{d\theta} \sin \lambda - \frac{\mathbf{R} \bullet \mathbf{R}'}{\|\mathbf{R}\|} \cos \lambda \right) + W_{b2} \|\mathbf{R}\| \cos \phi \cos \lambda}{\|\mathbf{R}\|^2 \cos^2 \lambda} \quad (\text{A.35})$$

where

$$W_{b1} = \left( a - v \frac{\mathbf{R} \bullet \mathbf{R}'}{\|\mathbf{R}\|^2} \right) \cos \phi \quad (\text{A.36})$$

$$W_{b2} = j - a \frac{\mathbf{R} \bullet \mathbf{R}'}{\|\mathbf{R}\|^2} - v \frac{(\mathbf{R}' \bullet \mathbf{R}' + \mathbf{R} \bullet \mathbf{R}'') \|\mathbf{R}\|^2 - 2(\mathbf{R} \bullet \mathbf{R}')^2}{\|\mathbf{R}\|^4} \quad (\text{A.37})$$

$$\mathbf{R}' = \frac{d\mathbf{R}}{d\theta} = \begin{cases} -a[\sin \phi \cos(\theta + \phi) + \sin \theta] - W_{b3} \sin(\theta + \phi) \\ -a[\sin \phi \sin(\theta + \phi) - \cos \theta] + W_{b3} \cos(\theta + \phi) \end{cases} \quad (\text{A.38})$$

$$\mathbf{R}'' = \frac{d^2 \mathbf{R}}{d\theta^2} = \begin{cases} W_{b4} \cos(\theta + \phi) + W_{b5} \sin(\theta + \phi) - j \sin \theta - a \cos \theta \\ W_{b4} \sin(\theta + \phi) - W_{b5} \cos(\theta + \phi) + j \cos \theta - a \sin \theta \end{cases} \quad (\text{A.39})$$

in which, the parametric vector equations of the theoretical cam profile coordinates,  $\mathbf{R}$ , are shown in Eq. (2.33), and

$$W_{b3} = L \cos \phi + e \sin \phi \quad (\text{A.40})$$

$$W_{b4} = -(j + e) \sin \phi - L \cos \phi \quad (\text{A.41})$$

$$W_{b5} = a \sin \phi - v \cos \phi \quad (\text{A.42})$$

### A.3 DISK CAM WITH AN OSCILLATING ROLLER FOLLOWER

The velocity and acceleration error functions for disk cams with an oscillating roller follower are presented below.

**Velocity and acceleration errors caused only by  $\Delta f$ :**

The velocity and acceleration error functions caused by  $\Delta f$  are respectively the first and second derivatives of displacement error function  $\Delta S_f$  with respect to time. Therefore, differentiation of Eq. (3.59) once and twice, respectively, gives

$$\Delta V_f = \frac{d(\Delta S_f)}{dt} = \frac{d(\Delta S_f)}{d\theta} \frac{d\theta}{dt} = \frac{d(\Delta S_f)}{d\theta} \omega_2 \quad (\text{A.43})$$

$$\Delta A_f = \frac{d^2(\Delta S_f)}{dt^2} = \frac{d^2(\Delta S_f)}{d\theta^2} \omega_2^2 + \frac{d(\Delta S_f)}{d\theta} \alpha_2 \quad (\text{A.44})$$

where

$$\frac{d(\Delta S_f)}{d\theta} = -\frac{\Delta f}{l} \left[ \left( v + \frac{d\phi}{d\theta} \right) \cos(\xi + \phi) + \frac{d\phi}{d\theta} \tan \phi \sin(\xi + \phi) \right] \sec \phi \quad (\text{A.45})$$

$$\begin{aligned} \frac{d^2(\Delta S_f)}{d\theta^2} = -\frac{\Delta f}{l} & \left\{ \left[ 2 \left( \frac{d\phi}{d\theta} \tan^2 \phi - v \right) \frac{d\phi}{d\theta} + \tan \phi \frac{d^2\phi}{d\theta^2} - v^2 \right] \sin(\xi + \phi) \right. \\ & \left. + \left[ a + 2 \left( v + \frac{d\phi}{d\theta} \right) \frac{d\phi}{d\theta} \tan \phi + \frac{d^2\phi}{d\theta^2} \right] \cos(\xi + \phi) \right\} \sec \phi \end{aligned} \quad (\text{A.46})$$

in which, from Eq. (2.47), the first and second derivatives of the pressure angle  $\phi$  with respect to the cam rotation angle  $\theta$  are

$$\frac{d\phi}{d\theta} = -\frac{d\alpha}{d\theta} - \nu \quad (\text{A.47})$$

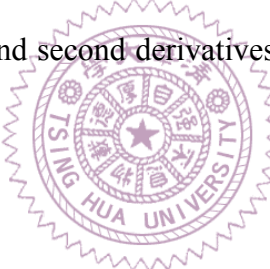
$$\frac{d^2\phi}{d\theta^2} = -\frac{d^2\alpha}{d\theta^2} - a \quad (\text{A.48})$$

also, from Eq. (2.42), the first and second derivatives of the angle  $\alpha$  with respect to the cam rotation angle  $\theta$  are

$$\frac{d\alpha}{d\theta} = \frac{l}{(\text{QC})^2} \left[ v(\text{QC}) \cos \xi - \frac{d(\text{QC})}{d\theta} \sin \xi \right] \sec \alpha \quad (\text{A.49})$$

$$\begin{aligned} \frac{d^2\alpha}{d\theta^2} = & \frac{l}{(\text{QC})^3} \left\{ \left[ (\text{QC})^2 \left( a + v \frac{d\alpha}{d\theta} \tan \alpha \right) - 2v(\text{QC}) \frac{d(\text{QC})}{d\theta} \right] \cos \xi + \left[ 2 \left( \frac{d(\text{QC})}{d\theta} \right)^2 \right. \right. \\ & \left. \left. - (\text{QC}) \left( v^2(\text{QC}) + \frac{d^2(\text{QC})}{d\theta^2} + \frac{d(\text{QC})}{d\theta} \frac{d\alpha}{d\theta} \tan \alpha \right) \right] \sin \xi \right\} \sec \alpha \end{aligned} \quad (\text{A.50})$$

where, from Eq. (2.41), the first and second derivatives of the distance QC with respect to the cam rotation angle  $\theta$  are



$$\frac{d(\text{QC})}{d\theta} = \frac{W_{c1}}{\text{QC}} \quad (\text{A.51})$$

$$\frac{d^2(\text{QC})}{d\theta^2} = \frac{(\text{QC}) \left[ W_{c2} + \left( \frac{dq}{d\theta} \right)^2 + (f+q) \frac{d^2q}{d\theta^2} \right] - W_{c1} \frac{d(\text{QC})}{d\theta}}{(\text{QC})^2} \quad (\text{A.52})$$

$$W_{c1} = l \left[ v(f+q) \sin \xi - \frac{dq}{d\theta} \cos \xi \right] + (f+q) \frac{dq}{d\theta} \quad (\text{A.53})$$

$$W_{c2} = l \left\{ \left[ v^2(f+q) - \frac{d^2q}{d\theta^2} \right] \cos \xi + \left[ a(f+q) + 2v \frac{dq}{d\theta} \right] \sin \xi \right\} \quad (\text{A.54})$$

also, from Eq. (2.40), the first and second derivatives of the distance  $q$  with respect to the cam rotation angle  $\theta$  are

$$\frac{dq}{d\theta} = \frac{fa}{(1-v)^2} \quad (\text{A.55})$$

$$\frac{d^2 q}{d\theta^2} = \frac{f[j(1-v) + 2a^2]}{(1-v)^3} \quad (\text{A.56})$$

in which,  $\xi$ ,  $v$ ,  $a$ , and  $j$  are the angular displacement, velocity, acceleration, and jerk functions of the follower, respectively.

#### **Velocity and acceleration errors caused only by $\Delta r_f$ :**

The velocity and acceleration error functions caused by  $\Delta r_f$  are respectively the first and second derivatives of displacement error function  $\Delta S_{rf}$  with respect to time. Therefore, differentiation of Eq. (3.55) once and twice, respectively, gives

$$\Delta V_{rf} = \frac{d(\Delta S_{rf})}{dt} = \frac{d(\Delta S_{rf})}{d\theta} \frac{d\theta}{dt} = \frac{d(\Delta S_{rf})}{d\theta} \omega_2 \quad (\text{A.57})$$

$$\Delta A_{rf} = \frac{d^2(\Delta S_{rf})}{dt^2} = \frac{d^2(\Delta S_{rf})}{d\theta^2} \omega_2^2 + \frac{d(\Delta S_{rf})}{d\theta} \alpha_2 \quad (\text{A.58})$$

and

$$\frac{d(\Delta S_{rf})}{d\theta} = \frac{\Delta r_f}{l} \frac{d\phi}{d\theta} \tan \phi \sec \phi \quad (\text{A.59})$$

$$\frac{d^2(\Delta S_{rf})}{d\theta^2} = \frac{\Delta r_f}{l} \left[ \frac{d^2\phi}{d\theta^2} \tan \phi + \left( \frac{d\phi}{d\theta} \right)^2 (1 + 2 \tan^2 \phi) \right] \sec \phi \quad (\text{A.60})$$

in which, the first and second derivatives of the pressure angle  $\phi$  with respect to the cam rotation angle  $\theta$  are shown in Eqs. (A.47) and (A.48).

#### **Velocity and acceleration errors caused only by $\Delta l$ :**

The velocity and acceleration error functions caused by  $\Delta l$  are respectively the first and second derivatives of displacement error function  $\Delta S_l$  with respect to time. Therefore, differentiation of Eq. (3.63) once and twice, respectively, gives

$$\Delta V_l = \frac{d(\Delta S_l)}{dt} = \frac{d(\Delta S_l)}{d\theta} \omega_2 \quad (\text{A.61})$$

$$\Delta A_l = \frac{d^2(\Delta S_l)}{dt^2} = \frac{d^2(\Delta S_l)}{d\theta^2} \omega_2^2 + \frac{d(\Delta S_l)}{d\theta} \alpha_2 \quad (\text{A.62})$$

where

$$\frac{d(\Delta S_l)}{d\theta} = \frac{\Delta l}{l} (1 + \tan^2 \phi) \frac{d\phi}{d\theta} \quad (\text{A.63})$$

$$\frac{d^2(\Delta S_l)}{d\theta^2} = \frac{\Delta l}{l} (1 + \tan^2 \phi) \left[ 2 \tan \phi \left( \frac{d\phi}{d\theta} \right)^2 + \frac{d^2\phi}{d\theta^2} \right] \quad (\text{A.64})$$

### **Velocity and acceleration errors caused only by $\Delta r$ :**

The velocity and acceleration error functions caused by  $\Delta r$  are respectively the first and second derivatives of displacement error function  $\Delta S_r$  with respect to time. Therefore, differentiation of Eq. (3.65) once and twice, respectively, gives

$$\Delta V_r = \frac{d(\Delta S_r)}{dt} = \frac{d(\Delta S_r)}{d\theta} \omega_2 \quad (\text{A.65})$$

$$\Delta A_r = \frac{d^2(\Delta S_r)}{dt^2} = \frac{d^2(\Delta S_r)}{d\theta^2} \omega_2^2 + \frac{d(\Delta S_r)}{d\theta} \alpha_2^2 \quad (\text{A.66})$$

where

$$\frac{d(\Delta S_r)}{d\theta} = \frac{\Delta r}{l} \left( \frac{d\phi}{d\theta} \tan \phi \cos \lambda - \frac{d\lambda}{d\theta} \sin \lambda \right) \sec \phi \quad (\text{A.67})$$

$$\begin{aligned} \frac{d^2(\Delta S_r)}{d\theta^2} &= \frac{\Delta r}{l} \left\{ \left[ (1 + 2 \tan^2 \phi) \left( \frac{d\phi}{d\theta} \right)^2 + \frac{d^2\phi}{d\theta^2} \tan \phi - \left( \frac{d\lambda}{d\theta} \right)^2 \right] \cos \lambda \right. \\ &\quad \left. - \left( 2 \frac{d\lambda}{d\theta} \frac{d\phi}{d\theta} \tan \phi + \frac{d^2\lambda}{d\theta^2} \right) \sin \lambda \right\} \sec \phi \end{aligned} \quad (\text{A.68})$$

in which, from Eq. (3.64), the first and second derivatives of the shift angle  $\lambda$  with respect to the cam rotation angle  $\theta$  are

$$\frac{d\lambda}{d\theta} = \frac{W_{c3}}{\|\mathbf{R}\| \cos \lambda} \quad (\text{A.69})$$

$$\frac{d^2\lambda}{d\theta^2} = \frac{W_{c3} \left( \|\mathbf{R}\| \frac{d\lambda}{d\theta} \sin \lambda - \frac{\mathbf{R} \bullet \mathbf{R}'}{\|\mathbf{R}\|} \cos \lambda \right) + (W_{c4} \cos \alpha + W_{c5} \sin \alpha) \|\mathbf{R}\| \cos \lambda}{\|\mathbf{R}\|^2 \cos^2 \lambda} \quad (\text{A.70})$$

where

$$W_{c3} = \left( \frac{dq}{d\theta} - q \frac{\mathbf{R} \bullet \mathbf{R}'}{\|\mathbf{R}\|^2} \right) \sin \alpha + q \frac{d\alpha}{d\theta} \cos \alpha \quad (\text{A.71})$$

$$W_{c4} = q \frac{d^2\alpha}{d\theta^2} - \left( q \frac{\mathbf{R} \bullet \mathbf{R}'}{\|\mathbf{R}\|^2} - 2 \frac{dq}{d\theta} \right) \frac{d\alpha}{d\theta} \quad (\text{A.72})$$

$$W_{c5} = \frac{d^2q}{d\theta^2} - \frac{dq}{d\theta} \frac{\mathbf{R} \bullet \mathbf{R}'}{\|\mathbf{R}\|^2} - q \left[ \left( \frac{d\alpha}{d\theta} \right)^2 + \frac{(\mathbf{R}' \bullet \mathbf{R}' + \mathbf{R} \bullet \mathbf{R}'') \|\mathbf{R}\|^2 - 2(\mathbf{R} \bullet \mathbf{R}')^2}{\|\mathbf{R}\|^4} \right] \quad (\text{A.73})$$

$$\begin{aligned} \mathbf{R}' &= \frac{d\mathbf{R}}{d\theta} \\ &= \left\{ \begin{array}{l} \frac{d(\text{QC})}{d\theta} \cos(\theta + \alpha) - (\text{QC} - r_f) \left( 1 + \frac{d\alpha}{d\theta} \right) \sin(\theta + \alpha) - \frac{dq}{d\theta} \cos \theta + q \sin \theta \\ \frac{d(\text{QC})}{d\theta} \sin(\theta + \alpha) + (\text{QC} - r_f) \left( 1 + \frac{d\alpha}{d\theta} \right) \cos(\theta + \alpha) - \frac{dq}{d\theta} \sin \theta - q \cos \theta \end{array} \right\} \end{aligned} \quad (\text{A.74})$$

$$\mathbf{R}'' = \frac{d^2\mathbf{R}}{d\theta^2} = \left\{ \begin{array}{l} W_{c6} \cos(\theta + \alpha) - W_{c7} \sin(\theta + \alpha) - \left( \frac{d^2q}{d\theta^2} - q \right) \cos \theta + 2 \frac{dq}{d\theta} \sin \theta \\ W_{c6} \sin(\theta + \alpha) + W_{c7} \cos(\theta + \alpha) - \left( \frac{d^2q}{d\theta^2} - q \right) \sin \theta - 2 \frac{dq}{d\theta} \cos \theta \end{array} \right\} \quad (\text{A.75})$$

in which, the parametric vector equations of the theoretical cam profile coordinates,  $\mathbf{R}$ , are shown in Eq. (2.46), and

$$W_{c6} = \frac{d^2(\text{QC})}{d\theta^2} - (\text{QC} - r_f) \left( 1 + \frac{d\alpha}{d\theta} \right)^2 \quad (\text{A.76})$$

$$W_{c7} = 2 \frac{d(\text{QC})}{d\theta} \left( 1 + \frac{d\alpha}{d\theta} \right) + (\text{QC} - r_f) \frac{d^2\alpha}{d\theta^2} \quad (\text{A.77})$$

## A.4 DISK CAM WITH AN OSCILLATING FLAT-FACED FOLLOWER

The velocity and acceleration error functions for disk cams with an oscillating flat-faced follower are presented below.

**Velocity and acceleration errors caused only by  $\Delta f$ :**

The velocity and acceleration error functions caused by  $\Delta f$  are respectively the first and second derivatives of displacement error function  $\Delta S_f$  with respect to time. Therefore, differentiation of Eq. (3.77) once and twice, respectively, gives

$$\Delta V_f = \frac{d(\Delta S_f)}{dt} = \frac{d(\Delta S_f)}{d\theta} \frac{d\theta}{dt} = \frac{d(\Delta S_f)}{d\theta} \omega_2 \quad (\text{A.78})$$

$$\Delta A_f = \frac{d^2(\Delta S_f)}{dt^2} = \frac{d^2(\Delta S_f)}{d\theta^2} \omega_2^2 + \frac{d(\Delta S_f)}{d\theta} \alpha_2 \quad (\text{A.79})$$

where

$$\frac{d(\Delta S_f)}{d\theta} = \frac{\Delta f}{u^2} \left( \frac{du}{d\theta} \sin \xi - vu \cos \xi \right) \quad (\text{A.80})$$

$$\frac{d^2(\Delta S_f)}{d\theta^2} = \frac{\Delta f}{u^3} \left[ \left( v^2 u^2 + u \frac{d^2 u}{d\theta^2} - 2 \left( \frac{du}{d\theta} \right)^2 \right) \sin \xi + \left( 2vu \frac{du}{d\theta} - au^2 \right) \cos \xi \right] \quad (\text{A.81})$$

in which, from Eq. (3.73), the first and second derivatives of the distance  $u$  with respect to the cam rotation angle  $\theta$  are

$$\frac{du}{d\theta} = \frac{dq}{d\theta} \cos \xi - v(f+q) \sin \xi \quad (\text{A.82})$$

$$\frac{d^2 u}{d\theta^2} = \left[ \frac{d^2 q}{d\theta^2} - v^2(f+q) \right] \cos \xi - \left[ a(f+q) + 2v \frac{dq}{d\theta} \right] \sin \xi \quad (\text{A.83})$$

also, from Eq. (2.53), the first and second derivatives of the distance  $q$  with respect to the cam rotation angle  $\theta$  are

$$\frac{dq}{d\theta} = \frac{fa}{(1-v)^2} \quad (\text{A.84})$$

$$\frac{d^2 q}{d\theta^2} = \frac{f[j(1-v) + 2a^2]}{(1-v)^3} \quad (\text{A.85})$$

in which,  $\xi$ ,  $v$ ,  $a$ , and  $j$  are the angular displacement, velocity, acceleration, and jerk functions of the follower, respectively.

#### **Velocity and acceleration errors caused only by $\Delta e$ :**

The velocity and acceleration error functions caused by  $\Delta e$  are respectively the first and second derivatives of displacement error function  $\Delta S_e$  with respect to time. Therefore, differentiation of Eq. (3.81) once and twice, respectively, gives

$$\Delta V_e = \frac{d(\Delta S_e)}{dt} = \frac{d(\Delta S_e)}{d\theta} \omega_2 \quad (\text{A.86})$$

$$\Delta A_e = \frac{d^2(\Delta S_e)}{dt^2} = \frac{d^2(\Delta S_e)}{d\theta^2} \omega_2^2 + \frac{d(\Delta S_e)}{d\theta} \alpha_2 \quad (\text{A.87})$$

where

$$\frac{d(\Delta S_e)}{d\theta} = \frac{\Delta e}{u^2} \left( \frac{du}{d\theta} \right) \quad (\text{A.88})$$



$$\frac{d^2(\Delta S_e)}{d\theta^2} = \frac{\Delta e}{u^3} \left[ u \frac{d^2 u}{d\theta^2} - 2 \left( \frac{du}{d\theta} \right)^2 \right] \quad (\text{A.89})$$

#### **Velocity and acceleration errors caused only by $\Delta r$ :**

The velocity and acceleration error functions caused by  $\Delta r$  are respectively the first and second derivatives of displacement error function  $\Delta S_r$  with respect to time. Therefore, differentiation of Eq. (3.83) once and twice, respectively, gives

$$\Delta V_r = \frac{d(\Delta S_r)}{dt} = \frac{d(\Delta S_r)}{d\theta} \omega_2 \quad (\text{A.90})$$

$$\Delta A_r = \frac{d^2(\Delta S_r)}{dt^2} = \frac{d^2(\Delta S_r)}{d\theta^2} \omega_2^2 + \frac{d(\Delta S_r)}{d\theta} \alpha_2 \quad (\text{A.91})$$

where

$$\frac{d(\Delta S_r)}{d\theta} = -\frac{\Delta r}{u^2} \left( \frac{du}{d\theta} \cos \lambda + u \frac{d\lambda}{d\theta} \sin \lambda \right) \quad (\text{A.92})$$

$$\begin{aligned} \frac{d^2(\Delta S_r)}{d\theta^2} = & -\frac{\Delta r}{u^3} \left\{ \left[ u^2 \left( \frac{d\lambda}{d\theta} \right)^2 - 2u \frac{du}{d\theta} \frac{d\lambda}{d\theta} \right] \sin \lambda + \left[ u^2 \left( \frac{d\lambda}{d\theta} \right)^2 + u \frac{d^2 u}{d\theta^2} \right. \right. \\ & \left. \left. - \left( \frac{du}{d\theta} \right)^2 \right] \cos \lambda \right\} \end{aligned} \quad (\text{A.93})$$

in which, from Eq. (3.82), the first and second derivatives of the shift angle  $\lambda$  with respect to the cam rotation angle  $\theta$  are

$$\frac{d\lambda}{d\theta} = \frac{W_{d1}}{\|\mathbf{R}\| \cos \lambda} \quad (\text{A.94})$$

$$\frac{d^2\lambda}{d\theta^2} = \frac{W_{d1} \left( \|\mathbf{R}\| \frac{d\lambda}{d\theta} \sin \lambda - \frac{\mathbf{R} \bullet \mathbf{R}'}{\|\mathbf{R}\|} \cos \lambda \right) + (W_{d2} \cos \xi + W_{d3} \sin \xi) \|\mathbf{R}\| \cos \lambda}{\|\mathbf{R}\|^2 \cos^2 \lambda} \quad (\text{A.95})$$

where

$$W_{d1} = \left( \frac{dq}{d\theta} - q \frac{\mathbf{R} \bullet \mathbf{R}'}{\|\mathbf{R}\|^2} \right) \cos \xi - vq \sin \xi \quad (\text{A.96})$$

$$W_{d2} = \frac{d^2 q}{d\theta^2} - \frac{dq}{d\theta} \frac{\mathbf{R} \bullet \mathbf{R}'}{\|\mathbf{R}\|^2} - q \left[ v^2 - \frac{2(\mathbf{R} \bullet \mathbf{R}')^2}{\|\mathbf{R}\|^4} + \frac{(\mathbf{R}' \bullet \mathbf{R}' + \mathbf{R} \bullet \mathbf{R}'')}{\|\mathbf{R}\|^2} \right] \quad (\text{A.97})$$

$$W_{d3} = v \left( q \frac{\mathbf{R} \bullet \mathbf{R}'}{\|\mathbf{R}\|^2} - 2 \frac{dq}{d\theta} \right) - aq \quad (\text{A.98})$$

$$\mathbf{R}' = \frac{d\mathbf{R}}{d\theta} = \begin{cases} -(QE + e)(1 - v) \cos(\theta - \xi) - \frac{d(QE)}{d\theta} \sin(\theta - \xi) - \frac{dq}{d\theta} \cos \theta + q \sin \theta \\ -(QE + e)(1 - v) \sin(\theta - \xi) + \frac{d(QE)}{d\theta} \cos(\theta - \xi) - \frac{dq}{d\theta} \sin \theta - q \cos \theta \end{cases} \quad (\text{A.99})$$

$$\mathbf{R}'' = \frac{d^2\mathbf{R}}{d\theta^2} = \begin{cases} W_{d4} \cos(\theta - \xi) + W_{d5} \sin(\theta - \xi) - \left( \frac{d^2q}{d\theta^2} - q \right) \cos \theta + 2 \frac{dq}{d\theta} \sin \theta \\ W_{d4} \sin(\theta - \xi) - W_{d5} \cos(\theta - \xi) - \left( \frac{d^2q}{d\theta^2} - q \right) \sin \theta - 2 \frac{dq}{d\theta} \cos \theta \end{cases} \quad (\text{A.100})$$

in which, the parametric vector equations of the theoretical cam profile coordinates,  $\mathbf{R}$ , are shown in Eq. (2.59), and

$$\frac{d(\text{QE})}{d\theta} = v(f + q) \cos \xi + \frac{dq}{d\theta} \sin \xi \quad (\text{A.101})$$

$$\frac{d^2(\text{QE})}{d\theta^2} = \left[ a(f + q) + 2v \frac{dq}{d\theta} \right] \cos \xi + \left[ \frac{d^2q}{d\theta^2} - v^2(f + q) \right] \sin \xi \quad (\text{A.102})$$

$$W_{d4} = a(\text{QE} + e) - 2(1 - v) \frac{d(\text{QE})}{d\theta} \quad (\text{A.103})$$

$$W_{d5} = (\text{QE} + e)(1 - v)^2 - \frac{d^2(\text{QE})}{d\theta^2} \quad (\text{A.104})$$

where, the distance QE is shown in Eq. (2.54).



# APPENDIX B

## GENERATION OF FIFTH-DEGREE HERMITE INTERPOLATION CURVES

By using a coordinate measuring machine (CMM), the Cartesian coordinates of  $N$  sequentially discrete points  $A_1, A_2, \dots, A_i, A_{i+1}, \dots, A_N$  at a three-dimensional surface can be measured. A fifth-degree Hermite interpolation curve, a spatial curve, passing through two adjacent points  $A_i$  and  $A_{i+1}$  at the three-dimensional surface, can be expressed in its parametric form by [91]:

$$\mathbf{H}(w) = \begin{Bmatrix} H_x(w) \\ H_y(w) \\ H_z(w) \end{Bmatrix} \equiv [w^5 \ w^4 \ w^3 \ w^2 \ w \ 1] \mathbf{U} \quad \text{for } 0 \leq w \leq 1 \quad (\text{B.1})$$

where  $w$  is the independent parameter to describe the spatial polynomial curve, and  $\mathbf{U}$  is a 6-by-3 coefficient matrix of the curve, which can be expressed as

$$\mathbf{U} = \begin{bmatrix} \mathbf{U}_5 \\ \mathbf{U}_4 \\ \mathbf{U}_3 \\ \mathbf{U}_2 \\ \mathbf{U}_1 \\ \mathbf{U}_0 \end{bmatrix} = \begin{bmatrix} U_{5x} & U_{5y} & U_{5z} \\ U_{4x} & U_{4y} & U_{4z} \\ U_{3x} & U_{3y} & U_{3z} \\ U_{2x} & U_{2y} & U_{2z} \\ U_{1x} & U_{1y} & U_{1z} \\ U_{0x} & U_{0y} & U_{0z} \end{bmatrix} \quad (\text{B.2})$$

Then differentiating Eq. (B.1) by  $w$  once and twice gives the following:

$$\mathbf{H}'(w) = [5w^4 \ 4w^3 \ 3w^2 \ 2w \ 1 \ 0] \mathbf{U} \quad (\text{B.3})$$

$$\mathbf{H}''(w) = [20w^3 \ 12w^2 \ 6w \ 2 \ 0 \ 0] \mathbf{U} \quad (\text{B.4})$$

The curve is supposed to have positional vector  $\mathbf{A}_i$  (the coordinate of point  $A_i$ ), tangent vector  $\mathbf{A}'_i$ , and second derivative vector  $\mathbf{A}''_i$  at  $w = 0$ , and positional vector  $\mathbf{A}_{i+1}$  (the

coordinate of point  $\mathbf{A}_{i+1}$ ), tangent vector  $\mathbf{A}'_{i+1}$ , and second derivative vector  $\mathbf{A}''_{i+1}$  at  $w = 1$ .

That is,

$$\mathbf{H}(0) = \mathbf{A}_i \quad (\text{B.5})$$

$$\mathbf{H}(1) = \mathbf{A}_{i+1} \quad (\text{B.6})$$

$$\mathbf{H}'(0) = \mathbf{A}'_i \quad (\text{B.7})$$

$$\mathbf{H}'(1) = \mathbf{A}'_{i+1} \quad (\text{B.8})$$

$$\mathbf{H}''(0) = \mathbf{A}''_i \quad (\text{B.9})$$

$$\mathbf{H}''(1) = \mathbf{A}''_{i+1} \quad (\text{B.10})$$

Therefore,

$$\begin{bmatrix} \mathbf{A}_i \\ \mathbf{A}_{i+1} \\ \mathbf{A}'_i \\ \mathbf{A}'_{i+1} \\ \mathbf{A}''_i \\ \mathbf{A}''_{i+1} \end{bmatrix} = \begin{bmatrix} 0 & 0 & 0 & 0 & 0 & 1 \\ 1 & 1 & 1 & 1 & 1 & 1 \\ 0 & 0 & 0 & 0 & 1 & 0 \\ 5 & 4 & 3 & 2 & 1 & 0 \\ 0 & 0 & 0 & 2 & 0 & 0 \\ 20 & 12 & 6 & 2 & 0 & 0 \end{bmatrix} \mathbf{U} = \begin{bmatrix} 0 & 0 & 0 & 0 & 0 & 0 & 1 \\ 1 & 1 & 1 & 1 & 1 & 1 & 1 \\ 0 & 0 & 0 & 0 & 1 & 0 & 0 \\ 5 & 4 & 3 & 2 & 1 & 0 & 0 \\ 0 & 0 & 0 & 2 & 0 & 0 & 0 \\ 20 & 12 & 6 & 2 & 0 & 0 & 0 \end{bmatrix} \begin{bmatrix} \mathbf{U}_5 \\ \mathbf{U}_4 \\ \mathbf{U}_3 \\ \mathbf{U}_2 \\ \mathbf{U}_1 \\ \mathbf{U}_0 \end{bmatrix} \quad (\text{B.11})$$

Thus, the coefficient matrix  $\mathbf{U}$  can be solved by

$$\mathbf{U} = \begin{bmatrix} 0 & 0 & 0 & 0 & 0 & 1 \\ 1 & 1 & 1 & 1 & 1 & 1 \\ 0 & 0 & 0 & 0 & 1 & 0 \\ 5 & 4 & 3 & 2 & 1 & 0 \\ 0 & 0 & 0 & 2 & 0 & 0 \\ 20 & 12 & 6 & 2 & 0 & 0 \end{bmatrix}^{-1} \begin{bmatrix} \mathbf{A}_i \\ \mathbf{A}_{i+1} \\ \mathbf{A}'_i \\ \mathbf{A}'_{i+1} \\ \mathbf{A}''_i \\ \mathbf{A}''_{i+1} \end{bmatrix} = \begin{bmatrix} -6 & -6 & -3 & -3 & -0.5 & 0.5 \\ 15 & -15 & 8 & 7 & 1.5 & -1 \\ -10 & 10 & -6 & -4 & -1.5 & 0.5 \\ 0 & 0 & 0 & 0 & 0.5 & 0 \\ 0 & 0 & 1 & 0 & 0 & 0 \\ 1 & 0 & 0 & 0 & 0 & 0 \end{bmatrix} \begin{bmatrix} \mathbf{A}_i \\ \mathbf{A}_{i+1} \\ \mathbf{A}'_i \\ \mathbf{A}'_{i+1} \\ \mathbf{A}''_i \\ \mathbf{A}''_{i+1} \end{bmatrix} \quad (\text{B.12})$$

By using the central difference method, the first and second derivatives of points  $\mathbf{A}_i$  and  $\mathbf{A}_{i+1}$  can be obtained by

$$\mathbf{A}'_i = \frac{d\mathbf{A}_i}{dw} \approx \frac{\Delta\mathbf{A}_i}{\Delta w} = \frac{\mathbf{A}_{i+1} - \mathbf{A}_{i-1}}{2} \quad (\text{B.13})$$

$$\mathbf{A}'_{i+1} = \frac{d\mathbf{A}_{i+1}}{dw} \approx \frac{\Delta\mathbf{A}_{i+1}}{\Delta w} = \frac{\mathbf{A}_{i+2} - \mathbf{A}_i}{2} \quad (\text{B.14})$$

$$\mathbf{A}''_i = \frac{d\mathbf{A}'_i}{dw} \approx \frac{\Delta\mathbf{A}'_i}{\Delta w} = \frac{\mathbf{A}'_{i+1} - \mathbf{A}'_{i-1}}{2} = \frac{\mathbf{A}_{i+2} - 2\mathbf{A}_i + \mathbf{A}_{i-2}}{4} \quad (\text{B.15})$$

$$\mathbf{A}''_{i+1} = \frac{d\mathbf{A}'_{i+1}}{dw} \approx \frac{\Delta\mathbf{A}'_{i+1}}{\Delta w} = \frac{\mathbf{A}'_{i+2} - \mathbf{A}'_i}{2} = \frac{\mathbf{A}_{i+3} - 2\mathbf{A}_{i+1} + \mathbf{A}_{i-1}}{4} \quad (\text{B.16})$$

where  $\mathbf{A}_{i-2}$ ,  $\mathbf{A}_{i-1}$ ,  $\mathbf{A}_i$ ,  $\mathbf{A}_{i+1}$ ,  $\mathbf{A}_{i+2}$ , and  $\mathbf{A}_{i+3}$  are the known positional vectors of six sequentially measured points  $\mathbf{A}_{i-2}$ ,  $\mathbf{A}_{i-1}$ ,  $\mathbf{A}_i$ ,  $\mathbf{A}_{i+1}$ ,  $\mathbf{A}_{i+2}$ , and  $\mathbf{A}_{i+3}$  at the three-dimensional surface, and  $\Delta w = 1$ . Substituting Eqs. (B.13)~(B.16) into Eq. (B.12) to solve the coefficient matrix  $\mathbf{U}$  can obtain the fifth-degree Hermite interpolation curve passing through points  $\mathbf{A}_i$  and  $\mathbf{A}_{i+1}$ . For a machined disk cam,  $N$  sequentially discrete points  $\mathbf{A}_1, \mathbf{A}_2, \dots, \mathbf{A}_i, \mathbf{A}_{i+1}, \dots, \mathbf{A}_N$  with the same axial position at the cam surface are usually measured in a full circle on the cam contour, and the initial point  $\mathbf{A}_1$  and the final point  $\mathbf{A}_N$  are also adjacent points. Thus,  $N$  segments of the fifth-degree Hermite interpolation curves can be generated to model the whole cam contour. The advantage of using the fifth-degree Hermite interpolation curves against the cubic Hermite interpolation curves [91] to model cam contours is that they ensure continuous slopes and curvatures of the measured points.

In practice, the positional vectors of the  $N$  measured points  $\mathbf{A}_1, \mathbf{A}_2, \dots, \mathbf{A}_i, \mathbf{A}_{i+1}, \dots, \mathbf{A}_N$  at the cam surface are expressed parametrically in terms of their corresponding cam rotation angles as  $\mathbf{A}_1(\theta_1), \mathbf{A}_2(\theta_2), \dots, \mathbf{A}_i(\theta_i), \mathbf{A}_{i+1}(\theta_{i+1}), \dots, \mathbf{A}_N(\theta_N)$ . Thus, for generating an interpolation curve passing through points  $\mathbf{A}_i$  and  $\mathbf{A}_{i+1}$ , when  $\theta = \theta_i$ ,  $w = 0$  is assumed, then when  $\theta = \theta_{i+1}$ ,  $w = 1$  is assumed. In fact, the correlation between  $\theta$  and  $w$  is nonlinear and may not be expressed analytically. However, if the increment of the cam rotation angle,  $\Delta\theta$  ( $= \theta_{i+1} - \theta_i$ ), for the two adjacent measured points  $\mathbf{A}_i$  and  $\mathbf{A}_{i+1}$  is small enough (i.e., the number of measured points is large enough), a linear approximation may be given by

$$w(\theta) \approx \frac{\theta - \theta_i}{\Delta\theta} = \frac{\theta - \theta_i}{\theta_{i+1} - \theta_i} \quad \text{for } \theta_i \leq \theta \leq \theta_{i+1} \quad (\text{B.17})$$

If so, after the coefficient matrix  $\mathbf{U}$  has been solved, the interpolated cam contour segment between points  $A_i$  and  $A_{i+1}$  may be expressed as

$$\mathbf{H}(\theta) = [w^5(\theta) \ w^4(\theta) \ w^3(\theta) \ w^2(\theta) \ w(\theta) \ 1] \mathbf{U} \text{ for } \theta_i \leq \theta \leq \theta_{i+1} \quad (\text{B.18})$$

Note that Eqs. (B.17) and (B.18) may be inaccurate when the number of measured points is not large enough. In such a situation, applying some numerical methods to find out the nonlinear correlation between  $\theta$  and  $w$  is suggested instead.



# APPENDIX C

## MEASURING FIXTURES FOR OTHER TYPES OF CONJUGATE CAM MECHANISMS

### C.1 CONJUGATE DISK CAMS WITH AN OFFSET TRANSLATING ROLLER FOLLOWER

Figure C.1 shows a conjugate cam mechanism with an offset translating roller follower. There are two disk cams A and B, fixed on a common shaft. Two follower rollers C and D, mounted to a common follower, are each pushed in opposite directions by the conjugate cams. In this case,  $e$  represents the follower offset,  $d$  represents the center distance between rollers C and D, and  $r_f$  represents the radii of rollers C and D. By setting

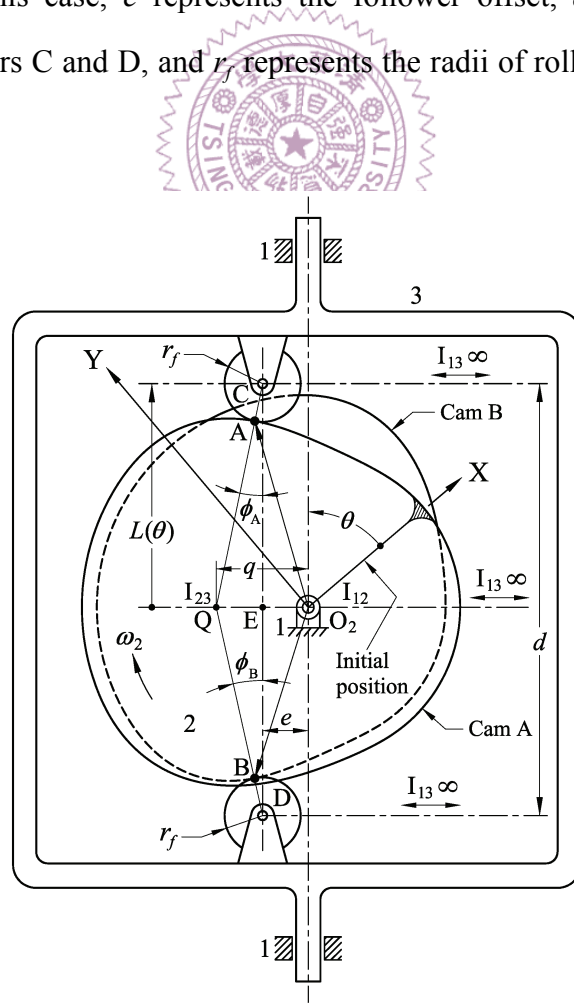


**Figure C.1** Conjugate disk cams with an offset translating roller follower.

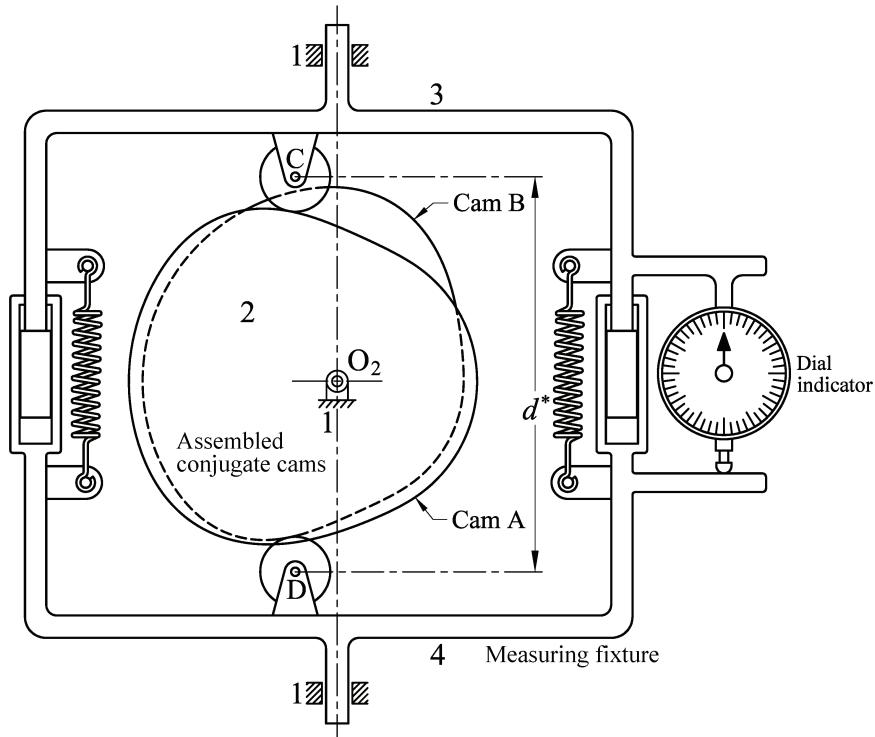


**Figure C.2** Assembled conjugate cams with a measuring fixture consisting of two offset translating roller followers.

up a Cartesian coordinate system X-Y fixed on the cam and with its origin at the fixed pivot  $O_2$ , the cam profile coordinates may be expressed in terms of the cam rotation angle  $\theta$ , which is measured against the direction of cam rotation from the reference radial to cam centerline parallel to follower translation.

Normally, the center distance between follower rollers,  $d$ , is a constant. If, as shown in Fig. C.2, a prismatic joint is intentionally added such that the center distance between follower rollers,  $d^*$ , is changed to be variable, the mechanism will no longer be overconstrained. When the cams rotate, in the perfect condition that the machined conjugate cams have no profile errors, the center distance between follower rollers  $d^*$  will always equal the constant  $d$ , and thus the added prismatic joint will be redundant. In practice, for the machined conjugate cams with profile errors, the magnitude of distance  $d^*$  will vary with respect to the cam rotation angle  $\theta$ , and the variation of the center distance between follower rollers,  $\Delta d (= d^* - d)$ , may indicate the variation of profile errors. Thus, a measuring fixture simply consists of sliders 3 and 4. The magnitude of the center distance

variation,  $\Delta d$ , can be measured by a dial indicator, which is mounted to slider 3 with its contact tip touching the extended end of slider 4. Then through actually measuring the magnitude of  $\Delta d$  with respect to  $\theta$ , the cam profile errors can be indirectly examined.

## C.2 CONJUGATE DISK CAMS WITH AN OFFSET TRANSLATING OBLIQUE FLAT-FACED FOLLOWER

Figure C.3 shows a conjugate cam mechanism with an offset translating oblique flat-faced follower. There are two disk cams A and B, fixed on a common shaft. Two follower faces with constant breadth are each pushed in opposite directions by the conjugate cams. In this case,  $e$  represents the follower offset,  $b$  represents the breadth of the flat-faced follower, and  $\phi$  represents the oblique angle of the follower (i.e., the invariant pressure angle). By setting up a Cartesian coordinate system X-Y fixed on the cam and with its origin at the fixed pivot  $O_2$ , the cam profile coordinates may be expressed in terms of the cam rotation angle  $\theta$ , which is measured against the direction of cam rotation from the

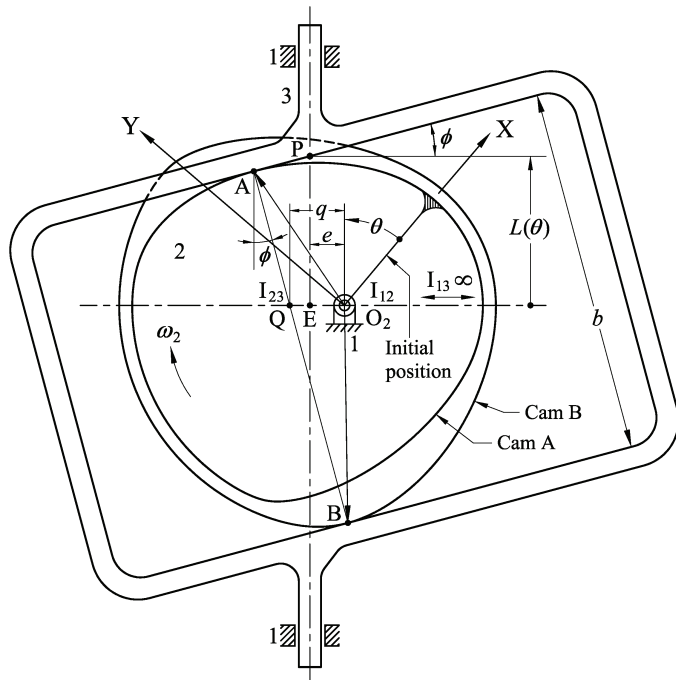


**Figure C.3** Conjugate disk cams with an offset translating oblique flat-faced follower.

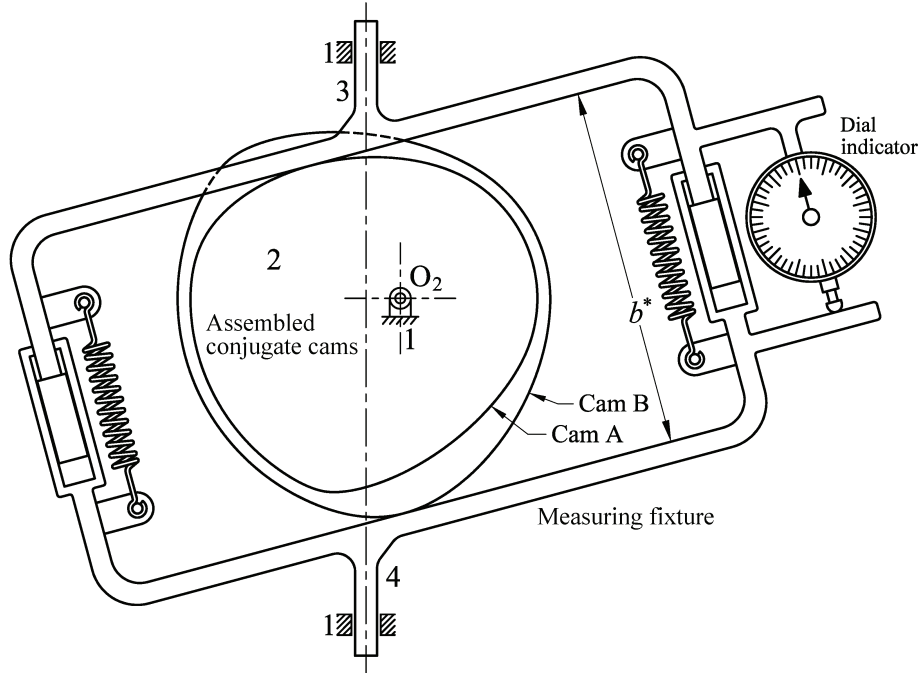


**Figure C.4** Assembled conjugate cams with a measuring fixture consisting of two offset translating oblique flat-faced followers.

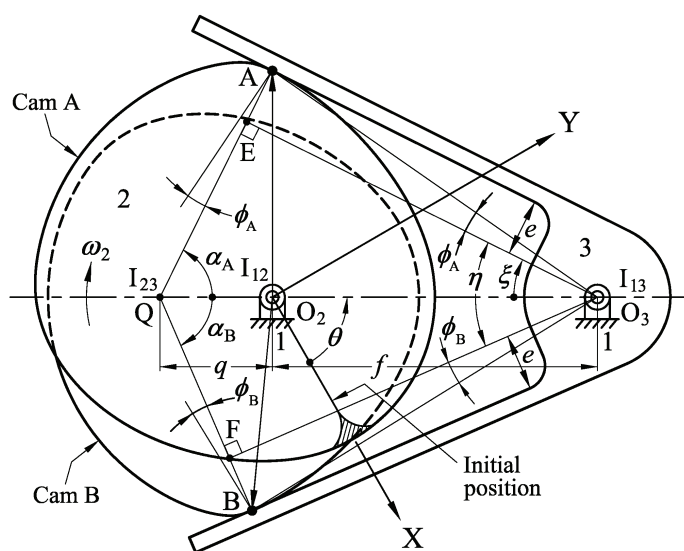
reference radial to cam centerline parallel to follower translation.

Normally, the follower breadth,  $b$ , is a constant. If, as shown in Fig. C.4, a prismatic joint is intentionally added such that the follower breadth,  $b^*$ , is changed to be variable, the mechanism will no longer be overconstrained. When the cams rotate, in the extreme case that the machined conjugate cams have no profile errors, the follower breadth  $b^*$  will always equal the constant  $b$ , and thus the added prismatic joint will be redundant. In practice, for the machined conjugate cams with profile errors, the magnitude of breadth  $b^*$  will vary with respect to the cam rotation angle  $\theta$ , and the variation of the follower breadth,  $\Delta b (= b^* - b)$ , may indicate the variation of profile errors. Thus, a measuring fixture simply consists of sliders 3 and 4. The magnitude of the follower breadth variation,  $\Delta b$ , can be measured by a dial indicator, which is mounted to slider 3 with its contact tip touching the extended end of slider 4. Then through actually measuring the magnitude of  $\Delta b$  with respect to  $\theta$ , the cam profile errors can be indirectly examined.

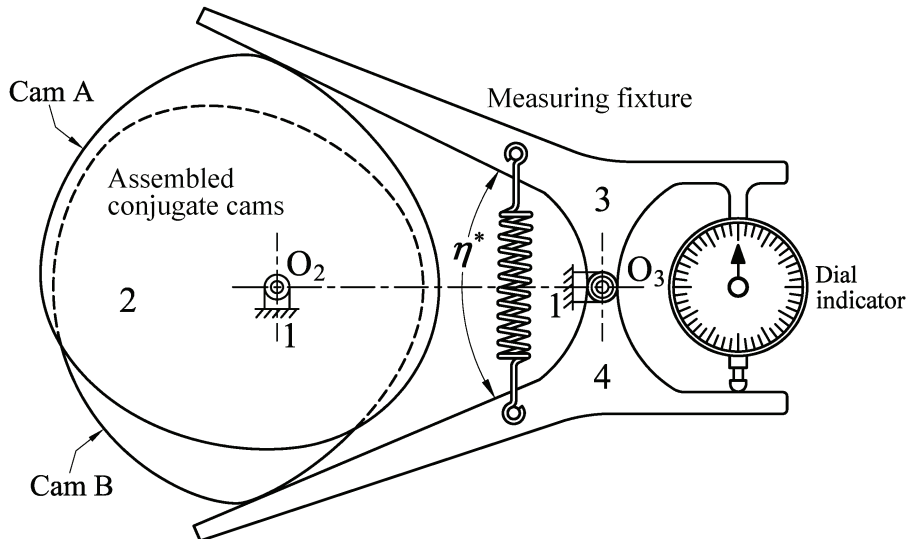
### C.3 CONJUGATE DISK CAMS WITH AN OSCILLATING FLAT-FACED FOLLOWER

Figure C.5 shows a conjugate cam mechanism with an oscillating flat-faced follower. There are two disk cams A and B, fixed on a common shaft. Two follower faces with constant subtending angle are each pushed in opposite directions by the conjugate cams. In this case,  $f$  represents the distance from the cam center  $O_2$  to the follower pivot point  $O_3$ ,  $e$  represents the follower face offsets from the follower pivot point, and  $\eta$  represents the subtending angle of the follower faces. By setting up a Cartesian coordinate system X-Y fixed on the cam and with its origin at the fixed pivot  $O_2$ , the cam profile coordinates may be expressed in terms of the cam rotation angle  $\theta$ , which is measured against the direction of cam rotation from the reference radial on the cam to the line between the cam center and the follower pivot point.

Normally, the subtending angle of the follower faces,  $\eta$ , is a constant. If, as shown in Fig. C.6, a revolute joint is intentionally added such that the subtending angle of the follower faces,  $\eta^*$ , is changed to be variable, the mechanism will no longer be overconstrained. When the cams rotate, in the extreme case that the machined conjugate cams have no profile errors, the subtending angle of the follower faces  $\eta^*$  will always equal



**Figure C.5** Conjugate disk cams with an oscillating flat-faced follower.



**Figure C.6** Assembled conjugate cams with a measuring fixture consisting of two oscillating flat-faced followers.

the constant  $\eta$ , and thus the added revolute joint will be redundant. In practice, for the machined conjugate cams with profile errors, the magnitude of angle  $\eta^*$  will vary with respect to the cam rotation angle  $\theta$ , and the variation of the subtending angle of the follower faces,  $\Delta\eta$  ( $= \eta^* - \eta$ ), may indicate the variation of profile errors. Thus, a measuring fixture simply consists of oscillating arms 3 and 4. The magnitude of the subtending angle variation,  $\Delta\eta$ , can be measured by a dial indicator mounted to arm 3 with its contact tip touching the extended end of arm 4. Then through actually measuring the magnitude of  $\Delta\eta$  with respect to  $\theta$ , the cam profile errors can be indirectly examined.

On the other hand, the distance from the cam center  $O_2$  to the follower pivot center  $O_3$ ,  $f$ , is also a constant. If, as shown in Fig. C.7, a slider (link 4) is intentionally added to connect the frame (link 1) and the follower (link 3) such that the center distance,  $f^*$ , is changed to be variable, the mechanism will no longer be overconstrained. When the cams rotate, in the extreme case that the machined conjugate cams have no profile errors, the center distance  $f^*$  will always equal the constant  $f$ , and thus the added slider will be redundant. Because the machined conjugate cams are unavoidably with profile errors, the magnitude of distance  $f^*$  will vary with respect to the cam rotation angle  $\theta$ , and the variation of the center distance,  $\Delta f$  ( $= f^* - f$ ), may indicate the variation of profile errors.

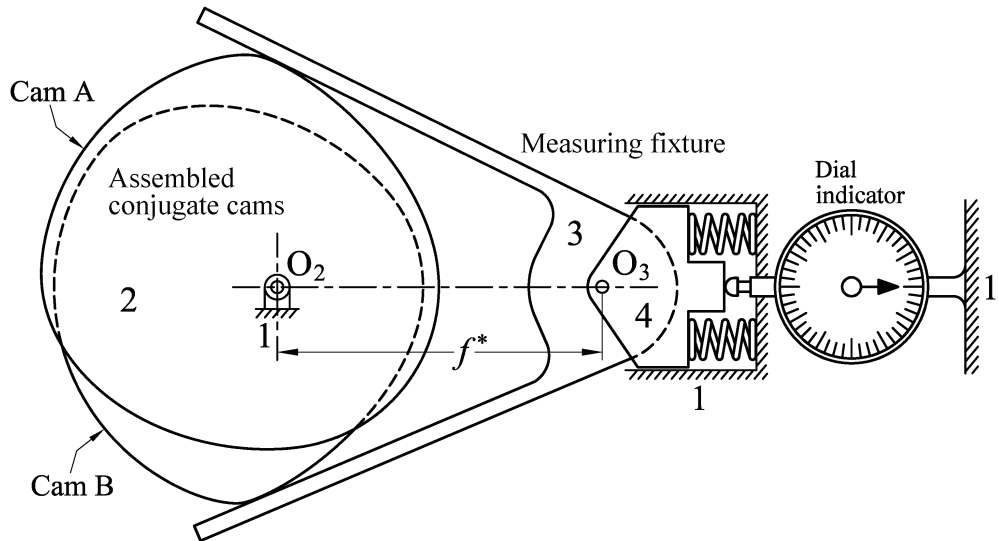


**Figure C.7** Assembled conjugate cams with a measuring fixture consisting of a floating flat-faced follower pivoted on a slider.

Thus, a measuring fixture simply consists of floating link 3 pivoted on slider 4. The magnitude of the center distance variation,  $\Delta f$ , can be measured by a dial indicator mounted to the frame with its contact tip touching slider 4. Then through actually measuring the magnitude of  $\Delta f$  with respect to the cam rotation angle  $\theta$ , the cam profile errors can be indirectly examined.

## REFERENCES

- [1] Chen, F. Y., 1982, *Mechanics and Design of Cam Mechanisms*, Pergamon Press, New York, pp. 1-128, pp. 152-177, pp. 305-330.
- [2] Jenson, P. W., 1987, *Cam Design and Manufacture—Second Edition*, Marcel Dekker, New York, pp. 1-57.
- [3] Koloc, Z. and Václavík, M., 1993, *Cam Mechanisms*, Elsevier, New York, pp. 9-19, pp. 23-165, p. 383, pp. 411-413.
- [4] Reeve, J., 1995, *Cams for Industry: a Handbook for Designers of Special-Purpose Machines*, Mechanical Engineering Publications, London, pp. 1-8, pp. 22-89, pp. 262-279.
- [5] 日本カム工業会技術委員会（編），1996，カム機構図例集，機械設計，第 40 卷，第 14 號，9 月臨時増刊號，2-130 頁，148 頁。(in Japanese)
- [6] Norton, R. L., 2002, *Cam Design and Manufacturing Handbook*, Industrial Press, New York, pp. 1-11, pp. 27-150, pp. 233-241, pp. 315-334, pp. 378-379, pp. 393-450, pp. 475-520.
- [7] Rothbart, H. A. (Ed.), 2004, *Cam Design Handbook*, McGraw-Hill, New York, pp. 1-17, pp. 27-161, pp. 222-223, pp. 258-259, pp. 285-313, pp. 366-367, pp. 505-527.
- [8] 劉昌祺，牧野洋，曹西京，2005，凸輪機構設計，機械工業出版社，北京，1-5 頁，35-53 頁，112-118 頁，260-305 頁。(in Chinese)
- [9] Pukrabek, W. W., 1997, *Engineering Fundamentals of the Internal Combustion Engine*, Prentice-Hall, Upper Saddle River, New Jersey, p. 16, p. 24.
- [10] Hartenberg, R. S. and Denavit, J., 1964, *Kinematic Synthesis of Linkages*, McGraw-Hill, New York, pp. 59-63, pp. 140-144, pp. 295-308, pp. 315-320.
- [11] Grosjean, J., 1991, *Kinematics and Dynamics of Mechanisms*, McGraw-Hill, New York, pp. 75-78, pp. 82-83, pp. 111-121, pp. 267-285.

- [12] Wu, L. I., 2003, "Calculating conjugate cam profiles by vector equations," *Proceedings of the Institution of Mechanical Engineers, Part C: Journal of Mechanical Engineering Science*, Vol. 217, No. 10, pp. 1117-1123.
- [13] Grewal, P. S. and Newcombe, W. R., 1988, "Dynamic performance of high-speed semi-rigid follower cam systems—effects of cam profile errors," *Mechanism and Machine Theory*, Vol. 23, No. 2, pp. 121-133.
- [14] Norton, R. L., 1988, "Effect of manufacturing method on dynamic performance of cams—an experimental study. Part I—eccentric cams and Part II—double dwell cams," *Mechanism and Machine Theory*, Vol. 23, No. 3, pp. 191-208.
- [15] Yan, H. S. and Tai, H. M., 1996, "The effects of manufacturing errors on planar conjugate cams," *Journal of the Chinese Society of Mechanical Engineers*, Vol. 17, No. 2, pp. 145-153.
- [16] Spotts, M. F., 1985, *Design of Machine Elements—Sixth Edition*, Prentice-Hall, Englewood Cliffs, New Jersey, p. 611.
- [17] Dhande, S. G. and Chakraborty, J., 1975, "Mechanical error analysis of cam-follower systems—a stochastic approach," *Fourth World Congress on the Theory of Machines and Mechanisms—Proceedings*, Mechanical Engineering Publications, London, pp. 957-962.
- [18] Chakraborty, J. and Dhande, S. G., 1977, *Kinematics and Geometry of Planar and Spatial Cam Mechanisms*, Wiley Eastern, New Delhi, pp. 1-141.
- [19] Lin, P. D. and Hsieh, J. F., 2000, "Dimension inspection of spatial cams by CNC coordinate measuring machines," *Transactions of the ASME, Journal of Manufacturing Science and Engineering*, Vol. 122, No. 1, pp. 149-157.
- [20] Qiu, H., Li, Y., Cheng, K., and Li, Y., 2000, "A practical evaluation approach towards form deviation for two-dimensional contours based on coordinate measurement data," *International Journal of Machine Tools and Manufacture*, Vol. 40, No. 2, pp. 259-275.
- [21] Qiu, H., Li, Y. B., Cheng, K., Li, Y., and Wang, J., 2000, "A study on an evaluation

method for form deviations of 2D contours from coordinate measurement," *The International Journal of Advanced Manufacturing Technology*, Vol. 16, No. 6, pp. 413-423.

- [22] Qiu, H., Cheng, K., Li, Y., Li, Y., and Wang, J., 2000, "An approach to form deviation evaluation for CMM measurement of 2D curve contours," *Journal of Materials Processing Technology*, Vol. 107, No. 1-3, pp. 119-126.
- [23] Tsay, D. M., Tseng, K. S., and Chen, H. P., 2006, "A procedure for measuring planar cam profiles and their follower motions," *Transactions of the ASME, Journal of Manufacturing Science and Engineering*, Vol. 128, No. 3, pp. 697-704.
- [24] Mitutoyo Corp., <http://www.mitutoyo.co.jp/products/zahyou/legex.pdf>.
- [25] MacCarthy, B. L. and Burns, N. D., 1985, "An evaluation of spline functions for use in cam design," *Proceedings of the Institution of Mechanical Engineers, Part C: Journal of Mechanical Engineering Science*, Vol. 199, No. 3, pp. 239-248.
- [26] MacCarthy, B. L., 1988, "Quintic splines for kinematic design," *Computer-Aided Design*, Vol. 20, No. 7, pp. 406-415.
- [27] Tsay, D. M. and Huey Jr., C. O., 1988, "Cam motion synthesis using spline functions," *Transactions of the ASME, Journal of Mechanisms, Transmissions, and Automation in Design*, Vol. 110, No. 2, pp. 161-165.
- [28] Yoon, K. and Rao, S. S., 1993, "Cam motion synthesis using cubic splines," *Transactions of the ASME, Journal of Mechanical Design*, Vol. 115, No. 3, pp. 441-446.
- [29] Tsay, D. M. and Huey Jr., C. O., 1993, "Application of rational B-spline to the synthesis of cam-follower motion programs," *Transactions of the ASME, Journal of Mechanical Design*, Vol. 115, No. 3, pp. 621-626.
- [30] Tsay, D. M. and Huang, G. S., 1996, "The synthesis of follower motions of camoids using nonparametric B-splines," *Transactions of the ASME, Journal of Mechanical Design*, Vol. 118, No. 1, pp. 138-143.
- [31] Wang, L. C. T. and Yang, Y. T., 1996, "Computer aided design of cam motion

- programs," *Computers in Industry*, Vol. 28, No. 2, pp. 151-161.
- [32] Mosier, R. G., 2000, "Modern cam design," *International Journal of Vehicle Design*, Vol. 23, No. 1/2, pp. 38-55.
- [33] Qiu, H., Lin, C. J., Li, Z. Y., Ozaki, H., Wang, J., and Yue, Y., 2005, "A universal optimal approach to cam curve design and its applications," *Mechanism and Machine Theory*, Vol. 40, No. 6, pp. 669-692.
- [34] Farin, G., 1993, *Curves and Surfaces for Computer Aided Geometric Design: a Practical Guide—Third Edition*, Academic Press, San Diego.
- [35] de Boor, C., 2001, *A Practical Guide to Splines—Revised Edition*, Springer-Verlag, New York.
- [36] Rogers, D. F., 2001, *An Introduction to NURBS: with Historical Perspective*, Morgan Kaufmann Publishers, San Francisco.
- [37] Paul, B., 1979, *Kinematics and Dynamics of Planar Machinery*, Prentice-Hall, Englewood Cliffs, New Jersey, pp. 133-140, pp. 285-289.
- [38] Martin, G. H., 1982, *Kinematics and Dynamics of Machines—Second Edition*, McGraw-Hill, New York, pp. 128-132, pp. 208-216, pp. 471-474.
- [39] Mabie, H. H. and Reinholtz, C. F., 1987, *Mechanisms and Dynamics of Machinery—Fourth Edition*, John Wiley & Sons, New York, pp. 73-80.
- [40] Doughty, S., 1988, *Mechanics of Machines*, John Wiley & Sons, New York, pp. 124-127.
- [41] Uicker Jr., J. J., Pennock, G. R., and Shigley, J. E., 2003, *Theory of Machines and Mechanisms—Third Edition*, Oxford University Press, New York, pp. 203-211.
- [42] Waldron, K. J. and Kinzel, G. L., 1999, *Kinematics, Dynamics, and Design of Machinery*, John Wiley & Sons, New York, pp. 349-360.
- [43] Erdman, A. G., Sandor, G. N., and Kota, S., 2001, *Mechanism Design: Analysis and Synthesis, Volume I—Fourth Edition*, Prentice-Hall, Upper Saddle River, New Jersey, pp. 408-412.
- [44] Wilson, C. E. and Sadler, J. P., 2003, *Kinematics and Dynamics of Machinery—*

*Third Edition (International Edition)*, Prentice-Hall, Upper Saddle River, New Jersey, pp. 340-343, pp. 364-388.

- [45] Hanson, R. S. and Churchill, F. T., 1962, "Theory of envelopes provides new cam design equations," *Product Engineering*, 20 August, pp. 45-55.
- [46] Boltianskii, V. G., 1964, *Envelopes*, Pergamon Press, Oxford.
- [47] Backhouse, C. J. and Rees Jones, J., 1994, "The application of envelope theory to the surface geometry of spool winding cams," *Proceedings of the Institution of Mechanical Engineers, Part B: Journal of Engineering Manufacture*, Vol. 208, No. 2, pp. 153-156.
- [48] Hwang, G. S., Tsay, D. M., and Huang, M. H., 1996, "Profile determination of plate cams with oscillating convex arbitrary-shaped followers," *Proceedings of the Institution of Mechanical Engineers, Part C: Journal of Mechanical Engineering Science*, Vol. 210, No. 4, pp. 333-339.
- [49] Tsay, D. M. and Wei, H. M., 1996, "A general approach to the determination of planar and spatial cam profiles," *Transactions of the ASME, Journal of Mechanical Design*, Vol. 118, No. 2, pp. 259-265.
- [50] Yang, S. C., 2001, "Determination of spherical cam profiles by envelope theory," *Journal of Materials Processing Technology*, Vol. 116, No. 2-3, pp. 128-136.
- [51] Meng, J. L., Hsieh, K. E., and Tsay, C. B., 1987, "An analytical method for synthesis of cam profiles," *Journal of the Chinese Society of Mechanical Engineers*, Vol. 8, No. 4, pp. 271-276.
- [52] Litvin, F. L., 1989, *Theory of Gearing*, NASA Reference Publication 1212, Washington D.C., pp. 63-92, pp. 166-214, pp. 241-252.
- [53] Litvin, F. L., 1994, *Gear Geometry and Applied Theory*, Prentice-Hall, Englewood Cliffs, New Jersey, pp. 107-159, pp. 258-287.
- [54] Yan, H. S. and Cheng, W. T., 1998, "Axode synthesis of cam-follower mechanisms with hyperboloidal rollers," *JSME International Journal, Series C: Dynamics, Control, Robotics, Design and Manufacturing*, Vol. 41, No. 3, pp. 460-469.

- [55] Davidson, J. K., 1978, "Calculating cam profiles quickly," *Machine Design*, 7 December, pp. 151-155.
- [56] Rees Jones, J., 1978, "Mechanisms—cam cutting co-ordinates," *Engineering*, March, pp. 220-224.
- [57] Wu, L. I., Hung, G. H., and Chang, S. L., 2002, "The determination of disk-cam profile by vector equations," *Journal of Technology*, Vol. 17, No. 1, pp. 59-65. (in Chinese)
- [58] Wu, L. I., Chang, W. T., and Liu, C. H., 2007, "The design of varying-velocity translating cam mechanisms," *Mechanism and Machine Theory*, Vol. 42, No. 3, pp. 352-364.
- [59] Giordana, F., Rognoni, V., and Ruggieri, G., 1979, "On the influence of measurement errors in the kinematic analysis of cams," *Mechanism and Machine Theory*, Vol. 14, No. 5, pp. 327-340.
- [60] Giordana, F., Rognoni, V., and Ruggieri, G., 1980, "The influence of construction errors in the law of motion of cam mechanisms," *Mechanism and Machine Theory*, Vol. 15, No. 1, pp. 29-45.
- [61] Johnson, R. C., 1957, "Method of finite differences in cam design," *Machine Design*, 14 November, pp. 159-161.
- [62] Creveling, C. M., 1997, *Tolerance Design: a Handbook for Developing Optimal Specifications*, Addison-Wesley, Reading, Massachusetts, pp. 1-197.
- [63] Kim, H. R. and Newcombe, W. R., 1978, "Stochastic error analysis in cam mechanisms," *Mechanism and Machine Theory*, Vol. 13, No. 6, pp. 631-641.
- [64] Kim, H. R. and Newcombe, W. R., 1982, "The effect of cam profile errors and system flexibility on cam mechanism output," *Mechanism and Machine Theory*, Vol. 17, No. 1, pp. 57-72.
- [65] Rao, S. S. and Gavane, S. S., 1982, "Analysis and synthesis of mechanical error in cam-follower systems," *Transactions of the ASME, Journal of Mechanical Design*, Vol. 104, No. 1, pp. 52-62.

- [66] Rao, S. S., 1984, "Error analysis of cam-follower systems: a probabilistic approach," *Proceedings of the Institution of Mechanical Engineers, Part C: Journal of Mechanical Engineering Science*, Vol. 198, No. 12, pp. 155-162.
- [67] Wang, W. H., Tseng, C. H., Tsay, C. B., and Ling, S. F., 1993, "On the manufacturing tolerance of disk cam profile," *Journal of Materials Processing Technology*, Vol. 38, No. 1-2, pp. 71-84.
- [68] Watanabe, K., Yuasa, F., and Kon'no, M., 1993, "An exact analysis of plate cam mechanisms having errors in kinematic constants," *Transactions of the JSME, Part C*, Vol. 59, No. 561, pp. 1518-1526. (in Japanese)
- [69] Wang, W. H., Tseng, C. H., and Tsay, C. B., 1997, "Surface contact analysis for a spatial cam mechanism," *Transactions of the ASME, Journal of Mechanical Design*, Vol. 119, No. 2, pp. 169-177.
- [70] Wang, W. H., Tseng, C. H., and Tsay, C. B., 1999, "On the optimization of spatial cam mechanisms considering mechanical errors," *International Journal of Modelling and Simulation*, Vol. 19, No. 1, pp. 94-100.
- [71] Chiu, H., Ozaki, H., Sato, E., Suzuki, T., Oho, A., and Ariura, Y., 1993, "An analysis using offset curves for profiles, manufacturing and errors of plane cams," *JSME International Journal, Series C: Dynamics, Control, Robotics, Design and Manufacturing*, Vol. 36, No. 1, pp. 110-118.
- [72] Zhang, C. and Wang, H. P., 1993, "Tolerance analysis and synthesis for cam mechanisms," *International Journal of Production Research*, Vol. 31, No. 5, pp. 1229-1245.
- [73] Lin, P. D. and Hwang, S. G., 1994, "Modeling for error analysis of cam mechanisms by using  $4 \times 4$  homogeneous transformation matrix," *Mathematical and Computer Modelling*, Vol. 19, No. 5, pp. 33-42.
- [74] Wu, Z., ElMaraghy, W. H., and ElMaraghy, H. A., 1988, "Evaluation of cost-tolerance algorithms for design tolerance analysis and synthesis," *Manufacturing Review*, Vol. 1, No. 3, pp. 168-179.

- [75] Ostwald, P. F. and Blake, M. O., 1989, "Estimating cost associated with dimensional tolerance," *Manufacturing Review*, Vol. 2, No. 4, pp. 277-282.
- [76] Chase, K. W., Greenwood, W. H., Loosli, B. G., and Hauglund, L. F., 1990, "Least cost tolerance allocation for mechanical assemblies with automated process selection," *Manufacturing Review*, Vol. 3, No. 1, pp. 49-59.
- [77] Dong, Z. and Soom, A., 1990, "Automatic optimal tolerance design for related dimension chains," *Manufacturing Review*, Vol. 3, No. 4, pp. 262-271.
- [78] Chen, M. S., 1995, "Optimizing tolerance allocation for a mechanical assembly with nonlinear multiple constraints," *Journal of the Chinese Society of Mechanical Engineers*, Vol. 16, No. 4, pp. 349-361.
- [79] Chen, M. S., 1996, "Optimizing tolerance allocation for mechanical components correlated by selective assembly," *The International Journal of Advanced Manufacturing Technology*, Vol. 12, No. 5, pp. 349-355.
- [80] Kimura, F. (Ed.), 1996, *Computer-Aided Tolerancing*, Chapman & Hall, London.
- [81] Ji, S., Li, X., Ma, Y., and Cai, H., 2000, "Optimal tolerance allocation based on fuzzy comprehensive evaluation and genetic algorithm," *The International Journal of Advanced Manufacturing Technology*, Vol. 16, No. 7, pp. 461-468.
- [82] Dhande, S. G. and Chakraborty, J., 1973, "Analysis and synthesis of mechanical error in linkages—a stochastic approach," *Transactions of the ASME, Journal of Engineering for Industry, Series B*, Vol. 95, No. 3, pp. 672-676.
- [83] Chakraborty, J., 1975, "Synthesis of mechanical error in linkages," *Mechanism and Machine Theory*, Vol. 10, No. 2-3, pp. 155-165.
- [84] Choubey, M. and Rao, A. C., 1982, "Synthesizing linkages with minimal structural and mechanical error based upon tolerance allocation," *Mechanism and Machine Theory*, Vol. 17, No. 2, pp. 91-97.
- [85] Mallik, A. K. and Dhande, S. G., 1987, "Analysis and synthesis of mechanical error in path-generating linkages using a stochastic approach," *Mechanism and Machine Theory*, Vol. 22, No. 2, pp. 115-123.

- [86] Khare, A. K., 1988, "Mechanical error synthesis of 4-bar function generating mechanism using information theory," *Transactions of the Canadian Society for Mechanical Engineering*, Vol. 12, No. 3, pp. 149-152.
- [87] Rhyu, J. H. and Kwak, B. M., 1988, "Optimal stochastic design of four-bar mechanisms for tolerance and clearance," *Transactions of the ASME, Journal of Mechanisms, Transmissions, and Automation in Design*, Vol. 110, No. 3, pp. 255-262.
- [88] Shi, Z., 1997, "Synthesis of mechanical error in spatial linkages based on reliability concept," *Mechanism and Machine Theory*, Vol. 32, No. 2, pp. 255-259.
- [89] Kawasaki, Y., Yamamoto, S., Yamamoto, Y., Ito, K., Nagano, H., Inanobe, S., and Watanabe, Y., 1975, "Lift error on grinding cam profile," *CIRP Annals*, Vol. 24, No. 1, pp. 253-258.
- [90] Norton, R. L., Levasseur, D., Pettit, A., and Alamsyah, C., 1988, "Analysis of the effect of manufacturing methods and heat treatment on the performance of double dwell cams," *Mechanism and Machine Theory*, Vol. 23, No. 6, pp. 461-473.
- [91] Yamaguchi, F., 1988, *Curves and Surfaces in Computer Aided Geometric Design*, Springer-Verlag, Berlin.
- [92] Chiang, Y. M. and Chen, F. L., 1999, "Sculptured surface reconstruction from CMM measurement data by a software iterative approach," *International Journal of Production Research*, Vol. 37, No. 8, pp. 1679-1695.
- [93] Yin, Z., Zhang, Y., and Jiang, S., 2003, "A methodology of sculptured surface fitting from CMM measurement data," *International Journal of Production Research*, Vol. 41, No. 14, pp. 3375-3384.
- [94] Adcole Corp., <http://www.adcole.com/index.htm>.
- [95] Andreasen, M. M., Kahler, S., Lund, T., and Swift, K. G., 1988, *Design for Assembly—Second Edition*, IFS Publications/Springer-Verlag, Bedford, UK/Berlin.
- [96] Redford, A. and Chal, J., 1994, *Design for Assembly: Principles and Practice*, McGraw-Hill International, London.

- [97] Molloy, O., Tilley, S., and Warman, E. A., 1998, *Design for Manufacturing and Assembly: Concepts, Architectures and Implementation*, Chapman & Hall, London.
- [98] Boothroyd, G., Dewhurst, P., and Knight, W., 2002, *Product Design for Manufacture and Assembly—Second Edition*, Marcel Dekker, New York.
- [99] Hall Jr., A. S., 1981, *Notes on Mechanism Analysis*, Waveland Press, Prospect Heights, Illinois, pp. 1.8-1.35.
- [100] Hall Jr., A. S., 1961, *Kinematics and Linkage Design*, Waveland Press, Prospect Heights, Illinois, pp. 2-3, pp. 65-67.
- [101] McPhate, A. J. and Daniel Jr., L. R., 1962, “A kinematic analysis of four-bar equivalent mechanisms for plane-motion direct-contact mechanisms,” *Proceedings of the Seventh Conference on Mechanisms*, Purdue University, West Lafayette, Indiana, pp. 61-65.
- [102] Ting, K. L. and Long, Y., 1996, “Performance quality and tolerance sensitivity of mechanisms,” *Transactions of the ASME, Journal of Mechanical Design*, Vol. 118, No. 1, pp. 144-150.
- [103] Garrett, R. E. and Hall Jr., A. S., 1969, “Effect of tolerance and clearance in linkage design,” *Transactions of the ASME, Journal of Engineering for Industry, Series B*, Vol. 91, No. 1, pp. 198-202.
- [104] Rees Jones, J., 1978, “Mechanisms—cam curvature and interference,” *Engineering*, May, pp. 460-463.
- [105] Freudenstein, F., 1955, “Approximate synthesis of four-bar linkages,” *Transactions of the ASME*, Vol. 77, August, pp. 853-861.
- [106] Machine Engineering (MEG) Corp., 1996, *Products Guide Book*, Nagano, Japan, pp. 74-81. (in Japanese)
- [107] Arora, J. S., 1989, *Introduction to Optimum Design*, McGraw-Hill, New York.
- [108] The MathWorks Inc., 2007, *MATLAB Optimization Toolbox User’s Guide—Version 3.1.1*, Natick, Massachusetts.
- [109] Giddings & Lewis Sheffield Measurement, 1996, *Advanced Directinspect Level II*:

*Student Workbook*, Dayton, Ohio.

- [110] Gogu, G., 2005, "Mobility of mechanisms: a critical review," *Mechanism and Machine Theory*, Vol. 40, No. 9, pp. 1068-1097.
- [111] Shigley, J. E. and Mischke, C. R., 1989, *Mechanical Engineering Design—Fifth Edition*, McGraw-Hill, New York, pp. 470-473.
- [112] Slocum, A. H., 1992, *Precision Machine Design*, Prentice-Hall, Englewood Cliffs, New Jersey, pp. 60-61, pp. 421-550.
- [113] Nakazawa, H., 1994, *Principles of Precision Engineering*, Oxford University Press, Oxford, pp. 83-90.



## VITA



Wen-Tung Chang was born on August 24, 1978 in Taipei, Taiwan. He graduated from the Taipei Municipal Chenggong High School (臺北市立成功高中) in Taipei in 1996. In the same year, he entered the National Taiwan Ocean University (國立臺灣海洋大學) in Keelung, Taiwan, where he received the Degree of Bachelor of Science in Mechanical and Marine Engineering with the highest honors in June of 2000. The Mechanical Engineering is his major course and the Marine Engineering is his minor one. In September of 2000, he entered the Institute of Mechanical and Marine Engineering of National Taiwan Ocean University, where he received the Degree of Master of Science in June of 2002. His Master Thesis entitled “On the Force Transmission Performance of Planar and Spatial Linkage Mechanisms” won him a fine piece of writing in the 2002 Thesis Award of the Chinese Society of Mechanical Engineers (中國機械工程學會碩士論文獎佳作). Since September of 2002, he has been pursuing a Degree of Doctor of Philosophy at the Institute of Power Mechanical Engineering of National Tsing Hua University (國立清華大學) in Hsinchu, Taiwan. His research interests include kinematics and dynamics of machinery, analysis and design of linkage and cam mechanisms, innovative mechanism design, applied optimal design, and precision machine design.

# PUBLICATION LIST

## (A) JOURNAL PAPERS

- [1] Lin, C. C. and **Chang, W. T.**, 2002, "The force transmissivity index of planar linkage mechanisms," *Mechanism and Machine Theory*, Vol. 37, No. 12, pp. 1465-1485. (SCI, EI)
- [2] Liu, C. S. and **Chang, W. T.**, 2002, "Frictional behaviour of a belt-driven and periodically excited oscillator," *Journal of Sound and Vibration*, Vol. 258, No. 2, pp. 247-268. (SCI, EI)
- [3] Lin, C. C. and **Chang, W. T.**, 2003, "The force transmissibility of planar multiloop linkages," *Proceedings of the Institution of Mechanical Engineers, Part C: Journal of Mechanical Engineering Science*, Vol. 217, No. 11, pp. 1259-1270. (SCI, EI)
- [4] **Chang, W. T.**, Lin, C. C., and Lee, J. J., 2003, "Force transmissibility performance of parallel manipulators," *Journal of Robotic Systems*, Vol. 20, No. 11, pp. 659-670. (SCI, EI)
- [5] **Chang, W. T.**, Tseng, C. H., and Wu, L. I., 2004, "Creative mechanism design for a prosthetic hand," *Proceedings of the Institution of Mechanical Engineers, Part H: Journal of Engineering in Medicine*, Vol. 218, No. 6, pp. 451-459. (SCI, EI)
- [6] Wu, L. I. and **Chang, W. T.**, 2005, "Analysis of mechanical errors in disc cam mechanisms," *Proceedings of the Institution of Mechanical Engineers, Part C: Journal of Mechanical Engineering Science*, Vol. 219, No. 2, pp. 209-224. (SCI, EI)
- [7] **Chang, W. T.**, Lin, C. C., and Wu, L. I., 2005, "A note on Grashof's theorem," *Journal of Marine Science and Technology*, Vol. 13, No. 4, pp. 239-248. (EI)
- [8] **Chang, W. T.** and Wu, L. I., 2006, "Mechanical error analysis of disk cam mechanisms with a flat-faced follower," *Journal of Mechanical Science and Technology*, Vol. 20, No. 3, pp. 345-357. (SCI)
- [9] Wu, L. I., **Chang, W. T.**, and Liu, C. H., 2007, "The design of varying-velocity

translating cam mechanisms,” *Mechanism and Machine Theory*, Vol. 42, No. 3, pp. 352-364. (SCI, EI)

- [10] **Chang, W. T.** and Wu, L. I., 2006, “A simplified method for examining profile deviations of conjugate disk cams,” submitted to *Transactions of the ASME, Journal of Mechanical Design*, MD-06-1465, revised. (SCI, EI)
- [11] **Chang, W. T.**, Wu, L. I., Fuh, K. H., and Lin, C. C., 2007, “Inspecting profile errors of conjugate disk cams with coordinate measurement,” submitted to *Transactions of the ASME, Journal of Manufacturing Science and Engineering*, MANU-07-1094, accepted with revision. (SCI, EI)
- [12] **Chang, W. T.**, Tseng, C. H. and Wu, L. I., 2007, “Conceptual Innovation of a Prosthetic Hand Using TRIZ,” submitted to *Journal of the Chinese Society of Mechanical Engineers*, under review. (EI)

## (B) CONFERENCE PAPERS

- 
- [1] Lin, C. C. and **Chang, W. T.**, 2001, “A new force transmission index for planar linkage mechanisms,” *Proceedings of The 18th CSME National Conference on Mechanical Engineering*, Vol. 3, pp. 703-711, Taipei, Taiwan.
  - [2] **Chang, W. T.**, Lin, C. C., and Lee, J. J., 2002, “The force transmission performance of parallel manipulators,” *The 26th National Conference on Theoretical and Applied Mechanics*, Paper No. L007, Huwei, Taiwan.
  - [3] Lin, C. C., **Chang, W. T.**, and Lee, J. J., 2002, “The force transmission performance of planar multiloop linkages,” *The 26th National Conference on Theoretical and Applied Mechanics*, Paper No. L008, Huwei, Taiwan.
  - [4] 張文桐，林鎮洲，2003，「3-RRR 平台機構力量傳遞性能之最佳化設計」，中國機械工程學會第二十屆全國學術研討會論文集—固力與設計（Part C），947-954 頁，國立臺灣大學，臺北，臺灣。

## (C) PATENTS

- [1] 張文桐，曾錦煥，吳隆庸，2004 年 08 月 11 日，「可切換握持動作之義手構造」，中華民國專利新型第 M240200 號。
- [2] 張文桐，林鎮洲，吳隆庸，2004 年 10 月 11 日，「具有安全釋放功能之義手構造」，中華民國專利新型第 M245957 號。
- [3] 張文桐，林鎮洲，吳隆庸，劉俊賢，李維倫，2005 年 12 月 11 日，「人力推進載具用省力踏板驅動機構」，中華民國專利新型第 M282911 號。
- [4] 張文桐，吳隆庸，林鎮洲，李維倫，2007 年 01 月 01 日，「自行車之無段變速裝置」，中華民國專利發明第 I269749 號。

## (D) OTHER PUBLICATIONS

- [1] Chang, W. T., 2002, *On the Force Transmission Performance of Planar and Spatial Linkage Mechanisms*, Master Thesis, Department of Mechanical and Marine Engineering, National Taiwan Ocean University, Keelung, Taiwan.
- [2] 張文桐，2003，「非對稱運動曲線對凸輪機構接觸力之影響」，機構與機器設計—中華民國機構與機器原理學會會刊，第 14 卷，第 3 號，11-24 頁。
- [3] 吳隆庸，張文桐，2004，「盤形凸輪輪廓及其加工刀具路徑之解析計算法」，機械月刊，第 351 期，10 月號，72-87 頁。
- [4] 吳隆庸，張文桐，2005，「盤形共軛凸輪之共軛性的檢測方法」，機構與機器設計—中華民國機構與機器原理學會會刊，第 16 卷，第 4 號，39-50 頁。
- [5] 張文桐，吳隆庸，2006，「平面曲線之曲率半徑」，機構與機器設計—中華民國機構與機器原理學會會刊，第 17 卷，第 1 號，13-19 頁。